Analysis of Aerosol-Cloud Interaction from Space

Lorenzo Costantino

UNIVERSITE DE VERSAILLES SAINT-QUENTIN-EN-YVELINES

École Doctorale des Sciences de l'Environnement d'Ile-de-France - SEIF

Laboratoire des Sciences du Climat et de l'Environnement (LSCE) – UMR 8212

THÈSE DE DOCTORAT
DE L'UNIVERSITE DE VERSAILLES SAINT–QUENTIN–EN-YVELINES
Spécialité :
Météorologie, océanographie physique et physique de l'environnement

Présentée par :

Lorenzo Costantino

Pour obtenir le grade de Docteur de l'Université de Versailles Saint-Quentin-en-Yvelines

Analysis of Aerosol-Cloud Interaction from Space

Soutenue le : 13 Janvier 2012

Directeur de thèse : François-Marie, Bréon

Devant le jury composé de :

Rapporteurs :

Jérôme RIEDI	Professeur à l'Université de Lille, chercheur au LOA
Jean-Claude ROGER	Professeur à l'Université de Clermont-Ferrand, chercheur au LAMP

Examinateurs :

Philippe BOUSQUET	Professeur à l'UVSQ, chercheur au LSCE
Francois-Marie BRÉON	Chercheur au LSCE (directeur de thèse)
Jean-Pierre CHABOUREAU	Chercheur au Laboratoire d'Aérologie
Jacques PELON	Chercheur au LATMOS

Abstract

The aim of this work is to provide a comprehensive analysis of cloud and aerosol interaction over South-East Atlantic, to quantify the overall aerosol impact on the regional radiation budget. We used data from MODIS, PARASOL and CALIPSO satellites, that fly in close proximity on the same sun-synchronous orbit and allow for complementary observations of the same portion of the atmosphere, within a few minutes.
The main idea is to use CALIPSO vertical information to define whether or not aerosol and cloud layers observed by MODIS and PARASOL are mixed and interacting. We found evidences that, in case of interaction, cloud properties are strongly influenced by aerosol presence (first indirect effect). In particular, there is a decrease in cloud droplet effective radius and liquid water path with aerosol enhancement. On the other hand, we could not evidence any significant impact on the cloud reflectance.

We also analyzed the aerosol impact on precipitation (second indirect effect). In polluted low clouds over the ocean, we found evidence of precipitation suppression and cloud cover increase with increasing aerosol concentration. On the other hand, cloud fraction is shown to be affected by aerosol presence, even if pollution particles are located above cloud top, without physical interaction. This observation is interpreted as a consequence of the aerosol radiative effect.

Aerosol shortwave direct (DRF) and indirect (IRF) radiative forcing at TOA has been quantified, with the use of a radiative transfer model constrained by satellite observations. For the direct effect, there is a competition between cooling (negative, due to light scattering by the aerosols) and warming (positive, due to the absorption by the same particles). The regional six year (2005-2010), the spatial mean and the standard deviation is equal to -0.07±8.03 W/m² for DRF and -0.05±0.54 W/m² for IRF. Indirect forcing results from the balance of cloud albedo effect (-0.07±0.55 W/m²) and life time effect (0.02±0.12 W/m²). Total aerosol forcing is then negative (cooling) and equal to -0.12±8.02 W/m².

Résumé

Le but de cette thèse est de fournir une analyse exhaustive des interactions entre nuages et aérosols dans le Sud-Est de l'Atlantique, en quantifiant l'impact des aérosols sur le bilan radiatif régional en ondes courtes. Pour cet objectif, nous avons utilisé les données satellitaires de MODIS, PARASOL et CALIPSO, qui fournissent des observations complémentaires et quasi simultanées.
L'idée principale qui a permis une analyse originale est d'utiliser les observations du lidar CALIPSO pour identifier les cas pour lesquels les couches d'aérosols et nuages vues par MODIS et PARASOL sont en interaction (mélangées) et ceux pour lesquels ils sont clairement disjoints. Il ressort de cette analyse que les propriétés des nuages sont fortement influencées par l'interaction avec les aérosols (premier effet indirect). On observe une diminution du rayon efficace de gouttelettes et du contenu en eau sous l'effet d'une hausse de la concentration des particules polluantes. En revanche, nous n'avons pas mis en évidence une modification significative de la réflectance des nuages.

Lorsque les aérosols et les nuages sont mélangés, on observe aussi une diminution de l'occurrence des précipitations (second effet indirect) et l'augmentation de la couverture nuageuse. D'autre part, la fraction nuageuse est affectée par la présence d'aérosols, même si les particules de pollution sont situées au-dessus du sommet des nuages (sans interaction physique). Cette observation est interprétée comme étant une conséquence de l'effet radiatif des aérosols.

Pour quantifier le forçage radiatif direct et indirect des aérosols, nous avons utilisé un code de transfert radiatif rapide à onde courte, contraint par les observations satellitaires. Sur six ans (2005-2010), le forçage moyen et sa déviation standard sur toute la région sont égaux à -0.07±8.03 W/m² pour l'effet direct et -0.05±0.54 W/m² pour l'effet indirect. Ce dernier est déterminé par l'équilibre entre l'effet de la variation de l'albédo (-0.07±0.55 W/m²) et celui de la couverture nuageuse (0.02±0.12 W/m²). Le forçage total est donc négatif (refroidissement) et égal à -0.12±8.02 W/m².

Table of Contents

Analyse des interactions entre aérosol et nuages par mesures télédétectées

Synthèse

Ce travail porte sur l'analyse des interactions entre les aérosols et les nuages, avec, in-fine, l'objectif de quantifier l'impact radiatif des aérosols, en incluant l'effet indirect via la modification des caractéristiques microphysiques et macrophysiques des nuages. Pour mener à bien cette étude, nous avons utilisé des données de télédétection spatiale acquises par les capteurs MODIS, PARASOL et CALIPOP. Notre travail est focalisé sur une zone du Sud-Est Atlantique (au large de l'Angola) qui est une région particulièrement intéressante car sous le vent de l'Afrique et deux zones émettrices d'aérosol de brûlis, ainsi que des poussières d'origine saharienne. La principale originalité du travail, par rapport à d'autres études publiées ces dernières années, a été d'utiliser les mesures du lidar spatial CALIPSO, afin de pouvoir analyser la position respective des aérosols et des nuages. Nous avons mis en place une base de données statistiques donnant les distributions de divers paramètres décrivant les couches d'aérosols et de nuages, couplée à un code de transfert radiatif. Ce travail permet de tester un certain nombre d'hypothèses car, comme le signale le dernier rapport de l'IPCC, l'effet radiatif des aérosols et des nuages reste assez mal connu. Pour mieux suivre la démarche scientifique de ce sujet, le manuscrit se décompose en 8 chapitres (hors Introduction et Conclusion).

Dans le Chapitre 1, on pose les bases théoriques et les diverses principes de la formation, en présence d'aérosol, d'un nuage et des précipitations associées.

Dans le Chapitre 2, lui aussi introductif, nous abordons l'aspect télédétection spatiale. Alors que la première partie de ce chapitre est plus historique, la deuxième partie décrit comment les données satellitaires acquises par MODIS, PARASOL et CALIOP sont utilisées à des fins d'inversion des propriétés des nuages et des aérosols.

Le contenu du Chapitre 3 constitue une première approche vers l'analyse des interactions aérosols-nuages. A travers l'analyse des données MODIS sur les feux de forêt, on observe que la zone du Sud-Est Atlantique est une zone particulièrement favorable pour l'étude de ces interactions, étant donné l'injection saisonnière dans l'atmosphère d'aérosols fins générés lors des processus de brûlis. Ensuite, l'analyse s'attelle à une étude saisonnière (4 trimestres) et inter-annuelle (2005-2010) des propriétés optiques des aérosols et des nuages (données MODIS). On observe ainsi une très forte saisonnalité, tant pour les aérosols que pour les nuages, liée (1) au transport d'aérosols de brûlis au large de l'Angola lors de la période Juillet-Septembre, et (2) au transport d'aérosols désertiques dans le golfe de Guinée lors de la période Janvier-Mars (Figure 1). Par contre, les variations inter-annuelles sont limitées.

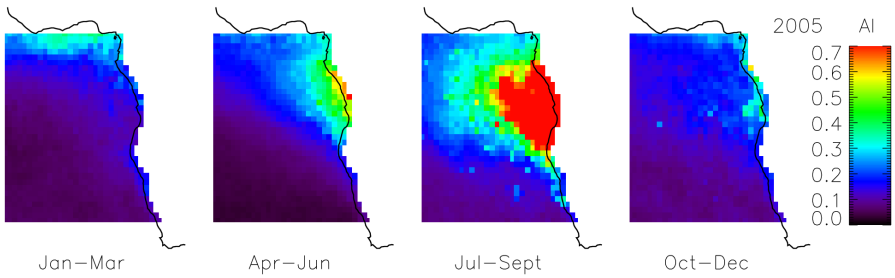

Figure 1: Moyenne saisonnière de l'indexe aérosol (AI), pour le 2005. AI est proportionnel à la concentration d'aérosol dans atmosphère.

Les résultats obtenus montrent une relation nette entre charge en aérosols et paramètres nuageux. Cependant, il apparaît que les corrélations observées peuvent être, au moins en partie, liées à effet météorologique qui couplerait les deux variables de manière fortuite. Une étude plus fine, incluant une analyse des structures temporelles et de la position respective des couches aérosols et nuages, est nécessaire.

Le Chapitre 4 fait un état de l'art, tant théorique qu'expérimental, de l'effet des aérosols sur les nuages et les précipitations associées.

Le Chapitre 5 se focalise sur la corrélation entre l'indice aérosol (AI) et le rayon des particules nuageuses (CDR), toujours sur la zone concernée et à partir de données MODIS. Dans un premier temps (données MODIS), on retrouve bien le même type de relation entre ces 2 paramètres que celle attendue par la théorie (le logarithme du CDR est inversement proportionnelle au logarithme de l'AI) mais avec un coefficient de linéarité très différent. On émet alors l'hypothèse que cela est dû à un problème de mélange aérosols-nuages. Grâce à la méthode MPC proposée, combinant les données de MODIS, PARASOL et CALIOP, on montre qu'il faut distinguer les cas pour lequel la couche d'aérosols est mélangée avec la couche de nuages des cas pour lesquels les 2 couches ne sont pas mélangées (Figure 2). Dans le premier cas (couches en interaction), la relation statistique moyenne est conforme à la théorie et aux résultats existants ; dans le deuxième cas, il n'existe quasiment pas de corrélation. Par conséquent, il est démontré que les aérosols de brûlis ont un effet important sur la microphysique des nuages, et que l'impact moyen observé est cohérent avec les prédictions théoriques [Costantino and Bréon, 2011].

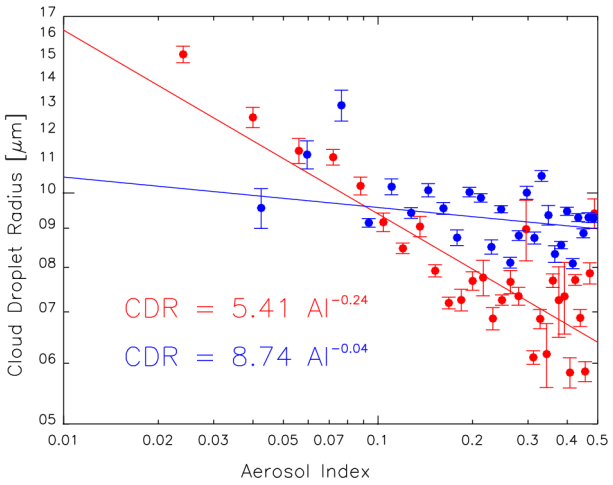

Figure 2: Relations entre le logarithme du CDR et le logarithme du AI, à travers une combinaison des données MODIS (AI), PARASOL (CDR) et CALIOP. L'information verticale apportée par CALIPSO permet de distinguer entre le cas pour lequel les couches d'aérosol et nouages sont mélangées (rouges) du cas pour lequel les 2 couches ne sont pas mélangées (bleu).

Le Chapitre 6 s'inscrit dans la continuité du chapitre précédent, en poursuivent l'étude de l'impact des aérosols de brûlis sur la microphysique des nuages à travers, cette fois, l'analyse de corrélations entre l'indice aérosols (AI) et le rayon des particules nuageuse (CDR), puis l'épaisseur optique des nuages (COT), et enfin le contenu intégré en eau condensée (LWP). Ces deux dernières relations sont, à ce jour, peu documentées et peu quantifiées. Pour cela, on développe cette fois la MMC méthode (MODIS, MODIS, CALIOP) afin de découpler les cas atmosphériques liés aux processus de météorologie locale et ceux des réelles interactions aérosols-nuages. Parallèlement, on confirme la synergie des instruments spatiaux en comparant le rayon des particules nuageuses (MODIS-PARASOL) et l'épaisseur optique des aérosols (MODIS-CALIOP).

Les résultats de la méthode MMC sont de plusieurs ordres. Tout d'abord, on montre que les interactions aérosols-nuages semblent largement dominer les effets météorologiques locaux. Cela permet d'appréhender concrètement l'effet Twomey: en cas de mélange le logarithme du CDR est inversement proportionnelle au logarithme du AI (Figure 3). On trouve aussi que la quantité en eau des nuages (LWP) décroit avec l'AI, en cas d'interaction entre les couches d'aérosol et de nuage (ce qui n'est pas attendu à priori). Après analyse, ce résultat est interprété comme résultant de la faible humidité relative de la masse d'air transportant l'aérosol et qui se mélange à celle du nuage (Figure 4). On montre enfin que l'AI n'est que très peu corrélé avec l'épaisseur optique (COT) des nuages pollués (Figure 5), ce qui aura son importance pour le calcul des impacts radiatifs.

Malgré que le LWP ne suit pas la théorie de Twomey, l'étude menée dans ce chapitre montre que la concentration des aérosols a un impact sur le cycle de vie des nuages et que donc

l'efficacité radiative des aérosols dépend du LWP.

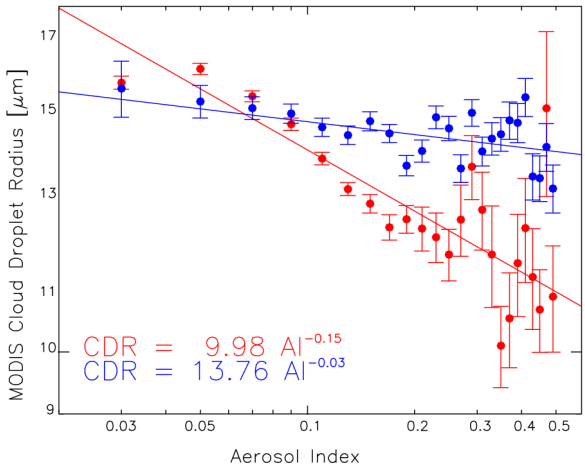

Figure 3: Relations entre le logarithme du CDR et le logarithme du AI, à travers une combinaison des données MODIS (AI), MODIS (CDR) et CALIOP. Le cas pour lequel les couches d'aérosol et nouages sont mélangées est indiqué en rouge, le cas pour lequel les 2 couches ne sont pas mélangées en bleu.

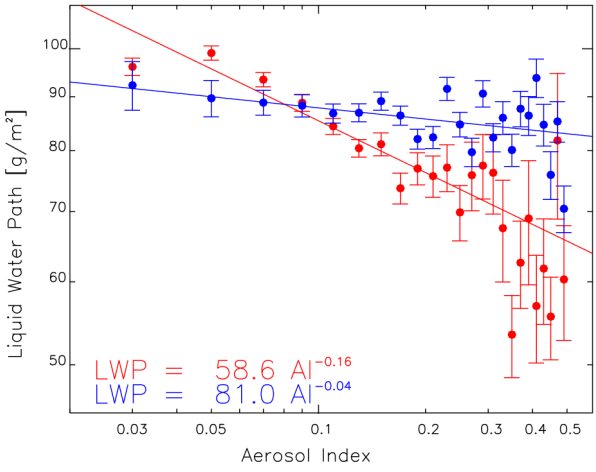

Figure 4: Relations entre le logarithme du LWP et le logarithme du AI, à travers une combinaison des données MODIS (AI), MODIS (LWP) et CALIOP. Le cas pour lequel les couches d'aérosol et nouages sont mélangées est indiqué en rouge, le cas pour lequel les 2 couches ne sont pas mélangées en bleu.

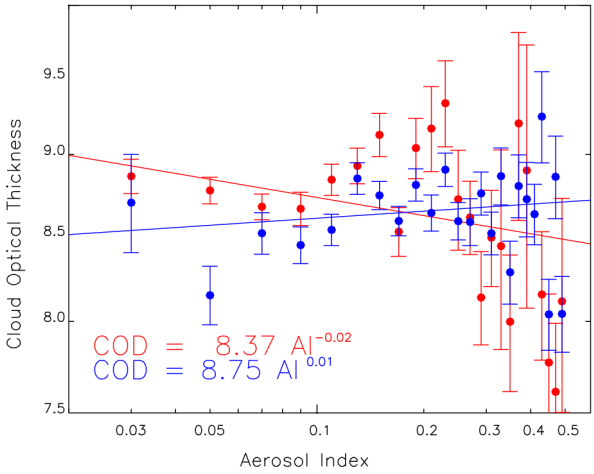

Figure 5: Relations entre le logarithme du COT et le logarithme du AI, à travers une combinaison des données MODIS (AI), MODIS (COT) et CALIOP. Le cas pour lequel les couches d'aérosol et nouages sont mélangées est indiqué en rouge, le cas pour lequel les 2 couches ne sont pas mélangées en bleu.

Le Chapitre 7 s'attelle à l'impact des aérosols sur le cycle de vie des nuages. Dans un premier temps, après un rappel théorique sur l'inhibition possible des précipitations due à la présence des aérosols, on met en évidence la diminution des précipitations des nuages pollués par les aérosols de brûlis dans la zone géographique considérée, pour le cas d'une couche d'aérosols mélangée avec les nuages. Pour COT > 10, les nouages pollués montrent une relation exponentielle entre CDR et COT moins faible que dans le cas des nuages propres (Figure 6), ce qui peut indiquer une inhibition des précipitations. Dans un deuxième temps (Figure 7, gauche), on confirme l'hypothèse (sur la durée de vie des nuages) selon laquelle une augmentation de la concentration en aérosols engendre une augmentation de la fraction nuageuse (CLF) selon une structure horizontale, paramétrée par la pression au sommet des nuages (CTP). Puis, on montre que les aérosols n'affectent pas, par contre, la structure verticale des nuages (Figure 7, droite).
Dans une dernière partie, on indique, à partir de données MODIS et CALIOP, que l'effet radiatif des aérosols (aérosol-nuages pas mélangés) est plus important que l'interaction aérosols-nuages elle-même sur la durée de vie des nuages (Figure 8).

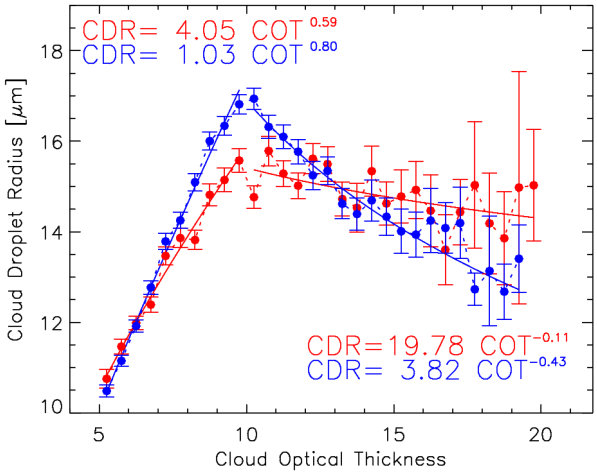

Figure 6: Relations entre CDR et COT, à travers une combinaison des données MODIS (AI), MODIS (COT) et CALIOP. Le cas pour lequel les couches d'aérosol et nouages sont mélangées est indiqué en rouge, le cas pour lequel les 2 couches ne sont pas mélangées en bleu.

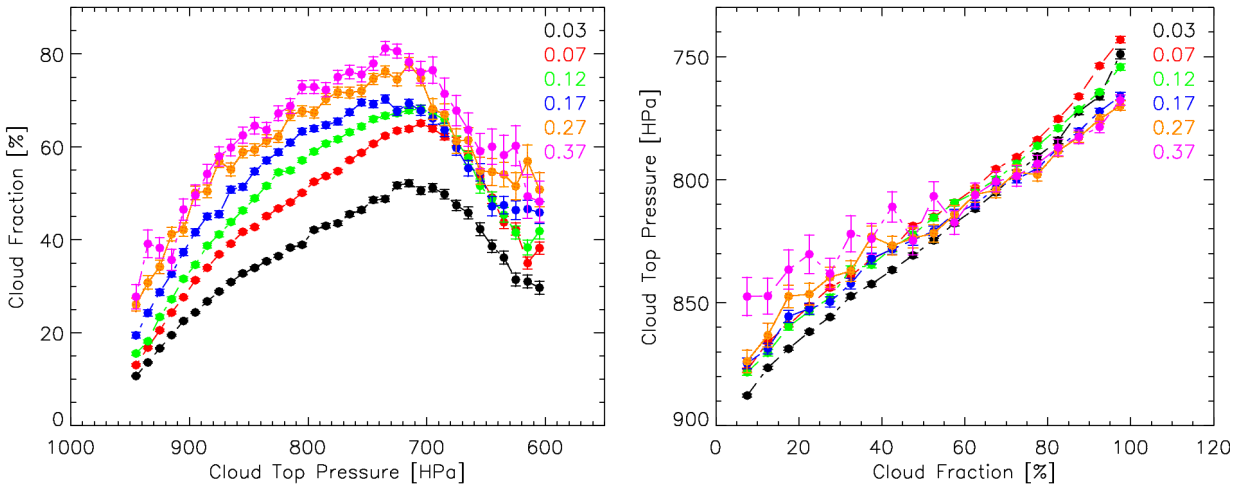

Figure 7: (gauche) Relation entre le CLF (MODIS) et le CTP (MODIS), pour différentes valeurs de l'indexe d'aérosol (MODIS).(droit) Relation entre le CTP et le CLF, pour différentes valeurs de l'indexe d'aérosol.

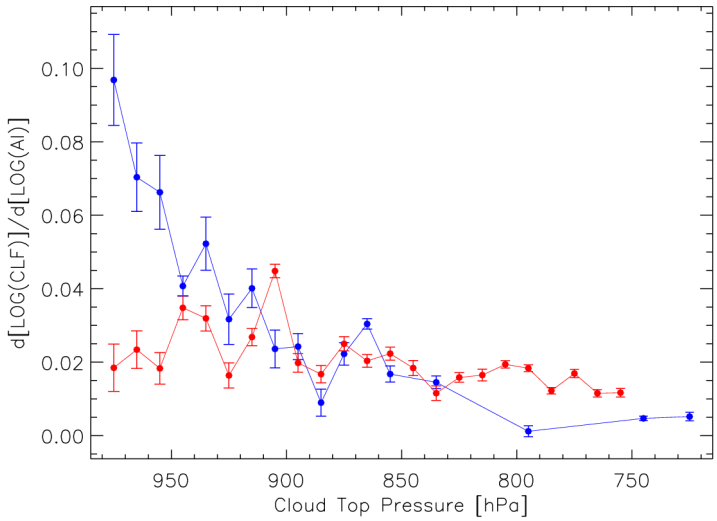

Figure 8: Coefficient de la régression linéaire entre le logarithme du COT et le logarithme du AI, en fonction du développement vertical des nuages, qui augmente quand CTP diminue. Le cas pour lequel les couches d'aérosol et nouages sont mélangées (interaction) est indiqué en rouge, le cas pour lequel les 2 couches ne sont pas mélangées (effet radiatif) en bleu.

Le dernier chapitre (Chapitre 8) aborde les aspects radiatifs des aérosols à travers leurs effets direct et indirect au sommet de l'atmosphère à l'aide d'un modèle de calcul rapide du transfert radiatif.

Pour l'effet direct, on sait que les principales sources d'incertitude sont la valeur de l'albédo de simple diffusion (SSA) et la distribution verticale des aérosols. Nous avons donc mis une attention particulière à ces deux paramètres, en proposant une paramétrisation du SSA avec le type d'aérosols observés, et en utilisant les statistiques de distribution verticale des aérosols et des nuages provenant de CALIOP.

On trouve une forte variabilité saisonnière des impacts directs moyens sur le Sud-Est Atlantique de l'ordre de -5 $W.m^2$ (refroidissement lors du premier trimestre en présence d'aérosols désertiques) à +6 $W.m^2$ (réchauffement lors du troisième trimestre en présence d'aérosols de brûlis) avec des maxima allant respectivement de -25 à +47 $W.m^2$ (Figure 9), ce qui n'est pas anodin. Ces résultats, pas forcément attendus, conduisent à une interprétation des diverses hypothèses utilisées par la communauté.

Le calcul des effets indirects (décomposés en 3 termes ici) montrent que ceux-ci sont d'un ordre inférieur ; de +0.02 $W.m^2$ ($2^{ième}$ trimestre) à -0.09 $W.m^2$ ($4^{ième}$ trimestre) avec des valeurs maximales allant localement de -4 à +4 $W.m^2$ (Figure 10). Cela peut paraître faible mais localement elles ne sont pas forcément négligeables au regard des valeurs globales. On montre donc, que l'effet direct prime largement sur l'effet indirect sur le Sud-Est Atlantique.

Par ailleurs, sur l'ensemble du jeu de données, l'impact radiatif sur la zone étudiée est faible (-0.07 $W.m^2$ en direct et -0.05 $W.m^2$ en indirect) et conduit à un refroidissement de -0.12 $W.m^2$ (Figure 11). On note que cet effet global très faible est dû à une compensation quasi parfaite

entre les impacts positifs et négatifs selon les zones. Localement, les effets sont beaucoup plus forts.

En conclusion, nous avons utilisé dans cette thèse un grand nombre d'observations spatiales, passives et actives, pour caractériser les distributions spatio-temporelles des aérosols et des nuages sur l'Atlantique Sud-Est. Plusieurs relations entre charge en aérosols et paramètres nuageux ont été établies de manière statistique à partir de ces distributions. La difficulté principale est de distinguer les corrélations causales (liée à un processus d'interaction aérosol-nuage) de celles qui sont fortuites (Variations météorologiques conduisant à des corrélation non causales). Dans le but d'identifier les relations causales, nous avons utilisé les mesures actives du lidar CALIPSO qui permettent d'identifier la position respective des couches d'aérosols et de nuages. Nous avons montré que l'impact des aérosols sur la microphysique des nuages est indéniable (décroissance du rayon moyen des gouttes en présence d'aérosols) mais que l'effet sur l'albédo du nuage était insignifiant. Ce résultat apparemment paradoxal est dû à une décroissance du contenu en eau du nuage en présence d'aérosols. Nous pensons qu'il s'agit là d'un effet de mélange de l'air sec (qui contient les aérosols) avec le nuage, conduisant à une diminution de son contenu en eau.
Les relations obtenues sur la dépendance aérosol-nuage, et les distribution tri-dimensionnelles des couches ont ensuite été utilisées dans un code de transfert radiatif afin d'estimer les forçages radiatifs, directs et indirects, des aérosols. Sur la zone d'étude, l'effet est plus faible qu'attendu, compte tenu de la charge importante en aérosols. En fait, les valeurs obtenues résultent d'une compensation entre des effets forts positifs (absorption, en présence de nuages sous-jacents) et des effets forts négatifs (diffusion, en ciel clair). En ce qui concerne les effets indirects, on trouve là encore des effets plus faibles qu'attendus, du fait de la compensation entre l'impact sur la microphysique (décroissance de la taille des gouttes) et diminution du contenu en eau.
Ces résultats pourraient être utilisés pour évaluer les modèles Chimie-Climat qui sont utilisés pour quantifier l'effet radiatif des aérosols à l'échelle globale, en particulier dans le cadre du prochain rapport de l'IPCC (Fifth Assessment Report; AR5).

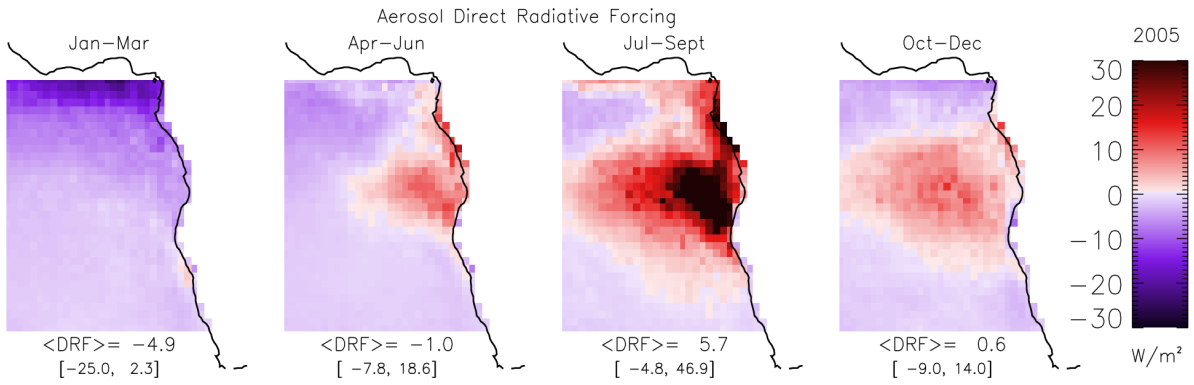

Figure 9: Moyenne saisonnière de l'impact direct sur le Sud-Est Atlantique, pour le 2005.

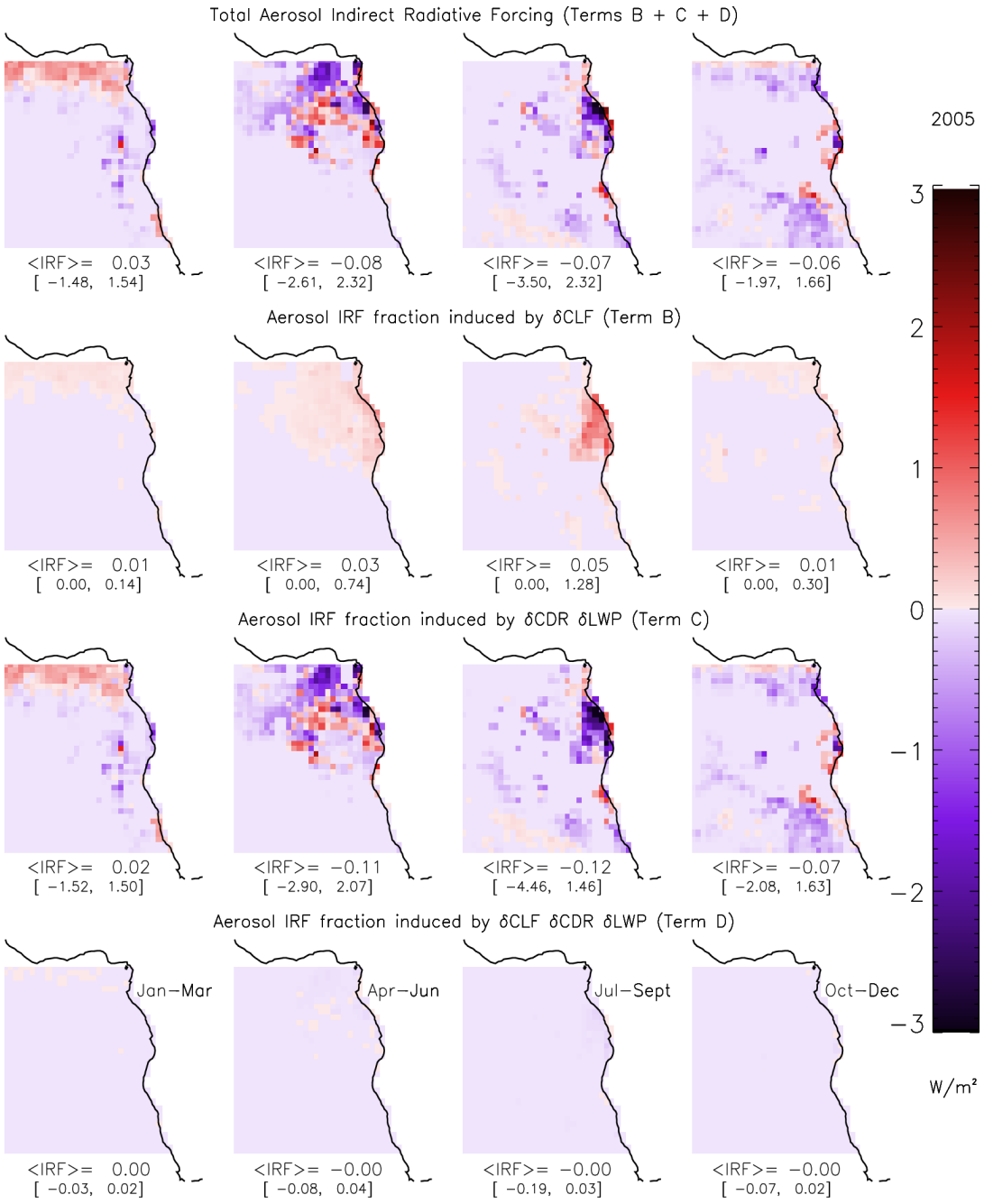

Figure 10: Moyenne saisonnière de l'impact indirect total sur le Sud-Est Atlantique pour le 2005 et décomposés en 3 termes: celui du à la variation du CLF (terme B), à la variation du CDR et COT (terme C), à la variation du CDR et COT dans la fraction nuageuse augmenté par l'effet de l'interaction entre nuages et aérosol (terme D).

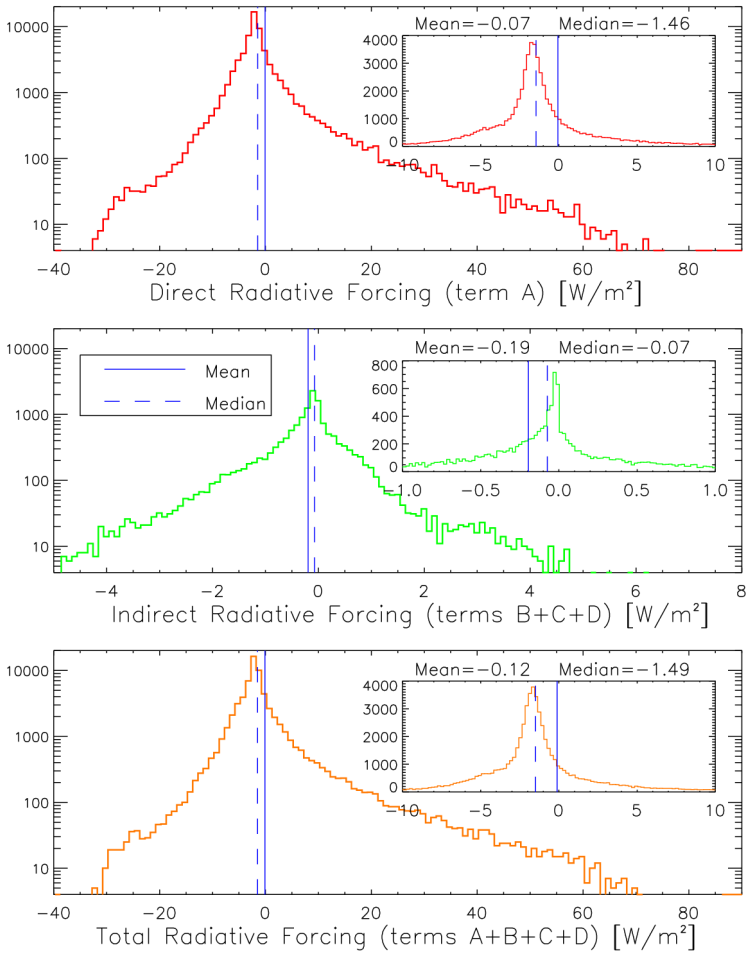

Figure 11: Histogramme de l'impact direct, indirect et total sur le Sud-Est Atlantique, sur l'ensemble des données de 2005 au 2010. La moyenne sur l'effet indirect, égale à 0.19W/m², est calculée sur les seuls valeurs différents de zéro. Si on considère tout la région, le forçage moyen est égale à -0.05 W/m².

Introduction

Anthropogenic aerosols are part of the Earth climate system. The consequence of their interaction with clouds is the primary uncertainty on anthropogenic forcing (Intergovernmental Panel on Climate Change, 2007). They originate from urban and industrial pollution or smoke from fires and may affect cloud microphysics, cloud life cycle, precipitation formation and the overall quantity of sunlight radiation reflected to space.

Aerosol effects on clouds and Earth's energy balance

Most aerosols are highly reflective compared to the molecular scattering of clean atmosphere. An increase in their concentration can raise planet's albedo and increase the portion of solar radiation reflected to space. Such effect reduces the amount of energy entering into the Earth climate system and the amount of solar radiation reaching planet surface, with respect to an aerosol-free atmosphere. This direct impact on Earth radiative balance cools the surface and reduces the global warming resulting from the increase of greenhouse gases.
Aerosols from smoke and urban haze contain organic compounds and black carbon, a strong absorber of solar radiation. The consequence of their interaction with incoming sunlight is twofold, cooling the surface and heating the atmosphere, with a warming rate that depends on the aerosol chemical composition and the albedo of the underling surface (clouds, ocean, land, etc). This mechanism, known as aerosol direct effect (ADE), may reduce the vertical temperature gradient of the atmosphere and cause a decline in evaporation and cloud formation (Hansen et al. 1997; Ackerman et al., 2000).

Aerosol can also interact with clouds during their formation process (cloud nucleation), acting as CCN (Cloud Condensation Nuclei). In polluted region, the increase in aerosol particle concentration can enhance cloud droplet number concentration (CDNC), resulting in a reduction of mean droplet size (Bréon et al. 2002). For the same spatial distribution of liquid water, a cloud made of more numerous small droplets, reflects more than a cloud with fewer and larger droplets (Twomey, 1974; Twomey, 1977). Thus, an increase in aerosol load can lead to an increase in cloud reflectance, if cloud water amount remains constant. This process, known with the name of 'Twomey's effect' or 'first aerosol indirect effect' (AIE #1), produces a negative forcing on Earth radiative balance with a net cooling effect on climate. The importance of anthropogenic aerosol impact on cloud albedo has been acknowledged by the Intergovernmental Panel on Climate Change (IPCC), 2007, with large uncertainty.
A strong feedback can rise from the higher concentration of smaller droplets in polluted clouds, where coalescence processes are suppressed and precipitation efficiency decreases (Albrecht, 1989). Inhibition of precipitation may increase cloud life time and cloud liquid water path, with a possible further increase in cloud optical thickness. This processes are known as 'second

aerosol indirect effect' (AIE #2) would ultimately modify cloud cover, in a way that is still poorly quantified.

The cooling effect of polluted clouds (first indirect effect) is still not completely characterized, while aerosol modification of cloud dynamics and precipitation patterns (second indirect effect) is even more uncertain. In fact, whereas aerosol impact on cloud microphysical is has been well established on global scale, the liquid water path response is far from being well understood. A number of studies show a significant positive correlation between liquid water path and CCN (Quaas et al. 2008; Loeb and Shuster, 2008, Quaas et al. 2009), some others a small but positive correlation (Nakajima et al., 2001; Sekiguchi et al., 2003), some others a negative correlation (Twohy et al. 2005; Matsui et al. 2006, Lee at al. 2009) while others affirm that this relationship can be positive or negative (Han et al. 2002) and depends on cloud regime (Lebsock, 2008) or only on meteorological variations (Menon et al. 2008).
These are complex processes to simulate in a model. In addiction, aerosol concentration and composition may largely vary in space and time. Long-term regional and global observations from satellites, ground stations and air-borne instruments are often needed to constraint models. At present days, we have limited direct observations of aerosol-cloud interaction impact on climate and state-of-the-art model estimates present large disparities (Lohomann and Feichter, 2005).
Many studies (Stevens and Feingold, 2009) agree on the fact that aerosol optical depth and low cloud incidence correlate well with the same meteorological parameters (surface wind speed, atmospheric moisture, stability, etc..). Local variations of one of these parameters can results in apparent correlations between aerosol and cloud retrievals. Therefore, one of the first and most difficult targets of present time research is to separate the impact of meteorology from aerosol-induced effects.

South-East Atlantic region is particularly suited to investigate radiative and physical effects of aerosol-cloud interaction. Large amount of aerosol load, produced from fires in Southern Africa, are injected into the atmosphere and transported by trade wind over Atlantic ocean, where a semi-permanent low cloud field is present. For their physical and chemical properties aerosols from biomass burning are very efficient CCN. In the absence of wet scavenging they can stay suspended in the atmosphere for days and weeks and be transported to considerable distances. In most cases, aerosol remains confined in the elevated layers of the atmosphere above cloud deck, well separated from it. As a consequence of their strong absorption properties, biomass burning particles may largely warm the atmosphere and produce a net positive forcing at the Top Of the Atmosphere (TOA). When aerosol gets mixed with the underlying cloud layer, the effect of their physical interaction can be statistically quantified by long term satellite observations.

Thesis structure and objectives

In this work, we perform a comprehensive analysis of the interaction between aerosol and warm clouds, in order to evaluate direct and indirect effects on South-East Atlantic radiative budget. Radiative forcing is considered the most simple and straightforward measure for the quantitative assessment of climate change mechanisms (Forster et al., 2005).
In Chapter 3 we study aerosol-cloud spatial and temporal variability over the area of interest, during 6 years of satellite observations. The first goal of this work has been to verify the expected aerosol effect on cloud microphysics. In Chapter 5 and Chapter 6, we quantify the decrease in cloud droplet radius with increasing aerosol concentration. In Chapter 6, we also investigate the expected increase in cloud optical thickness and cloud albedo as a consequence of droplet size diminution (AIE #1), as predicted by Twomey's hypothesis in case of constant liquid water path. Then, we analyze the liquid water path and cloud cover response to aerosol invigoration (AIE #2) and, in Chapter 7, we look for experimental evidence of precipitation suppression in polluted clouds. We quantified the strength of aerosol-induced effect with particular care in neglecting false correlations coming from local meteorology.
Chapter 8 focuses on the quantification of aerosol (and cloud) impact on the shortwave atmospheric radiation budget, over South-East Atlantic. We making use of the Rapid Response Transfer Model (RRTM_SW). We firstly deduced the shortwave radiative forcing due to the direct effect of aerosol on solar radiation, which depends on the aerosol optical properties coupled with the optical properties of its underling surface (ocean or clouds). Consequently we quantified the radiative forcing coming from the indirect effect of aerosol on cloud structure, which alters the way clouds interact with solar and thermal infrared radiation.

We use several aerosol and cloud parameters acquired from different satellite sensors: CALIOP lidar on board the CALIPSO satellite (for aerosol-cloud top and bottom layer altitudes), MODIS instrument on board of AQUA satellite (for cloud droplet radius, liquid water path, top pressure, cloud and aerosol optical depth, aerosol Angstrom coefficient, sea surface temperature), POLDER instrument on board of PARASOL satellite (for cloud droplet radius). Aerosol and cloud statistics are performed from co-located and time-coincided retrievals of the three A-train satellites, that fly in close proximity along the same orbit.
The main strategy of this work is to use CALIPSO data to analyze whether or not aerosol and cloud layers are mixed and interacting, in order to differentiate into two different classes the vertical integrated measurements of MODIS and PARASOL. For a given spatial location, if aerosol and cloud layers overlap or their altitudes are very close (within a certain threshold) they are considered interacting. In that case, a change in cloud properties with respect to a variation in aerosol concentration is interpreted as an aerosol driven process. On the other hand, if aerosol and cloud layers are well separated, the observed cloud change is considered as induced by other causes than cloud-aerosol interaction. This technique allows, to a certain degree, to isolate aerosol-induced effects from meteorology and obtain more reliable estimates of aerosol impact on clouds, than simple statistical satellite-based relationships between

vertically integrated observations of aerosol and cloud properties.

Chapter I – Principles of cloud and precipitation formation

1.1 Cloud Nucleation and role of Aerosol as CCN

The first condition for cloud formation is supersaturation of water vapor. Supersaturation is the measure of the excess of water vapor above 100% Relative Humidity (RH) (Twomey, 1977a), so that 101% RH is equal to 1% supersaturation. However, supersaturation required to create water droplet by collision of water vapor molecules (homogeneous nucleation) greatly exceeds supersaturation values of the atmosphere. The kinetic theory of homogeneous nucleation predicts that a RH values of 300% to 800% are needed for a cloud of droplets to form by the growth of small clusters of water molecules (embryos) into droplets (Pruppacher and Klett, 1997; Vehkamäki, 2006). This means that clouds form by a different mechanism, (heterogeneous nucleation) according to which water vapor condensates upon a subset of atmospheric aerosols at supersaturation levels usually achieved in clouds (0,1 – 1%), much lower than those needed for heterogeneous nucleation.
Since the particles which serve as nuclei have sharply curved surfaces, a greater partial pressure is required to prevent evaporation from the particle surface than for a flat surface (Hind, 1982). This phenomenon is called *Kelvin effect* and it is described by the Kelvin equation which relates the saturation ratio (actual partial pressure of vapor divided by the saturation vapor pressure for a flat liquid) required for equilibrium above a droplet and the droplet size for a pure liquid (usually water)

$$S_r = \frac{p}{p_s} = \exp\left(\frac{2\sigma M}{\rho R T r}\right) \quad (1)$$

S_r = supersaturation ratio
p_s = saturation vapor pressure for a flat liquid surface
p = actual partial pressure of vapor
σ = surface tension of the liquid
M = molecular weight of the liquid
ρ = density of the liquid
r = Kelvin equilibrium particle radius
R = ideal gas constant
T = absolute temperature

At the same time, in case of soluble CCN, the presence of a dissolved salt in water lowers the equilibrium vapor pressure above the water surface allowing activation to occur at a lower supersaturation with a soluble nucleus than with an insoluble one (Hinds, 1982). This process (generally known as “solute effect”) is described by the Raoult's law.

When a droplet evaporates, the Kelvin effect increases the vapor pressure due to the increase in the surface curvature of the droplet but at the same time the concentration of salt in the droplet increases (total amount of salt remains constant). These are the two competing factors controlling the relationship between the saturation ratio and the particle size required for growth, which can be couplet together in a single equation (Köeler equation)

$$S_r = \frac{p}{p_s} = \left(1 + \frac{i\, m_s M_w}{M_s \frac{4}{3}\pi \rho_w r^3}\right)^{-1} \exp\left(\frac{2\sigma_w M_w}{\rho_w R T r}\right) \tag{2}$$

m_s = mass of the dissolved salt
M_s = molecular weight of the dissolved salt
M_w = molecular weight of the water
σw= surface tension of the water
ρ_w = density of the water
i = numbers of ions each molecule of salt forms
r = particle radius

1.2 Köeler curves

This equation has not analytic solutions and a number of text provide a simplified form (expanding and taking only the firm therms of the expansion). If r is not too small it becomes

$$S_r = 1 + \frac{A}{r} + \frac{B}{r^3} \tag{3}$$

$A = \frac{2\sigma_w M_w}{RT\rho}$ Kelvin curvature term

$B = \frac{\epsilon\, i\, m M_w}{M_s \frac{4}{3}\pi \rho_w}$ Raoult (solute) term

ε = soluble mass fraction of dry particle.

Equation 2 assumes that the solute is completely soluble (so that droplet is assumed to be homogeneous) and that the surface tension and density of the growing droplet are equal to those of water . Atmospheric aerosol are not always completely soluble and Hanel (1979) proposed a the introduction in Raoult term of the soluble mass fraction of the dry particle. It is very interesting to study the Köhler curves given by the latter equation as a function of droplet radius, keeping constant all other parameters. For very small particles the equilibrium saturation

ratio is under the unity ($p < p_s$) allowing the presence of stable droplet of small size also if supersaturation condition is not satisfied. Beneath the peak value of supersaturation if the relative humidity increases slightly, the droplet will grow slightly along the curve. If the relative humidity drops, the droplet will evaporate slightly until the vapor pressure over the droplet surface is in equilibrium with the ambient vapor pressure. Particles on the ascending part of the curve are called *haze.* If the relative humidity is increased up the supersaturation peak, the droplet will grow to a *critical* radius and the particle is said to be *activated.* Beyond this critical point, the increase in droplet radius is no more dependent on an increase in ambient relative humidity and water will continue to condense onto the droplet (hence the droplet will continue to grow) for a sufficient source of water vapor. Aerosol upon which cloud droplets form and get activated, are called cloud condensation nuclei.

The dependence of activation on aerosol dry size is shown in figure 1, where Köhler (activation) curves are shown for a range of dry diameter of two salt particles frequently assumed as CCN, ammonium sulphate and sodium chloride, (NH4)2 SO4 with solid line, NaCl with dashed line.

This figure show the differences in the supersaturation as a function of both the chemical composition and dry size of a particle (Raoult and Kelvin effects) for completely soluble particles and containing 50% by mass insoluble core.

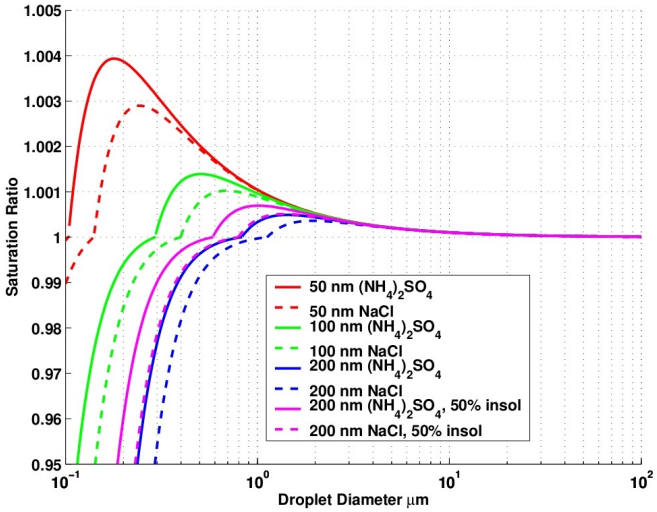

Figure 1: Köhler (activation) curves for a range of dry diameter of salt particles ((NH4)2 SO4 with solid line, NaCl with dashed line) and for 200 nm particles containing 50% by mass insoluble core (magenta). From McFiggans et al. (2006).

For a given aerosol composition, the larger is the size of a particle that serve as CCN, the more readily it gets wet by water and the greater is its solubility, the lower is the supersaturation at which the particle can serve as CCN and let star the cloud nucleation process. Pyrogenic organic emissions (biomass burning aerosol) with their relatively high solubility ave a key role

as CNN. The inorganic component (minor component)is made up of some insoluble dust and ash material, and soluble salts, and about half of the organic matter (major component) is water soluble (Reid et al. 2005; Decesari et al. 2006).

1.3 Particle growth and precipitation formation in warm clouds

When a air parcel rises, it expands and cools, so that it may reach saturation with respect to water. If it keeps cooling by a further lift, it may reach supersaturation values that begin to activate the most efficient CCN (the ones that need the lowest values of supersaturation) and cloud droplets form from the water vapor in excess of saturation. The cloud number concentration is equal to the number concentration of activated CCN. Yet from pioneering works of Squires (1958), Twomey and Warner (1967), Warner and Twomey (1967), and then confirmed in more recent 'in situ' observation (Garrett and Hobbs, 1995) and satellite images (Coakley et al. 1987; Durkee et al., 2000, 2001), it has been recognized that cloud droplet number concentration for clouds forming in clear environment have generally cloud droplet concentrations much lower than clouds forming in polluted atmosphere. Droplet concentration of cumulus clouds over ocean are generally lower than 100 cm-3, while clouds in polluted environment can reach values up to 1000 cm-3 (Squires, 1958)

Growing particles consume the disposable water vapor, so that the supersaturation begins to decrease, haze droplets to evaporate and only activated droplet continue to grow by condensation. Clouds forming at a temperature above 0 C are called *warm* clouds and are composed by liquid water only. In that case particle growth can be for *condensation* or *collision coalescence* processes.

1.3.1 Condensation growth

The rate of mass (M) grow with time (t) for condensation can be established from the equation

$$\frac{dM}{dt} = 4\pi x^2 D \frac{d\rho_m}{dx} \tag{4}$$

where D (m^2/s) is the coefficient of molecular diffusion and ρ_m the density of water molecules at the position x. Equation 4 leads, with some manipulations and approximations, to the analytical expression of grow rate

$$r dr = A\, dt \tag{5}$$

Where the term $A = \frac{D\, S_r \rho_m}{\rho_w}$ can considered approximately constant. Equation 5 can be integrated to give

$$r \approx A t^{1/2} \tag{6}$$

indicating that in the firsts instant after activation particle size grows rapidly, but rate of grow strongly decrease with time as particle size increase.

Theoretical calculation of Howell (1949) show that droplets growing by condensation approach a monodispersed size distribution after just 100 seconds after their activation. Typical droplet radius few hundreds meters above cloud base of non precipitating clouds, after 5 minutes from activation, is approximately 10 μm assuming condensations growth. This mechanism is too slow to produce rain droplets with typical radii of 1 or 2 millimeters.

1.3.2 Collision-coalescence process

Precipitation formation is given by collision-coalescence processes, that are based on the rapid growth of a cloud droplet as it falls through the cloud, colliding with the cloud droplets laying in its trajectory and forming a unique larger droplet (coalescence). Not all the droplets in the trajectory path are collected. Their number is proportional to the so called 'collision efficiency' (E) parameter, defined as the ratio of the cross-sectional area over which laying droplet (of radius r_2 and velocity v_2) are collected to the geometric cross-sectional area of the falling droplet, called 'collector' (of radius r_1 and velocity v_1 in general much higher than v_2). For collector particles with droplet radius smaller than 20 μm, the collision efficiency is very small, less than 0.1. For droplet radius larger than 20 μm the collision efficiency increases rapidly with droplet size (when r_2 is very similar to r_1 the efficiency can be larger than 1, as turbulence effects occur) so to have precipitation formation at least a few cloud droplets have to increase their size by condensation up to 20 μm, during the lifetime of a cloud. In a cloud with a density of water per volume unit ω_l (kg/m³) the mass grow rate can be expressed as

$$\frac{d\, M}{dt} = \pi r_1^2 E (v_1 - v_2)\, \omega_l \tag{7}$$

where $M = \frac{4}{3} \pi r^3 \rho_w$ and hence,

$$\frac{dr_1}{dt} = \frac{(v_1 - v_2)\,\omega_l E}{4\rho_l} \tag{8}$$

In the approximation of $v_1 >> v_2$

$$\frac{dr_1}{dt} = \frac{v_1 \omega_l E}{4\rho_l} \tag{9}$$

It is worthy to note that v_1 increases with increasing r_1 as well as E increases with r_1 so that the rate of grow increases time as particle size increases.

If the air within the cloud has an upward velocity, equation 9 can be modified adding a term taking into account the difference between the falling particle velocity and the upward air velocity. If h is the is the altitude from cloud base (positive upward), then $dh/dt = w - v_1$ and

$$\frac{dr_1}{dh} = \frac{v_1 \omega_l E}{4\rho_l} \frac{1}{w - v_1} \tag{10}$$

At the beginning of the collision process the droplet is small and the droplet grows lifting up from cloud base to higher altitudes (equation 10). When the particle has grown enough to reach velocity values larger than w, it will grow falling downward in the direction of cloud base, probably leaving the cloud and producing precipitation.

Chapter II – Satellites and remote sensing

2.1 Introduction

Just 65 years ago, the 24 October 1946, an unmanned V-2 rocket was launched into space from White Sands, New Mexico, to record the first picture of Earth from space (Figure 1), demonstrating the feasibility of observing our planet from beyond.
The V-2 rockets were the word's first long-range ballistic missile and the first human artifact to achieve sub-orbital spaceflight. Parts of almost 100 rockets were captured from Germany at the end of World War II and transported to United States.

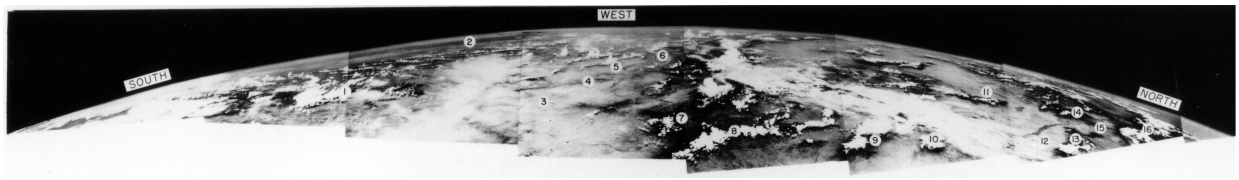

Figure 1: panorama of the Earth taken from a V-2 rocket fired from White Sands, New Mexico, on July 26, 1948. The area shown is approximately 2 million of square km, photographed from an altitude of 100 km. The rocket-borne camera climbed straight up, then fell back to Earth minutes later, slamming into the ground at 500 feet per second. The camera itself was smashed, but the film, protected in a steel cassette, was unharmed (image from Air & Space magazine).
The numbers on the photograph correspond to: 1-Mexico, 2-Gulf of California, 3-Lordsburg, New Mexico, 4-Peloncillo Mountains, 5-Gila River, 6-San Carlos Reservoir, 7-Mogollon Mountains, 8-Black Range, 9-San Mateo Montains, 10-Magadalena Mountains, 11-Mt. Taylor, 12-Albuquerque, New Mexico, 13-Sandia Mountains, 14-Valle Grande Mountains, 15-Rio Grande, 16-Sangre de Cristo Range.

The first satellite for atmospheric observations, the Explorer VII, was launched on October 13, 1959. In the first 40 years of satellite observations, measurements of meteorology and atmospheric composition, structure and dynamics dominated. In 1960, meteorologists presented the first iconic images of the Earth from the TIROS-1 (Television Infrared Observation Satellite) satellite, showing clouds and weather systems that visually identified features only seen on synoptic weather chart (Figure 2). However, the first instrument to probe air quality was not send to space before 1995. Since that moment several trace gases have been monitored in the stratosphere and troposphere in column measurements.

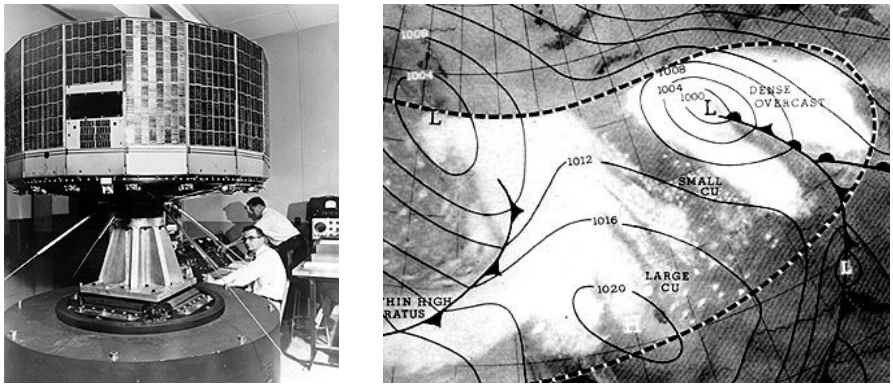

Figure 2: (left image) the first U.S. meteorological satellite, TIROS-1, launched by an Atlas rocket into orbit on April 1, 1960, looked similar to this later TIROS vehicle. (right image) One of the first images returned by TIROS-1. Superimposed on the cloud patterns there is a generalized weather map for the region.

Nowadays, numerous satellites are currently being tracked with thousands of Earth observing sensors in low (<2000 km, LEO, Low Earth Orbit), medium (2000-25000 km, MEO) and geosynchronous (35786 km, GEO) orbits.

GEO satellites must orbit the Earth precisely once for every rotation of the of the Earth in an equatorial position to maintain a fixed point on the planet. Communication satellites often use this orbit. This allow the use of a fixed orientation dish on the ground to communicate with the satellite.
Earth sensors on board of a GEO satellite can provide images of nearly the full hemisphere below the satellite.

LEO satellites orbit the planet with typical period of revolution of approximately 1.7 hours. Many satellites carrying ocean and atmospheric remote sensing instruments that require sunlight are placed in sun-synchronous orbits, crossing the equator at the same local time, each day. For orbit with altitude of about 705 km (as in case of A-train constellation), the angle between the orbit and the equatorial plane (referred as satellite inclination) is equal to 96.1 degrees. Sensor swath widths, which are the cross track extent of a measurement, can vary from 70 m for some nadir pointing radar (e.g., CloudSat) and lidar instruments (e.g., CALIOP) to 2330 km for wide swath imagers (e.g. MODIS, at 250 to 1000 m resolution, depending on the wavelength of the instrument channels).

MEO orbits combine some of the benefits and some of the deficits of GEO and LEO. They have longer periods and allow longer view times for any given point on the surface. On the other hand, MEO orbits precess, so they don't have a fixed point on the ground. These orbits are primarily reserved for communications satellites.

The TIROS-1 satellite was equipped with a black and white television camera with a visible wavelength channel encompassing 400 and 700 nm. Solar radiation was reflected by the planet, where bright clouds reflected much more sunlight than the darker surface of the ocean. Remote sensing from space is not much more complicate, in principle, than those early TIROS observation. Sensors on board of modern satellites see the contrast between photons emitted or reflected from the surface or underlying atmosphere and the photons scattered or emitted in the satellite direction from the element of interest (clouds, trace gases, etc..).

2.2 Remote sensing satellites for aerosol and clouds

Even though aerosol satellite measurements began in 1978 with TOMS (Total Ozone Mapping Spectrometer) instrument with the Nimbus-7 spacecraft, the first satellite sensor specifically designed to measure aerosols, POLDER (Polarization and Directionality of the Earth's Reflectances) was launched in 1996, on board Japan first Advanced Earth Observation Satellite (ADEOS). TOMS has two channels in the UV, particularly sensitive to absorbing aerosols over both land and ocean. Through 1980s and 1990s the most frequently used satellite to detect aerosol properties was the NOAA AVHRR (Advanced Very High Resolution Radiometer). The processing algorithm uses two channels to retrieve cloud and aerosol optical thickness over Ocean

In 2002 NASA launched the first satellite of the A-Train, a constellation of several satellites in close proximity, which flies in a sun synchronous orbit at an altitude of 705 km (Figure 3).

The train consists of 4 active satellites. 1-Aqua, launched on May 4, 2002, leads spacecraft formation; 2-CloudSat, launched on April 28, 2006, runs no more than 2 minutes behind Aqua; 3-CALIPSO, launched with CloudSat, follows CloudSat by 15±2.5 seconds; 4-Aura, launched on July 15, 2004, lags Aqua by 15 minutes, crossing the equator 8 minutes behind due to different orbital track to allow for synergy with Aqua (Stephens et al. 2002).

PARASOL, launched on December 18, 2004 lagged CALIPSO by 2 minutes; it was moved to a lower orbit on 2 December 2009, it is expected to be completely out of the A-train neighbourhood at the end of 2012. OCO was destroyed by a launch vehicle failure on February 24, 2009. In coming years the A-Train will expand also with the carbon-tracking Orbiting Carbon Observatory 2 (OCO-2) satellite. In addition, Japan Aerospace Exploration Agency (JAXA) plans to launch the Global Change Observation Mission-Water (GCOM-W1), which will monitor ocean circulation.

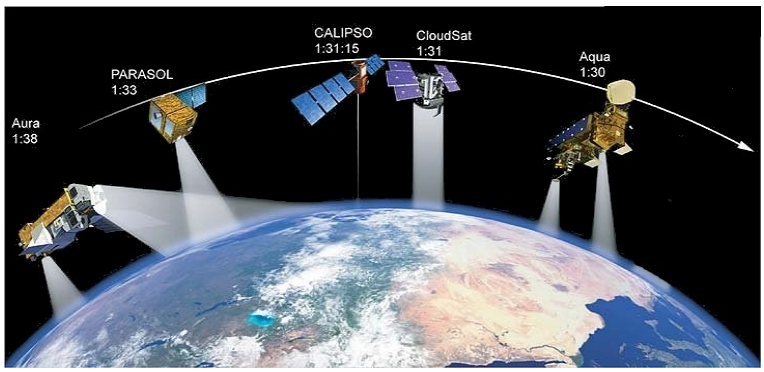

Figure 3: Artist's concept of the A-Train constellation. This work will make use of this satellite configuration, dated before December 2009. Listed under each satellite's name is its equator crossing time. Aura crosses the equator eight minutes behind Aqua, in terms of local time, because it is along a different orbit track, it actually lags Aqua by fifteen minutes. Note that CALIPSO trails CloudSat by only 15 seconds to allow for synergy between Aqua, CloudSat, and CALIPSO. Photo from NASA collection.

The term "A-Train" has become a popular nickname for the Afternoon Constellation because Aqua is the lead member of the formation and Aura is in the rear.
Sensors aboard NASA's A-Train satellite are particularly well suited for studying the effects of aerosols and clouds on climate (Formation Flying: The Afternoon"A-Train" Satellite Constellation, NASA Facts, 2003). They give the unique opportunity to have co-located and near-simultaneous measurements of aerosol, clouds and precipitation, with PARASOL and MODIS for passive aerosol and cloud observations in the visible to IR, the OMI instrument for aerosol observations in the UV to visible, the CALIPSO lidar for aerosol and cloud vertical profiling and CloudSat radar for cloud liquid water profiling and structure. Note that satellite data are subdued to long and accurate validation precesses by in-situ ground-base remote sensing instruments (e.g. AERONET, Aerosol Robotic Network and MPL, Micro-Pulse Lidar, for aerosol properties; ARM, Atmospheric Radiation Measurement, sites for aerosol effects on clouds; etc.) and in-situ air-born measurements.

2.3 POLDER, MODIS and CALIOP

It is now of interest to describe in more detail the satellite instruments that will be used in this work: POLDER (aboard PARASOL), MODIS (aboard AQUA), and CALIOP (aboard CALIPSO).

2.3.1 Remote sensing of cloud properties with POLDER

POLDER flew aboard ADEOS 1 and 2 in 1996-1997 and 2003. From December 2004 it flies aboard PARASOL microsatellite. POLDER measures the solar radiance reflected by the Earth's surface and atmosphere in the visible and the near infrared (440 to 910 nm). In addition it has two main characteristics: the ability to measure linear polarization of the radiance in three spectral band and to measure the directional variation of that reflectance. It acquires up to fourteen views of a specific target, that allows the instrument to infer the direction signature of reflectance.

POLDER instrument has been chosen because it provides an innovative method to retrieve cloud top droplet effective radius (CDR), based on cloud bow analysis by means of polarized radiance measurements (Bréon and Doutriaux, 2005). This method is very precise and no known causes for error or biases. However it is applicable only in case of extended and homogeneous cloud field (150×150 km) with a narrow droplet size distribution at the cloud top and only for liquid droplets. The angular position of the maxima and minima in the polarized phase function (and then in the polarized reflectance, which is proportional to the polarized phase function to the first order) is extremely sensitive to the droplet effective radius and is little sensitive to the effective variance of the size distribution (as the size distribution gets broader than a certain threshold values, secondary maxima and minima are smoothened out). A clear narrow size distribution has been indicated as an effective variance of 0.05 or less. This condition is generally well satisfied for warm clouds, especially in the south tropics and over high latitude ocean. The range of scattering angle considered is (145°,165°), but unfortunately the angular sampling of POLDER is on the order of 10°. For that reason, spatial homogeneity to combine all measurements from an area of 150×150 km² has been hypothesized.

Bréon and Doutriaux (2005), compared POLDER cloud droplet effective radius measurements with daily MOD08 MODIS products, with 1×1 degree resolution (from the original 1 km resolution cloud retrievals). They find out a very high coherence between the two instruments over ocean, although a 2 μm bias (larger particle retrievals for MODIS). Over land the reflectance contribution from the surface is suspected to generate a noise in MODIS retrievals. The bias over ocean is supposed to be due partly to the assumed size distribution in MODIS retrieval algorithm, that is too wide for most stratocumulus clouds taken into account (a Gamma distribution with an effective variance of 0.10) and partly to specific vertical profile of cloud droplet radius (for example smaller CDR at the very cloud top when mixing with drier air occurs).

In their conclusion, they argue that the spectral method (MODIS) allows a much better statistics than the directional method (POLDER), but this latter is less sensitive to biases and errors resulting from cloud heterogeneity, assumption on size distribution and surface contribution to reflectance.

2.3.2 Remote sensing of aerosol properties with MODIS

MODIS began collecting data on February 2000 aboard the Terra satellite and on June 2002 from Aqua. In this work we will make use of the MODIS product from the Aqua satellite (13:30 of ascending orbit equatorial crossing time), to allow synergies with the other A-Train satellite sensors. Aerosol characteristics over ocean and land are derived by means of two different algorithms. Both algorithms were conceived and developed before the Terra launch and are described in depth in Tanré et al. (1997) and Kaufman et al. (1997), while Remer et al. (2009) provide a more recent description, which describes in depth how mechanics and details of the algorithms have evolved .

For aerosol retrieval, MODIS uses the seven spectral channels (Table 1)

Channel	**1**	**2**	**3**	**4**	**5**	**6**	**7**
Wavelength [µm]	0.66	0.86	0.47	0.55	1.24	1.64	2.12
Resolution [m]	250	250	500	500	500	500	500

Table 1: spectral characteristics and spatial resolution of aerosol bands used in MODIS.

Orbit data are separated into 5 minute chunks called ‘granules’ and only data from MODIS daytime orbits are considered for aerosol retrieval. The aerosol product resolution is a 10×10 km² grid box (Level 2, L2, product), which has been chosen as the retrieval resolution because single 500 m pixels are insufficiently sensitive to characterize aerosol (Remer et al. 2009). If all pixels within the 10 km box are considered water, the algorithm proceeds with the over-ocean retrieval. However, if any pixel is considered land, then it proceeds with the over-land algorithm. Whether ocean or land aerosol retrieval was performed, the products are assigned a QA ‘confidence’ flag (QAC) that represents the aggregate of all the individual QA flags. This QAC value ranges from 3 to 0, where 3 means ‘good’ quality and 0 means ‘bad’ quality.

All atmospheric products (for both aerosol and clouds) are averaged on a 1×1 degree grid box (on daily, weekly, and monthly time scale), and are known as Level 3, L3, products. QAC flag is used for weighting the 10 km product onto the 1° grid.

MODIS data are organized by collections, that consist of products by similar version of the retrieval algorithms. Tanré et al. (1997) and Kaufman et al. (1997) describe pre-launch

algorithms. Collection C003 provided first validated data of aerosol products over ocean (Remer et al 2002) and land (Chu et al.,2002) with ground based sunphotometer data (Ichoku et al. 2003) of AERONET (Holben et al., 1998). Ichoku et al. (2003) founded that single scattering albedo was in fact lower than previously assumed for southern African biomass burning. Collection 004 have been validated with 132 AERONET station (Remer et al. 2005) all around the World, of which 14 ocean-only, 88 land-only and 30 ocean and land. MODIS Aerosol optical thickness measurements are founded to be in accurate agreement with theoretical, prelaunch expectation (Tanré et al., 1997; Kaufman et al., 1997) of $\Delta\tau(0.55\mu m)=\pm 0.03\pm 0.05\tau$ over oceans (with generally random errors with no significant bias and a bias of about 10% in case of dust aerosol) and $\Delta\tau(0.55\mu m)=\pm 0.05\pm 0.15\tau$ over land. Remer et al (2005) find out that MODIS retrievals are not affected by cloud contamination (for the eight scattered globally sites considered). After the validation efforts of C004 over ocean and over land algorithms evolved to the V5.2 version and products to Collection 005. Version V5.2 includes a complete overhaul of the aerosol retrieval over land (Levy et al., 2007a, 2007b) and new assumptions about coarse aerosol properties over ocean (Remer et al., 2009). The next generation of MODIS data products, Collection 006, is expected to begin production late 2011.

The core of the over ocean retrieval algorithm still remains similar to the process described in Tanré et al. (1997). Following Tanré et al. 1996, the algorithm uses the measured spectral reflectance at 500 m resolution (degrading the resolution of the 250 m channels) from six MODIS bands (0.55 – 2.13 μm) and the inversion is based on a LUT (lookup table). This LUT now consists of four fine modes and five coarse modes, following Levy et al. (2003), and differs from the 11 possible modes listed in Tanré et al. (1997). Radiative transfer calculations are pre-computed for a set of aerosol and surface parameters and compared with the observed radiation field. The algorithm assumes that one fine and one coarse log-normal aerosol modes can be combined with proper weightings to represent the ambient aerosol properties over the target. Spectral reflectance from the LUT is compared with MODIS measured spectral reflectance to find the 'best' (least-squares) fit. Like all previous versions, also the C005 ocean (C005-O) LUT was created with the radiative transfer code developed by Ahmad and Fraser (1981) (Remer et al. 2009) .

In case of cloud free, glint free scenes MODIS (Martins et al. 2002) retrieves aerosol optical depth at 0.55 μm, as well as the fraction of optical depth contributed by fine aerosol mode, f, and the effective radius of the aerosol (Tanré et al. 1997).

Also over land retrieval algorithm is substantially similar to the one described by Kaufman et al. (1997). However in its recent version three MODIS wavelengths (0.44, 0.66 and 2.1 μm) at 500 m resolution are used simultaneously. C005 land (C005-L) family algorithms assume that the 2.1 μm channel contains information about coarse mode aerosol as well as the surface reflectance. Aerosol optical thickness at 0.55 μm and fine mode aerosol fraction at 10 km resolution and surface reflectance at 2.1 μm are provided.

2.3.3 Remote sensing of cloud properties with MODIS

Cloud top properties, such as cloud top temperature, cloud top pressure and effective emissivity are determined using radiances measured in spectral bands located within the broad 15 μm CO2 absorption region. The CO2 slicing technique is based on the atmosphere becoming more opaque due to CO2 absorption as the wavelength increases from 13.3 to 15 μm. In this way radiances obtained from these spectral bands are sensitive to different layers in the atmosphere. MODIS provides measurements at 1 km resolution and at four wavelengths located in the broad 15 μm CO2 band (both day and night). For MODIS, cloud top properties are produced for 5×5 pixel arrays wherein the radiances for the cloudy pixels are averaged to reduce radiometric noise. Thus, the CTP is produced at 5 km spatial resolution in Collection 5 (L2 product). The MODIS cloud pressure is converted to cloud height and cloud temperature through the use of gridded meteorological products that provide temperature profiles. Additionally, an IR cloud phase is inferred from the MODIS 8.5 and 11 μm brightness temperatures at 5×5 pixel resolution (Menzel et al. 2010).

Cloud effective radius and cloud optical depth L2 products are derived using the six visible and near infrared wavelengths (King et al. 1998; Table 2)

Channel	Wavelength [μm]	Resolution [m]	Atmospheric Purpose
1	0.66	250	Cloud optical thickness over land
2	0.86	250	Cloud optical thickness over ocean
5	1.24	500	Cloud optical thickness over snow/ice
6	1.64	500	Snow/cloud discrimination; termodynamic phase
7	2.12	500	Cloud effective radius
20	3.75	1000	Cloud effective radius; cloud/surface temperature

Table 2: spectral characteristics, spatial resolution and principal purposes of cloud bands used in MODIS.

All clouds products contains a cirrus reflectance product at a visible wavelength to remove

cirrus scattering effects from land surface.

In this range of wavelengths, reflectance decreases when droplet size increase, for a constant cloud optical depth. Non absorbing channels are chosen to minimize the surface contribution, so that over land, ocean and snow (ice) are respectively used the three channels at 0.66, 0.86, and 1.24 μm. Each radiance is compared with a base radiance at 2.12 μm (and eventually at 1.64 and 3.75 μm). The main concept is very similar to the aerosol retrieval algorithm. The couple of retrieved radiances are compare with a pre-computed LUT. Bréon et al. (2005) show that a misunderstanding of 20% in the cloud cover (an overcast pixel is assumed, with a real cloud fraction of 0.8) can lead to overestimate the cloud droplet radius by up to 2 μm. Is then evident that MODIS cloud retrieval algorithm is very sensitive to cloud heterogeneity, which can be a significant source of error in cloud droplet radius measurement if cloud cover is not property estimated. It is interesting to wonder if aerosol can affect cloud optical properties measurements. In general cloud retrievals are thought to be little affected by biomass burning and dust aerosol for retrievals based on the 0.86/2.1 μm combination.

2.3.4 Remote sensing of aerosol and cloud properties with CALIOP

CALIPSO combines the passive visible and and infrared imagers with the first satellite lidar optimized for aerosol and cloud measurements, CALIOP. This is the first polarization lidar in space, and is based on a Na:YAG laser. Two orthogonally polarized channels at 532 nm and one at 1064 measure the total backscattered signal (Winkler et al. 2007). Its footprint, with a laser pulse diameter of 70 m on the ground, is very narrow, so that CALIPSO covers just 0.2% of the Earth surface (Khan et al. 2008). Retrievals with CALIOP need strong efforts to overcome the difficulties that comes from several factors generally not present in ground based lidar: the very large distance from the target, the very high speed of the satellite and the consequent low signal to noise ratio (SNR). The SNR is improved with horizontal and vertical averaging, in accordance with the spatial scale of the interested target. Signal from high atmosphere tend to be weaker, requiring more signal averaging. Fortunately, the composition of the atmosphere tend to became spatially uniform with altitude. The averaging scheme, shown is Table 3, has been developed to keep a high spatial resolution in the lower atmosphere and lower in the upper layers (Winkler et al., 2004).

Altitude Range [km]	Horizontal Resolution [Km]	532 nm Vertical Resolution [m]	1064 nm Vertical Resolution [m]
30.1 to 40.0	5.0	300	---

20.2 to 30.1	1.67	180	180
8.2 to 20.2	1.0	60	60
-0.5 to 8.2	0.33	30	60
-2.0 to -0.5	0.33	300	300

Table 3: averaging scheme of CALIOP (Winkler et al. 2004) for Level 1 data products (Attenuated Backscatter).

CALIPSO mission is supposed to probe vertical structure and properties of aerosol and cloud layers over the globe. CALIOP is able to detect and characterize weak aerosol fields and thin clouds with optical depth of 0.001 or less (McGill et al. 2007) Note that the lidar signal is fully attenuated for optical thickness greater than 3 (Winker et al., 2009).

More precisely, CALIPSO data are classified in Level 1 and Level 2 products. Level 1 CALIPSO data products provide vertical profiles of Attenuated Backscatter values. Level 2 CALIPSO data provides geophysical products. They are separated in Level 2 layer data (with optical and geometrical properties of identified atmospheric layers) and Level 2 profile data (vertical profiles within the altitude ranges where the layer identification algorithm recognizes aerosol or cloud layers). In this work we are particularly interested in Level 2 data, provided at three different horizontal resolutions for clouds (333 m, 1 km and 5 km) and only one for aerosol (5 km).

Kim et al. (2008) validated the ability of CALIPSO in discriminating cloud and aerosol layers, with reliable detection of layer top and bottom altitudes, generally in agreement with ground based lidar measurements within 0.1 km. Mielonen et al. (2009) compared AERONET and CALIPSO observations in 38 sites spread across the world, finding that 70% of the daily mean aerosol types of the two instruments are in good agreement.

2.3 Other remote sensing instruments

Hereafter, we mention other spaceborne intruments not used in this work, on board of AQUA and CLOUDSAT satellites, that can provide similar and complementar information to MODIS, CALIOP and PARASOL data, for the study of Earth's atmosphere and radiation budget.

In addition to MODIS spectroradiometer, Aqua satellite carries five more instruments:

- AMSR-E (Advanced Microwave Scanning Radiometer-EOS) measures precipitation rate, cloud water, water vapor, sea surface winds, sea surface temperature, ice, snow, and soil moisture. The Earth-emitted microwave radiation is collected at six different wavelengths 6.925, 10.65, 18.7, 23.8, 36.5, and 89.0 GHz. Spatial resolution of the individual measurements varies from 5.4 km at 89 GHz to 56 km at 6.9 GHz.

- AMSU-A (Advanced Microwave Sounding Unit) was designed primarily to obtain temperature profiles in the upper atmosphere (especially the stratosphere). With a frequency range of 15-90 Ghz, AMSU-A provides atmospheric temperature measurements from the surface up to 40 km.

- AIRS (Atmospheric Infrared Sounder) measures the Earth's outgoing radiation at 0.4 to 1.0 μm and 3.7 to 15.4 μm. It is an advanced sounder aimed at obtaining highly accurate temperature profiles within the atmosphere. AIRS has 1 K temperature of retrieval accuracy per 1 km layer in the troposphere and 0.05 emissivity accuracy. It is the highlighted instrument in the AIRS/AMSU-A/HSB triplet centered on measuring accurate temperature and humidity profiles throughout the atmosphere.

- HSB (Humidity Sounder for Brazil) is a passive radiometer with 4 channels at 150 and183 GHz, which provides atmospheric water vapor profiles. Furnished by Instituto Nacional de Pesquisas Espaciais of Brazil. The HSB instrument has been in survival mode since May 25, 2003.

- CERES (Cloud and the Earth's Radiant Energy System) measures broadband radiative energy flux. It consists of two broadband scanning radiometers: one cross-track mode and one rotating plane (biaxial scanning). The cross-track scanning instrument will allow continuation of measurements made by the Earth Radiation Budget Experiment (ERBE) satellite while the biaxial scanner was created to improve/double the accuracy of those measurements. Its purpose is to measure Earth's radiation budget and atmospheric radiation from the top of the atmosphere to the surface and to provide cloud property estimates. CERES operates in the ultraviolet through thermal infrared in three wide bands between 0.3-100 μm, with a window at 8-12 μm. It has a low 20-km resolution and complete global coverage every one hour. A copy of the CERES sensor fly aboard the Terra satellite.

CloudSat satellite carries the Cloud Profiling Radar (CPR), to allow for the first global survey

of the synoptic (large scale) and seasonal variations of cloud vertical structure and frequency of occurrence. It provides quantitative information on cloud-layer thickness, cloud base and top altitudes, cloud optical thickness, cloud water and ice contents, and the heating of the atmosphere by clouds. It has a vertical resolution of 500 m, a cross-track resolution of 1.4 km and an along-track resolution of 1.7 km. This 94-GHz nadir-looking radar has a strong heritage from the many cloud radars already in operation in ground-based and airborne applications, so that its overall desin is simple and well-understood. It measures the power of backscattered radiation by clouds as a function of distance from the radar. Sensitivity and antenna gain increase with frequency while atmospheric transmission and transmitter efficiency decrease with frequency. When very thick clouds or heavy precipitation is present, the CloudSat radar will not be able to penetrate to the cloud base.

Chapter III – Aerosol properties and geographical distribution over West and Southern Africa, and South-East Atlantic

3.1 Introduction

In Africa a large amount of biomass burning events occurs annually (Ichoku et al., 2003; Edwards et al., 2006). In the Northern Hemisphere (NH), fires take place from December to April, burning savanna of the Sahel region south the Sahara desert, at latitudes just north the Equator. From April, fire location moves southward, following the dry season during the year. In July, August and September heavy smoke layers originate from fires across Southern Africa (Angola, Namibia, Democratic Republic of Congo, Zambia and Mozambique) with little burning in the semiarid and arid southwest of the continent. These fires are not generally wildfires but result from agricultural burning. Biomass burning plumes are injected within the mixing layer (Labonne et Bréon, 2007) and may be transported by trade winds over the Atlantic Ocean off the coasts of Angola and Namibia. They can remain suspended in elevated layers of the atmosphere, above cloud top, or mix with moist air masses and clouds. These twofold possibility makes the South-East Atlantic region of unique and particular interest to observe interactions between cloud, aerosol and regional climate. In fact, apart from a significant amount of inorganic compound, aerosol released from forest and cropland fires, generally referred to biomass burning aerosol, mostly contains organic carbon (OC) with various amounts of black carbon (BC, emitted primarily in efficient flaming fires), depending on the particular fuel, oxygen availability and combustion phase (Andreae and Merlet, 2001). If aerosol lies over cloud deck, the elevated absorption properties of black carbon can greatly influence the atmospheric radiative balance, producing a positive forcing which results in a net warming of the atmosphere [Keil et al., 2003]. On the other hand, in case of cloud and aerosol mixing, biomass burning particles can become hydrophilic enough to be activated as CCN and affect cloud properties, modifying cloud development and microphysical characteristics.

A typical condition that occurs in this area is shown in right image of Figure 7, which is a vertical profile at 532 nm of the CALIPSO lidar, for the night of 9 September 2009. CALIPSO footprint crossing the selected region is shown in the inner figure. A color scale is associated with the attenuated backscatter signal magnitude. Purple and blue indicate low backscatter values, denoting a clean atmosphere; green indicates larger values generated by the aerosol layers; yellow and red indicate very high values of the signal, generated by clouds. Aerosol layers have moderate optical depths (typically lower than 1) that allow CALIPSO lidar to see the underlying atmosphere. Cloud field at lower latitudes (right side of the image) is optically thick so that lidar signal cannot fully penetrate the cloud, with no useful information from the atmosphere below. The yellow and black lines are respectively the boundary layer altitude,

according to ECMWF data (available with a 3-hourly and 25 km resolution), and the ground level altitude, which is constant and equal to zero over the ocean.
Over the continent (left side the figure), aerosol load is within the boundary layer. When aerosol is transported over the ocean, where the mixing layer is much thinner, it passes into the free troposphere at altitudes (~2 km) higher than those of the cloud field (~1 km), lying upon the boundary layer top. The two different conditions are clearly shown in the figure. Aerosol field remains well separated from cloud deck near the coast lines, while it appears somewhat mixed with the cloud layer over the ocean, at lower latitude.

Previous studies (Garstang et al., 1996; Cattani et. al 2005; Edward et al. 2006) have shown that during the Austral biomass burning season, Southern Africa and the adjacent Atlantic Ocean are located in a region of large-scale subsidence. A high pressure system occurs in correspondence of the descending branch of the Hadley cell and part of the Ferrel cell of Southern Hemisphere general circulation. This results in a strongly stable layered vertical structure of lower troposphere, that serves as trapping mechanism for trace gases and haze.
In winter, general meteorological condition over land is dominated by the absence of precipitation and low absolute humidity. During that period, trade winds transport dry continental air masses together with large quantities of aerosol particles from Southern Africa over the South-East Atlantic, where a semipermanent field of shallow boundary layer clouds is present.

In the following chapter we perform a comprehensive analysis of temporal and spatial variations of aerosol and cloud fields during 6 years (2005-2010) of measurements, provided by the MODIS instrument on board of Aqua satellite. The study area [4N, -30N; -14E, 18E] is shown in left image of Figure 7 (within the yellow square), together with active fires detected by MODIS on July 1st, 2007 (red spots).
The object of this chapter is to provide a comprehensive, multi-year description of aerosol and cloud properties over the South-East Atlantic region.

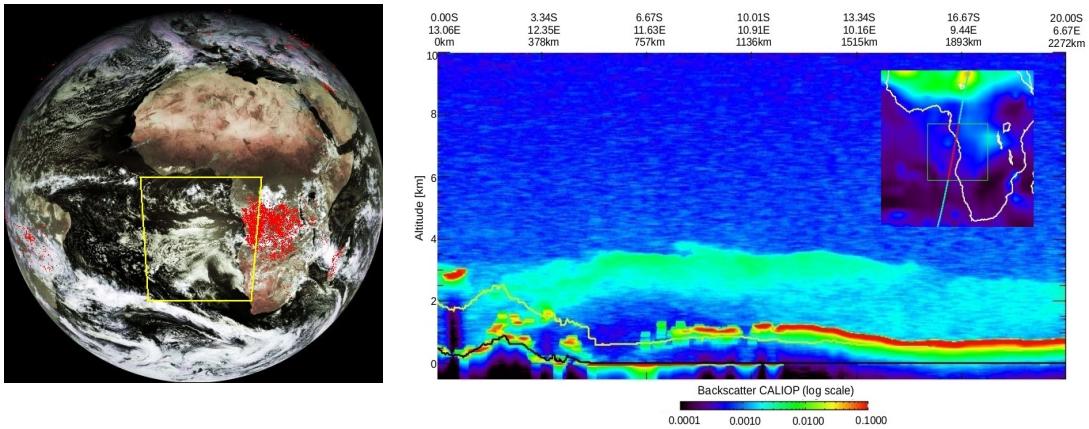

Figure 4: (left image) Meteosat-7 full disc image realized through the combination of two

sensors, the broad-band visible high-resolution channel (HRV) and the far-IR channel centred on 10.8mm. The visible channel has been histogram equalized and sharpened and displayed as brightness. The thermal channel has been re-sampled to the same resolution as the visible channel, converted into temperature, and used to supply the hue of the color component of the output image. Overlaid on the original image the yellow square represents our study area, and the red spots represent all active fires seen from MODIS for July 1st 2006. Each active fire location represents the center of a 1km pixel (approximately) flagged as containing one or more actively burning fires within that pixel.
(right image) Profile of 532 nm backscatter signal ($sr^{-1}km^{-1}$) from CALIPSO lidar Level-1 Scientific Data Set, showing the vertical distribution of aerosol and clouds for July 9th 2009 (night time), together with ECMWF boundary layer top hight (yellow line). The black line represents the ground level, blue/green colors are associated with tenuous backscattering (aerosol layers) and strong backscattering is shown in red (cloud layers). The color shading of the inlay figure represents the total aerosol optical depth with the location of the CALIPSO footprint (purple/blue line).

3.2 Fire occurrence and wind field

In each hemisphere fires occur mainly in the respective winter season. Figure 11, obtained from MODIS Active Fire Product (Giglio et al., 2010), shows monthly fire locations for 2005, detected by MODIS instrument aboard Terra and Aqua satellites. Color-scale represents the number of active fires (within each 1×1 degree gird box) detected at a nominal resolution (at nadir) of 1 km.

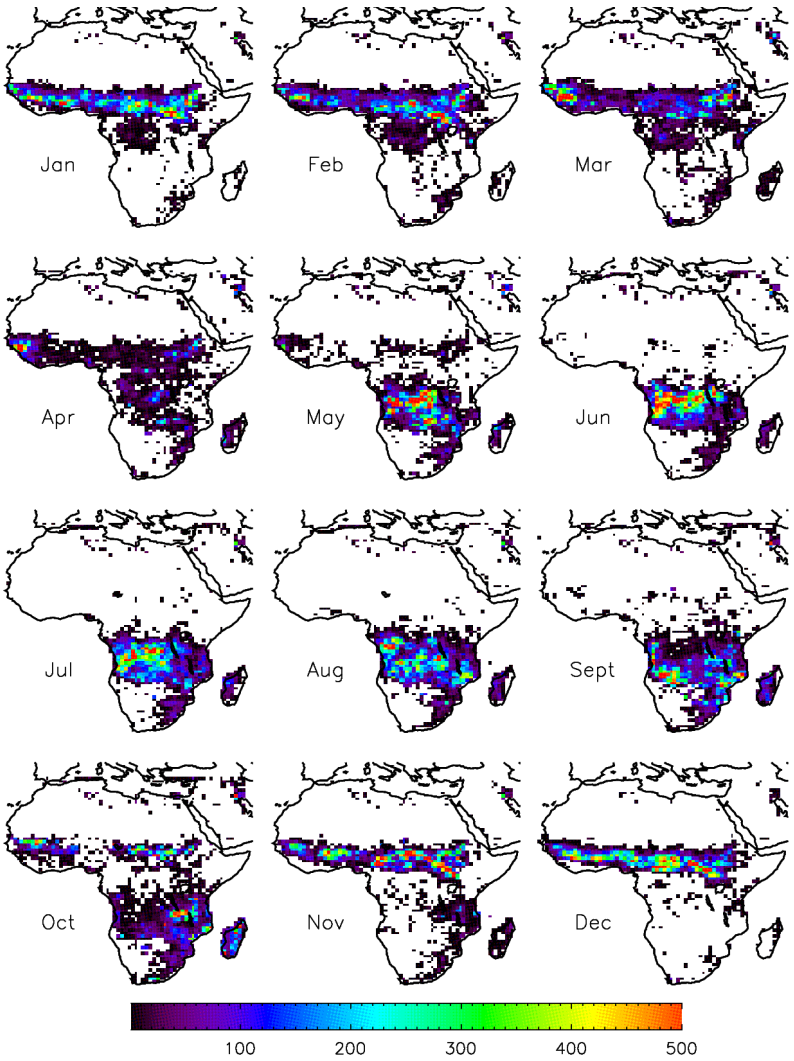

Figure 5: fire occurrence for 2005, according to MODIS Active Fire Product. Color-scale represents the number of active fires detected each month, at a nominal resolution (at nadir) of 1 km, within a 1°×1° gird box.

From November to March, fires are concentrated in a region south the Sahara desert and North the Equator, extending approximately from the West coast of Mauritania to Ethiopia, crossing East-West almost the entire continent. From May to September fires are mainly located in Southern Africa, covering almost the entire subcontinent, between 0S and 20S. April and October are characterized by fires burning in both regions, north and south the Equator.

Figure 10 shows seasonal maps of wind speed and direction at 950, 850 and 750 mbar (corresponding approximately at 0.6, 1.5 and 2.5 km of altitude) during 2005, computed from monthly averages provided by the European Center for Medium-Range Weather Forecasts (ECMWF). Each arrow indicates the direction of the wind at any given location and the intensity of the speed field in that point. Wind speed is expressed in degrees per day.

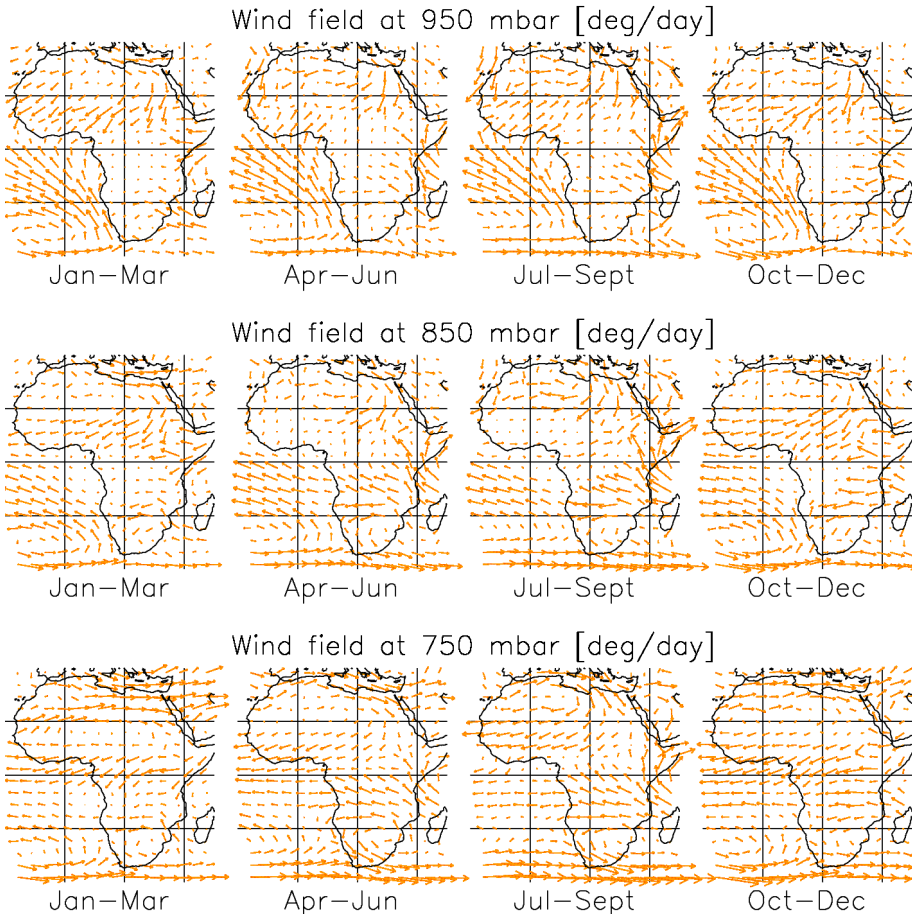

Figure 6: wind fields at 950, 850 and 750 mbar (corresponding approximately to 600 m, 1.5 km and 2.5 km of altitude) for 2005. Seasonal maps are obtained from monthly mean of wind speed provided by the ECMWF. Arrows show wind direction for any given location and wind speed in degrees per day. Arrows lengths represent the displacement of the air mass in one day.

Low level circulation (950 mbar), over South-East Atlantic between 0S and 60S, is characterized by elevated wind speeds in the N-NW direction. During Apr-Jun and Jul-Sept, oceanic air masses from the South penetrate into the inner continent, over the Sahel region. On the other hand, during Jan-Mar and Oct-Dec, the Gulf of Guinea becomes a convergence zone between the northward wind flow from South-East Atlantic and the southward flow from Sahel.
At pressure levels of 850 and 750 mbar, winds of Northern Hemisphere (between 20N and 0N) turn W-SW, while those of Southern Hemisphere (between 0S and 20S) turn W-NW. During Apr-Jun and Jul-Sept, the wind speed over Southern Africa increases consistently. Coincident with the peak of fire occurrence in Southern African, a strong easterly air transport from the inner continent over ocean, is established. During Jan-Apr and Oct-Dec, air masses from Sahel Sahara are advected westward and southward over the Gulf of Guinea.
Two anticyclone-like pathways, centred over Southern Africa and South-East Atlantic, characterize the 850-750 mbar atmospheric circulation, below 20S.

3.3 Aerosol Daily Product

Data are from MODIS Level 3 aerosol daily product over ocean, at 1 degree resolution, of Collection 005. They are generated by aggregating 5-minutes Level 2 products at 10 km resolution onto a grid of 1 degree resolution, on a daily basis.
For six years, from 2005 to 2010, "seasonally" averaged maps of vertically integrated aerosol measurements are reported. Each year is divided in four time periods that differ from classical seasons, going from January to March, from April to June, from July to September (biomass burning season of Southern Hemisphere) and from October to December. This temporal organization permits to better describe the annual cycle of aerosol load.

3.3.1 Aerosol Optical Depth

Aerosol Optical Depth (AOD) at 550 nm is used to quantify the atmospheric aerosol load. It is defined as the aerosol attenuation of a perpendicular direct beam through a vertical column of the atmosphere. Its variability for 2005 is shown in Figure 9. Elevated AOD, approximately between 0.5 and 0.8, are detected during the Jan-Mar time period when aerosols principally lie over the Gulf of Guinea, within [5N, -5N]. The spatial mean AOD estimate for the whole South-East Atlantic is equal to 0.22 (ranging from near zero over most of the region, to approximately 0.8 in the northern part), with a large standard deviation of 0.18 (i.e. 81% of the mean value).
During the SH biomass burning season (Jul-Sept), AOD has its maximum off the coasts of Angola, close to biomass burning fire locations of Southern Africa. A large area within [0S, 20S] and [2.5E, 12.5E] shows the presence of an optically thick layer, whose AOD varies between 0.5 and 1. Aerosol load is particularly large near the continent, decreasing over deep ocean at lower longitudes.

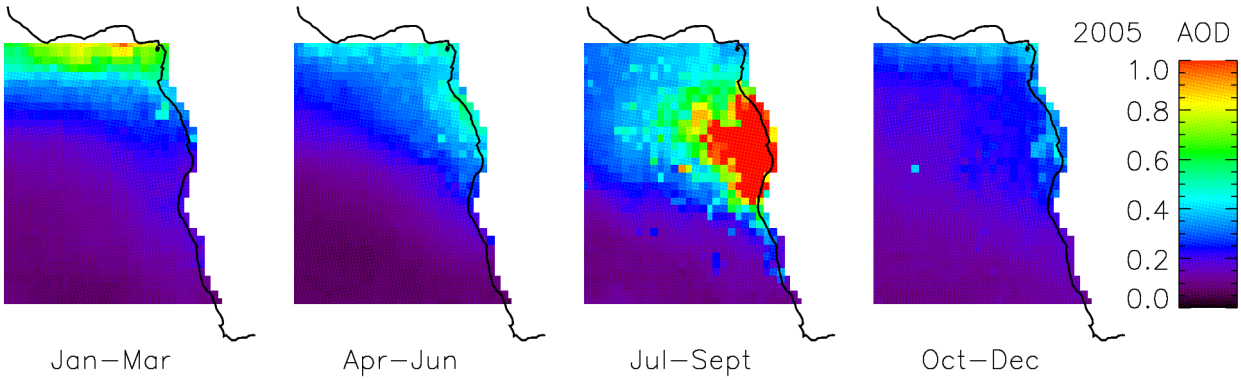

Figure 7: maps of seasonally averaged measurements of Aerosol Optical Depth over ocean for 2005, within [4N, -30N; -14E, 18E].

Figure 8 suggests an efficient easterly transport of aerosol particles from Southern Africa to very long distance, as far as 10^3 km away from coast line. During that season, we observe the highest aerosol optical depth of the whole year. The spatial mean AOD estimate is equal to 0.37, with a large standard deviation of 0.31 (i.e. 84% of the mean value), as a consequence of the strong geographical variability of aerosol field.
Apr-Jun and Oct-Dec appear as two transition periods. With respect to Jan-Mar and Jul-Sept, they are characterized by the presence of optically thinner layers, mainly located over the Gulf of Guinea and off the Angolan coast, with AOD equal to 0.3-0.6 (Apr-Jun) and 0.2-0.4 (Oct-Dec). In both periods, spatial mean AOD estimates are relatively small, equal to 0.19. The reduced geographical variability of AOD is attested by reduced standard deviations, equal to 0.12 during Apr-Jun and 0.07 during Oct-Dec (63% and 37% of the mean value).
Maps for 2006, 2007, 2008, 2009 and 2010 (Figure 14) reveal a strong AOD annual cycle, similar to that of 2005. Spatial means and standard deviations of AOD for 2005-2010 are reported in Table 4.

AOD	Jan Feb Mar	Apr May Jun	Jul Aug Sept	Oct Nov Dec
2005	0.22±0.18	0.19±0.12	0.37±0.31	0.19±0.07
2006	0.18±0.13	0.16±0.09	0.32±0.28	0.19±0.08
2007	0.25±0.21	0.16±0.08	0.36±0.30	0.17±0.06
2008	0.23±0.19	0.17±0.10	0.36±0.29	0.20±0.08
2009	0.19±0.14	0.16±0.08	0.36±0.31	0.16±0.07
2010	0.20±0.17	0.17±0.10	0.40±0.34	0.21±0.09

Table 4: seasonally averaged Aerosol Optical Depth over ocean within [4N, -30N; -14E, 18E], together with its spatial standard deviation, computed from geographical variations of AOD seasonal means.

3.3.2 Aerosol Index

An essential parameter retrieved by MODIS instrument is the Angstrom exponent (ANG, computed from measurements at 550 and 865 nm). It expresses the spectral dependence of aerosol optical depth, providing additional information on aerosol size (the larger the coefficient, the smaller the particle). It is defined as

$$\tau(\lambda)=\tau(\lambda_0)\left(\frac{\lambda_0}{\lambda}\right)^{\alpha} \qquad (11)$$

where λ is the wavelength, τ is the spectral AOD and α is the Angstrom exponent. When the Angstrom exponent is lower than 1, coarse-mode (marine aerosol, dust) dominates aerosol type. On the other hand, an Angstrom exponent larger than 1 indicates that fine-mode particles (biomass burning aerosol) are the most abundant (Smirnov, 2002; Queface et al. 2003; Thieuleux, 2005).

Aerosol Index (AI) is defined as the product of aerosol optical depth with Angstrom exponent. It allows for a more accurate quantification of aerosol column number concentration, than aerosol optical depth (Nakajima et al., 2001). It is used to give more weight to small particles (those which act as cloud condensation nuclei) and is well suited for the remote sensing of smoke, which belongs to fine-mode.

Aerosol index and Angstrom exponent maps for 2005 are shown in Figure 8 and Figure 4. During Jan-Mar, AI reaches its maximum value over a small area in the northern part of the region, where it is much lower than AOD, as a result of an Angstrom exponent lower than one. Over the Gulf of Guinea, aerosol index ranges between 0.2 and 0.35, AOD between 0.5 and 0.8 and Angstrom exponent is around 0.5 or lower. Other particles than biomass burning dominate aerosol type. High AOD combined to very low values of ANG suggest the presence of dust, transported southward from Sahel and Sahara regions, by local wind field (Figure 10). The spatial mean AI estimate is quite low (with respect to average AOD) and equal to 0.11, with a relatively modest standard deviation of 0.07 (64% of the mean value). The mean Angstrom exponent is 0.56, with a standard deviation of 0.13 (23% of the mean value).

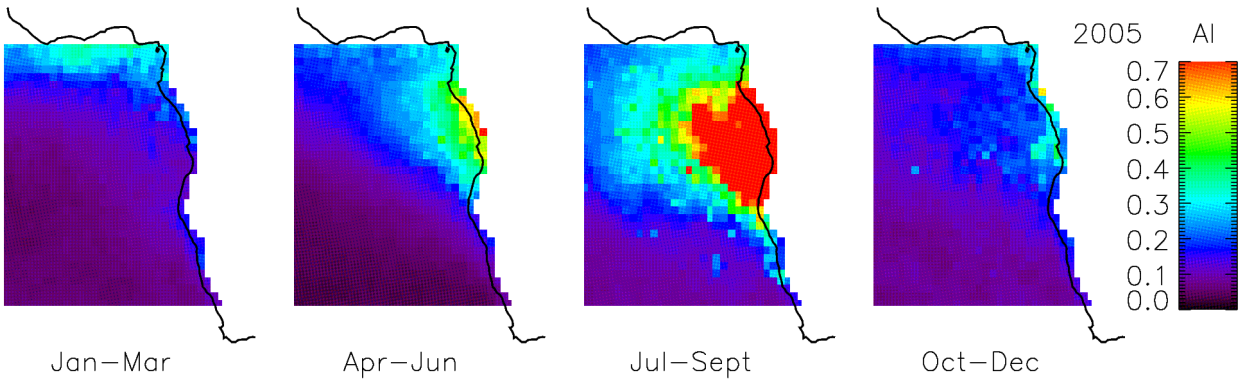

Figure 8: maps of seasonally averaged measurements of Aerosol Index for 2005. AI seasonal variability is high but somewhat different from that of AOD, because aerosol composition and hence Angstrom exponent vary during the year.

From April to June, when fires begin to occur in Southern Africa, aerosol load sensibly

increases over coastal areas between the Gulf of Guinea and Angola, where AI increases up to 0.5 and more. Angstrom exponent varies between 0.8 and 1.1, suggesting an easterly transport of smoke particles from Southern Africa over ocean, by winds at 850 and 750 mbar (Figure 10). Optically thickest aerosol layers are mainly located off the coasts of Angola, while southern and western parts of South-East Atlantic are relatively clean. With respect to previous trimester, the spatial mean AI estimate is little larger and equal to 0.15, as well as the resulting standard deviation of 0.12 (80% of the mean value). With respect to Jan-Mar time period, mean Angstrom exponent is increased by 17%, and equal to 0.67, with a spatial standard deviation of 0.16 (24% of the mean value).

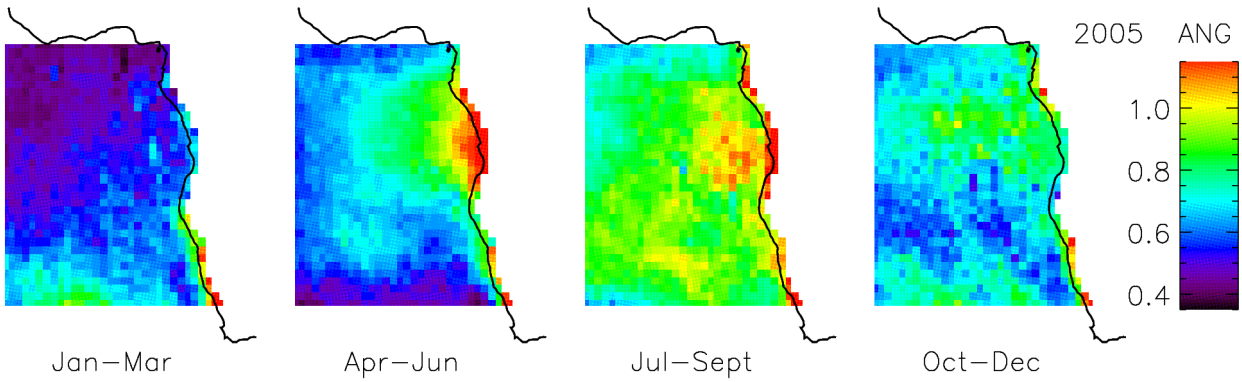

Figure 9: maps of seasonally averaged measurements of Angstrom exponent for 2005.

As expected, the heaviest aerosol concentration are observed during the biomass burning season (Jul-Sept). AI is particularly elevated over a wide area off the coasts of Angola, between 0.5 and 1.5 (not visible in Figure 8, that shows value up to 0.7 only). Angstrom exponent over the whole area is generally larger than 0.7, exceeding the unity (yellow and red points in Figure 4) near coast lines and off the coast of Angola. The spatial mean AI estimate is very large, equal to 0.33. Geographical variability of aerosol concentration is strong, as AI is almost zero over certain areas (southern part), and its spatial standard deviation results equal to 0.31 (94% of the mean value). Mean Angstrom exponent is equal to 0.87, with a standard deviation of 0.11 (13% of the mean value).

Over South-East Atlantic, the global amount of sea-salt aerosol (reasonably produced by the strong and constant surface wind, see Figure 10) is not supposed to have a strong annual cycle. During Jul-Sept, however, average Angstrom exponent is significantly higher than in other seasons. This indicates an increase in fine-mode fraction, with respect to total aerosol concentration, that confirms the enhancement of biomass burning concentration in the atmosphere.

From October, fire occurrence in Southern Africa decreases significantly. During Oct-Dec, average AI is about three time smaller than during Jul-Aug. The spatial mean estimate is equal

to 0.14, with a standard deviation of 0.06 (43% of the mean value). Angstrom exponent is equal to 0.14, about 20% lower than previous season, with a spatial standard deviation of 0.11 (79% of the mean value).
Aerosol index and Angstrom exponent maps for 2006-2010, are reported in Figure 14. Seasonal variability of aerosol production and transport over the area of interest is comparable to that of 2005. Inter annual variations are relatively modest, in comparison to the annual cycle. Spatial mean AI and ANG estimates, together with their standard deviations, are reported in Table 5 and Table 6.

AI	Jan Feb Mar	Apr May Jun	Jul Aug Sept	Oct Nov Dec
2005	0.11±0.07	0.15±0.12	0.33±0.31	0.14±0.06
2006	0.10±0.06	0.12±0.08	0.27±0.28	0.14±0.08
2007	0.14±0.09	0.12±0.08	0.31±0.29	0.12±0.04
2008	0.13±0.08	0.12±0.09	0.30±0.28	0.15±0.06
2009	0.10±0.06	0.11±0.07	0.30±0.31	0.12±0.06
2010	0.12±0.08	0.12±0.09	0.33±0.32	0.16±0.07

Table 5: seasonally averaged Aerosol Index over ocean within [4N, -30N; -14E, 18E], together with its spatial standard deviation, computed from geographical variations of AI seasonal means.

ANG	Jan Feb Mar	Apr May Jun	Jul Aug Sept	Oct Nov Dec
2005	0.56±0.13	0.69±0.16	0.87±0.11	0.71±0.11
2006	0.56±0.10	0.67±0.16	0.81±0.13	0.75±0.11
2007	0.63±0.15	0.70±0.15	0.79±0.12	0.71±0.09
2008	0.62±0.12	0.68±0.17	0.78±0.12	0.73±0.11
2009	0.59±0.12	0.68±0.14	0.77±0.13	0.72±0.10
2010	0.64±0.11	0.66±0.10	0.76±0.12	0.74±0.09

Table 6: same of Table 5, but for Angstrom exponent.

3.3.4 Aerosol Effective Radius

Aerosol optical depth and aerosol index are the most common parameters to quantify, with some differences, the overall aerosol load and concentration, over a certain region. Nevertheless, MODIS has the unique capability to retrieve aerosol particle effective radius from space, so as to differentiate quantitatively between fine- and coarse-mode.

According to Ichoku et al. (2004), fine-mode (smoke) is characterized by an aerosol effective radius smaller than 0.5 µm, mid-size aerosols (dust and sea-salt) have an effective radius between 0.5 µm and 1.0 µm while large particles (sea-salt) have an effective radius > 1 µm .

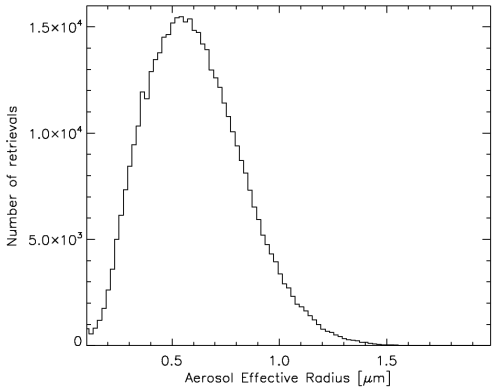

Figure 10: daily mean histogram of aerosol effective radius, at 1 degree resolution, for the whole 2005-2010 time period.

The histogram of MODIS daily AER retrievals over South-East Atlantic, for 2005-2010, is shown in Figure 6. In the 87% of cases, particles radius ranges between 0.2 and 0.9 µm (small and mid-size aerosol), with the highest AER occurrence between 0.5 and 0.6 µm. Figure 5 shows seasonally averaged maps of aerosol effective radius, for 2005.

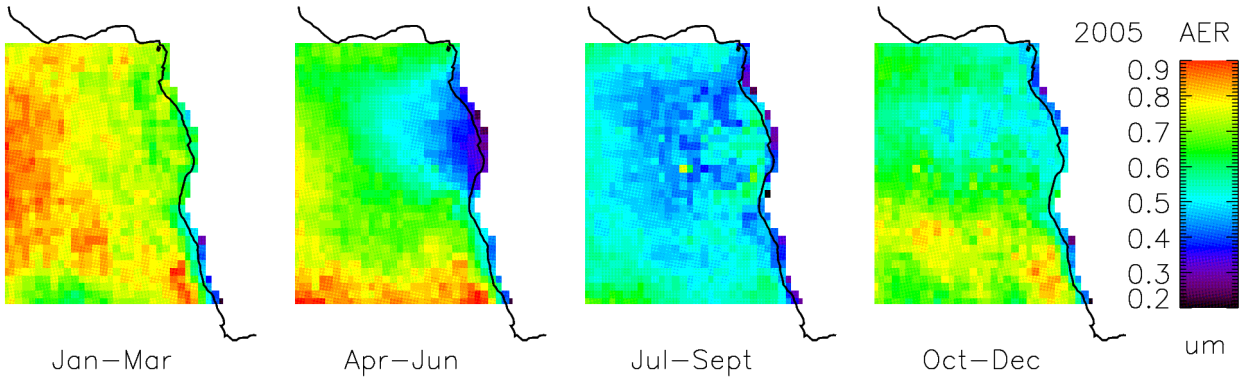

Figure 11: maps of seasonally averaged measurements of aerosol effective radius for 2005.

During the Jan-Mar time period, aerosol load is dominated by mid-size particles with effective radii between 0.6 and 0.9 µm. Smaller particles (0.6-0.8 µm) are detected closer to coast lines, while over the deeper western ocean AER is 1-2 µm larger (0.8-0.9 µm). During Apr-Jun, mean particle radius decreases of about 2-3 µm with respect to previous season (except over southern

ocean). During biomass burning season, fine particles with AER radius between 0.3 and 0.5 μm largely dominate the whole region, while from October, an overall higher aerosol droplet size, with AER of 0.6-0.7 μm, is retrieved almost everywhere. A limited area off the Angolan coast shows the persistence of smaller particles (0.5 μm), probably because fires over southern Africa still occur during October, while over southern ocean aerosol particles with AER of about 0.8 μm (probably sea-salt) are dominant again.
Maps of aerosol effective radius for 2006-2010 (Figure 14) show a spatial and temporal AER variability similar to that observed in 2005.

3.3.5 A simple method for aerosol classification over South-East Atlantic

Seasonal averages of retrieved aerosol optical depth, Angstrom exponent and effective radius can be combined together to allow for aerosol classification. Coupling indications from previous studies (Dubovick et al., 2002; Ichoku el al., 2004; Toledano et al., 2007; Raut and Chazette, 2008; Kaskaoutis et al., 2011) simple selection rules can be defined to rudely identify the dominant aerosol type of each area.

- Anthropogenic pollution (and hence biomass burning) is considered as dominant if Angstrom exponent is larger than 1, effective radius smaller than 0.6 μm and aerosol optical depth larger than 0.2.

- Desert dust events are generally characterized by very turbid atmospheres, with a very similar AOD for all wavelengths (Smirnov et al., 1998; Husar et al. 2001), that results in a low Angstrom exponent. Desert aerosol is considered as dominant if average Angstrom exponent is lower than 0.2, affective radius equal or larger than 0.5 μm and lower than 1 μm, and aerosol optical depth larger than 0.25.

- Maritime aerosol is considered as dominant if average value of Angstrom exponent is lower than 1.3, effective radius equal or larger than 0.5 and optical depth (in general substantially lower than that of desert dust) smaller than 0.15.

Remaining cases do not belong to any of the above groups and are considered as mixed-undetermined aerosols. Particles classification for 2005 is shown in Figure 12.
Maritime aerosols (in blue) cover southern ocean during most of the time. Biomass burning particles (in red) are manly concentrated off the coast of Angola, during SH dry season (Apr-Jun and Jul-Sept). Pure desert dust does not seem to dominate during any of the four seasons. However, during the Jan-Mar, the Gulf of Guinea is characterized by the presence of a consistent aerosol load with AOD larger than 0.25, ANG between 0.4 and 0.6 and AER between

0.3 and 1 (in orange). We infer the presence of a mixture of smoke and desert dust. This is coherent with Figure 11 and Figure 10, that show a convergence zone of low level winds (950 mbar), slightly north of 10 N. Analyzing data from the DABEX (Dust And Biomass-burning Experiment) field campaign in West Africa, Haywood et al. (2008) found that north of proximately 11 N, mineral dust is transported southward from the Sahara desert, where a strong static stability prevent dust from mixing vertically and trap aerosol in a layer between 900 and 850 mbar. South of 11 N, biomass burning particles from savanna burning are subjected to a northward advection, coming in contact with the desert particle flow. The hotter air mas from biomass burning overrides the cooler dust and is lifted to higher altitudes, probably mixing with part of the lower dust flow. With decreasing pressure level, local wind at 850-750 mbar turns southward and westward, allowing for transport of smoke-dust polluted air over the Gulf of Guinea.

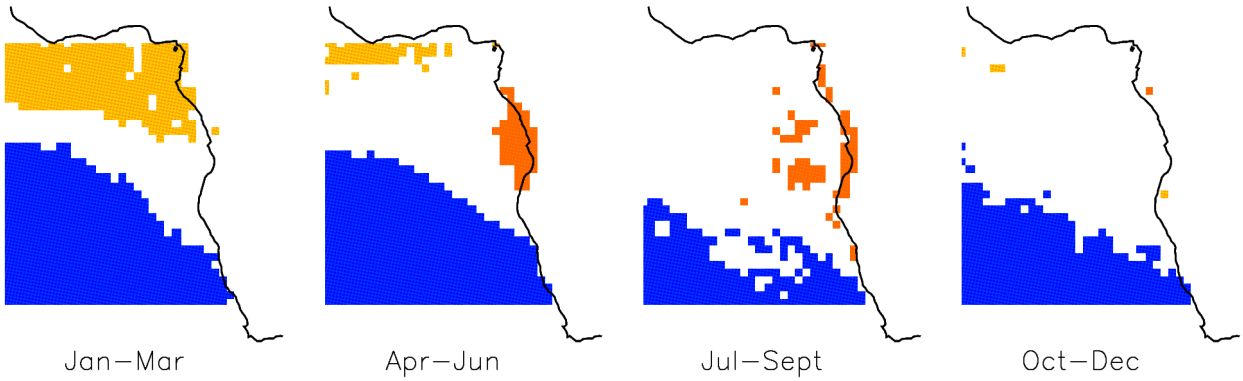

Figure 12: Aerosol classification for 2005, following the selection rules specified in the text maritime aerosols are in blue and biomass burning in red. In orange is underlined a zone where a mix of smoke aerosol and dust particles from Sahara desert probably occurs.

Results confirm the presence of a sea-salt dominated aerosol regime, characterized by local intrusion of heavy smoke layers, during the biomass burning season.
Figure 13 represents the histogram of six year AI observations, from MODIS daily product at 1 degree resolution (in red). Fine-mode fraction, calculated as the number of retrievals with AER lower than 0.5 μm divided by the total number of measurements, is shown in blue with dashed line. The corresponding scale, from zero to one, is reported on the right y-axis. For very low aerosol concentration, mid-size and coarse-mode are predominant but as AI increases from 0.3 to 1.0, fine-mode shifts to 65-95%.

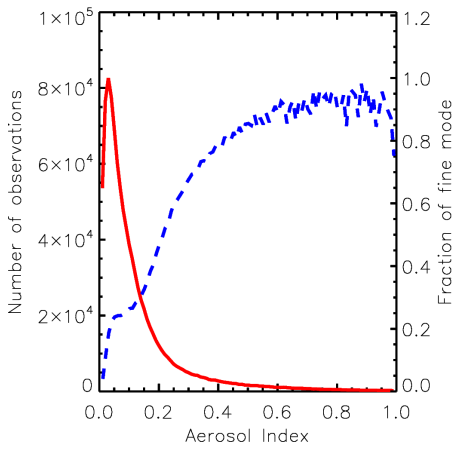

Figure 13: histogram of total Aerosol Index (solid red line, corresponding scale on left side of y-axis) and the fraction of fine-mode AI retrievals with respect to the total number of measurements (dashed blue line, corresponding scale on right side of y-axis), for the whole 2005-2010 time period. Data are from MODIS daily product over ocean, at 1×1 degree resolution.

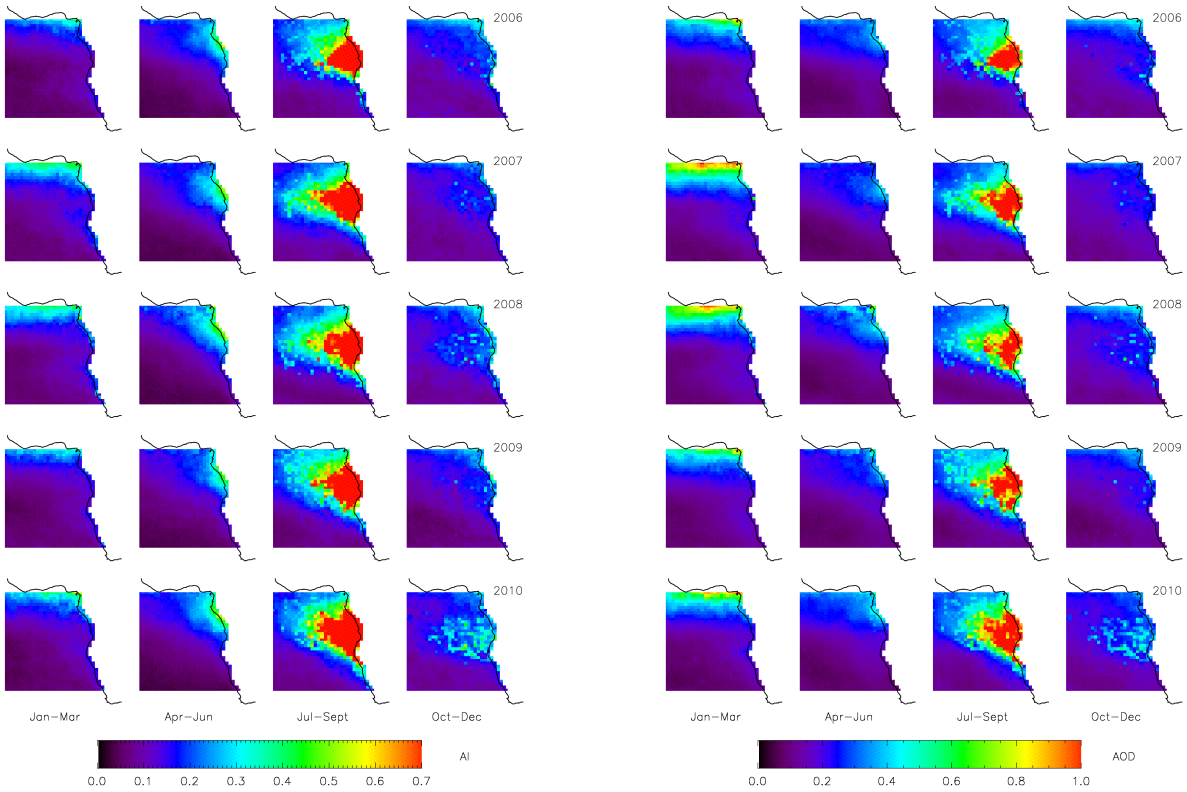

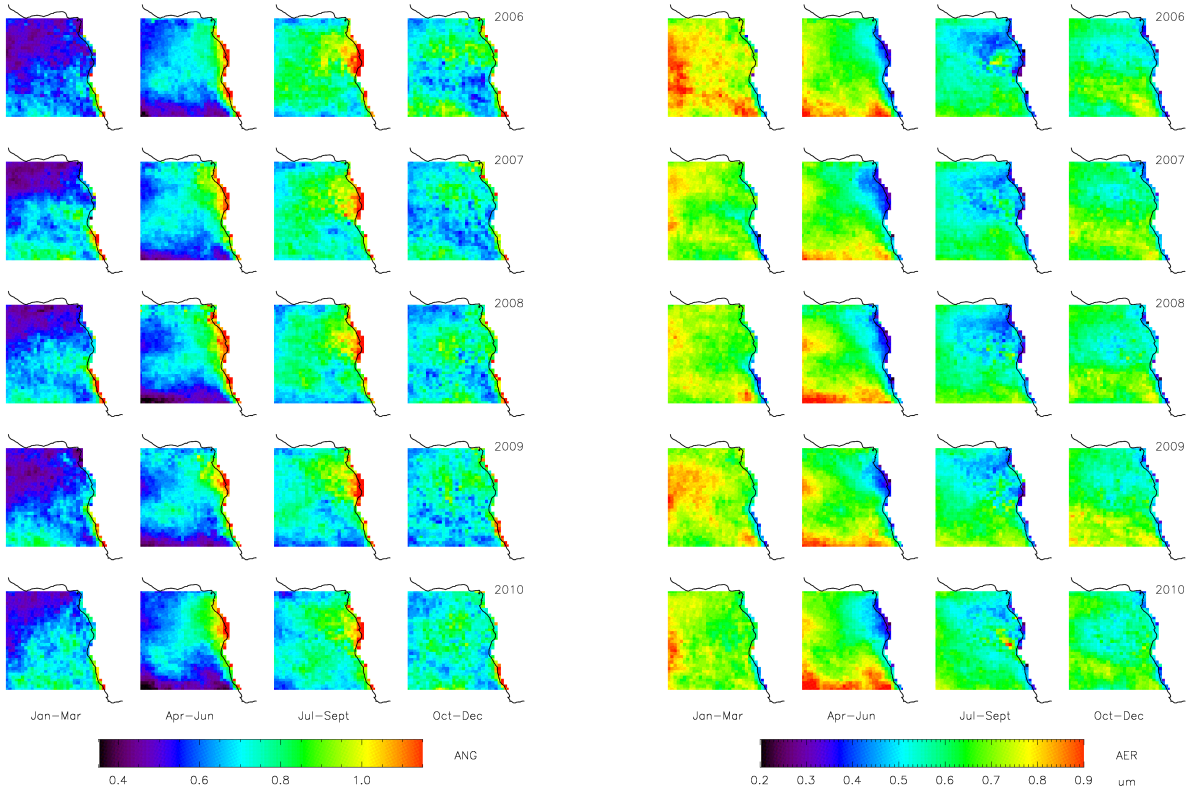

Figure 14: maps of seasonally averaged measurements of Aerosol Optical Depth (left top), Aerosol Index (right top), Angstrom exponent (left bottom) and aerosol effective radius (right bottom) for 5 years, from 2006 to 2010.

3.4 Cloud Daily Product

Seasonal characteristics of cloud field, for 2005-2010, are described hereafter. Data are from MODIS Level 3 cloud daily product over ocean of Collection 005, at 1 degree resolution. They are generated by aggregating the 5-minutes Level 2 products (at 1 km or 5 km resolution, depending on cloud parameter) onto a grid of 1×1 degree, on a daily basis.

3.4.1 Cloud Fraction

Level 3 cloud fraction represents the number of L2 cloudy pixels at 5 km resolution, divided by the total number of non-fill pixels, within a 1×1 degree box.

Level 2 cloud fraction, used to compute L3 product, is obtained by reading the 1×1 km cloud mask "Cloudiness Probability Flags", which can have the following settings: 0 = confident cloudy, 1 = probably cloudy, 2 = probably clear, 3 = confident clear. Computing cloud fraction,

the first two flags are considered 100% cloudy, while last two 100% clear. L2 cloud fraction is obtained from the fraction number of 1 km cloudy pixels, within a 5×5 km L2 box. It has been shown by Hubanks et al. (2008) that cloud fraction retrieval algorithm may interpret as cloud the blowing dust that west of Sahara Desert and over the Arabian Sea.

Figure 15 represents seasonal maps of L3 cloud fraction, that show a clear increase of cloud coverage throughout the year, from Jan-Mar to Sept-Dec. During Jan-Mar, fractional cloud coverage varies between 0.2 and 0.4 (with slightly larger values off the coasts of Southern Africa), increases up to 0.7-0.8 in Apr-Jun (off the coast of Namibia) and reaches its maximum values during Jul-Sept (0.8-0.9). It then remains particularly high also during Oct-Dec. Apart from Jan-Mar, central part of South-East Atlantic results characterized by a very persistent cloud field, with a fractional coverage between 60 and 90%.

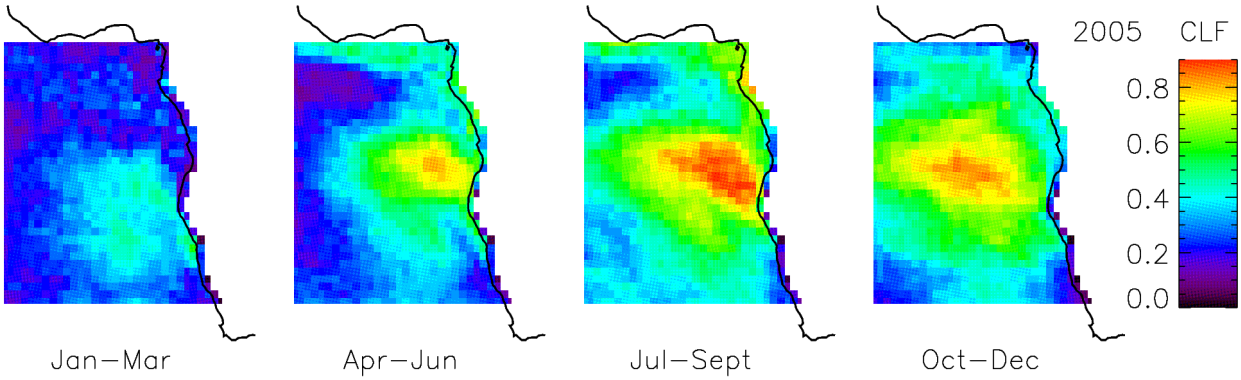

Figure 15: maps of seasonally averaged measurements of cloud fraction, for 2005.

Spatial mean CLF estimates shown in Table 7 indicate that the peak of cloud fraction occurs during the biomass burning season and Oct-Dec (49% and 48%, respectively), decreasing of about 20% during Jan-Mar. A similar annual cycle is observed in each year from 2006 to 2010 (Figure 20). In first approximation, there is a certain spatial and temporal correlation between biomass burning aerosol concentration and shallow cloud occurrence, except during Oct-Dec, when CLF is high even though smoke production is sensibly reduced. These observations are not in contrast with Albrecht's hypothesis (Albrecht, 1989), which links cloud cover enhancement to fine aerosol invigoration. However, in order to separate aerosol-induced effect from local meteorology, so as to infer a real cause-effect relationship between changes in AI and those in CLF, a more accurate analysis is needed, involving individual values rather than seasonal averaging.

CLF	Jan Feb Mar	Apr May Jun	Jul Aug Sept	Oct Nov Dec
2005	0.26 ± 0.08	0.36 ± 0.15	0.49 ± 0.16	0.48 ± 0.16
2006	0.26 ± 0.10	0.27 ± 0.11	0.51 ± 0.18	0.50 ± 0.15
2007	0.30 ± 0.11	0.28 ± 0.10	0.50 ± 0.18	0.47 ± 0.14
2008	0.27 ± 0.11	0.25 ± 0.10	0.46 ± 0.19	0.50 ± 0.15
2009	0.26 ± 0.10	0.30 ± 0.12	0.50 ± 0.17	0.45 ± 0.14
2010	0.26 ± 0.10	0.33 ± 0.13	0.49 ± 0.17	0.46 ± 0.15

Table 7: seasonally averaged Cloud Fraction over ocean within [4N, -30N; -14E, 18E], together with its spatial standard deviation, computed from geographical variations of CLF seasonal means.

3.4.2 Cloud Optical Thickness

Seasonal averages of cloud optical thickness over South-East Atlantic are shown in Figure 16. From April to December, optically thick layers (COT ≥ 9) are usually present in the northern part of the area, over coast lines of Cameron, Gabon, Congo and Namibia. They probably belong to the continental cloud field. Over ocean, marine stratocumulus are in general optically thinner, with COT larger over deep ocean than near coast lines.

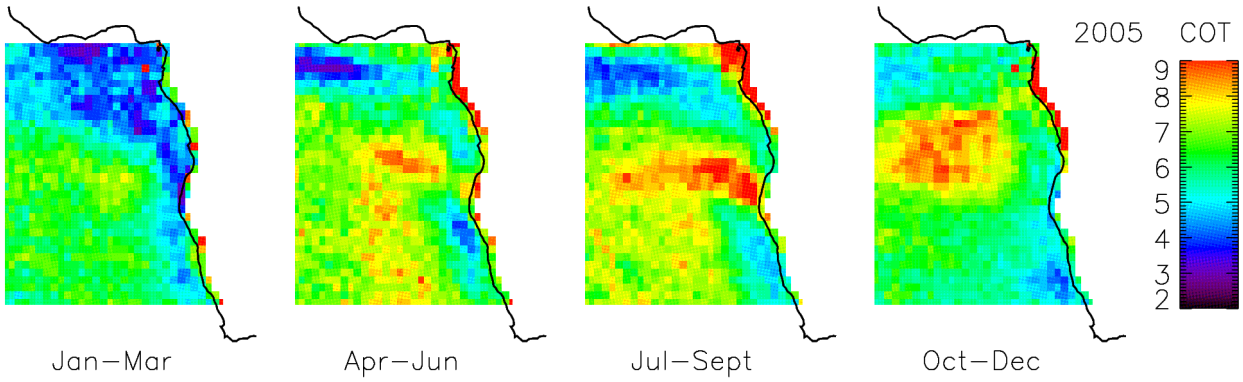

Figure 16: maps of seasonally averaged measurements of cloud optical thickness, for 2005.

Figure 16 (2005) and Figure 20 (2006-2010) suggest that COT seasonal variability is not particularly strong, as confirmed by spatial mean estimates, reported in Table 8. Biomass burning season is always characterized by the optically thickest clouds and average COT between 6.56 (2008) and 7.14 (2006). The lowest COT values mostly occur during Jan-Mar, with spatial means between 5.50 (2009) and 5.68 (2006).

COT	Jan Feb Mar	Apr May Jun	Jul Aug Sept	Oct Nov Dec
2005	5.54±1.10	6.63±1.25	6.74±1.40	6.38±1.15
2006	5.68±1.08	6.06±1.41	7.14±1.45	6.57±1.29
2007	5.55±1.12	5.99±1.13	6.83±1.38	6.34±1.01
2008	5.59±1.15	5.83±1.27	6.56±1.32	6.47±1.08
2009	5.50±1.10	6.17±1.22	6.92±1.40	6.27±1.10
2010	5.63±1.16	6.15±1.27	6.89±1.40	6.18±0.97

Table 8: seasonally averaged Cloud Optical Thickness over ocean within [4N, -30N; -14E, 18E], together with its spatial standard deviation, computed from geographical variations of COT seasonal means.

During Jan-Mar, COT varies approximately between 3.0 and 5.0, off Central and Southern African coasts, increasing of about 2 μm (between 5.0 and 7.0) over deep ocean. This COT pattern is somewhat present also during the following three seasons, with specific COT features depending on time period. From April, clouds begin to become optically thicker over the central part of the ocean and during Oct-Dec COT increases up to 8-9, over a large area. It seems that cloud optical thickness maxima show a certain spatial correlation with peaks of fractional cloud cover.

3.4.3 Liquid Water Path

Similarly to COT, liquid water path (Figure 17) is much larger over deep ocean (70-100 g/m²) than off Central and Southern African coasts (30-40 g/m²). In particular, during Apr-Jun and Jul-Sept, clouds over the southern-western part of the region are characterized by extremely large water contents, reaching and over-passing 100 g/m².

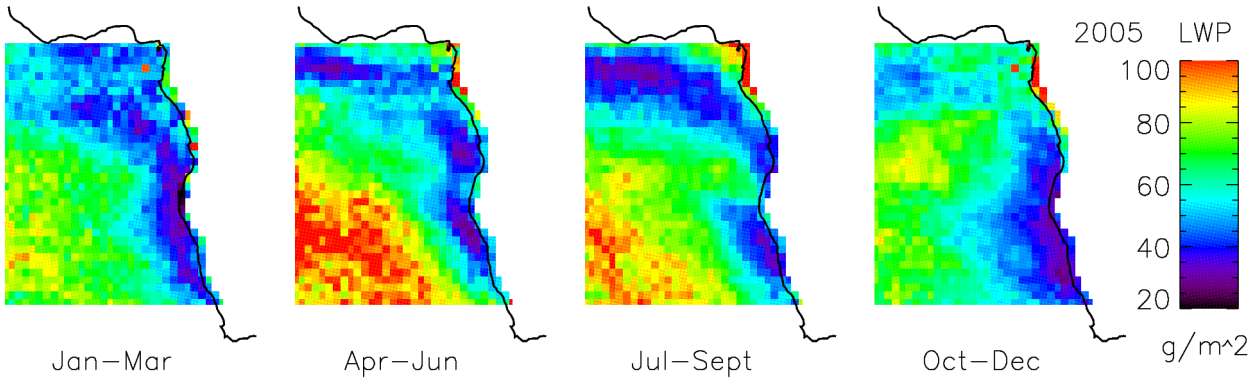

Figure 17: maps of seasonally averaged measurements of liquid water path, for 2005.

The comparison of LWP (Figure 17) with maps of AOD and AI (Figure 9 and Figure 8) does not stress any evident spatial correlation between peaks in particle concentration and those in liquid water path amount. In particular, reduced LWP values along the whole African coast line show little seasonal variability, in contrast with the strong annual cycle observed for AOD and AI. Moreover, during the biomass burning season, maxima of LWP over deep southern-western ocean are located very far away from the heaviest smoke layers, off the coast of Namibia. In very first approximation, results suggest that local meteorology is probably the main factor governing LWP variability, over such area. The seasonal average of spatial mean LWP estimates from 2005 to 2010 is shown in Table 9.

LWP [g/m²]	Jan-Feb-Mar	Apr-May-Jun	Jul-Aug-Sept	Oct-Nov-Dec
2005	58.4±14.7	68.1±20.9	64.3±19.0	59.1±13.6
2006	59.9±14.8	66.4±22.8	66.6±18.9	61.3±15.1
2007	57.2±14.6	65.3±19.3	64.9±17.1	61.1±13.5
2008	58.4±14.1	65.0±21.5	65.6±19.1	61.6±13.1
2009	58.0±14.0	67.0±19.2	65.7±18.6	58.3±12.7
2010	59.9±16.3	63.4±19.9	66.8±20.7	58.5±12.4

Table 9: seasonally averaged Liquid Water Path over ocean within [4N, -30N; -14E, 18E], together with its spatial standard deviation, computed from geographical variations of LWP seasonal means.

3.4.4 Cloud Droplet Radius

Mid-infrared refracted radiation from clouds is inversely proportional to droplet size, for a given cloud optical thickness. MODIS retrieval algorithm uses a precomputed set of reflectances to estimate COT and CDR over ocean, from measurements at 0.86 μm (0.65 and 1.2 μm over land and snow) for the non-absorbing channel (selected to minimize the contribution of the surface) and 2.1 μm for the absorbing channel (alternatively 1.6 and 3.7 μm can be also used, to probe different cloud depths).

Seasonal maps of cloud effective radius are shown in Figure 18. The smallest CDR estimates are generally observed off the coasts of Southern and/or Central Africa, varying between 10 and 13 μm. They are somewhat coincident with with the most elevated values of AI and Angstrom exponent (smoke polluted areas). This is in good agreement with Twomey's hypothesis, according to which fine-aerosol invigoration may induce to a decrease in cloud droplet effective radius. On the other hand, during Jan-Mar, CDR is particularly large (20-21 μm) over the Gulf of Guinea, where aerosol load is relatively high but dominated by coarse-mode particle type.

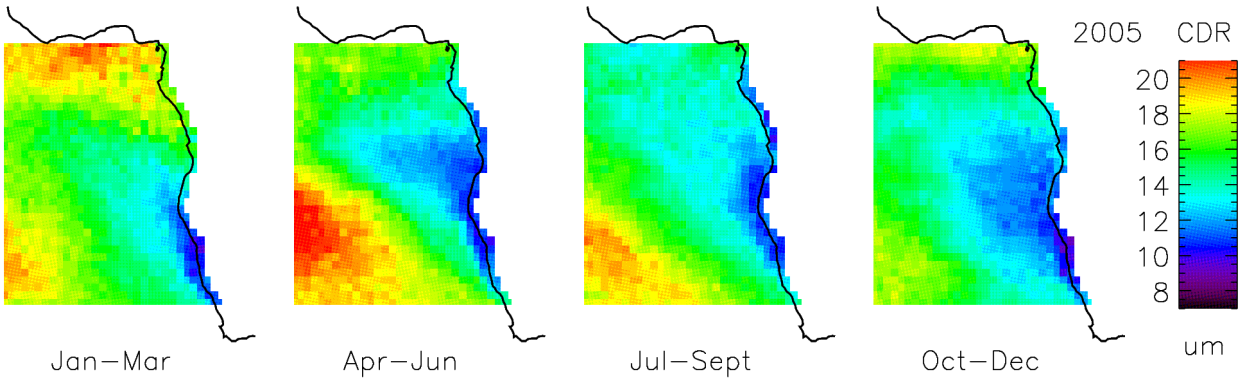

Figure 18: maps of seasonally averaged measurements of cloud droplet radius, for 2005.

Over the southern-western part of the region, CDR varies between 19 and 21 μm during most part of the year. It drops down to 15-17 μm in Oct-Dec, of each year from 2005 to 2010 (Figure 18 and Figure 20), without any evident variation in local aerosol concentration (AI remains low and approximately constant). At the same time, droplet size seems to correlate well (temporally and spatially) with LWP, suggesting the cyclic formation of well developed clouds (from January to September) with optical and physical features mainly governed by local

meteorology, more than aerosol-induced effect.

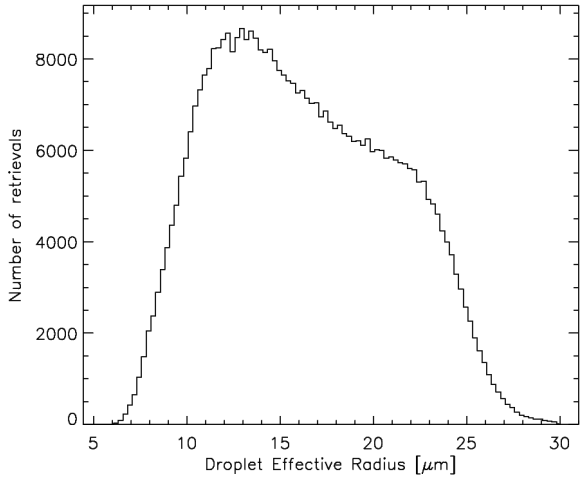

Figure 19: daily mean histogram of Cloud Droplet Radius, at 1 degree resolution, for the whole 2005-2010 time period.

The histogram of daily droplet radius retrievals at 1° resolution, for the whole 2005-2010 time period, shows that CDR over South-East Atlantic ranges between 9.5 and 23 μm, in the 84% case of cases, with maxima up to 28-30 μm (Figure 19). At the same time, spatial mean CDR estimates (Table 10) indicate a modest seasonal variability. During Jul-Sept and Oct-Nov, average CDR is about 1-2 μm smaller than during Jan-Mar and Apr-Jun. The lowest mean radius estimates are always observed during Oct-Dec, when the cloud field over the southern-western region (with elevated water amounts and large droplet sizes) is no more present.

CDR [μm]	Jan Feb Mar	Apr May Jun	Jul Aug Sept	Oct Nov Dec
2005	16.2±2.2	15.9±2.8	14.9±2.2	14.3±1.9
2006	16.0±1.9	16.6±2.3	14.5±2.6	14.3±1.8
2007	15.9±2.2	16.5±2.2	14.9±2.3	14.7±2.0
2008	16.2±2.1	16.8±2.5	15.5±2.4	14.7±1.9
2009	16.2±2.1	16.5±2.3	14.7±2.3	14.3±1.9
2010	16.3±2.2	15.9±2.6	15.1±2.8	14.6±1.8

Table 10: seasonally averaged Cloud Droplet Radius over ocean within [4N, -30N; -14E, 18E],

together with its spatial standard deviation, computed from geographical variations of CDR seasonal means.

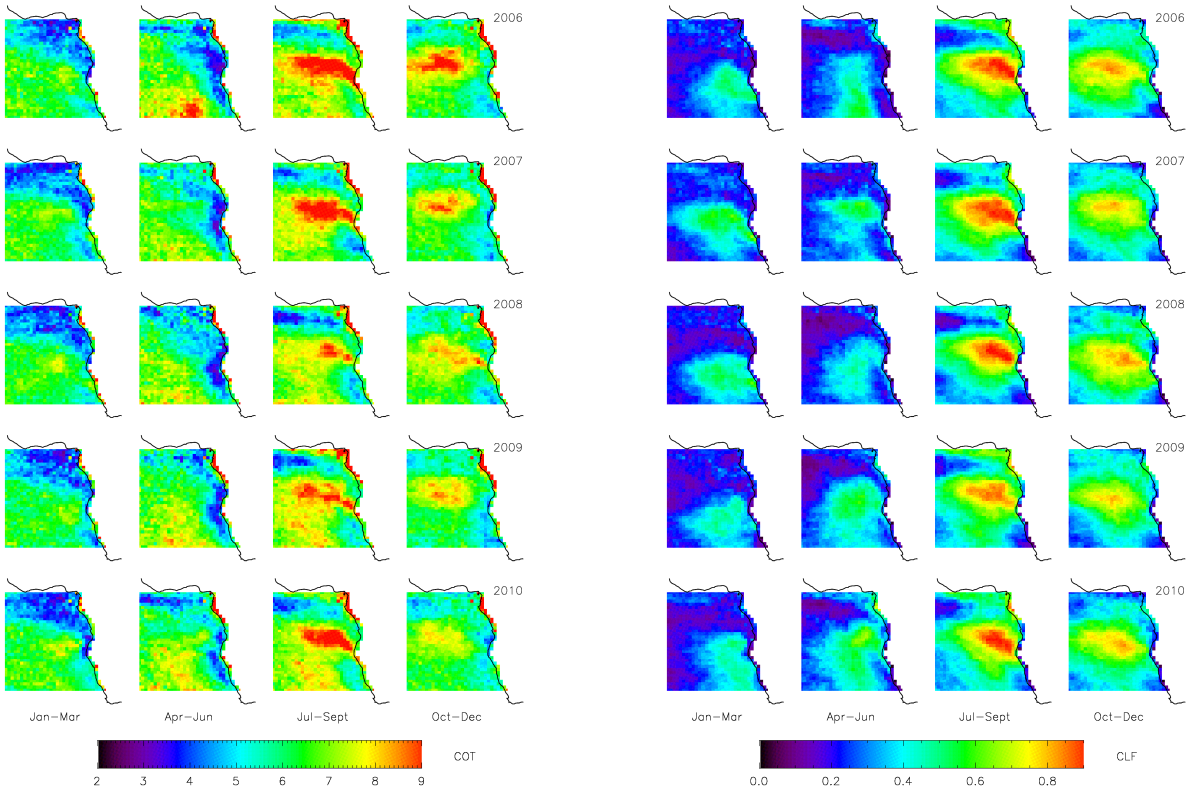

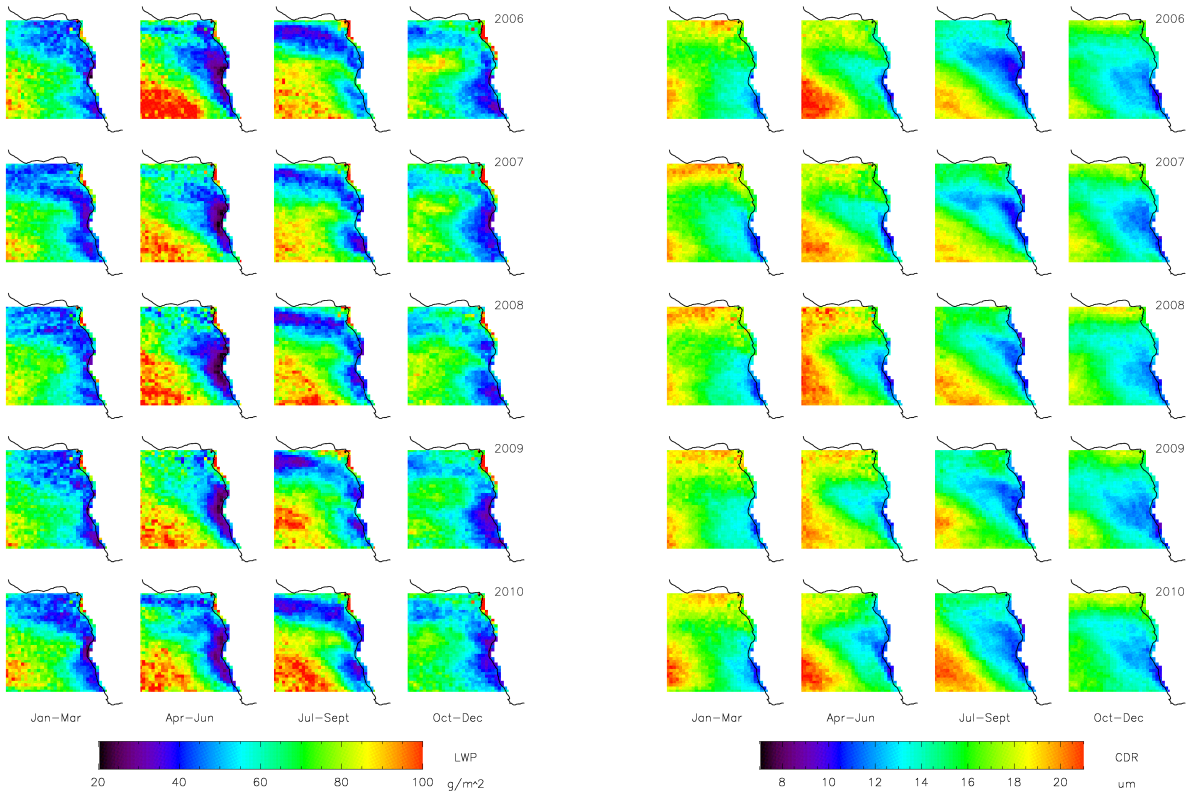

Figure 20: maps of seasonally averaged measurements of cloud fraction (left top), cloud optical depth (right top), liquid water path (left bottom) and cloud droplet effective radius (right bottom) for 5 years, from 2006 to 2010.

3.5 Summary and conclusions

The comparison of six year MODIS observations over South-East Atlantic, from 2005 to 2010, showed a strong annual cycle of aerosol production and transport, with modest inter-annual variability compared to seasonal variations, dominated by two different regimes. The first one, from October to March, is characterized by optically thin aerosol layers (with AI generally below 0.2) and Angstrom exponents usually smaller than one, sign of a coarse-mode dominated regime. The second one, marked by the presence of larger concentrations of smaller particles, begins on April and culminates during the biomass burning season, when AI and ANG get larger than one. Large quantity of fine-mode particles, of biomass burning type, are transported by trade winds from Southern Africa to very long distance over the ocean, where a semi-permanent low cloud field is present.

Smoke is an efficient CCN, that helps cloud formations and may affect cloud microphysical (CDR) and optical properties (COT), AIE#1, as well as cloud horizontal extent (CLF) and precipitation (LWP), AIE#2. Over South-East Atlantic, the occurrence of larger concentrations

of biomass burning particles appeared in some cases coincident with that of smaller cloud droplets and larger cloud fractions. However, there is no evident systematic correlation between aerosol invigoration and the change in any of the retrieved cloud parameters.

Results stress the need of a more accurate analysis to look for statistical evidence of aerosol-induced effects on marine boundary layer clouds and quantify the strength of aerosol impact. In this chapter, we used 1 degree seasonal mean estimates to describe overall characteristics of cloud and aerosol properties. Aerosol impact may be easier to observed from instantaneous retrievals, at higher spatial resolution (1, 5, 10 km).

In cloud-free conditions, aerosol reflects incoming solar radiation back to space, decreasing the amount of sunlight reaching the Earth surface and producing a negative radiative forcing at the top of the atmosphere. Absorbing aerosol (e.g. biomass burning particles, composed by large amounts of inorganic compounds, as black carbon), cooling the surface and warming the atmosphere, can yield to large positive forcing if the underlying surface is reflective enough (e.g. clouds). Over the South-East Atlantic, the occurrence of heavy smoke layers and extended low cloud fields is prone to produce both negative and positive forcing, depending on aerosol and cloud properties as well as vertical position.

The use of a atmospheric radiative transfer model, constrained by aerosol-cloud satellite observations, will allow for a near-realistic representation of local meteorological conditions and a reliable quantification of the overall aerosol forcing, over such region.

Chapter IV – The effect of aerosol on clouds and precipitations, overview

4.1 Theoretical background

4.1.1 Twomey's effect (or First Aerosol Indirect Effect)

Aerosol impact on cloud microphysics (cloud droplet concentration and size distribution) has been studied since late 50's by pioneering works, pointing out that high concentration of cloud condensation nuclei (CCN) from anthropogenic pollution, such as biomass burning aerosol, can increase the cloud droplet number concentration (CDNC).
Warner and Twomey (1967) and Warner (1967) reported of an increase of CCN number concentration, as consequence of the incorporation into clouds of smoke aerosol from sugar cane fires, with decrease of cloud droplet radius (maybe impeding the growth of rain drops for coalescence). Such effect can easily be described analytically. According to Platnick and Twomey (1994), the mass of water per unit volume within a cloud, the so called Liquid Water Content (LWC), can be expressed as

$$LWC = \rho_w \frac{4}{3} \pi \int r^3 n(r)\, dr \tag{12}$$

$$\rho_w \frac{4}{3} \pi \int r^3 n(r)\, dr = \rho_w \frac{4}{3} \frac{\pi \int r^3 n(r)\, dr}{\int n(r)\, dr} \int n(r)\, dr = \pi \rho_w \frac{4}{3} \bar{r^3} N \tag{13}$$

$$LWC = \pi \rho_w \frac{4}{3} \bar{r^3} N \tag{14}$$

r = cloud droplet radius [m]
n(r) = droplet size distribution as a function of radius [m^{-4}]
ρ_w = water density [kg/m^3]
N = cloud droplet number concentration [m^{-3}]

After particle activation, cloud droplet number concentration is equal to the number concentration of activated CCN. It is then reasonable to assume that clouds forming under the same circumstances, but with different CCN amounts, have the same amount of water vapor disposable for nucleation. In that case, the same mature clouds would have equal LWC. However, as a consequence of equation (12), the mean droplet size of the polluted cloud (with

higher cloud droplet number concentration) would be smaller then that of the clean one.
In 1974, Twomey proposed a link between pollution and cloud optical thickness, as a consequence of the increase of droplet concentration in polluted clouds, the so called *Twomey's effect* (Twomey, 1974). Cloud optical thickness expresses the quantity of radiation removed from a light beam (perpendicular to the target surface) by scattering or absorption, during its path through a medium (in this case a cloud). If I_0 is the intensity of radiation at the source and I is the observed intensity after a given path, then the optical thickness τ is defined, by the Beer's law, as

$$\frac{I}{I_0} = e^{-\tau} \tag{15}$$

For a cloud of geometrical thickness Δh with an incident radiation beam at the wavelength λ, cloud optical thickness can be evaluated as

$$\tau = \int Q_e(r/\lambda)\pi r^2 n(r)\,dr\,\Delta h \tag{16}$$

$$\int Q_e(r/\lambda)\pi r^2 n(r)\,dr\,\Delta h = \frac{\pi \int Q_e(r/\lambda) r^2 n(r)\,dr\,\Delta h}{\int r^2 n(r)\,dr} \frac{\int r^2 n(r)\,dr}{\int n(r)\,dr} \int n(r)\,dr\,\Delta h \tag{17}$$

$$\tau = \overline{Q_e}\,\pi\,\overline{r^2} N \Delta h \tag{18}$$

where $\overline{Q_e}$ is the mean extinction efficiency, which reaches an asymptotic value of ~2 in the visible and near infrared. In case of polluted clouds, cloud optical thickness will the result from the balance between two competing aerosol-induced effects, the increase in cloud droplet number concentration and the diminution in droplet effective radius. Solving equation (12) with respect to r and substituting the result in equation (18), we can express cloud optical thickness as a function of N and LWC only,

$$\tau = \overline{Q_e}\,\pi \left(\frac{3\,LWC}{\rho\,4\,\pi} \right)^{2/3} N^{1/3} \Delta h \tag{19}$$

so that if liquid water path remains constant $\tau \propto N^{1/3}$.

On the other hand, if we solve (12) with respect to N and substitute the result into (18), cloud optical thickness can be expressed as a function of r and LWC,

$$\tau = \frac{3}{2} \frac{LWC \, \Delta h}{\rho_w} \frac{\overline{r^2}}{\overline{r^3}} \tag{20}$$

In literature, the parameter

$$r_{eff} = \frac{\overline{r^3}}{\overline{r^2}} = \frac{\int r^3 n(r) dr}{\int r^2 n(r) dr} = \frac{r_v^3}{r_{rms}^2} \tag{21}$$

is generally referred as *cloud droplet effective radius*. It is the quantity retrieved from cloud reflection measurements, while r_v and r_{rms} are respectively the volume weight moment and the root mean square of the droplet size distribution. The relation between the mean volume droplet radius and the effective radius is generally estimated empirically in the form

$$r_v^3 = k \, r_e^3 \tag{22}$$

where *k* is supposed to varies between 0.8 and 0.9 from clean and polluted clouds (Palowska and Brenguier, 2000). The quantity

$$LWP = LWC \, \Delta h \tag{23}$$

is called Liquid Water Path [g/m²] and represents the mass of water per unit cloud surface. Substituting (21) and (14) into equation (15), we can express liquid water path as a function of cloud droplet number concentration, geometrical thickness and effective radius,

$$LWP = \pi \rho_w \frac{4}{3} k \, r_e^3 \, N \, H \tag{24}$$

Substituting (19) and (14) in equation (17), the particle size dependence of the optical thickness can be easily expressed as

$$\tau = \frac{3}{2} \frac{LWP}{r_e \rho_w} \tag{25}$$

Consequently, $\tau \propto r_{eff}^{-1}$ under the assumption of constant liquid water path. The importance of equation (15) is considerable, as it establishes a simple relationship between two integral

variables (optical thickness and liquid water path) and the microphysical parameter which characterizes most the effect of pollution on clouds (cloud effective radius).

4.1.2 Cloud droplet radius and cloud optical thickness dependence on aerosol number concentration

The relationship between aerosol number concentration (N_a) and cloud droplet concentration (N_c) can be expressed by the following approximation calculated by satellite-derived measurements and now considered well established (Twomey, 1984; Kaufman and Fraser, 1997; Nakajima et al., 2001)

$$\Delta \log N_c = g \Delta \log N_a \tag{26}$$

The coefficient g is smaller than one. It has been calculated to be equal to 0.7 for Kaufman et al. (1991) from aircraft measurements over ocean and land, equal to 0.5 for Nakajima et al. (2001) from satellite AVHRR measurements over ocean, and equal to 0.48 for Lohmann et al. (2000) from model simulations over ocean. Using this assumption, equation (13) yields to

$$\Delta \log LWP = g \Delta \log N_a + 3 \Delta \log r_e \tag{27}$$

If the LWP is considered constant, the latter relation becomes

$$\Delta \log r_e = -(\frac{g}{3}) \Delta \log N_a \tag{28}$$

The combination of equation (15) and (16) leads to a similar relationship, describing the change of cloud optical thickness as a function of aerosol number concentration,

$$\Delta \log \tau = (\frac{g}{3}) \Delta \log N_a \tag{29}$$

Thus, the “strength” of aerosol impact on droplet effective radius and that on cloud optical thickness are equal in magnitude, but opposite in sign. If we consider that aerosol index is proportional to anthropogenic aerosol number concentration, it results that

$$\Delta \log r_e = -\alpha \, \Delta \log AI \tag{30}$$

$$\Delta \log \tau = \alpha \, \Delta \log AI \tag{31}$$

$$\alpha = \frac{g}{3} \tag{32}$$

α = 0.23, with g = 0.7 (Kaufman et al., 1997)

α = 0.17, with g = 0.5 (Nakajima et al., 2001)

If we use the parametrization of Nakajima et al. (2001), the relationship between anthropogenic aerosol number concentration and satellite-retrieved aerosol index is not linear and can be expressed as

$$N_a = 4.57 \times 10^8 (AI)^{\gamma} \tag{33}$$

where $\gamma = 0.869$. According to (22), the linear slope between the logarithm of cloud droplet effective radius (cloud optical thickness) and aerosol index can be re-estimated, hence

$$\alpha = \frac{g\gamma}{3} \tag{34}$$

α = 0.20, with g = 0.7 (Kaufman et al., 1997) and γ = 0.869 (Nakajima et al., 2001)

α = 0.14, with g = 0.5 (Nakajima et al., 2001) and γ = 0.869 (Nakajima et al., 2001)

4.1.3 The lifetime effect (or Second Aerosol Indirect Effect)

The main idea of life time effect is that spatial cloud cover and liquid water content (consequently their optical parameters) are determined by precipitation efficiency, which is supposed to be partly regulated by aerosol. This hypothesis was developed by Albrecht in 1989 and is intrinsically different from Twomey's effect, since not defined for a fixed cloud structure.

Precipitation efficiency of shallow clouds is supposed to decrease monotonically as cloud droplet number concentration (CDNC) increases, as a consequence of coalescence process

suppression. As anthropogenic aerosols are very efficient CCN, an enhancement in their concentration may largely increase CDNC and hence reduce precipitation occurrence of polluted clouds. This idea finds its roots in the work of Squires (1958). Over south-eastern Australia, the adjacent seas and near Hawaii, he observed that *high droplet concentrations and small average and maximum drop sizes are associated with clouds of considerable depth failing to rain*, while *a spectrum characterized by relatively large average and maximum droplet sizes is favourable to the operation of the coalescence process*.

The conventional wisdom is that precipitation removes water from cloud, reducing cloud amount, whereas inhibition of precipitation leads to long-lived clouds, where liquid water remains constant or continues to augment depending on the water vapor supply.

As precipitation suppression is a positive function of cloud droplet number concentration, the increase in water content and cloud cover in polluted environments, with respect to clean atmospheres, is then expected to be somewhat proportional to aerosol concentration.

Cloud lifetime effect lacks of a simple analytical description, as in case of Twomey's theory, and it is far from being well establish. Large uncertainties rise from the fact that certain areas, as regions of slow atmospheric pressure, are convergent zones that tend to accumulate aerosol and water vapor and generate conditions favorable for cloud formation. In that way large-scale meteorological parameters can impact simultaneously both aerosol concentration and cloud development, generating false correlation between them. In addiction, satellite-based retrievals do not provide the temporal resolution, that would allow to infer a clear causality between changes in aerosol concentration and cloud properties.

Evidences of aerosol precipitation suppression, leading to a decrease in cloud cover, have been shown in a number of studies. Many others, however, suggest partially different or opposite conclusions. We describe hereafter two examples where macrophysical effects (e.g. cloud dynamics) buffer the system response to aerosol perturbations and show how aerosol lifetime effect can significantly be regime dependent (Stevens et Feingold, 2009).

Local inhibition of precipitation may help precondition the environment for deeper convection, raining more. Such theory tells that, at least for cumulus clouds, less precipitation means more liquid water lifted to the cloud top zone, where it evaporates cooling the cloud. This cooling destabilizes the environment allowing clouds to growth more. Deeper clouds produce more rain and the resulting precipitation can overcomes the initial suppression. Moreover, in case of deep convection and shallow convection over ocean, the longevity of the cloud system is linked to the development of precipitation, that may enhance cloudiness.

4.2 Remote Sensing of Aerosol Indirect Effect from Space: previous studies

4.2.1 Droplet Effective Radius and Cloud Optical Thickness

A number of satellite remote sensing studies have shown intriguing relationships between proxies of cloud-active aerosol and cloud microphysics. Most among them are coherent with the Twomey's hypothesis. Kaufman and Nakajima (1993), Kaufman and Fraser (1997), Bréon et al. (2002), Harsvardhan et al. (2002) and Schwartz et al. (2002) are concordant in finding an overall decrease in cloud droplet radius as a consequence of aerosol invigoration. In particular, Bréon et al. (2002) provide one of the first rigorous and analytical quantification of Twomey's effect from the analysis of a long time series (8 months) of POLDER retrievals. Measurements show a systematic decrease on global scale in droplet size with aerosol enhancement. According to equation (20), they quantify the strength of aerosol-cloud interaction calculating the linear regression of the log-log scale relationship between aerosol index and droplet effective radius. They find a slope equal to 0.085 over the ocean and 0.04 over land, much smaller than expected from theory (-0.23). The discrepancy with theoretical calculations is explained (among other causes) as being en effect of POLDER vertically integrated measurements of aerosol load, that may refer to aerosol layers partially or completely separated from clouds. In that case, there is a net overestimation of particle concentration that serves as CCN and an underestimation of the overall aerosol impact.
These studies, however, do not provide any clear evidence of an aerosol-induced effect on cloud optical thickness. Kaufman and Nakajima (1993) find no increase in cloud reflectance with increasing aerosol concentration. Han et al. (994) find an increase only for continental and thick clouds but not for most of thin clouds over ocean, while Harsvardhan et al. (2002) and Schwartz et al. (2002) find a very little evident increase. Only Kaufman and Fraser (1997), selecting a smaller subset of less developed clouds between those observed by Kaufman and Nakajima (1993), do find a decrease in droplet size (from 14 to 9 μm) followed by an increase in cloud reflectance (from 0.35 to 0.45) with aerosol invigoration (from AVHRR data, at 1 km resolution, during the dry-burning season of the Amazon region).

4.2.2 The role of Liquid Water Path and meteorology

Han et al. (1998), Harsvardhan et al. (2002) and Schwartz et al. (2002) suggested that the variability of liquid water path was the major reason for the discording observations of cloud optical thickness, concluding that only two radiative parameters measured from space were not sufficient to distinguish between changes in cloud structure due to local meteorology and pollution impact.

Brenguier et al (2003) stress this problem showing a case (from the ACE-2 CLOUDY-COLUMS database) of a positive relationship between cloud optical thickness and cloud effective radius in a polluted atmosphere. In such case back trajectories and meteorological analysis revealed that observed correlations between aerosol and cloud optical thickness were determined by mesoscale circulation.
Aerosol and clouds may correspond to different air masses. For instance, over South-East Atlantic region, dry air masses polluted by biomass burning particles are transported by trade winds over the ocean, where moist conditions allow for the development of a semi-permanent low cloud field. The sensibility of cloud liquid water path and precipitation to moisture and stability is extremely hight in the boundary layer. For example, in a boundary layer with an absolute humidity (mass of water vapor per cubic meter of total moist air) of 20 gm^{-3} topped with a cloud of 200 m thick, a small dry of the boundary layer equivalent to a decrease of 1% of absolute humidity correspond to a decrease of a factor of four of the liquid water path and only of a factor of two in cloud layer thickness (Levin and Cotton, 2009). The precipitation rate of boundary layer clouds is approximately proportional to LWP and inversely proportional to CDNC (Pawloswka et al., 2003). A decrease of 1% in absolute humidity might have the same impact that an increase of a factor of four in CDNC, due to aerosol indirect effect. At the same time a boundary layer warming of about 0.6° C, at constant humidity, leads to a decrease in cloud thickness of about 100 m. Shallow clouds are more sensitive to variations in the boundary layer moisture content, while deep clouds to those in the stability profile.
Quantify the meteorological contribution to cloud variability is a very complicated issue, moisture content as well as convective instability are thermodynamic fluctuations not detectable with accuracy by satellite.

4.2.3 Cloud microphysics and cloud structure

The emergence of a new generation of remote satellite sensors permits to provide a more detailed view of aerosol-cloud system. Many recent studies based on satellite retrievals and model simulations, such as Kaufman at al. (2005), Quaas et al. (2008, 2009), Menon et al. (2008), Lebsock et al. (2008), Loeb and Shuster (2008) are concordant in showing an overall decrease in cloud droplet size with increasing aerosol concentration. Therefore, the strength of cloud optical thickness response to aerosol enhancement remains more difficult to evaluate. Twomey's hypothesis is only valid under the condition of constant liquid water path, which is supposed to be correlated (as cloud cover) to aerosol burden (according to the lifetime hypothesis) and extremely dependent on local meteorology. Among the cited works, all find an increase in cloud optical thickness with aerosol concentration and most of them also an increase in liquid water path. The interpretation of such phenomena are discordant. Lifetime effect, as a consequence of aerosol inhibition of precipitation, is strongly invoked by Kaufman at al. (2005) also to explain the observed increase of cloud cover. That is fairly in agreement with satellite observations and model experiments of Quaas et al. (2008, 2009) and satellite retrievals of Loeb

and Shuster (2008), but in contrast with Menon et al. (2008). They infer a principal role of meteorological variability in macrophysical cloud changes. Lebsock et al. (2008). find evidence that aerosol inhibits precipitation only in precipitating clouds, while non precipitating cloud are mainly subjected to entrainment of dry air, with a consequent low but radiatively significant diminution of liquid water path. Kaufman et Koren (2006) propose a negative dependence of the lifetime effect on the absorption properties of the involved aerosol particles and show as cloud cover is more enhanced by non absorbing aerosol. A critical parameter missing in several analysis is the Relative Humidity (RH), Klein (1997) find that low cloud amount is positively correlated with RH in the cloud layer (850-950 mbar) and negatively correlated with RH immediately above the inversion. At the same time, aerosol optical depth also increases with increasing RH (Clarke et al. 2002). One could reasonably argue that the strong aerosol-cloud relationship found from the satellite-based observations are nothing more than the response of both aerosol and clouds to changes in RH.

4.2.4 Description and results of cited experiments

Kaufman at al. (2005) focus on shallow clouds (average cloud top pressure higher than 640 hPa) over ocean, using MODIS daily product at 1 degree resolution, during June-August 2002. They find a LWP increase between 6% and 35% with increasing aerosol load from 0.03 to 0.5 (in all but the biomass-burning zone, where LWP decreases by -32%), together with a systematic increase in cloud coverage by 0.2-0.4 and a reduction in the cloud droplet size by 10-30%. They conclude that aerosol inhibition of precipitation plays a major role in governing shallow water cloud cover over Atlantic, more than large-scale meteorology.
Kaufman et Koren (2006) go deeper into problem of the aerosol burden and cloud cover relation, looking at AERONET sun photometers data. They find an increase in cloud cover with increasing aerosol optical depth and an inverse dependence on the aerosol absorption of sunlight. They show that the slope of the linear relationship between cloud cover and the logarithm of aerosol optical depth decreases from 0.15 to 0, as the absorption aerosol optical depth increases from 0.01 to 0.05. The relationship seems to be invariant to geographical location or aerosol type. They quantify the overall effect of aerosol on shallow marine clouds in an increase in average cloud cover of about 5%.

Quaas et al. (2008, 2009) compared MODIS daily products at 1 degree resolution (from Terra and Aqua) with ten GCM models (SPRINTARS, LMDZ-INCA, GISS, GFDL, ECHAM5, CAM-UMICH, CAM-PNNL, CAM-Oslo, CAM-NCAR, ORAC), on a global scale.
The log-log slope of the fitted linear relationship between CDNC and AOD is about 0.08 and 0.25 over land and ocean respectively, as expected from Twomey's hypothesis. All the models overestimate the relationship over land by more than a factor of two (nine out of ten), while over ocean half of the models overestimate and the other half underestimate the relationship.

In the models, an increase in cloud droplet number concentration induces a decrease in the auto-conversion rate (i.e. the process of collision-coalescence that leads to the formation of new small drizzle drops), delaying precipitation formation, thus increasing cloud lifetime and cloud liquid water path. In conclusion, in the majority of cases LWP is significantly positively correlated with aerosol optical depth.
Aqua and Terra show consistent relationships between LWP and AOD, with similar magnitudes over land (with a slope of 0.074 for Terra and 0.1 for Aqua) and ocean (with a slope of 0.134 for Terra and 0.093 for Aqua). Models overestimate this relationship by more than a factor of two over land and (all but one) ocean, on a global scale. On a smaller scale, however, they generally find negative LWP-AOD relationships over the Tropical Atlantic Ocean (biomass-burning region) with log-log slopes varying between -0.01 and -0.05, during December-August, and equal to 0.03, during September-November.
Satellite retrievals indicate a strong positive relationship between cloud fraction and aerosol optical depth, with dramatically large slopes of about 0.5 over land and 0.3 over ocean (also over the Tropical Atlantic Ocean, where LWP decreases). Model simulations show a in good agreement with satellite observations, though in most cases slopes are not as strong and with more variability.
For what concerns planetary albedo, satellite-based statistics show a positive correlation with AOD, with a stronger effect over ocean than over land. All models (except two) reproduce a similar relationship, but with a wicker land-sea contrast.

Menon et al. (2008) analyze shallow (with cloud top pressure higher than 640) cloud response to aerosol optical depth variations, using MODIS and CERES (Clouds and Earth's Radiant Energy System) satellite observations and model simulations from the NASA Goddard Institute for Space Studies (GISS) global climate model (ModelE). Satellite data are at 1 degree resolution, for the entire Atlantic Ocean region between 60°N and 30°S, during June-August 2002.
They perform two main model experiments. In the first one they do not let aerosols affect cloud microphysics (Exp N), while in the second one they allow for aerosols to modify liquid cumulus and stratiform clouds, through changes in CDNC and auto-conversion rate (Exp C).
They find that cloud effective radius is smaller in polluted than in cleaner regions both for observations and Exp C. Slope values of the CDR-AOD linear regression in log-log scale are negative and equal to -0.11 (MODIS), -0.17 (CERES) and -0.02 (Exp C), as expected from Twomey's theory.
Experiments and observations also agree on the positive relationship between cloud optical thickness and aerosol load. Model simulations show slope values equal to 1.12 (Exp N) and 1.95 (Exp C, with aerosol-cloud interactions) much larger than MODIS (0.61) and CERES (0.75) estimates.
Liquid water path slightly decreases with increasing aerosol load in MODIS (slope of -0.004) and CERES (slope of -0.07) statistics, while it slightly increases in Exp C (slope of 0.005). Surprising Exp N, with no aerosol-cloud interaction, shows the strongest positive relationship

between LWP and AOD (slope of 0.09), indicating that meteorological effects play a major role in determining the LWP response in areas of large aerosol optical depth.
Log-log linear slopes of CLF-AOD relationship are always positive, especially robust in MODIS (0.40) and CERES (0.23) statistics and much smaller in model simulations (in both cases equal to 0.07). They conclude that also cloud fraction variations, as those in liquid water path, are mostly driven by meteorological variability.

Lebsock et al. (2008) collocated sixteen months of global observations from CloudSat Cloud Profiling Radar (CPR) with those of MODIS, AMSR-E (Advanced Microwave Scanning Radiometer) and CERES. They find an overall decrease in effective radius with increasing aerosol index and observe that such effect is stronger when liquid water path is larger. For non precipitating clouds, a modest but radiatively significant decrease of liquid water path is observed above aerosol index value of 0.15, suggesting that aerosol enhances entrainment and droplet evaporation, thereby reducing LWP. In contrast, they show that precipitating clouds undergo a dramatic increase of LWP with increasing aerosol index, resulting indicative of an inhibited coalescence process. Consequently, albedo enhancement of precipitating cloud is grater than that of non precipitating.

Loeb and Shuster (2008) studied MODIS and CERES data for September 2003, over the ocean off the African coasts between [0S, 30S] and [-50E, 20E], restricting the analysis to regions dominated by sulfate aerosol according to the MATCH model (Model for Atmospheric Transport and CHemistry). Each day, cloud and aerosol properties within the individual 5°×5° grid box are sorted into two populations according to whether aerosol optical depth retrievals in 1°×1° sub-regions are less than or greater than the 5°×5° averaged aerosol optical depth. Distributions of meteorological, cloud, aerosol and radiative flux parameters during the entire month are compared for the two populations, for each 5°×5° region (ensuring that both groups are affected by the same large-scale meteorological influence), during the entire month. Meteorological parameters (e.g., precipitable water, wind speed, and direction, wind divergence, 750-1000 mbar potential temperature differences, sea surface temperature), showed no significant differences between low and high aerosol optical depth populations. Cloud properties and Top Of the Atmosphere (TOA) radiative fluxes showed marked differences. The population with larger aerosol optical depth had systematically higher cloud cover, liquid water path and shortwave TOA fluxes. Temperature differences between sea surface temperature and cloud top also were greater and the longwave TOA fluxes were smaller, in the more polluted case, suggesting higher cloud tops. In addition, fine-mode fraction and Angstrom exponent (which decreases as aerosol effective radius increases) were significantly larger for the high aerosol optical depth population, even though no evidence of systematic latitude or longitude gradients between the aerosol population was observed. Repeating the analysis for all 5°×5° latitude-longitude regions over global oceans, they found similar results to those obtained off the African coasts.

Chapter V – A satellite analysis of aerosol effect on cloud droplet radius, over South-East Atlantic

5.1 Introduction

Annual variations of aerosol load over South-East Atlantic have been described in Chapter 3. We pointed out the presence of a strong annual cycle of particle concentration and production, with strong peaks of aerosol index during the SH biomass burning season. In that period, a large amount of smoke is injected into the atmosphere and transported by trade wind from Southern Africa over the Atlantic Ocean, potentially interacting with the semi-permanent stratocumulus cloud field.

Time series of monthly spatial mean estimates of aerosol and cloud properties, from MODIS daily product at 1 degree resolution, show a certain temporal correlation between the increase (decrease) in average AI and the decrease (increase) in CDR, during six years of measurements from 2005 to 2010 (Figure 21).

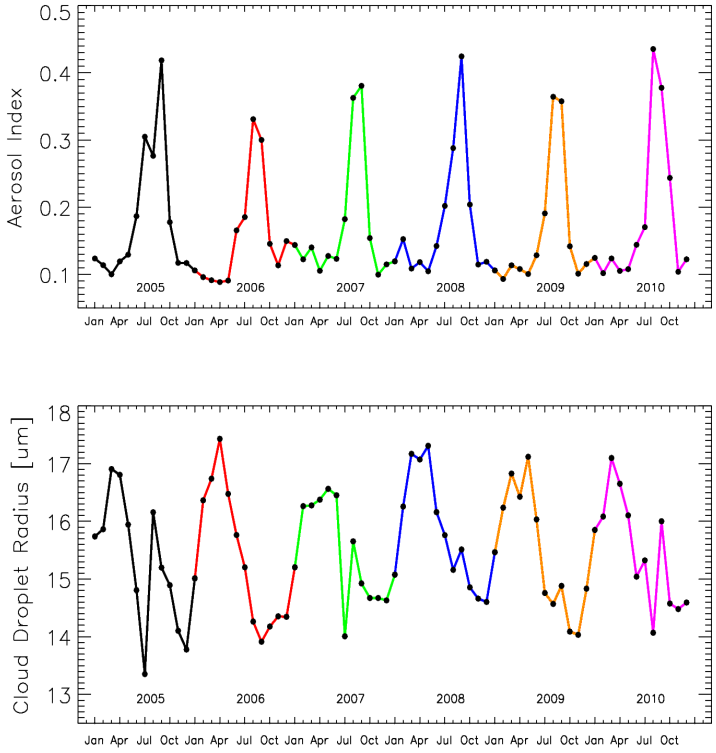

Figure 21: monthly mean (averaged over the whole South-East Atlantic region) of retrieved aerosol index (top figure) and cloud droplet effective radius (bottom figure) for six years of measurements, from 2005 to 2010 (each color identifies a different year).

Peaks of CDR (17 μm) are generally observed during April, when AI is minimum (0.1), while the lowest droplet radii (14 μm) are mostly concentrated during July-October, when aerosol index is maximum (0.4). This is somewhat in agreement with Twomey's hypothesis. If cloud water amount remains constant, Twomey theorizes a decrease in mean droplet size as a consequence of fine-mode aerosol enhancement.
The temporal anti-correlation shown in Figure 21, however, is far from being a consistent proof of Twomey's effect. We have no certitude that observed changes imply a cause-effect relationship or result from a real physical interaction between aerosol and cloud droplets. To solve part of this ambiguity, we will introduce a third information, relative to vertical position of retrieved aerosol and cloud fields, in order to differentiate between cases of mixed (interacting) or well separated layers.

5.2 CDR-AI relationship from MODIS daily products

The analysis of satellite retrieved measurements of CDR and AI allows to quantify the strength of the aerosol effect and compare it with the expected value. In Chapter 4 we have shown that aerosol impact can be quantified by the linear regression slope, α, of CDR-AI relationship in log-log scale,

$$\Delta \log r_e = -\alpha \, \Delta \log AI \tag{35}$$

In the usual approximation of $N_c = N_a^g$ (N_c = number concentration of cloud droplets; N_a = aerosol number concentration), considering g = 0.7 as calculated by Kaufman et al (1997), the theoretical slope coefficient is

$$\alpha_{th} = 0.23 \tag{36}$$

Figure 22 shows CDR estimates averaged over constant bin of AI, from MODIS daily product at 1 degree resolution. Only aerosol particles with Angstrom coefficient between 1.0 and 1.5 are selected, in order to consider only fine-mode aerosol of biomass burning type. Linear regressions are performed for each year, from 2005 to 2010. Cloud droplet radius decreases from typical values of 19 μm, for an almost clear atmosphere (AI = 0.03), to 12-15 μm (depending on the year) as aerosol index increases up to 0.5. The resulting slope (reported in figure) are lower in magnitude than the expected value of -0.23 and vary between -0.13 (2008) and -0.18 (2006).
The main parameter governing the first indirect effect is the CCN concentration in the atmospheric layer where clouds form. However, AI values obtained from MODIS vertically

integrated AOD estimates can largely overestimate the real concentration of cloud-active aerosol in the observed portion of the atmosphere. This may result in a net underestimation of overall aerosol impact, explaining why slopes of Figure 22 are smaller in magnitude than expected, in case of perfect and total cloud-aerosol mixing.

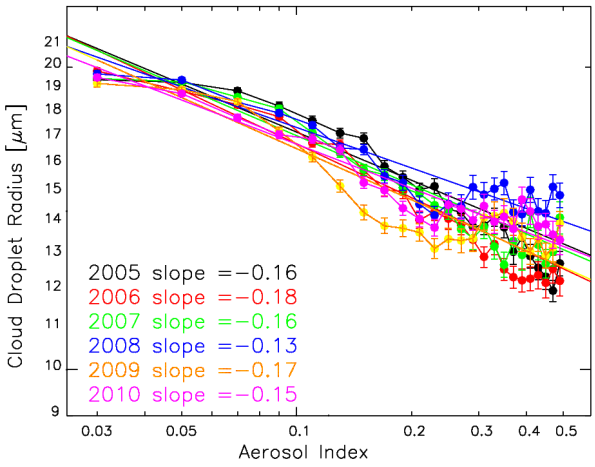

Figure 22: CDR-AI relationship from MODIS daily cloud and aerosol products, at 1 degree resolution, from 2005 to 2010 (for a total of 11009, 9777, 10028, 9667, 8642 and 9563 retrievals, respectively). Only aerosol particles with Angstrom coefficient between 1 and 1.5 are included, as well as cloud with cloud optical thickness between 5 and 35. Clouds with cloud top pressure larger than 600 mbar and liquid water path larger than 300 are excluded.

Figure 23 shows the season variability of CDR-AI relationship, from January to March, from April to June, from July to September and from October to December, for 2005-2010 (to allow for direct comparison, Figure 22 and Figure 23 have the same scale). It shows a strong dependence of CDR-AI relationship on time-period. The largest slopes are always observed during Apr-Jun, while during Oct-Dec droplet radius exhibits the lowest dependence on aerosol changes. From Apr-Jun to Oct-Dec, slope values decrease in magnitude more than a factor of two in 2007, of a factor of three in 2005 and 2008, of a factor of five in 2010 (in 2006 and 2009, seasonal variations are weaker).

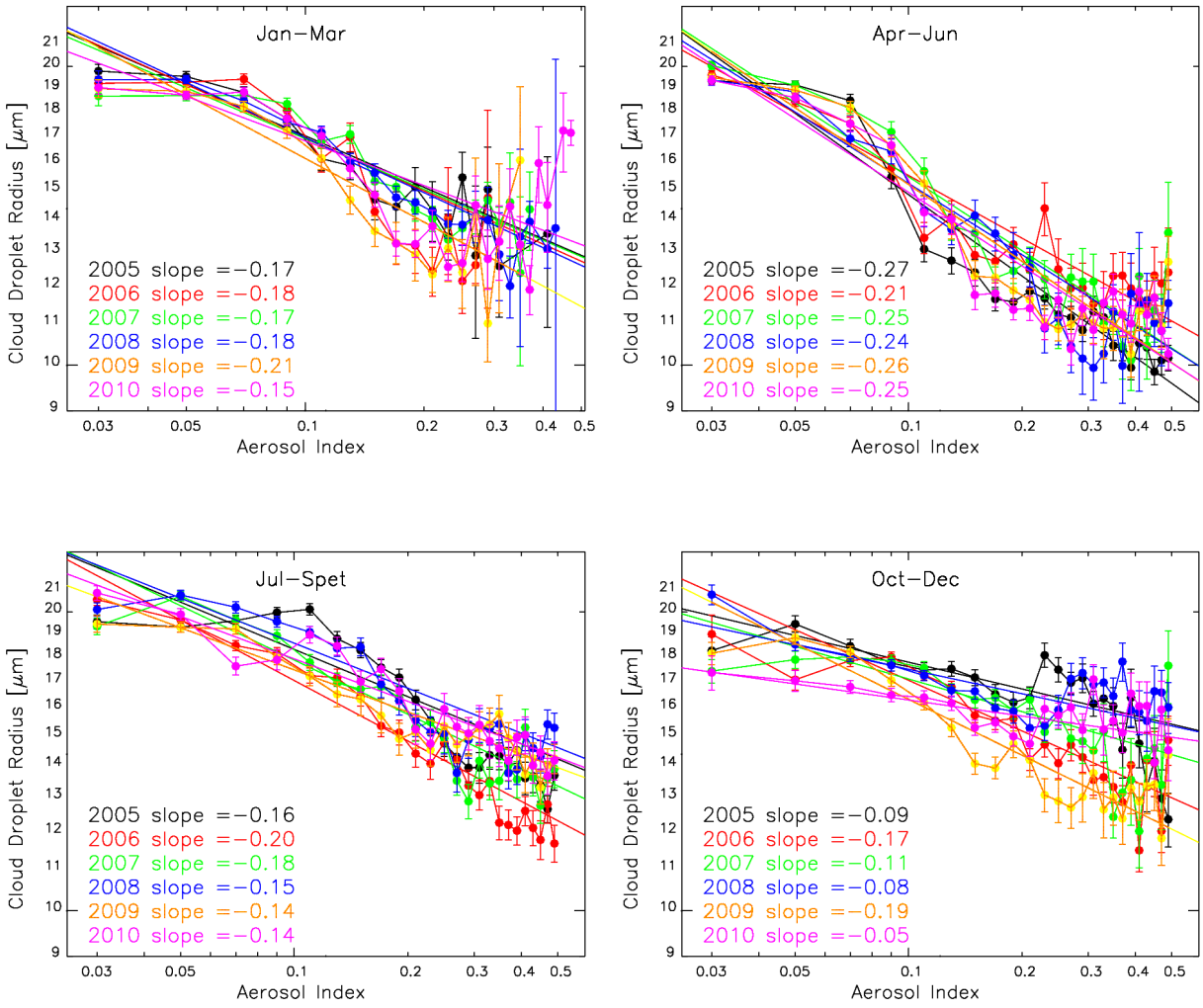

Figure 23: CDR-AI relationship from MODIS daily cloud and aerosol products, at 1 degree resolution, during the four time periods of January-March, April-June, July-September and October-December, from 2005 to 2010.

The ratio between the number of cases characterized by interacting or not interacting cloud and aerosol layers is expected to sensibly influence statistics. Droplet radius would result little affected by aerosol invigoration, if particles are mostly located above cloud top (few cloud-active CCN). On the other hand, a clear droplet size reduction should be evident when aerosol and clouds are well mixed and interacting. A seasonal variability in cloud-aerosol mutual position would explain the observed dependence of CDR-AI slopes (Figure 23) on time-period. Results point out the importance of vertical information to properly quantify aerosol indirect effects.

In Chapter 8, we will perform a seasonal analysis of the frequency of occurrence of mixed and unmixed condition, over South-East Atlantic. It will be shown that during Oct-Dec the

occurrence of mixed cloud-aerosol layers is actually much smaller than during Apr-Jun, in particular off the coasts of Angola.

5.3 The MPC method

The MPC method is based on coincident retrievals of three different instruments, MODIS (on board of Aqua satellite) for aerosol index, POLDER (on board PARASOL satellite) for cloud effective radius and CALIOP (on board of CALIPSO satellite) for cloud and aerosol layer altitudes (Table 11). The main idea is to use CALIPSO to provide vertical resolution to vertically integrated measurements of aerosol and clouds, from MODIS and PARASOL.

5.3.1 Dataset

Aerosol index is used to quantify aerosol concentration. It is calculated making use of *Effective_Optical_Depth_Best_Ocean* (0.55 μm) and *Angstrom_Exponent_1_Ocean* (0.55/0.86 μm) from MODIS Level 2 products of collection 5 (MYD04_L2.C5). These products correspond to 5 minutes of observation (*granule*, ~ 2000×2500 km) at 10 km spatial resolution. MODIS aerosol parameters are relative to clear sky of broken cloud condition only, when the small resolution of the spectroradiometer allows retrievals between clouds.
Cloud droplet effective radius is representative of the mean cloud droplet radius (Chapter 3) and is estimated by the imaging radiometer/polarimeter POLDER. This instrument is sensitive to the very cloud top (i.e., an optical depth of ~1). The estimate is only possible for fairly homogeneous water cloud fields and can be retrieved at a spatial resolution of about 150 km.
Information on cloud and aerosol layers is taken from Level 2 CALIPSO products. We make use of *Number_Layers_Found*, *Layer_Top_Altitude* and *Layer_Base_Altitude*, retrieved by CALIOP lidar at 5 km spatial resolution, for both aerosol and clouds.

	Dataset	**Horizontal Resolution**	**Sensor (Satellite)**
Aerosol and clouds	*Number_Layers_Found*	5 km	CALIOP (CALIPSO)
	Layer_Top_Altitude	5 km	
	Layer_Base_Altitude	5 km	
Aerosol	*Effective_Optical_Depth_Best_Ocean* (0.55 μm)	10 km	MODIS (Aqua)
	Angstrom_Exponent_1_Ocean (0.55 / 0.86 μm)	10 km	

Clouds	*CDR_L2*	150 km	POLDER (PARASOL)

Table 11: dataset name, resolution, sensor and satellite of each cloud and aerosol product used in the MPC method.

5.3.2 Space and time coincidences

The analysis requires near-simultaneous and coincident estimates of effective radius, aerosol index, clouds and aerosol layers altitudes. When CALIOP detects the presence of one or more aerosol and cloud layers, we look for MODIS and PARASOL retrievals within a radius of 150 km. MODIS spectroradiometer is not able to provide aerosol load estimates in the presence of clouds, so we take the nearest available MODIS aerosol retrieval to CALIOP target.
Aerosol and cloud layers are considered well separated if the distance between the bottom of the higher layer and the top of the lower one is greater than 250 meters. However, cases of aerosol underlying cloud are discarded. If cloud-aerosol distance is less than 250 m, layers are supposed to be interacting. This criteria is applied to the highest detected cloud, the only one visible for PARASOL, so that each lower layer is ignored. In case of multilayer aerosols, the criteria is applied to the lowest aerosol layer, not underling a cloud. Temporal coincidences are ensured by the coordinated orbits of the three satellites.

5.4 Quantification of aerosol impact on cloud microphysics

Data time window is from June 2006 to December 2008. MODIS has the unique capability to distinguish between fine and coarse mode particles. We decided to include in the statistics only fine-mode aerosol, with Angstrom coefficient values between 1.0 and 1.5, mostly representative of biomass burning particles.
Within a total of 8942 coincidences, 83% of cases (7438) are characterized by non interacting layers, with aerosol above cloud decks. The 17 % of retrievals (1504) belongs to the mixed case, with interacting cloud and aerosol fields. Statistics relative to cases of mixed (red) and well separated (blue) layers are reported in Figure 24, averaging values of cloud droplet effective radius over constant bins of aerosol index.
In case of no interaction, cloud droplet effective radius remains close to the constant value of 10 μm, for all aerosol regimes. Droplet size results relatively independent from aerosol index, with very limited correlation.

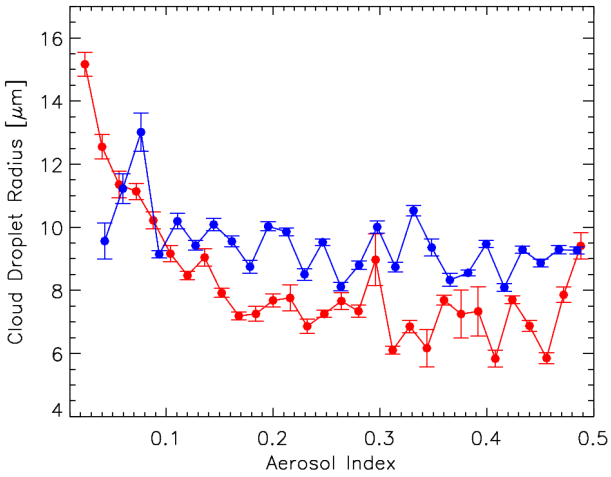

Figure 24: averaged values of cloud droplet effective radius for constant bins of aerosol index, for well separated (non interacting) cloud and aerosol layers (blue) and in case of mixed (interacting) layers (red). Error bars represent the confidence level of the mean values if one assumes independent data. They are calculated as $s/(n-2)^{1/2}$, where n is the number of CDR measurements within the bin and s their standard deviation.

On the other hand, cases of mixed and interacting layers exhibit a strong negative relationship between cloud droplet effective radius and aerosol index. Droplet radius undergoes a dramatic decrease of about 53 % (15-7 μm), as aerosol index increases from approximately 0.01 to 0.3. These is in good agreement with previous CDR estimates of clouds in clean and polluted environments of Kaufman and Nakajima (1993) and Peng et al. (2002).

The limited dependence of cloud properties on aerosol concentration, when no physical interaction is observed, is sign of reduced influence of meteorology on CDR-AI relationship. In case of mixed layers, cloud response can be almost entirely addressed to a real aerosol effect.

Figure 25 shows the same relationship of Figure 24, but in log-log scale. When aerosol and cloud intermingle (red), CDR-AI relationship present a strong linear correlations (r = -0.84).

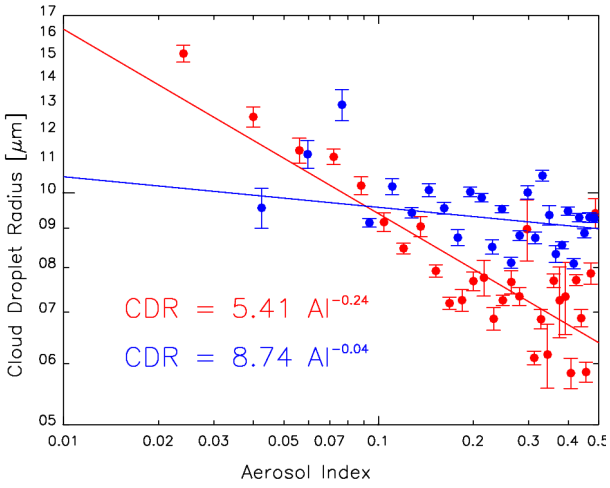

Figure 25: averaged values of cloud droplet effective radius for constant bins of aerosol index in log-log scale, with the relative linear regressions for well separated (non interacting) cloud and aerosol layers (blue) and in case of mixed (interacting) layers (red).

For large aerosol index, CDR values are averaged on fewer measurements, leading to larger statistical uncertainties. Accounting for these uncertainties, the computed linear regression slope in case of cloud-aerosol mixing is equal to (Costantino and Bréon, 2010)

$$\alpha_{mixed} = 0.24 \tag{37}$$

A much lower value results in the unmixed case, where $\alpha = 0.04$ and $r = -0.54$.
It is worthy to remind that selected AI values are representative of a precise subset of particles, with Angstrom coefficient between 1.0 and 1.5, mostly representative of biomass burning aerosol type (among the most active CCN). The slope obtained in case of mixed layers may be interpreted as the lower (larger in magnitude) limit in the strength of aerosol impact on CDR-AI relationship.
Further work is needed to investigate the seasonal variability of observed relationship, that present analysis does not allow, because of the limited number of coincident retrievals.

5.5 Summary and conclusions

With the use of near-simultaneous measurements from CALIPSO, MODIS and PARASOL, it has been shown that cases of well separated aerosol and cloud layers do not present any specific relationship between CDR and AI. On the other hand, when cloud and aerosol are well mixed, the Twomey's effect seems clearly detectable.
The result of this study confirms that aerosols have a strong impact on the cloud microphysics.

A quantitative analysis of the relationship between aerosol load and cloud droplet size should account for the respective position of the aerosol and cloud layer, which is now possible thanks to the CALIPSO lidar measurements. The assumption for a negative CDR-AI correlation due to the Twomey's effect has been widely discussed in the literature under the condition of constant cloud liquid water path. Note however, that the present work does not take into account this condition, so that further studies should address this issue.

Similar to other studies, we have not demonstrated the impact on the cloud albedo (first indirect effect). Further work and statistical analysis is required to quantify the albedo change induced by the aerosol, or the impact of aerosols on the cloud life cycle (second indirect effect). Indeed, there is no clear evidence that the huge amount of observations (Quaas et al., 2009) which link an increase of aerosol load to an increase of cloud albedo and an increase of cloud lifetime are strictly connected by a cause-effect relationship. The role of the local meteorology maybe the greatest uncertainty for a proper quantification of the aerosol effect on clouds. In addition, the effect of cloud microphysics altering droplet number concentrations remains to be determined, since a strict CDR-AI relationship does not necessarily quantify the first indirect effect.

The area under study is particular as it is affected by strongly absorbing aerosols, located above cloud top in 83% of the cases. These aerosols may largely warm the surrounding air, stabilizing the atmosphere (affecting cloud dynamics) and producing a net positive radiative forcing at the top of the atmosphere.

Chapter VI – A satellite analysis of aerosol effect on CDR, COT and LWP, over South-East Atlantic

6.1 Introduction

Although the connection between increasing aerosol index and decreasing cloud droplet radius, as well as their cause-effect relationship, are supported by many in situ and remote sensing observations, the response of cloud optical thickness (COT) or cloud fraction (CLF) is less well established and quantified.

According to Twomey's theory, an increase of cloud optical thickness is expected as a consequence of aerosol invigoration, if liquid water path is constant. Previous studies (see Chapter 4) have largely investigated the relationship between COT and AI. They point out that is not possible to properly evaluate cloud optical thickness response to aerosol enhancement, not accounting for relative changes in cloud water amount, as the condition of constant LWP is generally not valid.

Aerosol are transported by air masses that might have different vertical profiles of moisture and stability than those where cloud are present. The sensitivity of boundary layer clouds to changes in absolute humidity and temperature is very high, while deep clouds are mostly sensitive to the stability profile and low level convergence of sensible and latent heat. A change in moisture content within the boundary layer can affect liquid water path amount and consequently cloud optical thickness, even if cloud and aerosol layers remain. At the same time, in case of interaction, cloud optical thickness response to aerosol-induced changes in effective radius will be anyhow modulated by meteorological_driven changes in liquid water path. According to equation (38), obtained Chapter 4, cloud will suffer an overall drop off in optical thickness and reflectance if LWP decreases more than CDR.

$$COT = \left(\frac{3}{2\rho_w} \right) \frac{LWP}{CDR} \tag{38}$$

Vertically integrated measurements of COT and AI from space would then show a negative COT-AI relationship, definitely in contrast with Twomey's hypothesis. This result would lead to erroneous conclusions if not correctly interpreted. A meaningful statistical analysis of satellite-based relationships, between aerosol concentration and cloud parameters, cannot be possible without decoupling the impact of meteorology from aerosol-induced effects.

6.2 CDR-, LWP-, COT-AI relationships, from MODIS

Statistics of cloud droplet effective radius, optical thickness, liquid water path and aerosol index, from MODIS daily product at 1 degree resolution from 2005 to 2010, are presented hereafter. A series of screening criteria are applied to ensure data quality. Clouds with COT lower than 5 are excluded, since reflectance-CDR relationship use by MODIS retrieval algorithm is ambiguous for low optical thickness. Cases with cloud top pressure (CTP) lower than 600 hPa are also excluded, to avoid retrievals from low clouds topped with cirrus, as well as LWP larger than 300 g/m² and COT larger than 35, to avoid retrievals from very thick clouds mostly subjected to deep convective mechanisms (in such cases cloud response to aerosol enhancement may sensibly differ from thinner clouds).

MODIS retrieves integrated measurements of optical depth and Angstrom exponent. Their product (aerosol index) is somewhat proportional to the total number concentration of aerosol over the vertical, from the TOA to the surface. The quantity of cloud-active aerosol, however, is limited to those situated in the atmospheric layers where cloud forms (Chapter 5).

According to Twomey's theory, we can quantify aerosol impact by the linear slope of the relationship between the logarithm of a certain cloud parameter and the logarithm of aerosol index. This procedure may lead to an overall sub-estimation of calculated Twomey's effect, if AI is representative of a larger particle amount than that serving as CCN.

Figure 26 shows annual CDR-AI, LWP-AI and COT-AI relationships in log-log scale. Each cloud parameter is averaged over constant bin (0.02) of aerosol index. Computed linear regressions are reported in figure, together with their slope values.

Cloud droplet radius typically decreases of 22-33% (from approximately 18 to 14-12 µm), as AI increases from 0.03 to 0.5. Resulting slopes vary between -0.14 and -0.17 and are slightly less steep (~0.01) than those obtained selecting only fine-mode particles, with Angstrom coefficient between 1.0 and 1.5 (Chapter 5).

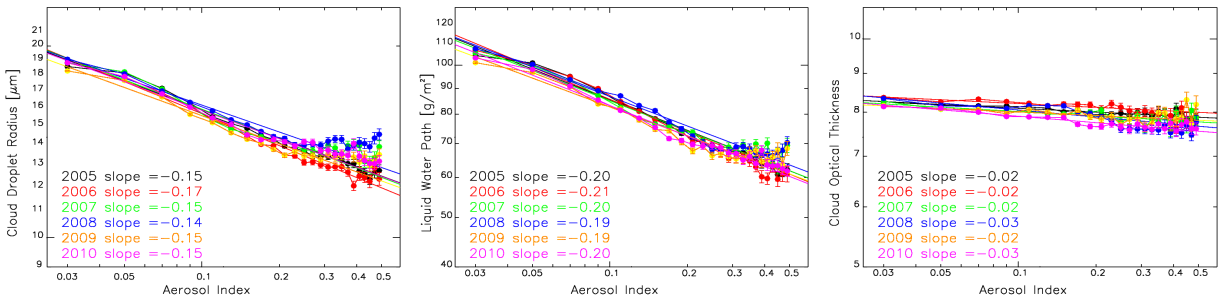

Figure 26: CDR-AI, LWP-AI and COT-AI relationships from MODIS daily cloud and aerosol products, at 1 degree resolution, from 2005 to 2010 (for a total of 68411, 65751, 66880, 64550, 64488 and 68827 retrievals, respectively). Each cloud parameter is averaged over constant bin

of aerosol index. The mean value of each AI interval is used for the position of the corresponding symbol.

Liquid water path exhibits an even stronger depletion of 36-40% (from 110-100 to 70-60 g/m²), as aerosol index goes from 0.03 to 0.5, and slopes values vary between -0.19 and -0.21.
If we do the logarithm of equation (38) and derive it with respect to the logarithm of AI, we obtain a simple expression to describe COT response to AI changes,

$$\frac{d\ln COT}{d\ln AI} = \frac{d\ln LWP}{d\ln AI} - \frac{d\ln CDR}{d\ln AI} \tag{39}$$

According to (39), LWP and CDR diminution with aerosol invigoration shown in Figure 26 would result in a negative relationship, between the logarithm of COT and the logarithm of AI, with slopes between -0.04 and -0.05. These values are little larger in magnitude but in good agreement with satellite-base COT-AI statistics of Figure 26, with log-log slopes between -0.02 and -0.03.

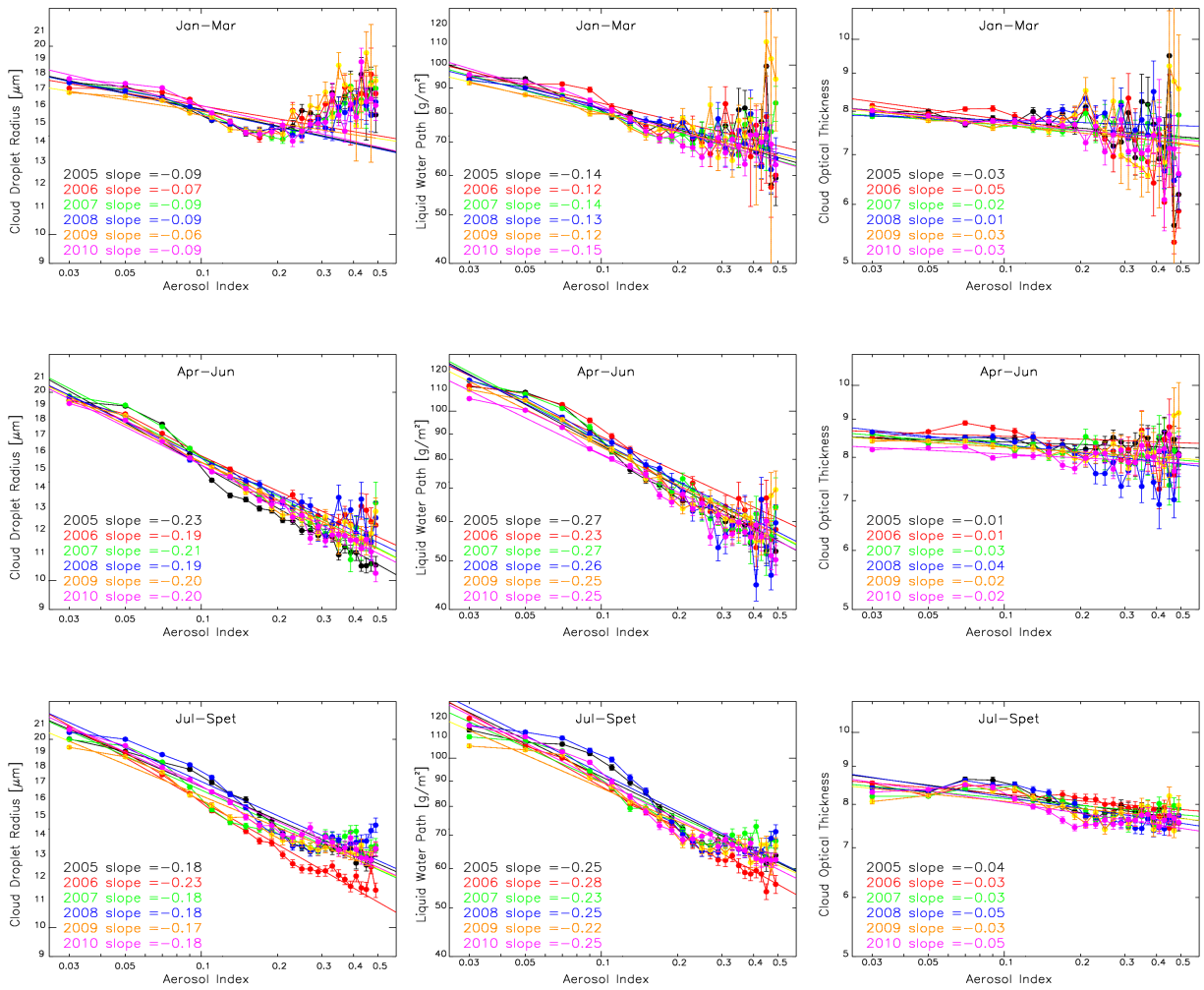

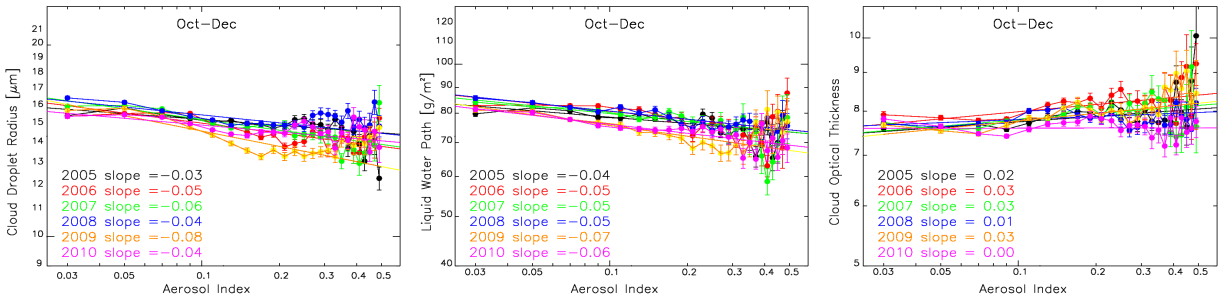

Figure 27: CDR-AI, LWP-AI and COT-AI relationships from MODIS daily cloud and aerosol products, at 1 degree resolution, during the four time periods of January-March, April-June, July-September and October-December, from 2005 to 2010.

In Figure 27 we analyze the seasonal variability of CDR, LWP and COT co-variation of with AI. During Jan-Mar, Apr-Jun and Jul-Sept, cloud-aerosol statistics are somewhat similar to annual trends of Figure 26. On the other hand, during Oct-Dec LWP, all cloud parameters show a limited dependence on AI changes, with respect to other seasons. Log-log scale linear slopes vary between -0.03 and -0.08 for CDR-AI, -0.04 and -0.07 for LWP-AI and COT is positively correlated with increasing AI, with slopes between 0.0 and 0.3.
Results indicate the presence of a puzzled system, where changes of COT are modulated by changes in CDR and LWP, suggesting that other variables than AI may have a dominant effect on cloud physical and optical properties.

6.3 The MMC method

The MMC method (MODIS-MODIS-CALIPSO) is based on near-simultaneous and coincident retrievals of aerosol load from MODIS instrument (aboard Aqua satellite), cloud properties from MODIS and cloud-aerosol layer altitudes from CALIOP lidar (aboard CALIPSO satellite), as shown in Table 12.

The main idea is to use CALIPSO data to analyze whether or not aerosol and cloud layers are in interaction. This distinction may help us in separating the impact of meteorology from aerosol-induced effect.

6.3.1 Dataset

We use data acquired between June 2006 and December 2010. Cloud parameters are obtained

from MODIS Level 2 cloud product from collection C005 (MYD06_L2.C5) at 1 km resolution for *Cloud_Optical_Thickness* and *Cloud_Water_Path*, *Cloud_Effective_Radius,* 5 km resolution for *Cloud_Top_Pressure* and *Cloud_Fraction*.
Aerosol *Effective_Optical_Depth_Best_Ocean* (0.55 μm) and *Angstrom_Exponent_1_Ocean* (0.55/0.86 μm), used to estimate aerosol index and quantify aerosol number concentration, are from MODIS Level 2 aerosol product, collection C005 (MYD04_L2.C5), at 10 km resolution.

Cloud and aerosol layer altitudes are taken from Level 2 CALIPSO products. We make use of *Number_Layers_Found*, *Layer_Top_Altitude* and *Layer_Base_Altitude*, at 5 km resolution for both aerosol and clouds.

	Dataset	Horizontal Resolution	Sensor (Satellite)
Aerosol and clouds	*Number_Layers_Found*	5 km	CALIOP (CALIPSO)
	Layer_Top_Altitude	5 km	
	Layer_Base_Altitude	5 km	
Aerosol MYD04_L2.C5	*Effective_Optical_Depth_Best_Ocean* (0.55 μm)	10 km	MODIS (Aqua)
	Angstrom_Exponent_1_Ocean (0.55 / 0.86 μm)	10 km	
Clouds MYD06_L2.C5	*Cloud_Optical_Thickness*	1 km	
	Cloud_Water_Path	1 km	
	Cloud_Effective_Radius	1 km	
	Cloud_Top_Pressure	5 km	
	Cloud_Fraction	5 km	

Table 12: dataset name, resolution, sensor and satellite of each cloud and aerosol product used in the MPC method.

6.3.2 Space and time coincidences

When CALIPSO detects the presence of mono-layer aerosol and cloud fields, we look for MODIS coincidence within a radius of 20 km from CALIPSO target. All MODIS retrievals of a given cloud or aerosol parameter are averaged together, in order to provide single mean

estimates for each CALIPSO shot. Cases of clear-sky are not consider and MODIS will be able to retrieve aerosol only in broken cloud conditions, when the spectroradiometer can see between clouds. Time-coincidence of retrievals is assured by the A-train coordinated orbits of Aqua and CALIPSO.

Two aerosol and cloud layers are considered interacting if the distance of aerosol bottom altitude from cloud top altitude is smaller than 100 m, while well separated if this distance is larger than 250 m. Aerosol and cloud layers with distance between 100 and 250 m are considered nor interacting nor mixed and excluded, as well as aerosol underlying clouds.

Hereafter, footprints and retrievals of MODIS and CALIPSO instrument from 13:55 to 14:04 UTC, during their flight above South-East Atlantic on September, 14, 2010. Figure 28 shows maps of aerosol optical depth (left) and cloud optical thickness (right), obtained from the composite of three MODIS granules (5 min each). CALIPSO footprint (red line, not in scale) is over-imposed on the maps. All MODIS estimates of COT or AOT, coincident with CALIPSO target, are indicated with orange squares. To provide a more realistic picture of the atmosphere, cases of multi-layer aerosol and cloud fields (generally excluded by MMC selection rules) in both aerosol-free and clear-sky conditions are also reported.

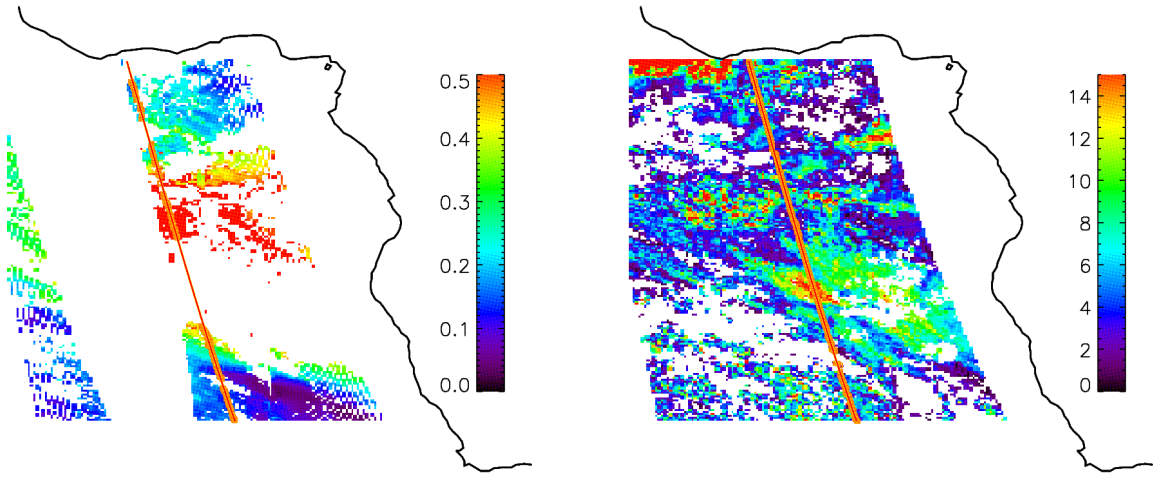

Figure 28: MODIS maps of aerosol optical depth (left) and cloud optical thickness (right), during the orbit flight on September, 14, 2010. The image is a composite of three MODIS granules (5 min each) in its along track direction, from 13:55 to 14:04 UTC. Cross track width is defined by MODIS swath. Red line is CALIPSO track and symbols indicate location of valid MODIS estimates of AOT and COT, coincident with CALIPSO target.

In top image of Figure 29, we make use of backscatter signal ($sr^{-1}km^{-1}$) profile at 532 nm of CALIPSO Level 1 product, on September 14, 2010. Color scale of top image indicates tenuous (light blue/light green), and stronger (green/yellow/red) backscatter signals, that generally identify aerosol and cloud layers, respectively. Bottom image of Figure 4 shows CALIPSO

Level 2 products relative to top/base altitudes of cloud (blue) and aerosol (red) layers, for the orbit over South-East Atlantic.

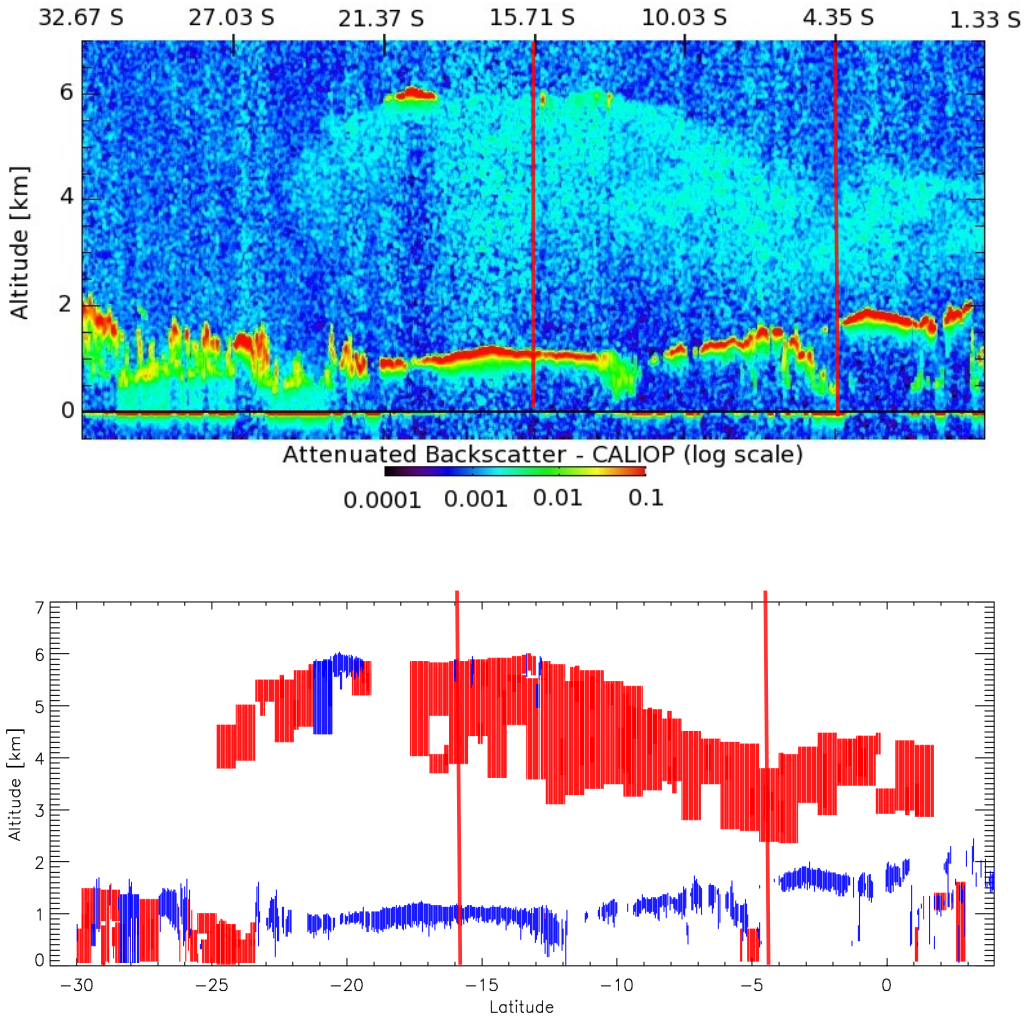

Figure 29: top image represents backscatter signal ($sr^{-1}km^{-1}$) at 532 nm from CALIPSO lidar Level 1 Scientific Data Set, from 0 to 7 km. Bottom image represents vertical position of cloud and aerosol layers retrievals, according to CALIPSO Level 2 data product, from 0 to 7 km. Both figures are relative to the same CALIPSO orbit (on September 14, 2010) within a similar range of latitude ([-32.67N, -1.33N] for top image and [-30N, 4N] for bottom image), to allow for direct comparison of L1 and L2 products. Latitudes of approximately 16S and 3.5S are indicated in both images with a red line.

CALIOP backscatter signal shows the presence of an extended stratocumulus cloud field (about 4000 km long) at an altitude between 1 and 2 km and an aerosol layer above cloud top, between 2 and 6 km, North 25S. A darker blue color below aerosol indicates a relatively clean region, where molecular backscatter dominates, sing that aerosol and cloud layers are well separated.

Level 2 product describes a very similar picture. Cloud and aerosol layers are detected correctly, at least North 23S, with top and bottom altitudes well reproduced. Horizontal inhomogeneities of cloud field seems to be resolved with accuracy. In particular, three small clouds at 21S, 16S and 13S are properly distinguished from surrounding aerosol, at 6 km of altitude. On the other hand, the geometrical thickness of first cloud is clearly overestimated. North 23S**,** at an altitude below 1.5 km**,** backscatter profile shows a broken cloud field reliably characterized by thin and thicker clouds. In this case, L2 product fails to recognize the presence of very thin clouds, classified as aerosol.

6.3.3 Data selection

In order to deal with shallow clouds only, cloud top pressure retrievals smaller than 600 hPa are excluded, as well COT larger than 5, because neither a clear distinction between aerosol and clouds, nor an accurate retrieval of cloud properties is reliably possible (Nakajima et al., 2001).
According to CALIPSO information, cases of multilayer aerosol and clouds (retrievals can be ambiguous in such cases) and aerosol with top layer altitude larger than 10 km, are also excluded. Once MODIS-CALIPSO coincidences are detected, all retrievals within a 20 km radius from CALIPSO target are averaged together, to provide single estimates of cloud and aerosol parameter for each CALIPSO shot. Cases with average COT larger than 35 and LWP larger than 300 g/m² are excluded, to avoid deep convective clouds.

6.4 MODIS and POLDER comparison of CDR retrievals

One of the main differences between MMC (MODIS-MODIS-CALIPSO) and MPC (MODIS-PARASOL-CALIPSO) methodologies is the choice of cloud product, which is from MODIS in the first case and from PARASOL in the second one. PARASOL is able to provide highly accurate droplet size retrievals under the assumption of cloud spatial homogeneity. Indeed, over broken cumulus clouds of the tropics, MODIS is expected to provide a much better statistics, with more valid measurements.
In order to verify the degree coherence between MMC and MPC, we compare coincident observations of droplet effective radius from MODIS and POLDER, that make use of two retrieval algorithms fully independent (Chapter 3). POLDER estimates are representative of a homogeneous cloud field within an area of approximately 150×150 km². To ensure a similar spatial resolution, all MODIS retrievals within a radius of 75 km from a single POLDER measurement are averaged together.
Figure 30 shows the histogram of coincident MODIS-POLDER retrievals of CDR, from 2005 to 2010. Color scale corresponds to arbitrary units proportional to the number of points in a bin of $\Delta r_e = 0.5$ μm. The function $y = x$ is over-plotted on the figure (red line).

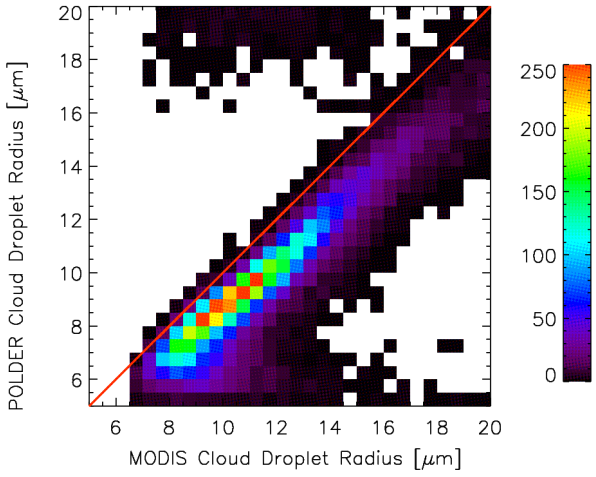

Figure 30: histogram of MODIS and POLDER estimates over ocean of cloud droplet effective radius. The scale corresponds to arbitrary units, proportional to the number of points in the bin, from coincident MODIS-POLDER retrievals, from 2005 to 2010.

As observed by Bréon and Doutriaux (2005), MODIS droplet radius is generally larger. Although the two datasets show very good coherence, the difference between MODIS and CALIPSO (Δr_{M-P}) seems to slightly increase with increasing droplet size. In Figure 31 we average Δr_{M-P} over constant bin of cloud optical thickness, from, by step of 0.03.
Mean Δr_{M-P} is large (3-7 µm) for very optically thin clouds ($1 < COT < 2$), decreasing gradually with increasing optical thickness. For COT between 5 and 15, it is fairly constant with an average value, equal to 1.7±2.3 µm, which is little smaller than the 2 µm bias found by Bréon and Doutriaux (2005).

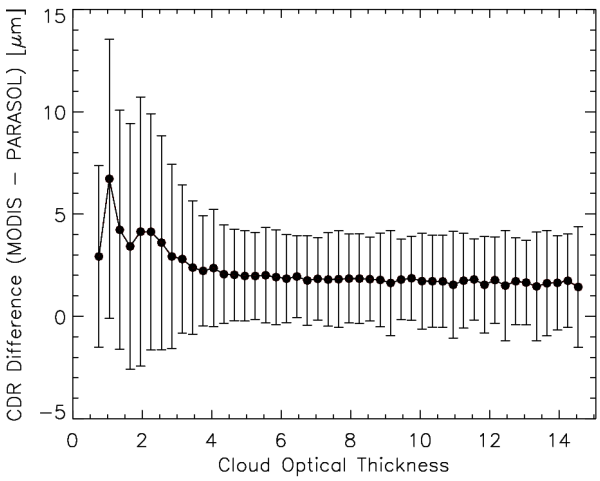

Figure 31: CDR retrieval differences, between MODIS and PARASOL, averaged over constant

bin (0.3) of cloud optical thickness. Error bars represent standard deviation.

Droplet size retrievals from POLDER are supposed to be independent from COT. This means that MODIS estimates tend to overestimate CDR as COT decreases below 5. This is probably due to the cloud retrieval algorithm. MODIS spectroradiometer measures the radiation reflected by clouds at two different wavelengths and compare it with a precomputed set of reflectance (MODIS lookup table), which is very ambiguous for low optical thickness. According to Nakajima et King (1990), results suggest that uncertainties in MODIS droplet radius retrievals are sensibly reduced for COT > 5.

6.5 MODIS and CALIPSO comparison of AOD retrievals

For what concerns aerosol product, MODIS has been preferred to CALIPSO in both MCP and MMP methods. A first analysis showed that CALIPSO aerosol optical depth is very noisy and less reliable than the equivalent MODIS parameter, as confirmed by Bréon et al. (2011) from the comparison of satellite- and ground-based (AERONET) measurements.

Figure 32 shows histograms of coincident MODIS-CALIPSO estimates of AOD from 2005 to 2010, in case of mixed and unmixed cloud-aerosol layers, according to selection rules of MMC methods. Color scale corresponds to arbitrary units proportional to the number of points in a bin of 0.02 and the $y = x$ function is over-plotted in red. Within the [0, 0.8] interval, MODIS generally retrieves larger AOD than CALIPSO, in particular when aerosol is located above cloud top (right image).

When aerosol is mixed with clouds (left image), the difference between MODIS and CALIPSO (Δ_{AOD}) is reduced. For an AOD range within [0, 1.0], the two dataset have a limited linear correlation (r = 0.07) and MODIS optical depth is generally larger (Δ_{AOD}=0.03±0.18). In few cases, however, CALIPSO may retrieves optical depth up to time times larger than coincident MODIS estimates (0.01-0.1). For AOD within [0, 0.3], the coherence between the two dataset is little larger (r = 0.09) and Δ_{AOD}=0.04±0.08.

In case case of aerosol above clouds linear correlation of MODIS and CALIPSO estimates is higher but the difference between the two dataset largely increases with increasing aerosol optical depth. For AOD within [0, 1.0], right image shows a linear correlations coefficient r = 0.61 and mean difference Δ_{AOD}=0.25±0.13. Reducing AOD range within [0, 0.3], r=0.3 and Δ_{AOD}=0.16±0.06.

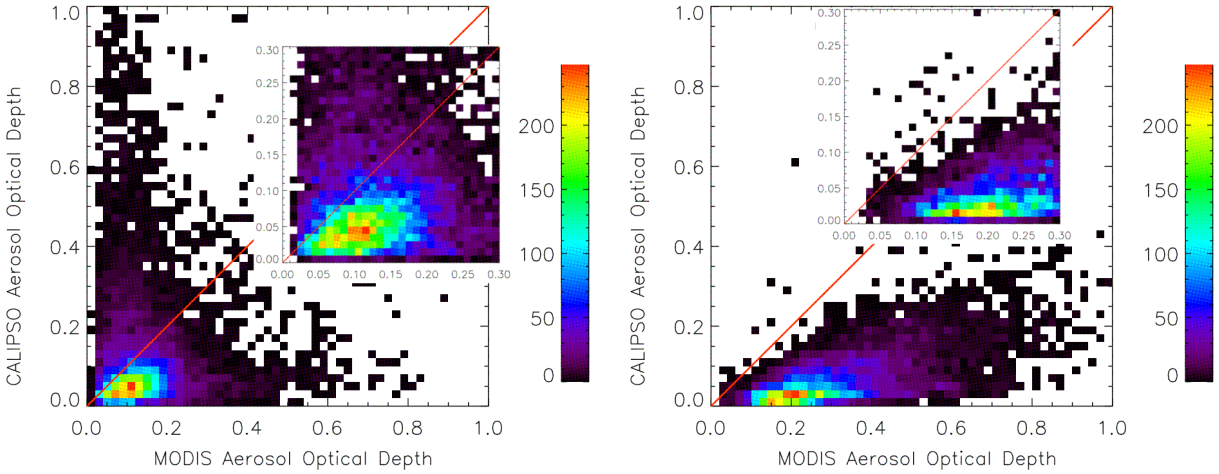

Figure 32: histogram of coincident MODIS-CALIPSO retrievals of AOD, in case of mixed and interacting cloud and aerosol layers (left image) and well separated layer (right image), for a cloud-aerosol distance threshold of 250 m. The color scale represents arbitrary units, proportional to the number of points in a box of $\Delta AI = 0.02$. Inner figure represents same dataset, with a zoom on the [0, 0.3] region.

Several studies analyzed possible error sources affecting MODIS estimates (Kaufman et al., 2005a; Kaufman et al., 2005b, Haywood et al., 2003; Cattani et al., 2005; Loeb and Shuster, 2008, Marshak et al., 2008) and all find that aerosol optical properties are retrieved with high accuracy. In particular, Kaufman et al. (2005b) provide an in-depth analysis of error estimates over ocean and calculated that cloud contamination causes a maximum error in MODIS AOD equal to 0.02±0.005. A similar result is found by Loeb and Shuster (2008), concluding that cloud contamination is not a relevant error factor. We then believe that a poor consistency between coincident MODIS-CALIPSO observations indicates a limited accuracy of CALIPSO AOD estimates, in both cases of mixed cloud-aerosol layers (linear correlation between MODIS and CALIPSO estimates is particularly low) and aerosol above cloud top (linear correlation is larger, but CALIPSO shows a systematic underestimation of aerosol optical depth, that increases for optically thicker layer).

A number of works points out a second important source of error for MODIS aerosol product, the so called cloud adjacent effect, when cloud-free pixels are brightened (or shadowed) by reflecting light from surroundings clouds. Marshak et al. (2008) find out that enhancement in column radiance is more pronounced at shorter wavelength ('blueing' effect). Wen et al. (2008) perform extensive radiative forcing calculations constrained by MODIS and ASTER observations of COT and for surface albedo, respectively. Over ocean, they show that scattered light by clouds in cloud free pixel is further scattered upward by molecules (Rayleigh scattering) located above cloud top, leading to cloud-induced enhancement of visible reflectance, when aerosol are trapped in the boundary layer. They find that this mechanism is valid for thin and thick clouds, as well as for a large range of aerosol optical depth (up to 1, at

wavelength of 0.47 µm and up to 0.2, at wavelength of 0.66 µm) and single scattering albedo. Their results do not apply to all atmospheric conditions, but only in case of boundary layer clouds with a clean troposphere above cloud top. Varnai and Marshak (2009) show that cloud adjacent effect may lead to significant over estimation of AOD retrievals in cloud-free pixels, as far as 15 km away from cloud.

MODIS products return the pixel position of each retrieved aerosol (10 km grid box) and cloud (1 km gird box) parameter. It is then possible, to a certain extent, to analyze the AOD difference between MODIS and CALIPSO (Δ_{AOD}) as a function of cloud-aerosol pixel distance (CAD), as shown in Figure 33. CALIPSO retrievals are not expected to be affected by cloud side-scattering. A decrease of Δ_{AOD} with increasing CAD may reasonably reflect an average decrease in MODIS AOD estimates, due to the diminution of adjacent effect as AOD is retrieved farther from cloud.

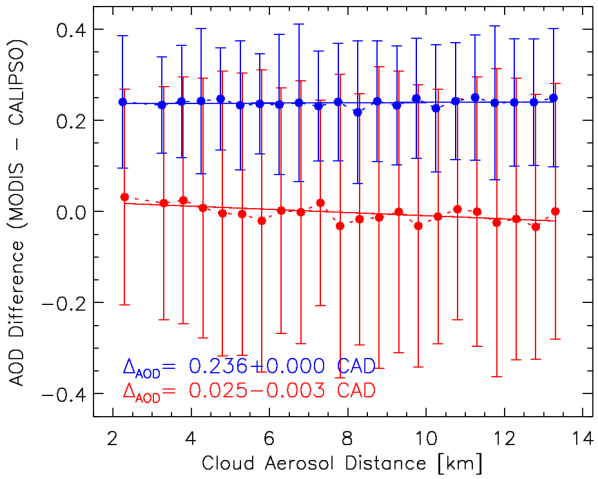

Figure 33: AOD retrieval differences, between MODIS and CALIPSO, averaged over constant bin of cloud-aerosol distance, by step of 0.5 km, in case of mixed cloud-aerosol layers (red) and aerosol above cloud top (blue). Linear regression are performed for each case. Error bars represent the Δ_{AOD} standard deviation within the bin.

In case of mixed layers, atmospheric conditions are very similar to those considered by Wen et al. (2008) in their experiment (aerosol overlying a dark surface and trapped in the PBL; clear troposphere above cloud top) and Δ_{AOD} shows a small but negative dependence on CAD. The difference between MODIS and CALIPSO estimates is reduced by about 0.034, when average cloud-aerosol pixel distance increases from 2 to 13.5 km. This is coherent with the expected decreased in MODIS retrieved column radiance contamination by photons scattered by adjacent cloud and after by molecules above cloud top, over clear gaps near cloud edge.

When aerosol and cloud are well separated, with aerosol located in the low free troposphere above cloud top, Δ_{AOD} (blue) does not show any sensible dependence on cloud-aerosol pixel distance. As observed in Figure 32, the difference between MODIS and CALIPSO AOD is much larger than in case of mixed layers, but constant with increasing CAD. We do not dispose of an in-depth and detailed analysis of 3D radiation processes in case of aerosol above cloud top, as such atmospheric condition is out of the assumption made by Wen et al. (2008). We can imagine, however, that upward scattered radiation by molecules gets attenuated by overlying aerosol and does not affect MODIS retrievals.

In conclusion, results suggest MODIS estimates of aerosol optical depth are biased high, whether aerosol layer is very close to clouds and at the same altitude. This error, reasonably due to the cloud adjacent effect, decreases in average with increasing aerosol distance from surrounding clouds and is not observed for aerosol above cloud top. As it is supposed to be stronger at shorter wavelengths (where molecular scattering is larger), it can affect the spectral dependence of AOD and lead to increased estimates of Angstrom exponent, near cloud edges. This would result in an apparent increase of aerosol fine mode fraction in the vicinity of clouds, as observed by Kaufman et al. (2005) over South Atlantic, that in turn interpreted this finding as the result of a real transition from marine aerosol to smoke. In this work we use aerosol index estimates as a proxy to estimate aerosol number concentration. It is evident that an increase of both AOD and ANG near clouds, due to the blueing effect, may strongly affect satellite derived statistics between cloud occurrence and aerosol concentration, enhancing the strength of CLF-AI relationship. In case of mixed layers, however, the maximum bias in AOD seems rather small and the typical distance between coincident aerosol-cloud pixels ranges approximately between 10 and 20 km (mean CAD is equal to 14.3±6.5 km), mostly out of adjacent effect radius of influence. For these reasons, we argue that Rayleigh enhancement of MODIS retrieved radiance in cloud-free pixel is not expected to produce any significative spurious correlation between aerosol concentration and cloud fraction.

Note, however, that AOD differences between MODIS and CALIPSO single estimates are subjected to an extremely high variability, that may depend on different factors. Resulting statistics, obtained by averaged all Δ_{AOD} values within a same CAD interval, cannot be interpreted as a conclusive proof of cloud adjacent effect.

6.6 CDR-AI relationship

Figure 34 shows CDR and AI retrievals from MODIS-CALIPSO coincidences, in case of mixed and interacting layers (upper image) and well separated cloud-aerosol layers (bottom image). For a total of more than 33000 valid points, 60% is representative of mixed layers, while 40% of well separated ones. Color scale represents arbitrary units, proportional to the number of measurements in a bin of $\Delta AI = 0.01$ and $\Delta CDR = 0.5$ μm.

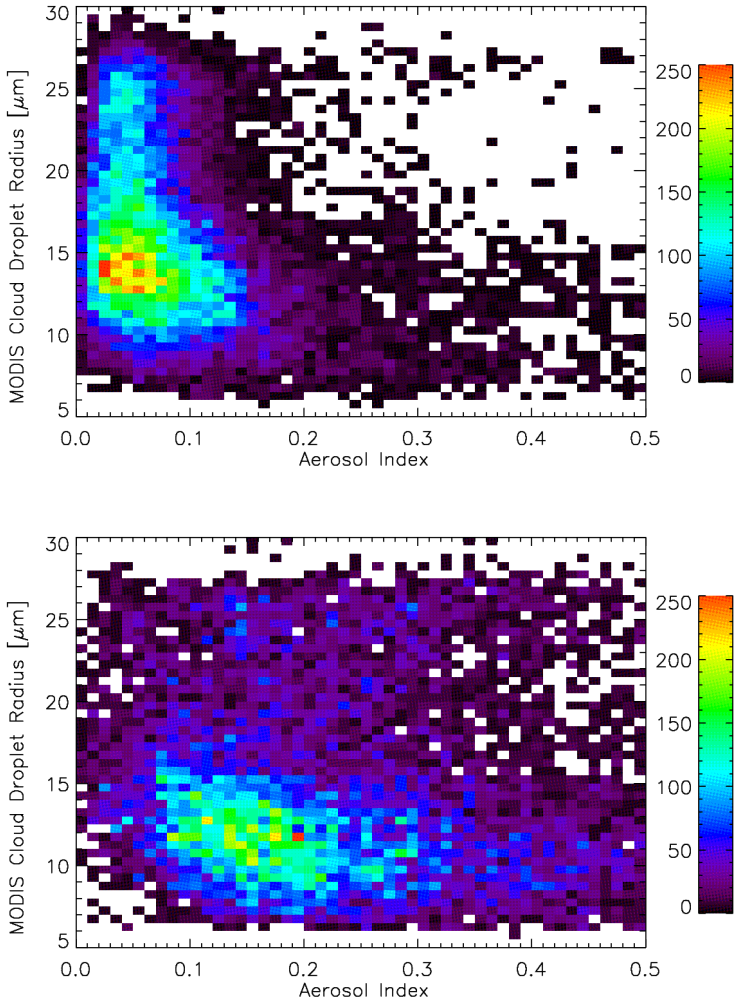

Figure 34: histogram of coincident MODIS-CALIPSO retrievals of CDR and AI, in case of mixed and interacting cloud-aerosol layers (top image) and well separated layer (bottom image), for a cloud-aerosol distance threshold of 250 m. The color scale represents arbitrary units, proportional to the number of points in a box of $\Delta AI = 0.01$ and $\Delta CDR = 0.5$ μm.

In case of cloud-aerosol interaction, retrievals are mainly concentrated in the region with AI within [0.02, 0.1] and CDR within [11, 23] μm. They become less and less numerous as aerosol index increases. Yet in moderately polluted clouds (AI > 0.15), the development of cloud particles with effective radius larger than 15 μm is strongly inhibited. This is not true for aerosol above cloud. Even though big droplets (CDR > 15 μm) are less numerous than smaller ones, the occurrence of both is little dependent on AI variations.

Figure 34 describes well the effect of aerosol invigoration, that prevents the formation of large droplets in polluted clouds. Results are in good agreement with Twomey's theory and imply a direct modification of cloud microphysics (decrease of mean droplet radius) as a consequence

of cloud interaction with aerosol particles, working as CCN.
Note that in case of well separated layers, there are very few retrievals at low aerosol regimes. This may reflect a limitation of CALIPSO retrieval algorithm to detect thin aerosol layers above clouds. In that case, a certain amount of solar radiation can be scattered by underlying cloud field within the CALIPSO field of view, producing a bias in retrieved daytime radiance. This effect is corrected, subtracting the expected amount of cloud-reflected radiance to total retrieved signal. An overestimation of cloud correction, in case of small AOD, may completely hide the overlying aerosol layer. This would explain why retrievals are much more numerous in cases of mixed layers or unmixed layers with large AI.
For AI < 0.1, mixed case retrievals present very large droplet radius, up to 25 μm, even if largest retrieval occurrence is concentrated between 12 and 15 μm. In case of aerosol above clouds the majority of CDR does not overpass 15 μm.
It is reasonable to wonder if mixed and unmixed dataset refer to clouds detected over the same geographical regions, formed and developed under similar meteorological conditions. In this case, observed differences in mixed and unmixed case statistics can be reliably interpreted as resulting from a real aerosol-induced effect, and not from changes in local meteorology.
Figure 35 shows the number of MODIS-CALIPSO coincidences over South-East Atlantic, within a 2×2 degree box. While mixed case data are retrieved over a very wide area, extending over the central and southern part of the region, unmixed statistics are concentrated over a smaller area, over the central part only.

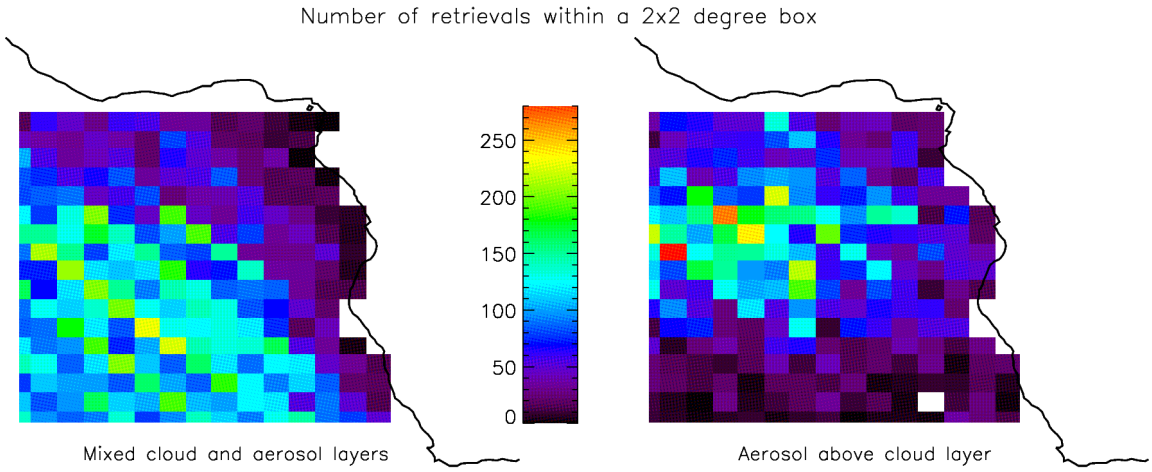

Figure 35: number concentration of coincident MODIS-CALIPSO retrievals. The color scale represents the number of measurements within a 2×2 degree box, in case of mixed cloud-aerosol layers (left image) and aerosol above clouds (right image), with a minimum distance threshold of 250 m.

Figure 36 shows that MODIS-CALIPSO coincidence with AI ≥ 0.1 are somewhat concentrated

over the central part of South-East Atlantic, for both mixed and unmixed cases.

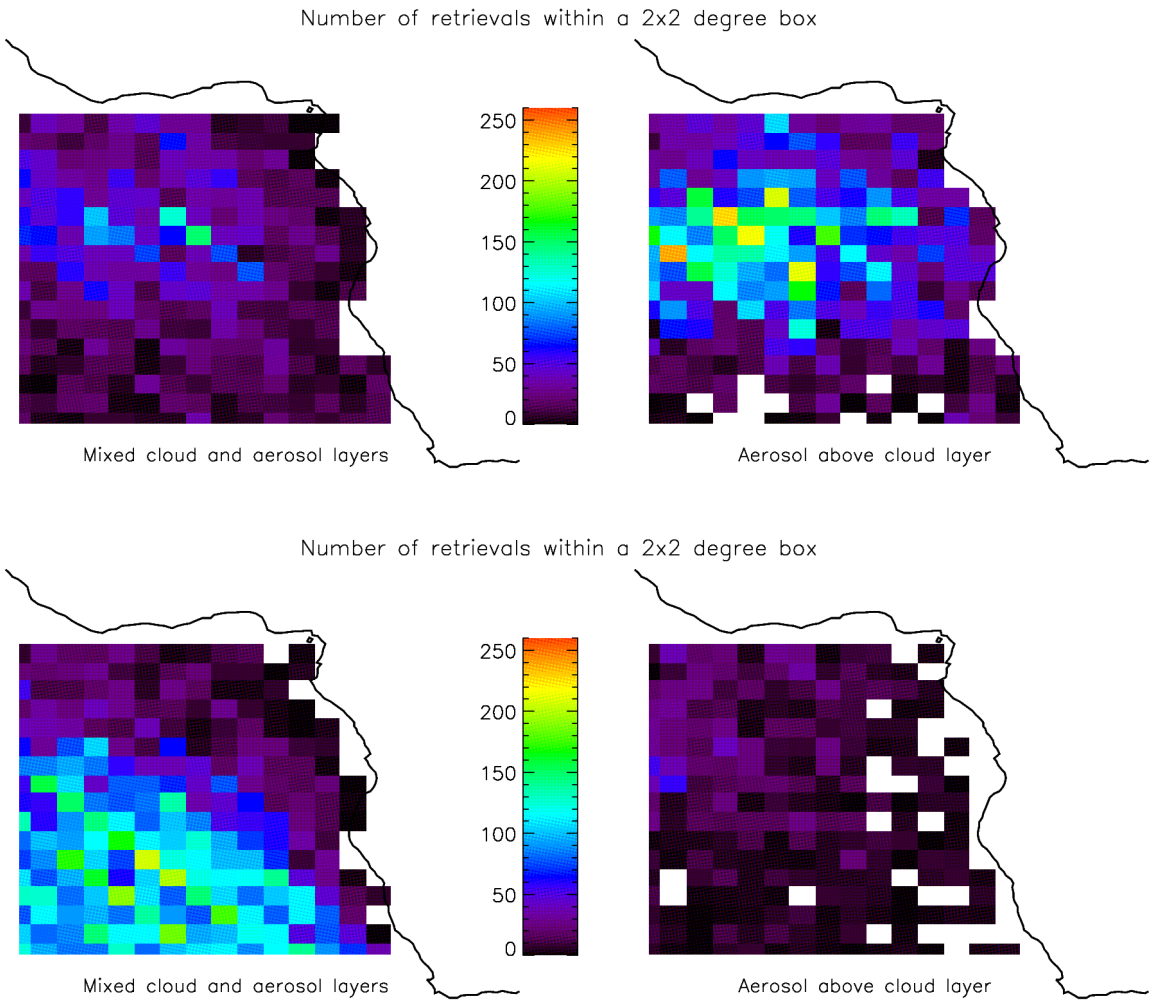

Figure 36: number concentration of coincident MODIS-CALIPSO retrievals for AI ≥ 0.1 (top image) and AI < 0.1 (bottom image). Color scale represent number of measurements within a 2×2 degree box, for the case of mixed cloud aerosol layers (left image) and the aerosol above clouds (right image).

On the other hand, for AI < 0.1, mixed layer retrievals are clearly representative of cloud systems over the southern part of South-East Atlantic. The unmixed case shows in turn very few retrievals.

Seasonal maps of CDR (and LWP) for 2005-2010 (Chapter 4) indicate that southern-western part of South-East Atlantic is a critical region, where formation and extinction of well developed clouds, with significant amounts of liquid water path and very big water droplets, is not associated to any significant change aerosol concentration. AI remains rather small during the whole year. The strong annual cycle of CDR and LWP seems to be largely influenced by

local meteorology.
These considerations give rise to a twofold problem. First of all, the reduced occurrence of unmixed retrievals for low aerosol concentration, with respect to mixed case, may lead to larger statistical uncertainties and less accurate relationships. More, cloud-aerosol statistics in case of medium and high aerosol regimes can be inconsistent with those of lightly polluted environments. Two dataset refer to clouds formed over distinct regions, central or southern part of South-East Atlantic.
Figure 37 shows coincident MODIS-CALIPSO estimates of cloud effective radius averaged over constant bin of AI, from 0.02 to 0.5, in case of mixed and well separated aerosol layers.
Regions of low aerosol index (AI < 0.1) are characterized by large droplet radii up to 17.3 μm and 16.5 μm, for mixed (red) and unmixed (blue) layers respectively. All king of cloud-aerosol geometry are concerned by similar CDR changes with increasing AI. The result suggest that droplet size radius diminution is not sensibly regulated by aerosol-induced effect. The most important contribution to the strong negative CDR-AI relationship can result from spurious correlation between local changes in meteorology and aerosol index, while aerosol impact is of lesser importance. The fact that mixed case CDR is about 1 μm larger that in case of unmixed layers may be caused by a possible stronger broken cloud condition, when aerosol is located between clouds. Cloud heterogeneity or partial cloud filling are a large source of error in CDR retrievals, that can bias high MODIS estimates.
For AI ≥ 0.1, mixed and unmixed statistics are mostly representative of cloud fields over central part of South-East Atlantic. When aerosol and clouds intermingle, mean droplet radius shows a net decrease of 21% (from 14 to 11 μm) with increasing aerosol number concentration. This CDR drop down, even if smaller than the 53% observed from MODIS-POLDER-CALIPSO coincidences, is in good agreement with Twomey's hypothesis. On the other hand, unmixed case does not show any significant correlation between changes in aerosol index and cloud droplet radius variations. CDR remains approximately constant, close to 14-15 μm, as AI varies from 0.1 to 0.5. Results seem to confirm that using cloud-aerosol retrievals from central South-East Atlantic (AI ≥ 0.1), aerosol-cloud microphysical interaction is detectable by the mixed-unmixed layer analysis.

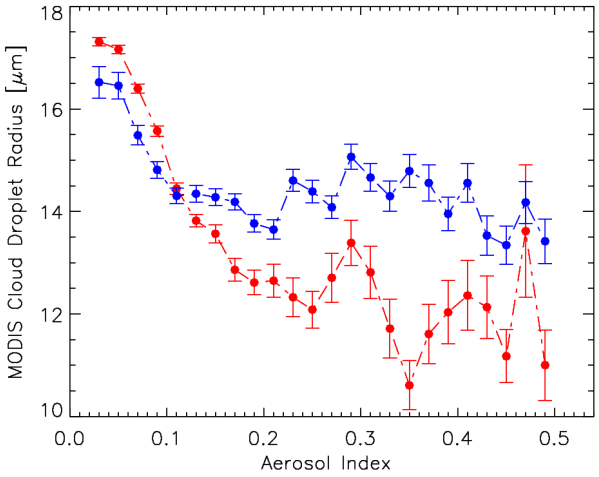

Figure 37: cloud droplet radius retrievals averaged over constant bin of aerosol index, in case of well separated cloud and aerosol layers (blue) and mixed and interacting layers (red), according to CALIPSO information. Study area is the whole South-East Atlantic region within [4N, -30N; -14E, 18E].

On the basis of previous considerations, we exclude from statistics all MODIS-CALIPSO coincidences that do not belong to central South-East Atlantic within [2S,15S], corresponding to the ocean region off the coast of Angola (Figure 38).

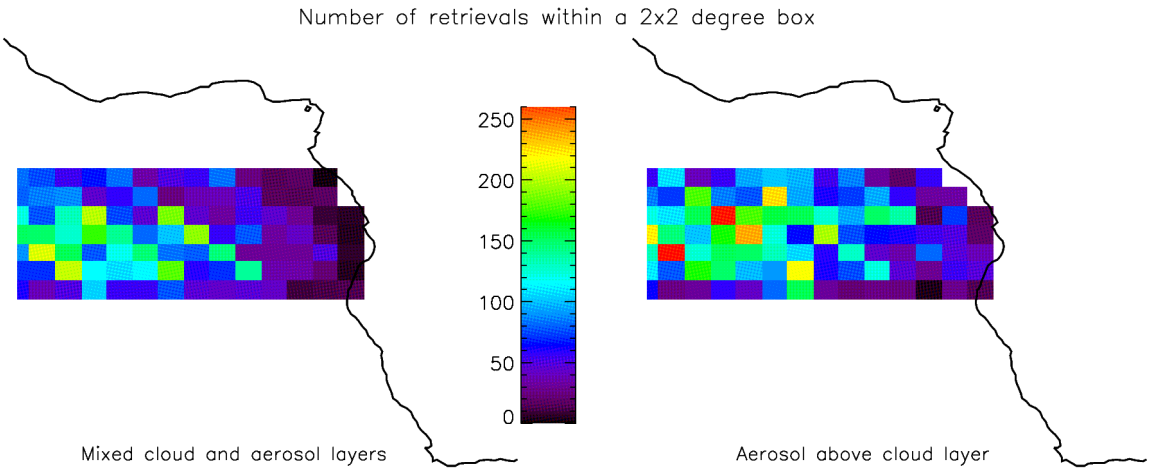

Figure 38: number concentration of coincident MODIS-CALIPSO retrievals for all aerosol regimes, within [2S, 15S]. Color scale represent number of measurements within a 2×2 degree box, for the case of mixed cloud aerosol layers (left image) and the aerosol above clouds (right image).

Figure 39 shows the resulting CDR-AI relationship when the narrower latitude range within [2S, 15S] is considered.

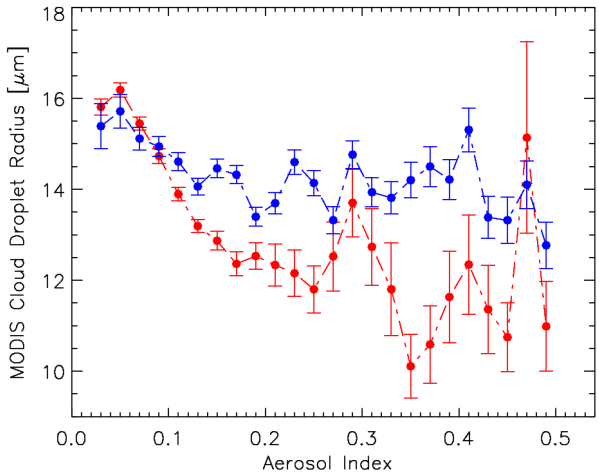

Figure 39: cloud droplet radius retrievals averaged over constant bin of aerosol index, in case of well separated cloud and aerosol layers (blue) and mixed and interacting layers (red), in the region within [2S, 15S; -14E, 18E].

For AI = 0.03, 0.05 and 0.07, CDR estimates shown of Figure 39 decreases (with respect to Figure 37) of 1.5, 1.0 and 1.0 μm in case of mixed layers and of 1.1, 0.7 and 0.4 μm, in case of unmixed layers.

As expected, mixed and unmixed statistics converge to very similar CDR values, as aerosol particle concentration goes to zero, of about 15.5 μm. With increasing AI, CDR of unmixed clouds remain almost constant, close to 14 μm. On the other hand, in case of cloud-aerosol mixing, the effect of the interaction results in total CDR diminution of 30%, and CDR = 11 μm as AI reaches 0.5.

The difference in droplet radius between clean and polluted low clouds over South-East Atlantic ocean, off the coast of Angola, is between 3 and 5 μm. The strength of aerosol impact can be quantified by the log-log scale linear slope of CDR-AI relationship (Chapter 4), in the form

$$\Delta \log r_e = -\alpha \, \Delta \log AI \qquad (40)$$

In good agreement with Twomey's hypothesis, Figure 40 shows that the logarithmic relationship between CDR and AI in case of mixed and interacting layers is linear, with a correlation coefficient equal to -0.76. The strong CDR sensitivity to aerosol invigoration is expressed by the calculated slope equal to -0.15, more than 3 times smaller than in case of unmixed layers (-0.04). To further improve the accuracy of unmixed statistics, a stronger screening criterium can be used to select well separated cloud-aerosol layers, increasing the minimum distance

threshold from 250 to 750 m. Excluding all aerosol layers closer than 750 m to cloud top, layer misclassification is reduced. The slope of CDR-AI relationship in log-log scale (r = -0.59) increases of 0.01, equal to -0.03, and the overall mean CDR estimate is 14.5 µm (Figure 40).

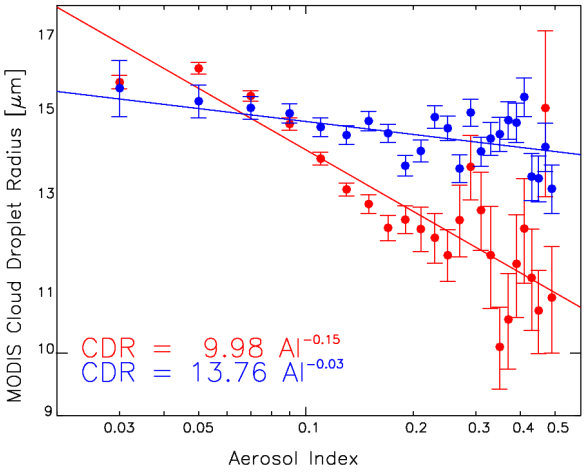

Figure 40: cloud droplet radius retrievals averaged over constant bin of aerosol index in log-log scale. Well separated cloud and aerosol layers are presented in blue, while mixed and interacting layers in red. The study area is within [2S, 15S] of latitude and minimum distance threshold between unmixed cloud and aerosol layers is increased from 250 to 750 m.

Histograms of MODIS-CALIPSO coincidences retrieved between 2S and 15S (Figure 41), show that CDR and AI estimates are within similar range of values, for both mixed as unmixed case dataset. Nevertheless, when cloud and aerosol interact, large droplet occurrence appears strongly inhibited by pollution.

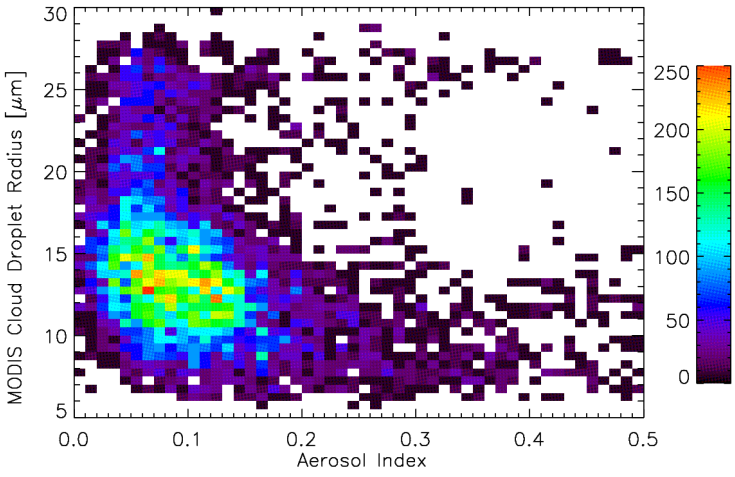

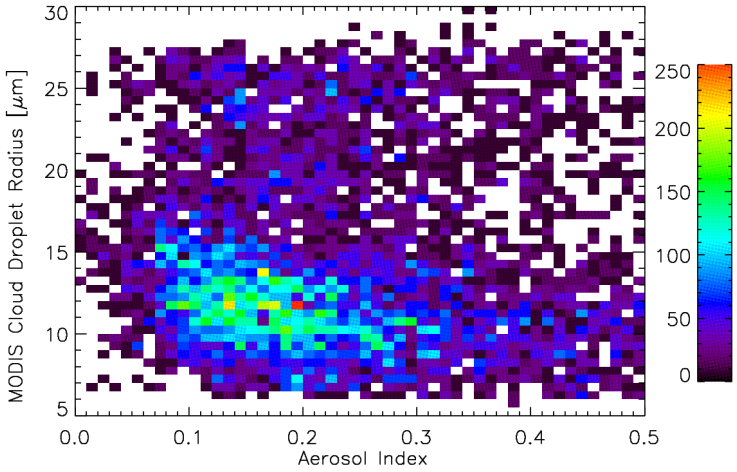

Figure 41: histogram of coincident MODIS-CALIPSO retrievals of CDR and AI, in case of mixed and interacting cloud and aerosol layers (top image) and well separated layer (bottom image), within [2S, 15S] of latitude. Unmixed case cloud-aerosol minimum distance threshold is 750 m. Color scale represents arbitrary units, proportional to the number of points in a box of $\Delta AI = 0.01$ and $\Delta CDR = 0.5$ μm.

We can compare the CDR-AI relationship of Figure 39 with that shown in previous chapter, using coincidences of MODIS-PARASOL-CALIPSO. In case of unmixed layers or mixed layers with large aerosol index, CDR estimates from MMC are about 4-5 μm larger than those obtained using MPC. This value is about two times larger than estimated 2 μm bias. Bréon et Doutriaux (2005) point out that MODIS algorithm, contrary to POLDER one, has a strong sensitivity to cloud heterogeneity. We argue that MODIS overestimates CDR, as cloud heterogeneity and partial coverage can be enhanced by intrinsic characteristics of present analysis (based on aerosol retrievals in broken cloud conditions), which is more likely to select heterogeneous than homogeneous cloud fields.

6.7 Relationship between LWP and AI

Averaging coincident MODIS-CALIPSO retrievals of liquid water path, within [2S, 15S], over constant bin of aerosol index, LWP-AI relationship (Figure 42) is somewhat similar to CDR-AI. In case of mixed layers, LWP is decreased by 37% (from 95 to 60 g/m²) as AI increases from 0.03 to 0.5. The resulting linear slope in log-log scale is equal to -0.16. Otherwise, when aerosol is situated in elevated atmospheric layers above cloud deck, LWP does not show any sensible dependence on aerosol concentration. Cloud water amount remains almost constant at approximately 80-90 g/m² for all aerosol regimes and the resulting log-log scale linear slope is equal to -0.04.

In good agreement with expectation, mixed and unmixed layer relationships converge to a same

LWP value (within statistical uncertainties), when AI decreases to 0.03. That is not true if the whole South-East Atlantic region [4N, -30N] is considered. In this case, mixed statistics show that LWP would increase up to 110 g/m², for AI approaching to zero (while unmixed LWP would remains almost unaltered).

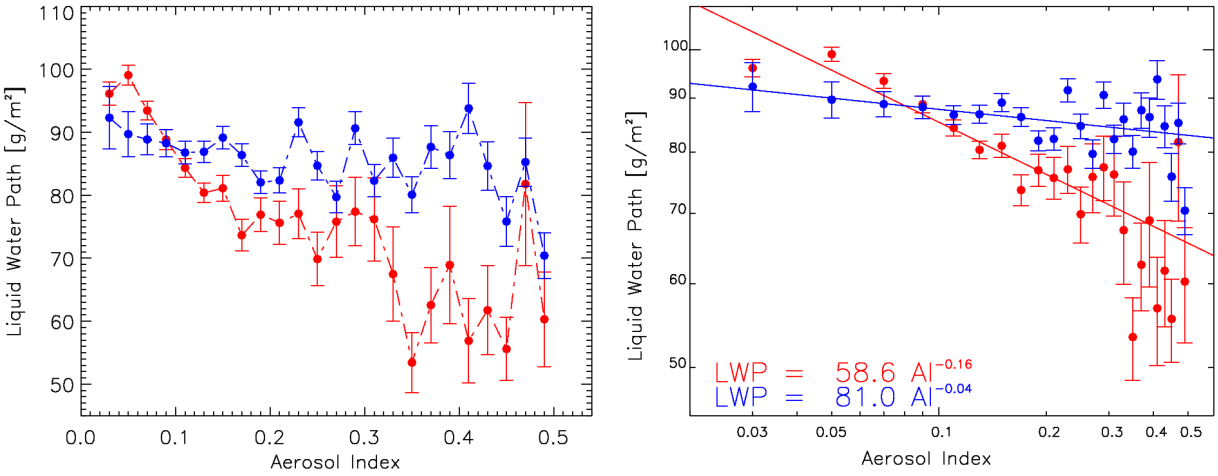

Figure 42: liquid water path retrievals averaged over constant bin of aerosol index (0.02), for cases of well separated (blue) and interacting (red) cloud-aerosol layers, in linear (left image) and log-log scale (right image). Latitude varies within [2S, 15S]. Unmixed case cloud-aerosol minimum distance threshold is 750 m.

Several researches have analyzed the liquid water path response to aerosol invigoration and have found widely different results. In this case, aerosol interaction with cloud field over South-East Atlantic produces a sensible diminution in cloud liquid water amount. We now try to interpret and understand the physical process that are responsible of this LWP-AI relationship, starting with the discussion of the different hypothesis that have been formulated in literature.
Albrecht (1989) has been one of the first to theorizes an increase in water path amount with increasing aerosol concentration, as a consequence of precipitation suppression. The basic idea is that clouds in polluted air masses consist of more droplets that coalesce into raindrop less efficiently, leaving longer-lived clouds.
Hypothesis of increasing LWP with increasing AI is in clear contrast with results of Figure 42 and Ackerman et al. (2004), that point out how aerosol-polluted boundary layers clouds are not generally observed to hold more water, but significantly less. They infer that cloud water response to precipitation suppression (due to increased droplet number concentration) is determined by the balance of two competitive factors: 1) moistening, from surface precipitation decrease, which tends to increase LWP; 2) drying, from increasing entrainment of dry overlying air, which tends to decrease LWP. Note that model simulations shows that entrainment rate

[cm/s] always increases with increasing droplet number concentrations, due to Twomey's effect. Only if overlying air is humid or droplet number concentration is very low, surface precipitation reduction is strong enough to dominate LWP response.

They identify relative humidity (RH) above boundary layer as the leading factor determining LWP response to changes in droplet concentration. If moisture is high enough, entrainment of air does not result in a dryness of cloud. For three different experiments at RH of 10%, 40% and 70%, for a droplet number concentration varying between 20 and 400 cm^{-1}, Ackerman et al. (2004) find respectively a net LWP decrease from ~100 to ~75 g/m^2 (except for very low droplet concentrations, when LWP slightly increase), a moderate increase from ~100 to 175 g/m^2 and a net increase from ~100 to ~ 250 g/m^2. Surface precipitation decreases in all cases.

Relative humidity is presently not detectable from satellites at high vertical resolution. However, assumptions required by Ackerman's hypothesis seem likely to be locally satisfied by South-East Atlantic meteorology. During the biomass burning season of Southern Africa, huge amount of aerosol particles is transported in elevated atmospheric layers by dry air masses, from inner Southern-Central Africa over ocean. It is reasonable to believe that aerosol-load air is dryer than that just above the inversion. When aerosol mixes with underlying cloud field, increase in cloud droplet number concentration (as a consequence Twomey's effect) may results in the observed LWP reduction, whose magnitude of 35 g/m^2 is comparable to that estimated by Ackerman et al. (2004) of ~ 25 g/m^2, for RH of 10%. If aerosol remains high in the atmosphere, well separated from cloud deck, no aerosol-cloud interaction is possible and LWP is expected to remains unaltered. This is in agreement with unmixed LWP trend of Figure 42, very little dependent on aerosol concentration.

Latter result is also important because it does not provide any experimental evidence to 'semi-direct' aerosol effect (Johnson et al., 2004), according to which moderately absorbing aerosols located above boundary layer may heat the air above the inversion, leading to a lower entrainment rate and a shallower, moister boundary layer, increasing LWP by 5 to 10 g/m^2 even without physical aerosol-cloud interaction.

There are a number of implications of our findings. First of all the concept of *inhibition of precipitation*, commonly related to LWP increase according to the so often invoked Albrecht's hypothesis, can be misleading. The increase of number droplet concentrations and decrease of coalescence efficiency, in clouds polluted by sub-micrometers aerosol, may lead to large loss of LWP even if surface precipitation is reduced. Under such condition, COT-AI relationship can be positive or negative, depending on the competitive effect of simultaneous LWP and CDR variations with AI.

There are other possible explanations for observed LWP variations. Local inhibition of precipitation means more water lofted to cloud top, with subsequent liquid evaporation that may cool the atmosphere and destabilizes the environment. Such effect can help conditions to the growth of deeper clouds ('deepening' effect) that produce more rains, compensating for the initial suppression of precipitation and decreasing LWP. In such cases, aerosol enhancement is expected to produce more rain, not less (Stevens and Feingold, 2009).

However, as it will be shown further, we find evidence of precipitation suppression in marine

stratocumulus by cloud-active aerosol. This suggest that Ackerman's hypothesis is the most appropriate to explain the observed LWP loss, when aerosol mixes with cloud field.
Nevertheless, we do not dispose of retrievals describing the entire cloud life-cycle and providing the temporal information that would permit a clear distinction between causes and effects. This is to say that previous speculations, even if consistent with experimental data, can not be considered as definitive evidence of a certain LWP response to aerosol perturbation.
One thing, however, seems to be clear. While droplet radius variation is governed by microphysical interaction between cloud droplet and cloud-active aerosol, macrophisical (cloud-dynamical) and/or meteorological conditions may also buffer the LWP response, which is almost certainly regime and/or regional dependent.

6.8 Relationship between COT and AI

Previous results show a log-log scale CDR-AI linear slope of -0.15 and a LWP-AI linear slope of the same order, equal to -0.16. From equation (39), we know that cloud optical thickness response to aerosol enhance can be estimated as the sum of these two parameters and no significant COT variation is expected, as AI increases from 0.02 to 0.5. Mean values of COT, averaged over constant bin of AI, are coherent with this estimate. Effect of liquid water path loss compensates droplet size decrease. Both for mixed than unmixed cases, COT results little dependent on aerosol concentration (Figure 43), varying between 8.5 and 9.0, for AI from 0.02 to 0.3. For higher AI values, larger error bars indicate stronger statistical uncertainties due to fewer disposable measurements. Resulting COT estimates are more variable and vary within a between 8.0 and 9.5.
The low COT sensitivity to aerosol invigoration is significantly quantified by the log-log scale linear regression slope (Figure 43). When cloud and aerosol are mixed and interacting, the slope is particularly small, even slightly negative, equal to -0.02. A statistical uncertainties in the slope value equal to ±0.06, together with a linear correlation coefficient of r = -0.47, stress the large variability of COT and its little dependence on AI.
When aerosol and cloud layers are well separated, linear slope is very small and equal to 0.01 (with statistical error of ±0.04 and linear regression coefficient r = 0.1), as expected if aerosol particles do not affect cloud properties.

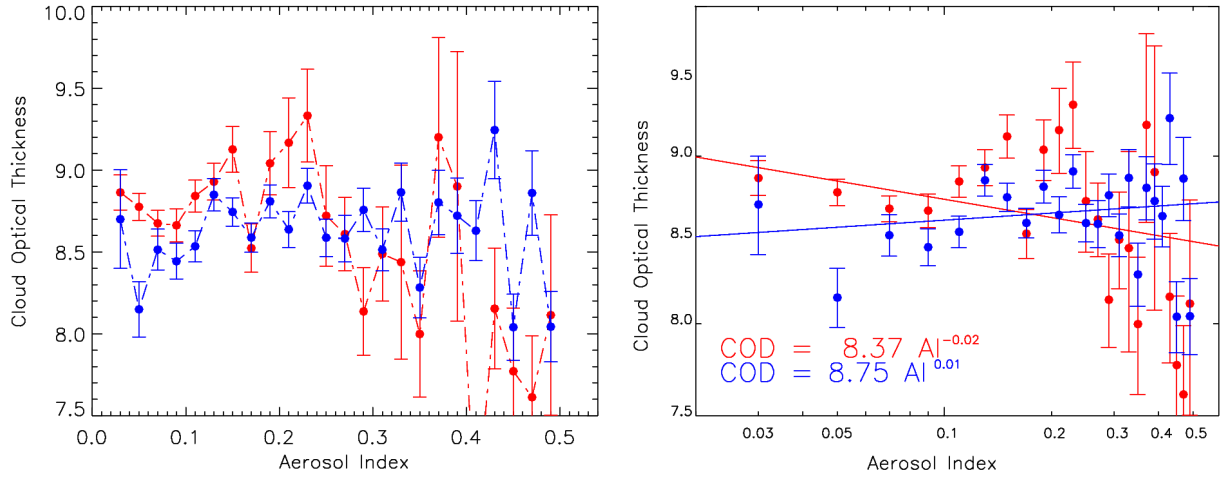

Figure 43: left image represents cloud optical thickness retrievals averaged over constant bin of aerosol index (0.02), in case of well separated (blue) and mixed (red) cloud-aerosol layers. Right image represents same relationship, but in log-log scale. Latitude varies within [2S, 15S].

This finding has a strong radiative impact. Even if Twomey's hypothesis is valid at microphysics scale, aerosol-induced diminution of droplet size does not produce any significative change in cloud reflectance, as a consequence of LWP loss. Consequently, also the resulting aerosol indirect radiative impact will be rather small.

6.9 CDR-AI and COT-AI relationship, under the assumption of constant LWP

Although constant liquid water path assumption does not seem to be valid over the area of interest, it is possible to analyze the constant liquid water path case. Figure 44 shows various CDR-AI relationships for mixed and interacting cloud and aerosol layers, stratified by very small intervals of liquid water path, equal to 3 g/m². The value has been chosen to allow for very small variation of LWP, in order to minimize the effect of changes in local meteorology on CDR(COT)-AI relationship. To increase the number of measurements, allowing for smaller statistical uncertainties and higher accuracy, we use a wide range of AI, from 0.025 to 0.7. Coincident CDR retrievals are averaged over constant bin of AI, equal to 0.025. Unmixed aerosol-cloud minimum distance threshold is hold at 250 m. Dataset includes all observations over the South-East Atlantic region.

Each curve of Figure 44 represents a linear (left image) and log-log scale (right image) CDR-AI relationship, for any given interval of liquid water path. The mean value of each interval is reported in black, together with the slope estimate (red).

Note that clouds with higher LWP always have larger CDR, for constant AI. For instance, for a fixed value of AI equal to 0.04, effective radius increases from 8.5 to 14 μm as LWP increases

from 28.6 to 61.5 g/m². At the same time, the slope of CDR-AI relationship in log-log scale (referred as droplet radius sensitivity, to a certain aerosol increase) decrease from -0.03/-0.04 to -0.07. Average cloud droplet size and its sensitivity are both positive functions of liquid water path.

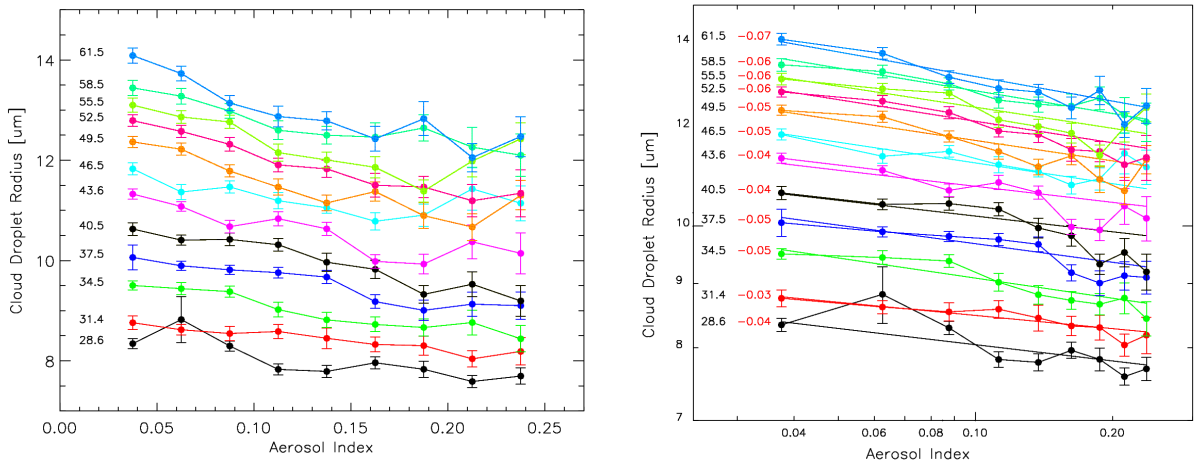

Figure 44: left image represents MODIS-CALIPSO coincident retrievals of droplet effective radius sorted by LWP (from 29 to 61 g/m², by step of 3 g/m³) and averaged over constant bin of AI (0.025), in case of mixed and interacting cloud and aerosol layers. Right image shows the same relationship, but in log-log scale. LWP interval mean value is reported in black, together with calculated linear slope, in red.

The dependence of COT and COT-AI relationship on liquid water path is shown in Figure 45. For AI = 0.04, COT increases from 5.5 to 6.7 as LWP varies from 8.6 to 61.5. At the same time, cloud optical depth sensitivity to aerosol invigoration increases from 0.4/0.5 to 0.7.

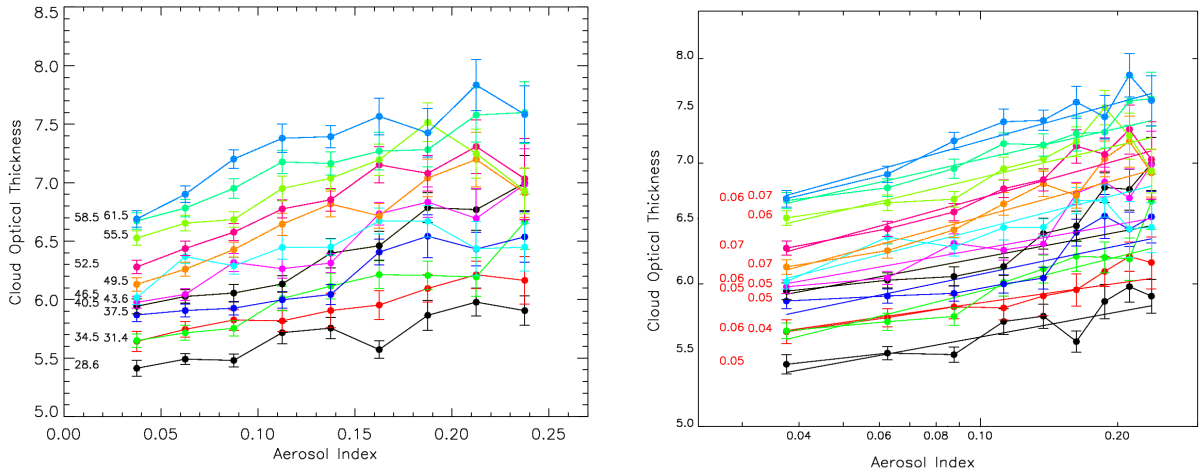

Figure 45: left image represents MODIS-CALIPSO coincident retrievals of cloud optical thickness sorted by LWP (from 29 to 61 g/m², by step of 3 g/m³) and averaged over constant bin of AI (0.025), in case of mixed and interacting cloud and aerosol layers. Right image shows the same relationship, but in log-log scale. LWP interval mean value is reported in black, together with calculated linear slope, in red.

Enhancement of cloud droplet radius and optical thickness efficiency with increasing liquid water path has been observed, but not quantified, by Lebsock et al. (2008). This effect can be predicted analytically, using the formulation of LWP (Chapter 4) expressed as a function of cloud droplet radius r_e and geometrical thickness H

$$LWP = \pi \rho_w \frac{4}{3} k\, r_e^3\, N\, H \tag{41}$$

where, k is a parameter that relates satellite retrieved effective radius and mean volume weighted droplet radius in the form $r_v^3 = k\, r_e^3$ (Pawlowska and Brenguier, 2000). Solving (41) for r_e and differentiating with respect to N, it results

$$\frac{\partial r_e}{\partial N} = -\left(\frac{3}{k 4 \pi \rho}\right)^{1/3} \frac{1}{3} \frac{LWP^{1/3}}{H^{1/3} N^{4/3}} \tag{42}$$

In case of mixed and interacting cloud-aerosol layers, AI is supposed to be proportional to cloud droplet number concentration (Chapter 5). This means that for a given aerosol perturbation, linear sensitivity of effective radius decreases (increasing in magnitude) proportionally to $LWP^{1/3}$.

Experimental data can be compared with latter relation. In left image of Figure 46, we compute linear regression slopes of CDR-AI relationships (in linear scale) for different intervals of LWP (3 g/m²), from approximately 20 to 100 g/m². In the right image of Figure 46, we show same

relationship but in log-log scale, in order describe the change in aerosol efficiency as an exponential function of cloud liquid water path. As CDR decreases with increasing AI, we consider the absolute value of calculated slope. As usual, mixed and unmixed statistics are indicated in red and blue.

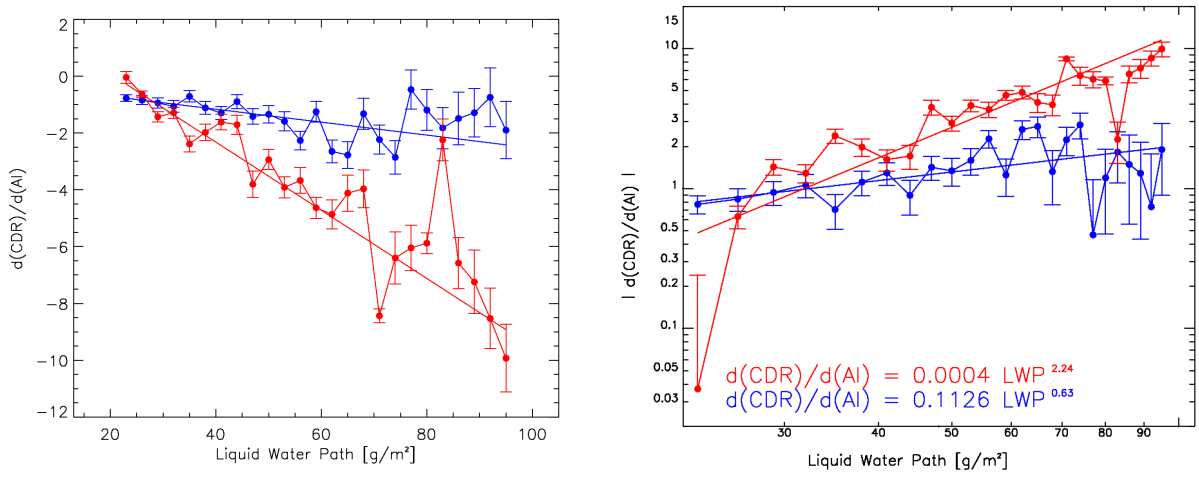

Figure 46: left image represents droplet radius linear sensitivity (i.e. the slope of each CDR-AI relationship, in linear scale, sorted by LWP by step of 3 g/m²) as a function of LWP, for mixed (red) and unmixed (blue) cloud-aerosol layers. Right image represents same relationship,but in log-log scale, where the absolute value of linear sensitivity is considered.

When cloud and aerosol layers are mixed and interacting, we obtain

$$\left|\frac{dCDR}{dAI}\right| \propto LWP^{2.24} \tag{43}$$

According to (43), linear sensitivity of CDR to aerosol invigoration is proportional to $LWP^{2.24}$, which is much higher than the expected value of $LWP^{1/3}$. When layers are well separated and cloud properties should be independent from aerosol load, CDR sensitivity is strongly reduced but still positive and proportional to $LWP^{0.63}$.

What is the cause of this apparent overestimation of aerosol effect? To obtain linear CDR sensitivity we sort data by LWP, from small to large water amount, by step of 3 g/m². Then we compute linear regression slopes of resulting CDR-AI relationships. Since the relationship between CDR and AI is more logarithmic than linear, the smaller the AI value where the CDR-AI curve is linearized, the deeper the slope is. In our case, subset of CDR sorted by LWP (from 20 to 95 g/m²) are characterized by decreasing values of average AI (from 0.24 to 0.10). This produce an increasing bias, with increasing LWP, that adds to aerosol-induced effect and might explain why the observed exponential relationship is stronger than expected.

This dependence on AI can be eliminated, quantifying droplet radius (cloud optical thickness) sensitivity to aerosol invigoration in the (logarithm) form

$$\frac{d\log(CDR/COT)}{d\log AI} = f(LWP) \tag{44}$$

In Figure 47, we compute droplet radius (left image) and optical thickness (right image) logarithmic sensitivities, S(CDR) and S(COT) respectively, in case of mixed and well separated cloud-aerosol layers.

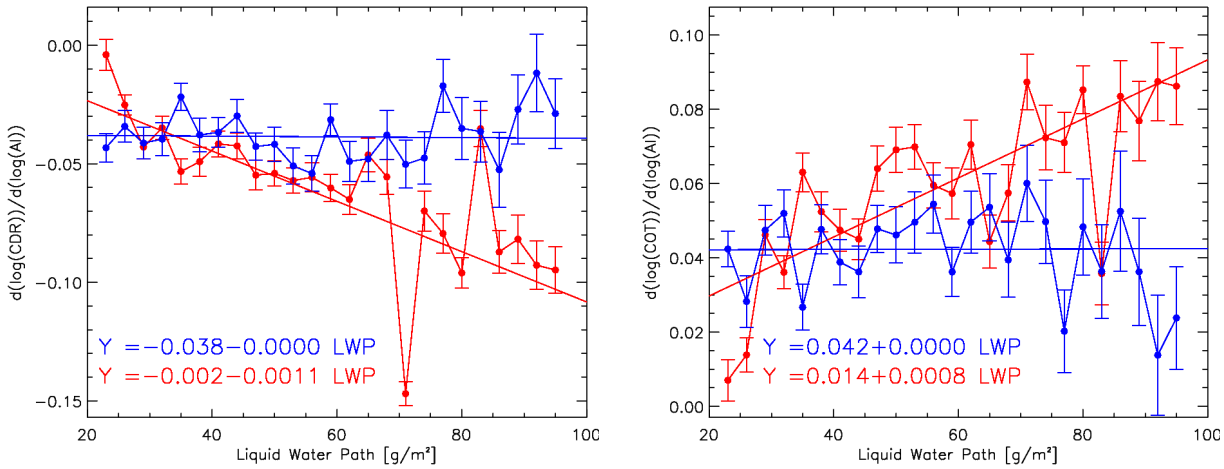

Figure 47: left image represents droplet radius sensitivity (i.e. the slope of each CDR-AI relationship, in log-log scale, sorted by LWP by step of 3 g/m²) as a function of LWP, for mixed (red) and well separated (blue) cloud and aerosol layers. Right image represents the change in cloud optical depth sensitivity.

In case of interacting layers, S(CDR) decreases from 0 to -0.10 and S(COT) increases from -0.05 to 0.85, as LWP varies approximately between 20 and 100 g/m². When aerosol is above cloud top (without physical interaction between the two layers), cloud sensitivity does not show any significant co-variation with cloud liquid water path. As expected, it remains approximately constant at 0.04 and -0.04, for S(COT) and S(CDR) respectively. Note that unmixed case S(CDR) is equal to unmixed case slope of CDR-AI relationship (in log-log scale) shown in Figure 42, where the assumption of constant LWP can be considered reasonably valid (LWP decreases by about 10g/m², as AI varies from 0.2 to 0.05).

Even though COT and CDR responses to aerosol enhancement show similar slope magnitudes, results cannot be interpreted as evidence of Twomey's hypothesis. They are necessary by construction of MODIS LWP estimate, calculated from COT and CDR observations using equation (38). An independent evaluation of cloud water amount would be necessary to analyze

aerosol impact on cloud droplet effective radius and cloud optical thickness, in constant LWP conditions.

Figure 47 clearly indicates that (al least) for low clouds over ocean aerosol-induced effect depends on LWP, and hence on cloud life cycle. Cloud sensitivity is stronger when liquid water amount is larger. This result supports recent hypothesis, according to which cloud response to aerosol invigoration cannot be considered as a simple function of aerosol concentration, but a more complicated regime-dependent process. According to mixed statistics, the dependence of aerosol impact efficiency on liquid water path is linear, with a strong correlation coefficient equal to 0.71 for CDR and 0.73 for COT. It can be expressed as

$$\frac{d\log CDR}{d\log AI} = -0.002 \pm 0.003 - (0.0011 \pm 0.0001)\, LWP \tag{45}$$

$$\frac{d\log COT}{d\log AI} = 0.014 \pm 0.003 + (0.0008 \pm 0.0001)\, LWP \tag{46}$$

Without aerosol-cloud interaction, cloud sensitivity is constant (even if not zero) with increasing LWP and computed slope of S(CDR)-LWP and S(COT)-LWP relationship is zero. Unmixed case statistics confirm that (45) and (44) probably describe a true aerosol-induced effect.

In Figure 48, we compute same relationships than figure Figure 47, making use of MODIS daily product.

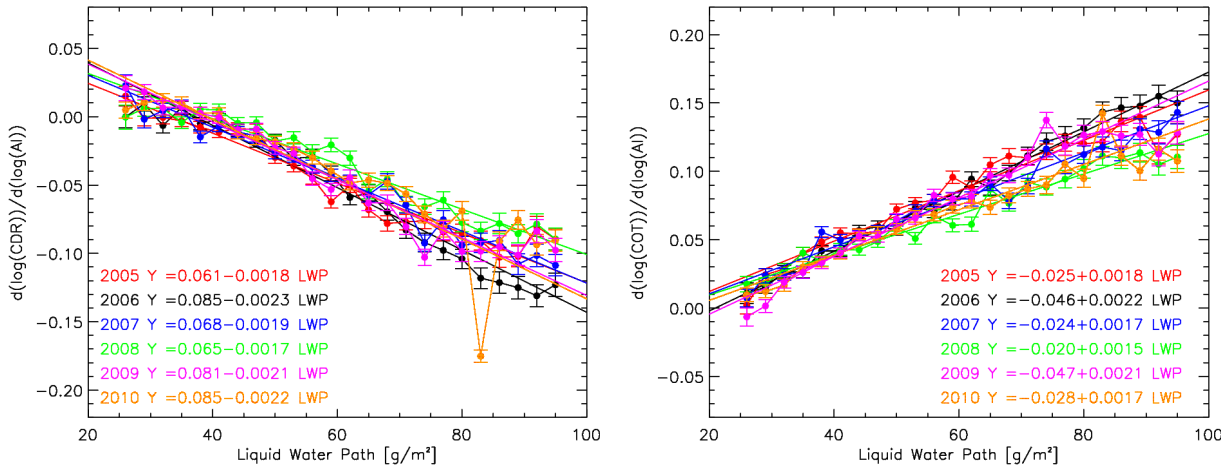

Figure 48: left image represents droplet radius sensitivity (i.e. the slope of each CDR-AI relationship, in log-log scale, sorted by LWP by step of 3 g/m²) as a function LWP interval (MODIS daily product). Right image represents the change in cloud optical depth sensitivity. The equation of computed linear regression is reported and indicated for each year with the same color relative symbol.

Even though MODIS daily products do not provide the vertical information that allow to differentiate between interacting and well separated layers, Figure 48 (MODIS alone) and Figure 47 (MODIS-CALIPSO mixed case) show similar trends of S(CDR) and S(COT) with increasing LWP. This proves that cloud sensitivity dependence on LWP is well reproduced by MODIS statistics. The presence of unmixed cloud-aerosol layers, characterize by constant sensitivities for every cloud water amount, does not produce any sensible effect on S(CDR)-LWP and S(COT)-LWP curve slopes.

Using MODIS daily product, we dispose of a very large dataset that reduces statistical uncertainties with respect to mixed-unmixed layer analysis. Computed linear fits of S(CDR) and S(COT), calculated over the whole 6 year time period, result

$$\frac{d\log CDR}{d\log AI} = 0.067 \pm 0.001 - (0.0018 \pm 0.0000)\, LWP \tag{47}$$

$$\frac{d\log COT}{d\log AI} = -0.028 \pm 0.001 + (0.0018 \pm 0.0000)\, LWP \tag{48}$$

The difference between aerosol impact efficiency dependence on LWP, observed from CALIPSO-MODIS and from MODIS daily product, can be estimated by comparing angular coefficients of (45) and (44) with those of (42) and (40). Using MODIS alone, the dependence on LWP is 1.6-2.2 times stronger.

In Figure 49 and Figure 50, we analyse seasonal variability of S(CDR)-LWP and S(COT)-LWP relationships over South-East Atlantic, from 2005 to 2010. Aerosol impact is always stronger when liquid water path is larger, with no significant dependence on time-period. In addition to evidences provided by mixed-unmixed layers analysis, temporal invariance of MODIS statistics confirms that the process we are looking at does not result from spurious correlations, between aerosol and cloud field, driven by changes in local meteorology.

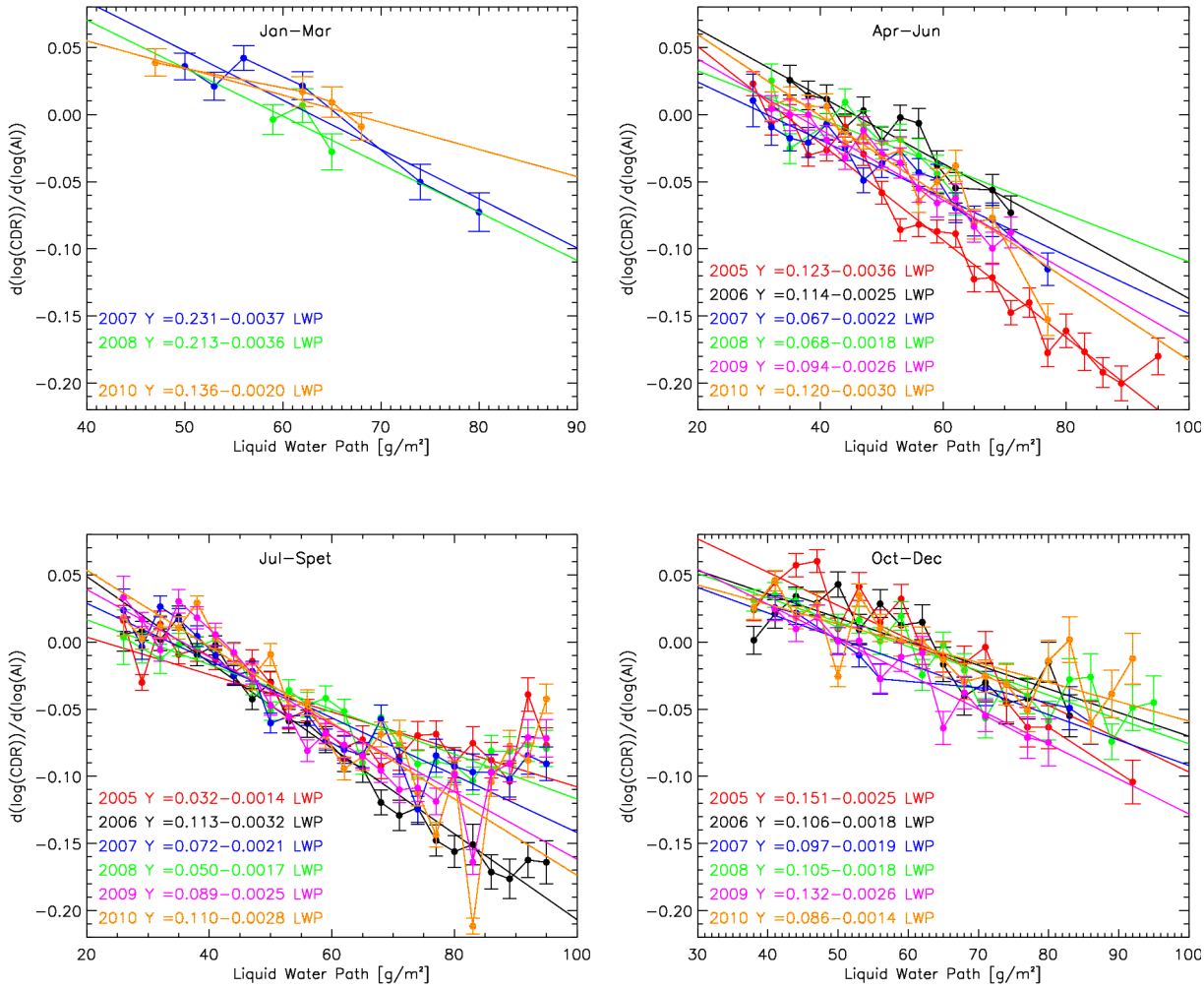

Figure 49: droplet radius sensitivity (i.e. the slope of each CDR-AI relationship, in log-log scale, sorted by LWP by step of 3 g/m²) as a function of LWP interval (MODIS daily product) for the four time periods of Jan-Mar, Apr-Jun, Jul-Sept, Oct-Dec.

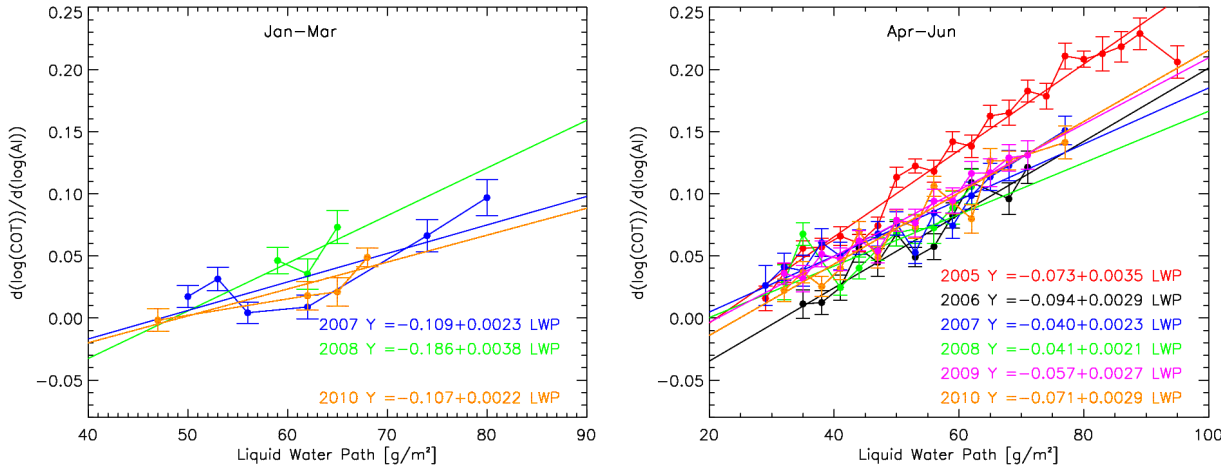

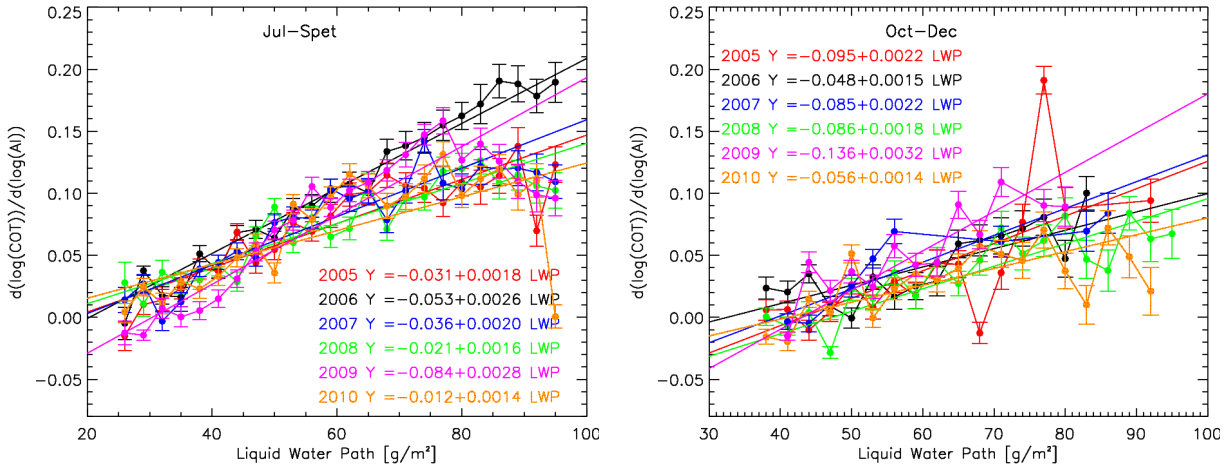

Figure 50: cloud optical thickness sensitivity (i.e. the slope of each COT-AI relationship, in log-log scale, sorted by LWP by step of 3 g/m²) as a function of LWP interval (MODIS daily product) for the four time periods of Jan-Mar, Apr-Jun, Jul-Sept, Oct-Dec.

6.10 Summary and conclusions

We used the MMC method, based on the analysis of simultaneous MODIS-CALIPSO retrievals, to show a clear decrease in cloud effective radius with increasing aerosol concentration, in case of mixed (interacting) cloud and aerosol layers. On the other hand, if layers are well separated, CDR does not present any significant dependence on AI. The result is in good agreement with Twomey's hypothesis. In addition, it provides strong evidence that aerosol-cloud interaction is main factor that leads to the negative correlations, between CDR and AI, found in many previous satellite-based studies.

The observed CDR-AI relationship is similar to that obtained in Chapter 3 from MODIS-PARASOL-CALIPSO observation. As shown in previous works (Bréon and Doutriaux, 2005), the comparison between coincident MODIS-PARASOL retrievals of CDR confirmed a good coherence the two dataset, with an average bias of about 1.7 µm for COT larger than 5 (according to MODIS product).

MODIS observation has been compared to coincident CALIPSO retrievals of AOD. We find limited coherence between the two dataset. A number of study attest MODIS ability to retrieve aerosol optical properties with high accuracy. According to MODIS product, CALIPSO algorithm strongly underestimates AOD especially in case of aerosol above clouds. On the other hand, CALIOP lidar is not expected to be sensibly affected by cloud adjacent effect, which is in turn supposed to increase MODIS AOD estimates in the vicinity of clouds. In case of mixed aerosol and cloud layers, mean AOD difference between MODIS and CALIPSO has been plotted as a function of cloud-aerosol distance. This analysis revealed a small bias up to 0.03, for average distance decreasing from 13 to 2 km.

Using coincident MODIS-CALIPSO estimates, it has been shown that LWP undergoes a strong decrease when aerosol and cloud intermingle. Such LWP trend is not observed when aerosol lies above cloud top and cannot affect the distribution of CDR and CDNC. LWP loss of polluted clouds is probably due to the enhanced entrainment of dry air above cloud top, that leads to an increase in droplet evaporation, with increasing cloud droplet number concentration due to Twomey's effect.

The response of cloud optical thickness to aerosol invigoration is a balance between the competing aerosol-induced effect on droplet radius and liquid water path. Statistics of MODIS-CALIPSO coincident retrievals show that COT does not present any specific dependence on AI. For both mixed and well separated layers, there is no significant change in the cloud reflectance with change in AI. Consequently, the resulting aerosol indirect radiative impact is supposed to be rather small.

According to Twomey's parametrization, we quantified the strength of aerosol-cloud interaction by the linear regression slope of the relationship, in log-log scale, between retrieved cloud parameter and aerosol index. We payed particular attention in distinguish between real aerosol-induced effects meteorological-driven co-variations of clouds and aerosol. Over South-East Atlantic, slope are equal to -0.15 for CDR-AI, -0.16 for LWP-AI and -0.02 for COT-AI.

It is evident that liquid water path assumption, invoked by Twomey's hypothesis, is invalid over the region. Anyway, we analyzed the constant LWP case sorting data by LWP, from 20 to 100 g/m^2, by step of 3 g/m^2. Statistics of CDR and COT showed that the strength of aerosol-cloud interaction is directly proportional to the cloud liquid water path. In case of mixed layers, slope magnitude of CDR-AI and COT-AI relationship (in log-log scale) increased linearly with increasing LWP. No significant variation was observed in case of aerosol above cloud top. We infer that cloud-aerosol interaction and its effect on cloud microphysics are leading factors governing CDR and COT co-variations with AI.

Statistics from MODIS daily product, sorted by season, confirm that first indirect effect is stronger when clouds have larger water amounts. This result do not depend on time-period and confirm that aerosol impact efficiency on cloud microphysical depends on LWP, and hence on cloud life cycle, as well as on aerosol concentration.

Chapter VII – Aerosol effect on cloud life-cycle

7.1 Introduction

We have shown in Chapter 5 and Chapter 6 how aerosol from biomass burning can strongly affect cloud microphysics in case of aerosol-cloud interaction. Acting as CCN, it can produce changes in cloud droplet concentration and size distribution. Over South-East Atlantic, an increase in aerosol concentration induces a clear decrease in cloud droplet radius, which results in a net decrease in cloud water amount. Such LWP response seems to be a consequence of enhanced entrainment of dry air above cloud deck, that causes droplet evaporation at cloud top. At the same time, according to Albrecht's hypothesis, the aerosol-induced increase in CDNC and the consequent decrease in CDR (for constant LWP amount) are supposed to suppress collision-coalescence processes between the droplets, decreasing precipitation and water removal from the cloud. In polluted environments, this mechanism then is expected to produce longer-lived clouds with larger LWP amounts, than in case of clean atmosphere. Inhibition of precipitation and droplet evaporation have competing effects on the final cloud liquid water path balance.

In addition, aerosol may affect cloud properties by a second main pathway. The presence of absorbing particles above cloud top can significantly warm the atmosphere and potentially change its vertical temperature gradient and stability profile, affecting moisture and heat fluxes from the surface, and hence cloud formation (Hansen et al. 1997; Ackerman et al, 2000).

MODIS daily product together with mixed and unmixed cloud-aerosol layers statistics can be used to find evidence of precipitation suppression in polluted clouds and quantify the ultimate impact of aerosol indirect and radiative effects on cloud cover.

7.2 Aerosol inhibition of precipitation, theoretical basis

Lohmann et al. (2000) use the ECHAM general circulation mode to explain differences in r_e-τ relationship between optically thin and thick clouds observed by Austin et al. (1999) off the coast of California, from AVHRR data.
This model is able to reproduce on global scale correlations between cloud effective radius r_e and optical thickness τ. They find that the change in sign of r_e-τ relationship slope from positive to negative can be attributed to the presence of precipitating versus non-precipitating clouds.

7.2.1 Precipitating clouds

In their model simulations, Lohmann et al. (2000) observe that precipitation reduces the range of variation of liquid water path, as cloud droplet radius increases. The more clouds develop and become optically thick the more water is removed from it through rain, so that LWP tends to remain constant. To understand the consequence on r_e-τ relationship, we consider the general equation obtained in Chapter 4

$$\tau = \frac{LWP}{r_e}\frac{3}{2\rho_w} \tag{49}$$

If precipitation works in the direction of keeping LWP constant, droplet radius will show an inverse dependence on optical thickness, of the form

$$r_e \propto \tau^{-1} \tag{50}$$

Studying the r_e-τ probability function obtained from model simulations in case of precipitation, Lohmann et al. (2000) find a negative exponential dependence of effective radius on optical thickness. The exponent, however, is much larger than expected (-1) and equal to -0.06.
On the other hand, in case of non-precipitating clouds, no specific assumption is made on LWP. Let then consider the general formula expressing cloud water amount as a function of cloud effective radius, droplet number concentration *N* and geometrical thickness *H* (Chapter 4),

$$LWP = \pi\rho_w \frac{4}{3} k\, r_e^3 N\, H \tag{51}$$

where the *k* is a parameter (generally between 0.7 and 1) that relates satellite retrieved cloud droplet effective radius to the mean volume weighted radius, in the form $r_v^3 = k\, r_e^3$ (Pawlowska and Brenguier, 2000). Substituting (50) into equation (49), follows that

$$\tau = 2\pi\, k\, r_e^2 N\, H \tag{52}$$

7.2.2 Non-precipitating clouds, the adiabatic model

If a stratiform boundary layer cloud is not precipitating and not influenced by entrainment, there is ample observational evidence (Pawlowska and Brenguier, 2000) that cloud Liquid Water Content (LWC) vertical profile follows the so-called adiabatic cloud model. This model

describes the evolution of a convective particle of moist air, when no surrounding air is mixed into the rising particles by turbulence.
The mixing ratio (which is a density ratio: the density of the substance in question divided by the density of the surroundings air) of total water q_{tot} can be expressed as the sum of the vapor and liquid mixing ratios:

$$q_{tot} = constant = q_{vap} + q_{liq} \tag{53}$$

At cloud base *cb*, total water mixing ratio is known and equal to the saturation vapor mixing ratio at that specific pressure p_{cb} and temperature T_{cb}, given by

$$q_{tot} = q_{vap}^{sat}(p_{cb}, T_{cp}) \tag{54}$$

At an altitude *z* above cloud base, the temperature follows the pseudo adiabatic lapse rate and decreases together with the saturation water vapor mixing ratio. From (54), assuming perfect saturation at every level *z* of the cloud at a given pressure *p* and temperature *T*, (53) becomes

$$q_{liq}(p_z, T_z) = q_{vap}^{sat}(p_{cb}, T_{cp}) - q_{vap}^{sat}(p_z, T_z) \tag{55}$$

Mixing ratio is just the ratio of the density of liquid to air and hence dimensionless. The density of liquid, called liquid water content, is

$$LWC(z)[g/m^3] = \rho_{air}\, q_{liq}(p_z, T_z) \tag{56}$$

The adiabatic water content at altitude *z* above cloud base, LWC(*z*), increases almost linearly with altitude, since the moist adiabatic condensation coefficient c_w [kg/m⁴] is almost constant in short stratocumulus clouds with geometrical thickness smaller than 1 km (Brenguier, 1991), depending slightly on the temperature (ranging between 1 and 2.5 × 10^{-3} g/m4 for T between 0° and 40° C), so that

$$LWC(z) = c_w z \tag{57}$$

The column integrated amount of liquid water within a cloud of geometrical thickness $H = z_{ct} - z_{cb}$, the liquid water path, is

$$LWP = \int_{z_{cb}}^{z_{ct}} LWC(z)\, dz = \int_{z_{cb}}^{z_{ct}} c_w z\, dz = \frac{1}{2} c_w H^2 \tag{58}$$

Substituting (56) into (50), we obtain

$$H = \frac{8}{3} \frac{\pi \rho k r_e^3 N}{c_w} \tag{59}$$

Equation (55) can be used to express H as a function of cloud droplet effective radius and number concentration in equation (52), that would now results

$$\tau = 2 \pi k r_e^5 N^2 \tag{60}$$

which means

$$r_e \propto \tau^{0.2} N^{0.5} \tag{61}$$

Adiabatic cloud droplet number concentration N is constant in a non-precipitating cloud, therefore droplet effective radius is expected to be an exponential function of cloud optical thickness, with exponent equal to 0.2. In good agreement with equation (51), Lohmann et al. (2000) find that non-precipitating clouds in the model exhibit an exponential r_e-τ relationship, where r_e is proportional to τ at the power of 0.156. They conclude that the change in sign of r_e-τ relationship can be reliably considered as an evidence of precipitation occurrence.

7.3 Evidence of precipitation suppression in polluted cloud, over South-East Atlantic

7.3.1 MODIS daily product

MODIS instrument provides long time-records of droplet radius and optical thickness, that allow for the analysis droplet effective radius dependence on cloud optical thickness. Figure 51 shows r_e estimates averaged over constant bin of τ over South-East Atlantic, within [4N, -30N; -14E, 18E], for 2005-2010. The change in sign of resulting r_e-τ relationship occurs for optical thickness of about 17.5, suggesting that the maximum value of mean droplet radius in non-precipitating clouds is about 17-19 μm.

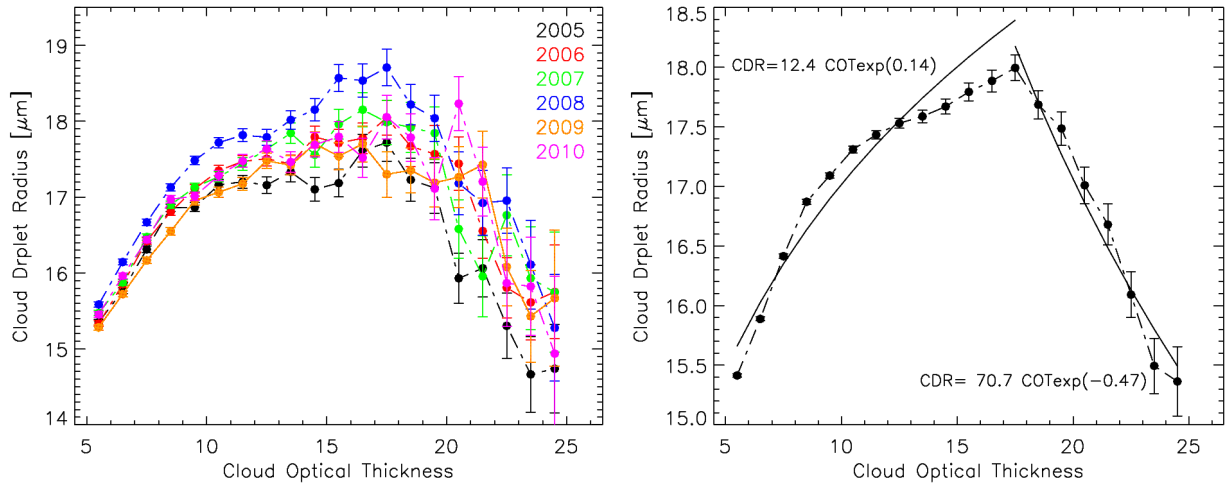

Figure 51: MODIS daily product retrievals, at 1×1 degree resolution, of cloud effective radius averaged over constant values of cloud optical thickness, for each year of 2005-2010 (left image) and globally, for the whole time-period (right image). Data are representative of low clouds (top pressure lower than 600 hPa) over South-East Atlantic, within [4N,-30N;-14E,18E], selected according to screening criteria for MODIS daily product, described in Chapter 6.

	$\tau \leq 17.5$ μm	$\tau \geq 17.5$ μm
2005	$r_e=12.8 \times \tau^{0.12}$	$r_e=97.5 \times \tau^{-0.59}$
2006	$r_e=12.3 \times \tau^{0.14}$	$r_e=69.8 \times \tau^{-0.47}$
2007	$r_e=12.3 \times \tau^{0.14}$	$r_e=63.5 \times \tau^{-0.44}$
2008	$r_e=12.1 \times \tau^{0.16}$	$r_e=80.3 \times \tau^{-0.51}$
2009	$r_e=12.2 \times \tau^{0.14}$	$r_e=41.4 \times \tau^{-0.30}$
2010	$r_e=12.5 \times \tau^{0.14}$	$r_e=61.0 \times \tau^{-0.42}$
Global	$r_e=12.4 \times \tau^{0.14}$	$r_e=70.7 \times \tau^{-0.47}$

Table 13: calculated exponential fit for r_e-τ relationships shown in Figure 51.

For $\tau \leq 17.5$, the exponent of the exponential fit calculated for each year between 2005 and 2010 varies between 0.12 and 0.16. It is equal to 0.14, if we consider the whole six year time period (Table 13). Such values are close to that expected for adiabatic clouds (0.20).
For $\tau \geq 17.5$, r_e-τ relationship is negative and computed exponent varies between -0.30 to -0.59, (2005-2010) and it is equal to -0.47, globally. This is approximately half of the theoretical value expected for constant LWP (-1). According to equation (49), a negative exponent larger than -1

indicates that LWP is not constant, but little increasing with increasing cloud droplet radius. Precipitation formation is given by collision-coalescence processes. The number of water droplets collected by a falling particle (collector) is proportional to the collision efficiency. Collision efficiency increases rapidly with droplet size, for collectors with radii larger than 20 µm. In order to have precipitation, it is then necessary that at least few cloud droplets increase their size up to 20 µm, during the lifetime of a cloud. This is in good agreement with experimental data shown in Figure 51. Statistics of MODIS daily product for the whole 2005-2010 time period clearly indicate that precipitative events dominate cloud regime when average droplet radius reaches 18 µm.

7.3.2 MODIS-CALIPSO coincident retrievals

To observe the effect of aerosol-cloud interaction on r_e-τ relationship, we make use of CALIPSO-MODIS coincident retrievals (selected according to the screening criteria of MMC methodology, described Chapter 6) over South-East Atlantic, within [4N, -30N; -14E, 18E]. Left image of Figure 52 shows cloud droplet effective radius retrievals averaged over constant bin of cloud optical thickness, in case polluted clouds (red), defined as mixed cloud-aerosol layers for AI larger than 0.09, and well separated layers (blue).

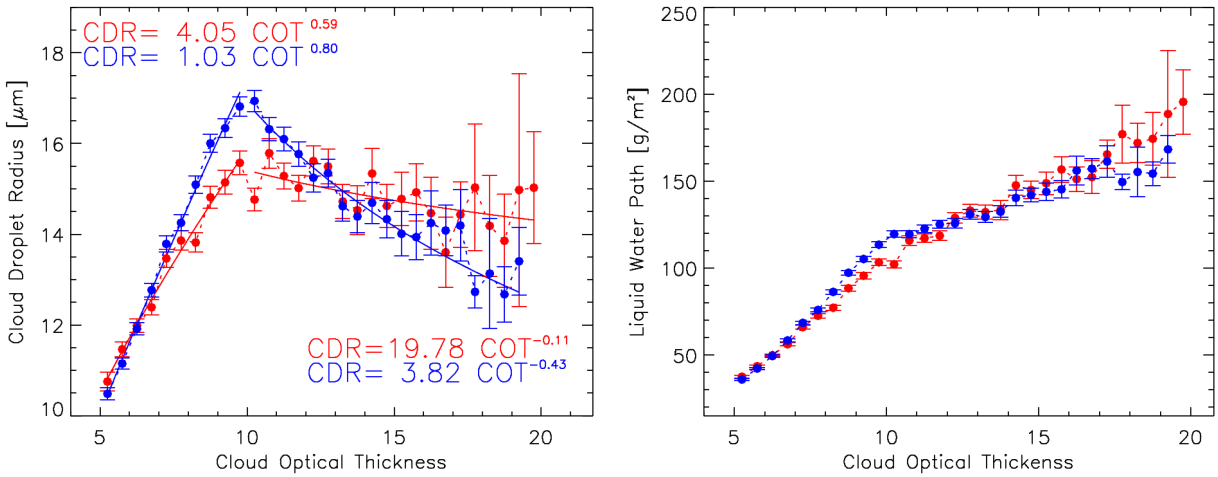

Figure 52: left image represents cloud droplet effective radius retrievals averaged over constant bin of cloud optical thickness, for mixed (red) and unmixed (blue) cloud-aerosol layers. Within mixed dataset, only retrievals with AI > 0.09 have been selected, in order to consider mixed clouds as representative of polluted cloud type. Right image represents liquid water path retrievals averaged over constant bin of optical thickness. Data are representative of low clouds (top pressure lower than 600 hPa) over South-East Atlantic, within [4N,-30N;-14E,18E], selected according to screening criteria of MMC methodology (Chapter 6).

When aerosol is above cloud top, droplet radius increases with increasing cloud optical thickness, up to $\tau = 10$. The change in sign of the r_e-τ relationship beyond this value indicates that precipitation mostly occurs for average droplet radius of about 17 μm, about 1 μm smaller than observed in Figure 51, but still consistent with expectation. Examining cloud-precipitation interaction by a combined use of radar and a solar/infrared radiometer on board of TRMM (Tropical Rainfall Measuring Mission), Kobayashi [2007] finds out that the largest effective radius for non-precipitating cloud is limited to between 15-20 μm.
The calculated exponential fit for $\tau < 10$ returns an exponent equal to 0.80. That is four times larger than expected value for adiabatic clouds (0.2) and sensibly larger than that observed using MODIS daily retrievals over the same area, for $\tau \leq 17.5$ (0.14). The difference between statistics resulting from MODIS-CALIPSO coincidences (retrieved at 5 km resolution) and MODIS observations (obtained merging 5 km onto 1 degree grid box) may indicate that warm clouds differ locally from adiabatic assumption, although it is valid at larger scale.
For $\tau > 10$, the computed exponent of r_e-τ relationship is negative and equal to -0.43, about half of value expected in case of constant LWP (-1), but in good agreement with MODIS daily retrievals, for $\tau \geq 17.5$ (-0.47). That indicates a non-constant but sensibly reduced increase of LWP as τ reaches 10, as a consequence of the water loss due to precipitation occurrence. The LWP dependence on τ is shown in right image of Figure 52, where LWP estimates are averaged over constant bin of cloud optical thickness.
We can conclude that if aerosol does not interact with clouds, optically thin clouds are mostly non-precipitating. LWP increases rapidly with increasing optical thickness (from 40 to120 g/m² as τ grows from 5 to 10). Optically thicker clouds are characterized by a stronger precipitation occurrence, that works in the direction of keeping LWP constant (varying between 120 and 150 g/m² as τ increases from 10 to 19). This is in good agreement with the results of Lohmann et. al. (2000), that identify $\tau = 10$ as the threshold value below which precipitation little forms. At the same time, a large difference with MODIS daily product is evidenced, according to which precipitation mostly occurs for $\tau > 17.5$.

Also in case of mixed layers, thin polluted clouds ($\tau < 10$) show a positive r_e-τ relationship. However, the exponent of calculated fit is equal to 0.59, little smaller than in case of well separated layers (0.80). This is coherent with Twomey's effect, according to which the effective radius of polluted droplets is smaller in average than that of unmixed and (presumably) clean clouds.
Again, a cloud optical thickness of approximately 10 defines the threshold value beyond which r_e-τ relationship changes in sign. For τ between 9 and 11, r_e reaches a maximum value of 15.5 μm (about 1 μm smaller than in case of well separated cloud-aerosol layers) sufficiently large to allow for precipitation production. For $\tau \geq 10$, the calculated exponential fit returns an exponent of -0.11, which is four times larger than in case of unmixed layers (-0.43) and nine times larger than the expected value in case of constant LWP (-1). In the hypothesis that precipitation occurrence reduces the range of variation of liquid water path, as cloud optical thickness

increases, results may indicate a decrease of water loss, as a consequence of an aerosol-induced inhibition of precipitation in polluted clouds.
In right image of Figure 52, mixed liquid water path is increased by 90 g/m² (from 100 to 190 g/m²) as cloud optical thickness increases from 10 to 19, while unmixed liquid water path by only 50 g/m² (from 120 to 170 g/m²). The percentage difference between the two goes approximately from -15 to 15%, as τ varies from 10 to 19 (Figure 53).

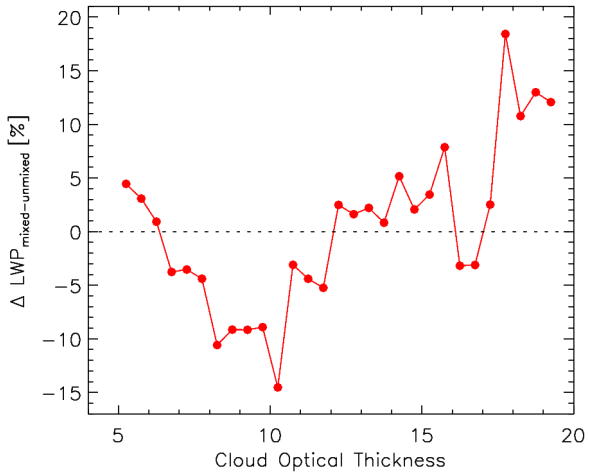

Figure 53: percentage difference between mixed and unmixed LWP shown in figure, with respect to unmixed LWP amount, as a function of constant interval of cloud optical thickness.

In conclusion, thin liquid clouds (τ < 10) over ocean have in average smaller water amount if they are mixed with polluted atmospheric layers (AI > 0.09). That is in good agreement with LWP-AI and COT-AI relationships observed in Chapter 6, where average cloud optical thickness is ~9 g/m² in case of mixed and unmixed layers and mixed LWP decreases, with respect to unmixed one, as aerosol index overpasses 0.09.
The production of large droplets by coalescence-suppression processes is strongly inhibited in polluted environments, so that droplet radius of non-precipitating clouds is limited at ~15 μm. For τ > 10 polluted clouds rain less than clean ones. Beyond τ = 12, the LWP amount in case of mixed cloud-aerosol layers (where less water is removed through rain) exceeds that of well separated layers.
Results provide simple but consistent evidence of precipitation suppression by cloud-active aerosol. One of the major uncertainties in assessing aerosol impact on precipitation relates to the tendency of aerosol to correlate strongly with meteorological conditions. As it is difficult to control meteorological effect on clouds, we cannot usually separate aerosol from meteorological contribution. Present analysis, in the attempt of solving this longstanding issue, shows that cloud-aerosol interaction is a dominant factor in preventing the development of rain.

7.4 A satellite study of aerosol effect on cloud fraction

The so called cloud lifetime hypothesis has a long history and served for much research since its first steps, in 1989. The basic idea is quite simple, as explained in Chapter 4 and 6. As a consequence of precipitation suppression by cloud-active aerosol, whose experimental evidence has been shown in previous paragraph, polluted cloud lifetime is expected to be longer (less water is removed through rain), leading to a more persisting and extended cloud field than in case of clean clouds. The result is that aerosol enhancement increases cloud cover.
We have large evidence, however, that cloud liquid water path decreases with increasing aerosol concentration, in contrast with the lifetime hypothesis. Cloud fraction response to aerosol perturbation is then presumably determined by the balance of these two competing aerosol-induced effects on LWP.
In present paragraph, we wonder if an increase in aerosol concentration does effectively result in an average increase in cloud fraction, as hypothesized by Albrecht (1989). This is probably one of the most important issue to quantify aerosol radiative impact, since a little increase in stratocumulus extent would strongly alter Earth's radiation budget and increase the amount of solar radiation reflected to space. Nevertheless, it is also one of the most difficult, for the large and numerous uncertainties related to the remote sensing of cloud fraction. First of all, it is complicated to distinguish radiatively between cloud and aerosol. If aerosol load is very large, it can be interpreted as a cloud. Cloud side-scattering effects can lead to over-estimate aerosol optical depth near cloud.
In addition, other explanations to the strong satellite-derived relationship between CLF and AI may be possible, than a simple aerosol-induced effect. Aerosol and cloud fields can correlate with the same meteorological parameters and cause apparent correlations between them. Relative humidity, for example, regulates cloud amount but also aerosol optical depth, since aerosol size may increase in the air surrounding clouds, where RH is high (swelling effect). Similarly, relative humidity, cloud fraction and aerosol load can be positively correlated in case of strong trade-wind convection. A strong surface wind would increase surface evaporation and sea-spray concentration (leading to larger aerosol optical depth retrievals) and favor a more humid and deeper cloud layer (Loeb and Schuster, 2008).
Vertical resolution is fundamental to know whether or not cloud and aerosol intermingle. Mixed and unmixed cloud-aerosol layer analysis has been shown to be very useful to provide evidence of aerosol-induced effects. However, the deficiency of temporal resolution still does not allow to fully assess causality from statistics. This is a limitation that should be always kept in mind when interpreting cloud and aerosol satellite data.
Previous studies based on satellite data have largely shown a strong CLF-AI relationship. For instance Menon et al. (2008) and Quaas et al. (2009) analyze MODIS daily products and find log-log scale linear regression slopes equal to 0.4 and 0.31-0.29 (Terra-Aqua), respectively.
CLF-AI relationships from model simulations have in general lower slopes. Quaas et al. (2009) study cloud cover response to aerosol variations for ten different GCM models: CAM-NCAR

(Community Atmospheric Model), CAM-Oslo, CAM-PNNL, CAM-Umich, ECHAM5, GFDL, GISS (Goddar Institute for Space Studies), HadGEM (Hadley Centre Global Environmental Model), LDMZ-INCA, SPRINTAS. Seven models show a weaker relationship than MODIS, with slope ranging from 0.00 to 0.26 (over ocean). Only two produce larger slopes, equal to 0.59 and 1.09. These models include some parametrization of cloud lifetime effect (an increase of aerosol concentration leads to a decrease in the autoconversion rate, increasing lifetime, liquid water path and cloud fraction). They are also expected to reproduce CLF-AI co-variance due to meteorological dynamics. Humidity swelling effect, that would increase aerosol optical depth in the proximity of cloud, is also considered. They conclude that strong correlation of satellite data remains controversial, though in most cases models show positive correlations not so strong and with more variability.

A more recent study of Quaas et al. (2010) analyzes cloud cover sensitivity in ECHAM5. This GCM shows over ocean a CLF-AI log-log scale linear slope that decreases by 50%, if aerosol indirect effect is switched off, suggesting that about 50% of observed correlation between cloud occurrence and aerosol presence is due to meteorology. They infer, however, that in satellite based retrievals humidification of aerosol in the vicinity of clouds is the dominant effect contributing to the strong CLF-AI relationship, followed by cloud lifetime effect, while other effect (meteorological co-variations, side scattering, etc.) are likely of lesser importance.

Menon et al. (2008) use the GISS model to compare two simulations, with and without letting aerosol interact with cloud microphysics. In both cases, they find the same CLF-AI log-log scale linear slope, equal to 0.07 (against the value of 0.15, obtained by Quaas et al. (2009) coupling aerosol-cloud microphysical interactions and meteorology). They conclude that only meteorology has a significant role in increasing cloud cover.

From AERONET sun-photometers data, Kaufman and Koren (2006) suggest an interesting dependence of CLF-log(AI) relationship on absorption properties of aerosol that serve as CCN: the more aerosol is absorbing the smaller is the slope (and hence cloud cover sensitivity to aerosol enhancement). High reflective aerosol (τ_{abs} ~0.01) would then induce a strong increase in cloud cover (CLF-log(AI) slope of about 0.15), with a consequent increase in shortwave radiation reflected to space and planetary cooling. On the other hand, more absorbing aerosols (τ_{abs} ~0.05) do not affect cloud cover. They calculate that anthropogenic aerosol causes an annual increase in mean cloud cover of 5%, for shallow clouds over ocean.

7.4.1 MODIS daily product

The cloud lifetime problem is confirmed to be particularly complex, since none of the hypothesis discussed in literature can uniquely explain the observed satellite-derived relationships.

Statistics of MODIS daily product over South-East Atlantic are in good agreement with the global CLF-AI relationship (and log-log slope values) found by Menon et al. (2008) and Quaas et al. (2009). In Figure 54, cloud fraction is averaged over constant bin of aerosol index. Cloud

coverage increases from about 20 to 70% as AI increases from 0.01 to 0.5, for each year from 2005 to 2010. Log-log scale linear slopes vary between 0.30 and 0.32.

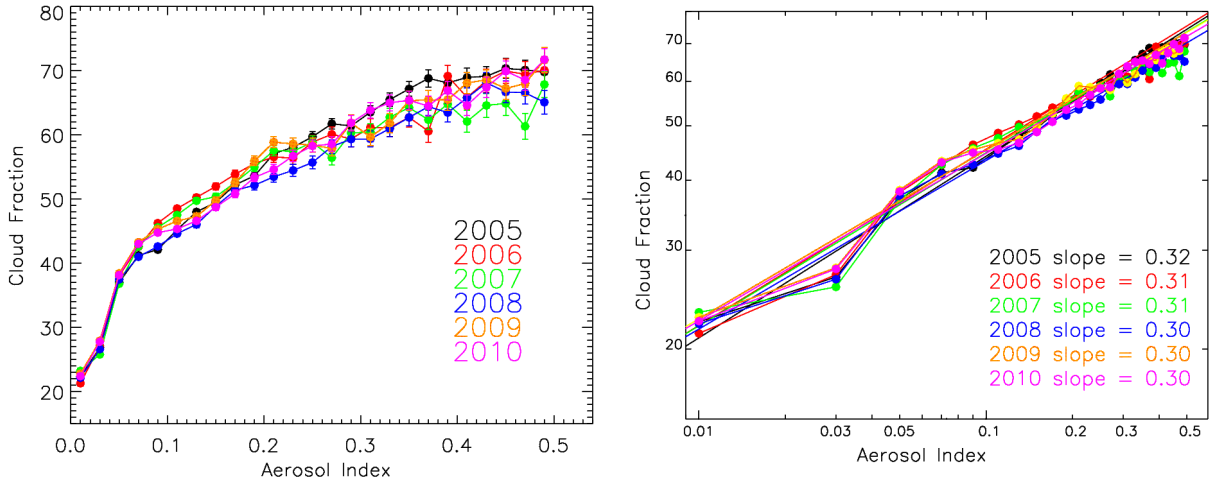

Figure 54: CLF-AI relationship from MODIS daily cloud and aerosol products, at 1 degree resolution, from 2005 to 2010 in linear (left image) and log-log scale (right image). Data are representative of low cloud cover (top pressure lower than 600 hPa) over South-East Atlantic, within [4N,-30N;-14E,18E], selected according to the screening criteria of MODIS daily product, described in Chapter 6.

Cloud fraction correlates well with cloud top pressure (CTP), which is a proxy to roughly estimate cloud vertical development. Lower top pressure may indicates taller clouds that reach higher level of the atmosphere. MODIS CTP retrieval algorithm, described in Chapter 2, as been validated by several ship- aircraft- and ground-based remote-sensing estimates as described in Menzel et al. (2008), Garay et al. (2008) and Harshvardan et al. (2009). Cloud top pressure estimates are found to be within 50 hPa of lidar determinations in single-layer clouds, mostly in case of high optically thin cirrus and mid level clouds. In case of two cloud layers, MODIS top pressure is representative of the mean pressure level between the two layers, if the upper-layer cloud is semi transparent. In atmosphere dominated by strong inversion (e.g. marine stratocumulus regions), MODIS algorithm places the layer above the inversion, up to 200 hPa off its true position. The error in cloud top height can be ass much as 1000-3000 km. Over the selected area, then, the bias in MODIS retrieved cloud top pressure error can be particularly high. In our analysis, however, we account only for low clouds with top pressure larger than 600 hPa. We then expect that large errors in CTP estimates, placing cloud top altitude in elevated layers of the atmosphere, are mostly avoided. The occurrence of multilayer clouds is not unusual over South-East Atlantic, and this can generate some ambiguity in the analysis of MODIS product. On the other hand, using the MMC method, CALISPO vertical information allows for the discrimination of multilayer cloud cases, that are excluded from statistics.

Upper left image of Figure 55 shows CLF estimates averaged over constant bin of CTP. Up to 700 hPa, the tallest clouds are characterized by the largest horizontal extension. Lower left image of Figure 55 indicates that the inverse relationship is also true. The most extended clouds have the highest cloud top, suggesting that horizontal and vertical development are strongly related.

For each year from 2005 to 2010, a maximum in cloud fraction occurs in the middle atmosphere at 700 hPa (~ 3km), with a reduction above this value, which produces a typical boomerang shape of CLF. A diminution of cloud coverage for CTP larger than 700 hPa may indicate the occurrence of 'high' clouds with larger cloud base altitude (in that case CTP is no more representative of cloud vertical extension) or multilayer cloud conditions, where CTP is not representative of the cloud top pressure of a real cloud field (in that case the CTP-CLF relationship has to be considered meaningless).

In the upper right image of Figure 55 we consider the whole 2005-2010 time period, sorting data from clean to polluted by AI and dividing them into six sample subsets, by step of 0.05. The mean AI value of each subset is reported in figure. All aerosol regimes show the maximum in CLF at approximately 700 hPa and the boomerang shape of CLF. At every pressure level, higher aerosol concentration are characterized by larger cloud coverages.

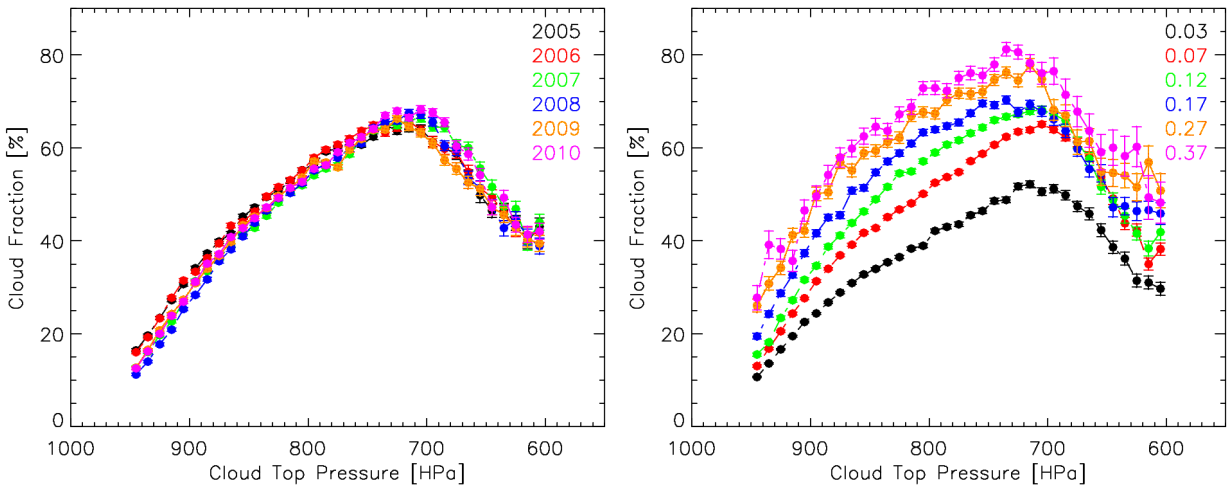

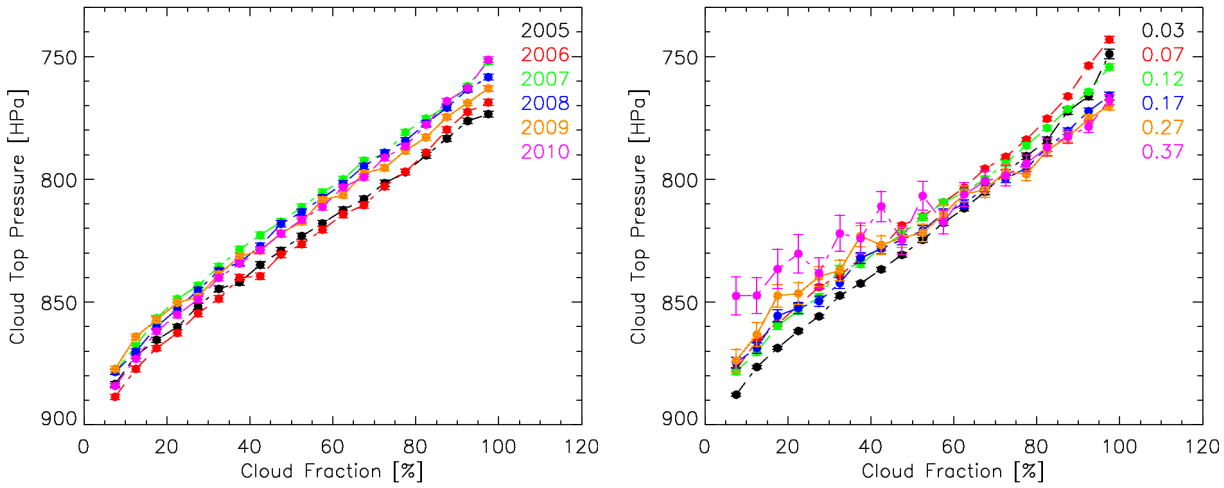

Figure 55: CLF-CTP (top row) and CTP-CLF (bottom row) relationships from MODIS daily products, at 1 degree resolution. In the left column, colors represent dataset from different years (2005-2010, as reported in figure). In the right column, dataset is sorted by AI, from little to high polluted atmosphere, by step of 0.1. Colors represent different aerosol index intervals (mean AI values are reported in figure). Data are representative of low cloud cover (top pressure lower than 600 hPa) over South-East Atlantic, within [4N,-30N;-14E,18E], selected according to the screening criteria of MODIS daily product, described in Chapter 6.

On the other hand, CTP does not show any significant dependence on AI, if CLF does not change. Figure 55 (lower right image) shows that CTP variations, averaged over constant bin of CLF, are very limited as AI varies between 0.03 and 0.37. For CLF larger than 60%, they fall within the 2005-2010 annual variability. Slightly larger CTP variations, with increasing AI, are observed for CLF < 60%. In that case, larger error bars indicate fewer retrievals and averages with smaller representativity. For constant values of CLF, higher aerosol concentration are not always associated to smaller top pressure, suggesting that CTP variations are not induced by aerosol-cloud interaction.

In the hypothesis that aerosol does affect cloud structure, we can conclude that its primary effect is more likely to increase horizontal extension than producing taller and more convective clouds.

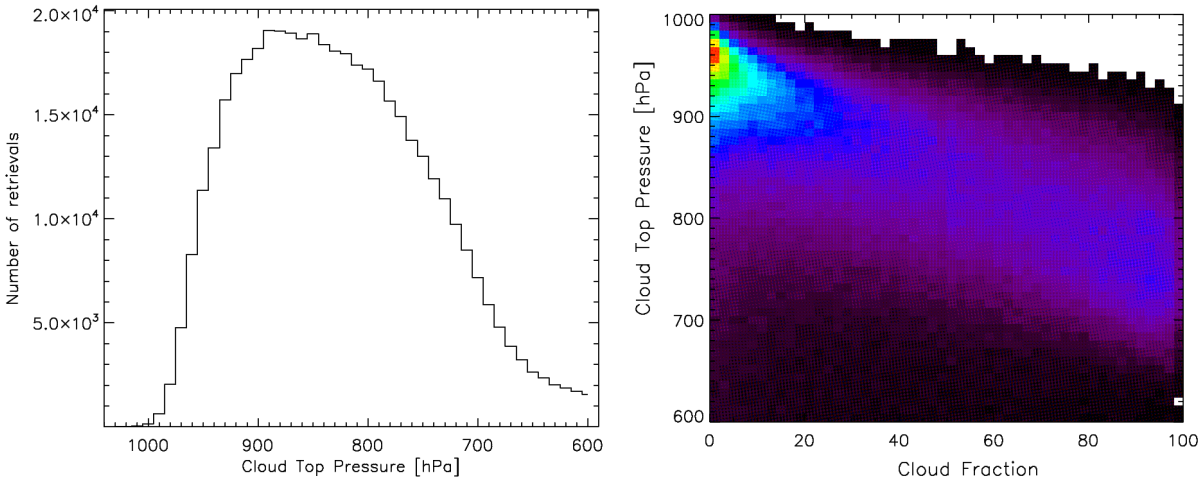

Figure 56: histogram of cloud top pressure (left) and histogram of CLF vs CTP (right), from MODIS daily product over South-East Atlantic, for the whole 2005-2006 time period. Color scale represents arbitrary units proportional to the number of point within each bin.

We analyze the CLF response to aerosol invigoration, from low to high atmosphere levels. Figure 57 shows CLF sensitivity (defined as the slope of the linear fit of CLF-AI relationship, in log-log scale) calculated sorting data into constant sample subsets of CTP, by step of 10 hPa.
Low clouds, with top pressures larger than 900 hPa, have large CLF sensitivities that vary between 0.37 and 0.25, while taller clouds have smaller sensitivity decreasing monotonically up to 0.05 as CTP reaches 670 hPa (seven times lower than CLF sensitivity at CTP = 980 hPa).
Beyond 670 hPa, high clouds or multilayer clouds seem to be most likely to occur. Resulting statistics, that exhibit and a positive relationship between S(CLF) and cloud top altitude, are less reliable as purely representative of CLF and CTP of low cloud field.
Histograms in Figure 56 show that South-East Atlantic is mainly characterized by the occurrence of clouds with CTP between 930 and 800 hPa (CLF fraction between 20 and 50%, Figure 55 and Figure 56), explaining why log-log scale linear coefficients of CLF-AI relationships for 2005-2010 (Figure 54) are so large.
These results, however, are not conclusive to define the leading factor (among real aerosol effects, meteorological induced co-variations of CLF and AI and measurement artifacts) governing this complicated could size-dependent relationship of CLF sensitivity.

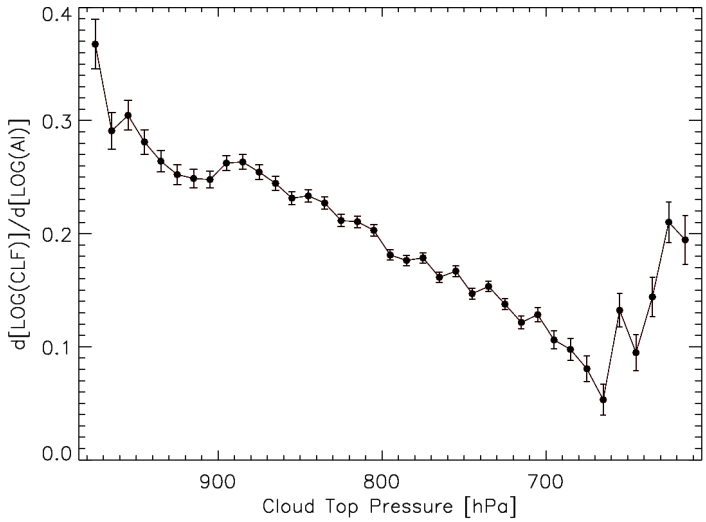

Figure 57: cloud fraction sensitivity (i.e. the slope of each CLF-AI relationship, in log-log scale, sorted by CTP, by step of 10 hPa) as a function of CTP. Data are from MODIS daily products, at 1 degree resolution, over South-East Atlantic for the whole 2005-2010 time period.

7.4.2 MODIS-CALIPSO coincident retrievals

In the attempt to isolate meteorological effects, we analyze CLF-AI statistics from mixed (interacting) and well separated (not interaction) cloud-aerosol layers, obtained by MMC methodology (Chapter 6).

First of all, it should be noted that cloud fraction from coincident MODIS-CALIPSO retrievals at 5 km resolution (L2 product) sensibly differs from that of MODIS daily L3 product, at 1 degree resolution. L2 cloud fraction is derived from 1 km resolution cloud mask, equal to 0 in the absence of cloud and to 1 for cloudy conditions. It is calculated by computing the fraction of cloudy 1 km cloud mark pixels. In MODIS daily product at 1 degree resolution, a grid box at the equator has an area of about 12,321 km². L3 cloud fraction is obtained by averaging all 5 km L2 cloud fractions in each 1°×1° box, including those equal to zero.

In the MMC method, when CALIPSO detects one cloud layer, we look for the nearest valid MODIS L2 cloud retrieval. As cloud free pixels are not considered, average cloud fraction of mixed-unmixed analysis are expected to be larger than in MODIS statistics.

Data are representative of the zone within [-2N, -15N; -14E, 18E], the central part of South-East Atlantic. According to considerations of Chapter 6, this area is less characterized by strong meteorological variations (affecting both mixed and unmixed statistics) than the whole region.

As explained previously, the basic hypothesis is that unmixed statistics are representative of cloud fields not interacting with aerosol particles, while mixed statistics are, so that resulting differences between the two cases can be interpreted as aerosol-induced effect. The comparison of two dataset over Central part of SE Atlantic is expected to be more representative of aerosol

induced effects, than over the whole region, where meteorology dominates aerosol-cloud statistics.

Hereafter, we present CLF retrievals averaged over constant bin of aerosol index (Figure 58, left image), from 0.02 to 0.5. When cloud and aerosol layers are mixed (red) there is an increase of cloud fraction by 4-9% (from about 87% to 91-96%) as AI increase from 0.02 to 0.5, while in case of unmixed layers (blue) CLF shows a larger increase by 10% (from 86% to 96%).

As expected, the two cases converge to a same single value for very low aerosol load. As aerosol number concentration rises, case with mixed aerosol-cloud layers show a systematically lower cloud fraction than clouds below aerosol. For very high AI, mixed CLF continues to increase up to values little smaller but comparable to those of unmixed CLF, which remains substantially constant between 0.95 and 0.96%, for AI larger than 0.2. It follows that mixed CLF presents actually a larger log-log scale linear slope, equal to 0.04, about two times larger than that of unmixed CLF-AI relationship, equal to 0.02.

In case of aerosol above clouds, well separated from cloud deck, the strong positive relationship between CLF and AI is completely independent of the effective microphysical aerosol-cloud interaction. This result provides strong evidence that satellite-derived correlations between cloud cover and aerosol concentration are prone to measurement artefacts and/or other factors than than a real aerosol indirect effect.

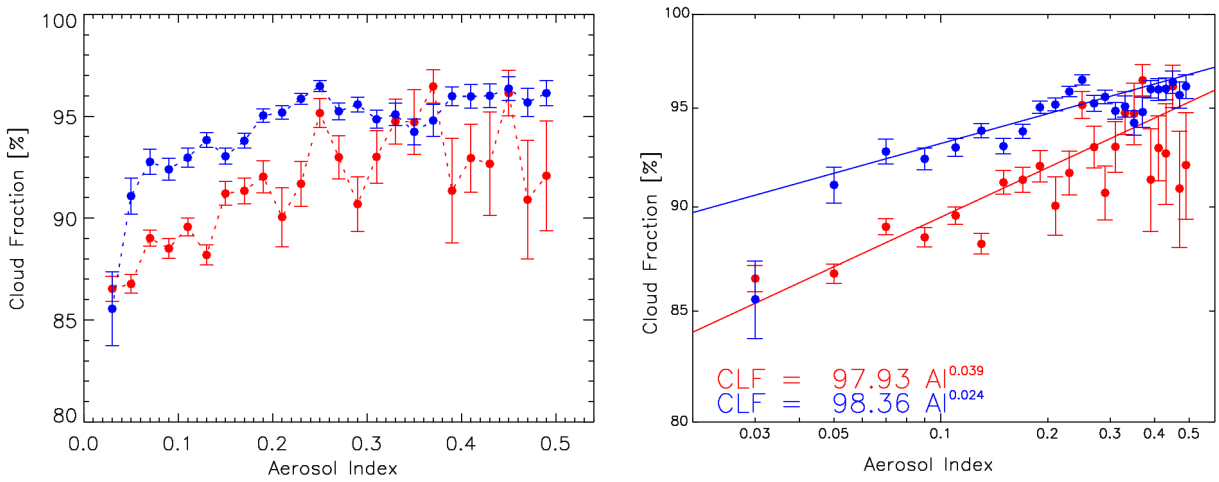

Figure 58: MODIS-CALIPSO coincident retrievals of cloud fraction, averaged over constant bin of aerosol index, by step of 0.02, in linear (left) and log-log scale (right). Case of mixed and interacting layers are reported in red, while cases of aerosol above cloud top in blue.

On Figure 59, we notice that in case of unmixed layers clouds also show a systematically smaller cloud top pressure (higher top altitude) than mixed cloud cases, sign that clouds under unmixed condition undergo larger vertical and horizontal developments as AI increases.

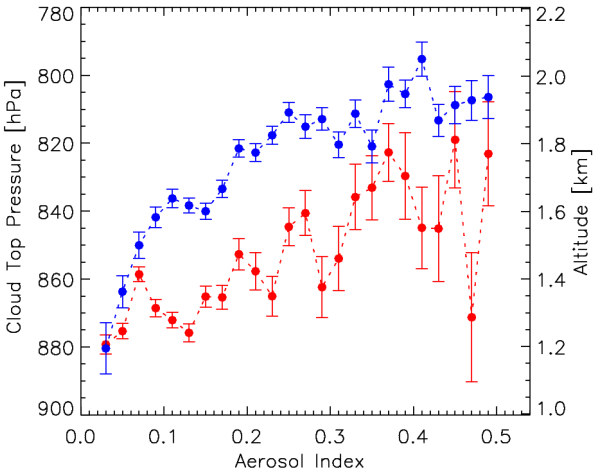

Figure 59: MODIS-CALIPSO coincident retrievals of cloud top pressure, averaged over constant bin of aerosol index, by step of 0.02. Case of mixed and interacting layers are reported in red, while cases of aerosol above cloud top in blue.

As shown from MODIS observations of Figure 55, larger CTP implies in average larger CLF, as well as larger CLF implies larger CTP, at least up to 700 hPa. We then believe it is better to compare CLF responses of clouds with similar vertical development. Cloud top pressure was found to be rather independent of aerosol interaction with cloud (Figure 55). Keeping it constant, we exclude CLF variations caused by considering clouds with largely different CTP (due to different local meteorological conditions), without loosing any significant information on the strength of aerosol effect.

According to these considerations, we make use of data from the whole South-East Atlantic [4N,-30N;-14E,18E], including those regions previously excluded, when performing simple CLF-AI correlations. Mixed and unmixed MODIS-CALIPSO coincidences are then sorted by AI, from clean to polluted, and divided in four equal sample subsets. Left image of Figure 60 represents the four CLF-CTP relationships in case of mixed layers, as AI increases from 0 to 0.4, by step of 0.1. The mean AI value of each interval is reported in figure. Right image represents same relationship, but for unmixed cloud and aerosol layers.

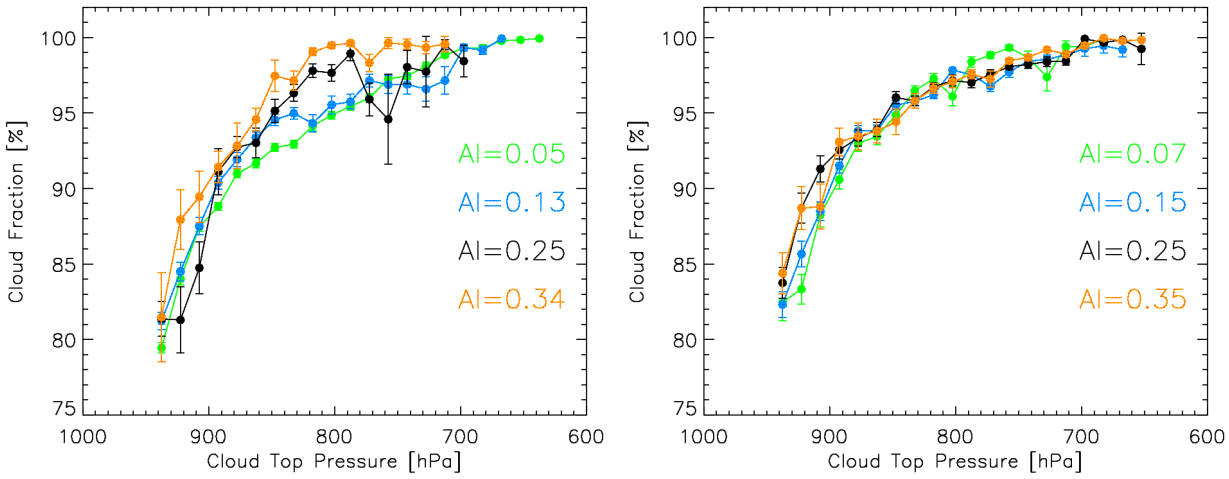

Figure 60: CLF-CTP relationships for mixed (left) and unmixed (right) cloud-aerosol layers, sorted by AI from little to large polluted atmosphere, by AI step of 0.1. Colors represent CLF-CTP data for different AI intervals (mean AI value is reported in figure).

If aerosol and cloud layers are mixed and interacting, the consequence of aerosol an increase is small but significant. More polluted clouds have in general larger cloud fraction, for constant cloud top pressure levels.

If aerosol is located above cloud, CLF is not always a positive function of CLT. In particular, for CTP<850 hPa CLF shows a lower dependence on AI than in mixed case and the different CLF-CTP curves relative to the different aerosol concentrations are closer to each other. For CTP>850 hPa, however, unmixed cloud fraction variations with increasing aerosol concentrations becomes more evident. Results suggest a regime-dependent response, where cloud cover depends on aerosol concentration and position, but also on cloud top pressure.

To provide a more accurate description of mixed and unmixed CLF sensitivity variation with cloud top pressure, we sort the whole MODIS-CALIPSO dataset by CTP, from lower to higher top altitudes, by constant step of 10 hPa. CLF retrievals of each subset are averaged over constant bin of AI (from 0 to 0.7) by step of 0.2. The linear regression slope of each CLF-AI relationship in log-log scale is calculated and plotted in function of the correspondent CTP interval. This process is performed twice, once for the mixed (red) and once the unmixed case (blue), as shown in Figure 61.

Note that very high clouds are generally characterized by extremely large cloud cover (almost equal to 100% even at very low AI) that would obviously results in CLF-AI slopes equal to zero. Only cases with CLF lower than 97% for AI = 0.01 are then considered.

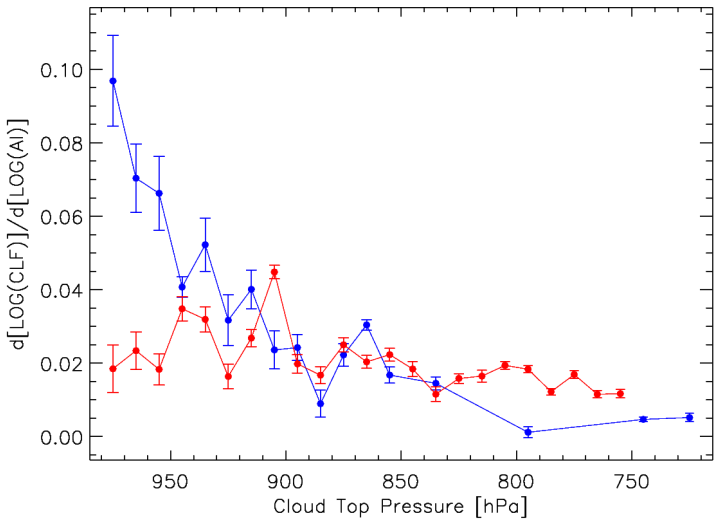

Figure 61: cloud fraction sensitivity (i.e. the slope of each CLF-AI relationship, in log-log scale, sorted by CTP, by step of 10 hPa) as a function of CTP, for mixed (red) and unmixed (blue) cloud and aerosol layers.

In case of mixed and interacting layers, there is a positive relationship between CLF and AI, characterized by small S(CLF) values with no specific dependence on CTP. The error bars indicate the statistical uncertainties. Apart from few points with CTP between 950 and 900 hPa, cloud fraction sensitivity varies between 0.025 and 0.015, with an overall mean value equal to 0.020.

In case of aerosol above cloud CLF sensitivity, S(CLF), variations with CTP are compelling. S(CLF) is almost zero when top layer altitude is larger than 2 km (CTP < 800 hPa). As cloud top pressure exceeds 800 hPa, however, CLF dependence with AI becomes positive. S(CLF) undergoes a dramatic increase positively related to cloud top altitude diminution. CLF sensitivity reaches a maximum value of 0.10 for very low clouds (CTP = 970 hPa), five times larger than that observed in unmixed statistics, for cloud top layers at a same altitude.

Unmixed relationships are supposed to reproduce CLF-AI co-variations induced by other causes than aerosol-cloud interaction, so where do these positive CLF-AI relationships come from? And why are they so strongly related with CTP?

When aerosol is located above clouds, an increase in low tropospheric stability (LTS) with increasing aerosol concentration would explain the observed CLF positive sensitivity, in case of unmixed statistics. Low tropospheric stability is defined as the difference between the potential temperature of the free troposphere (700 hPa) and the surface, LTS = $\theta_{700} - \theta_0$ (Klein and Hartmann, 1993; Klein, 1997; Wood and Hartmann, 2006). The idea that cloud incidence tends to increase with increasing LTS goes back to the beginning of the twentieth century, with the stratocumulus studies of Blake (1928). In a more recent work, Klein and Hartmann (1993) find a linear relationship between seasonal mean LTS and low cloud amount, for regions in the subtropics.

Aerosol absorption of solar radiation may largely warm lower free troposphere if aerosol reside above cloud cover. Over the Atlantic ocean off the coast of Angola, Wilcox (2010) simulate the radiative effect of a an aerosol layer (with single scattering albedo of 0.89±0.03) distributed between 1.5 and 4.2 km, with a peak at 3 km, and a stratocumulus cloud field (cloud optical thickness of 12) between 0.5 and 1.3 km (according to a statistics based on CALIPSO retrievals from July to September 2006-2008). For and AOD = 1, they find a peak of heating rate of 3.5 Kd^{-1} (within a range of ±0.05 Kd^{-1} for range of ±0.03 in single scattering albedo variation) at pressure level slightly below 700 hPa, about 2.5 Kd^{-1} larger than in case of no aerosol. In addition, they find that the air temperature at 700 hPa in case of high smoke load is systematically warmer on average by nearly 1 K, than in case low smoke samples.

The warmer condition of the troposphere may cause an increase in low tropospheric stability, increasing the strength of the inversion, suppressing cloud vertical extent and maintaining a well-mixed and moist boundary layer. This process is expected to enhance low cloud cover over ocean and it is reasonable to believe that the effect is proportional to absorbing aerosol concentration.

Unmixed statistics of Figure 61 shows a positive CLF sensitivity to aerosol invigoration, smaller for higher cloud top altitudes but very large in case of shallow clouds. This suggests an aerosol-driven increased inversion strength, more effective at trapping moisture within the boundary layer, as leading factor in governing the (positive) relationship between low cloud coverage and concentration of absorbing aerosol above clouds.

However, when aerosol lies within the boundary layer, aerosol warming of air below the inversion is not expected to produce any increase in cloud cover. By means of large eddy simulation of stratocumulus clouds, Johnson et al. (2004) find that aerosol located within well-mixed boundary layer may in turn enhance entrainment of dry air and decrease cloud liquid water path and cloud fraction (semi-direct effect). Figure 61 shows a constant and positive CLF sensitivity (CLF increases with increasing aerosol concentration) in function of CTP, in case of mixed cloud and aerosol layers. This indicates that aerosol radiative effect is not dominant (it would at least induce a decrease but not an increase of cloud cover). Therefore, mixed statistics may then reflect the effect of aerosol-cloud microphysical interaction, in the way theorized by Albrecht, where precipitation suppression by cloud-active aerosols leads to more longer-lived clouds.

Considerations made inhere fit well with observations. However, even if physical processes that has been identified as major responsible of observed cloud and aerosol co-variation cannot be ruled out by present results, further experimental evidence is needed. In any case, it is evident that cloud fraction responses to aerosol invigoration in case of cloud-aerosol mixing and in case of non interaction are not driven by the same physical process, since they have a significantly different dependence on CTP.

In case of low clouds, unmixed CLF shows a strong dependence on aerosol concentration which is much larger than that observed for mixed cloud-aerosol layers. This result seems to suggest that the so often invoked 'swelling effect' is not probably the main factor governing the observed CLF and AI co-variations. Humidification of aerosol in the vicinity of clouds would

induce to retrieve a stronger (at least equal) positive CLF sensitivity in case when aerosol particles are closer to clouds (mixed condition) and not farther (unmixed condition, with an aerosol-cloud distance threshold of 0.7 km).
Figure 61 suggests a second consideration. Assuming that aerosol indirect effect drives the cloud cover response in case of mixed and interacting layers, it contributes to only a small part of the total CLF sensitivity, that would be observed if no vertical distinction is made between interacting and not interacting layers.
In the hypothesis that A) mixed S(CLF) effectively results from aerosol-cloud interactions, B) its average value can be reliably considered constant at every cloud top pressure level, and C) the radiative effect of aerosol on unmixed cloud cover goes to zero beyond a certain value of CTP, we can try to estimate S(CLF) also from MODIS daily product (Figure 56).
Mixed-unmixed analysis of monolayer aerosol and cloud fields of Figure 61 shows that hypotheses A, B and C are valid from 1000 to 700 hPa. In that atmospheric region, also MODIS retrievals are expected to be mostly representative of monolayer clouds. This is suggested by the CLF-CTP relationship obtained from MODIS L3 product (Figure 55), in good agreement with that observed using MODIS-CALIPSO coincidences. We then assume that also MODIS daily retrievals, for clouds top pressure levels up to ~700 hPa, respect A, B and C.
According to previous hypothesis, S(CLF)-CTP relationship of Figure 56 is an "average" between the radiative contribution to S(CLF), decreasing with decreasing CTP (unmixed case), and the microphysical contribution, constant with CTP (mixed case). The minimum of S(CLF)-CTP relationship, at about 670 hPa, can be then considered as the point where the radiative contribution reaches its smallest efficiency.
In first approximation, assuming that the radiative contribution to cloud cover sensitivity is zero at CTP = 670 hPa (Figure 56), the effect of cloud-aerosol microphysical interaction can be estimated as ~0.10 (two times larger than the corresponding S(CLF) value of 0.05 at this specific CTP).
We arrive at a similar conclusion, considering the S(CLF) value at CTP = 980 hPa, where radiative effect (unmixed case, Figure 61) is about five times larger than microphysics one(mixed case). As the "average" between radiative and microphysical effect at this specific CTP is about 0.37 (Figure 56), the latter is equal to ~0.12.
This result is far from being an accurate estimate of the indirect aerosol effect on cloud cover. However, it indicates that if this effect exists (as mixed statistics confirm) its magnitude is just a small fraction of that -0.3 value obtained from MODIS daily product (Figure 54). At least 2/3 of the satellite-derived CLF-AI slope (in log-log scale) are due to other factors than a true aerosol-cloud microphysical interaction. Among these factors, the tendency of cloud fraction to correlate with aerosol-driven changes in low tropospheric stability seems to be the main actor.

7.5 Summary and conclusions

In this chapter we investigated the aerosol signature on satellited-based observations of cloud droplet radius and cloud optical thickness. Previous works (Lohmann et al., 2000; Peng et al., 2002) suggest that the change in sign of CDR-COT relationship from positive to negative, as COT increases, can be attributed to the transition from precipitating to non-precipitating clouds. MODIS-CALIPSO coincident retrievals show that, in case of well separated cloud and aerosol layers, the variation of COT with increasing CDR indicates that precipitation mainly occurs in optically thicker clouds, while thinner ones are non-precipitating. In good agreement with Lohmann et al. (2000), we found that COT = 10 can be reliably considered as the threshold value to distinguish between precipitating and non-precipitating clouds.

On the other hand, when aerosol (characterized by AI > 0.09) and cloud layers mix, there is strong evidence of precipitation suppression for clouds with COT > 10. Results confirmed that aerosol decrease collision-coalescence efficiency, reducing the amount of water removed through rain.

MODIS statistics of thin non-precipitating warm clouds over ocean are in good agreement with the adiabatic cloud model at regional scale (1 degree), although MODIS-CALIPSO retrievals indicate that adiabatic assumption is not valid at smaller scale (5 km). Similarly to other studies (Kobayashi, 2007), we found that the largest effective radius for non-precipitating cloud is limited between 15-20 μm.

Aerosol effect on cloud cover has been investigated as well. MODIS-CALIPSO coincidences showed that in case of mixed and interacting layers aerosol invigoration is associated with increased cloud fraction. We payed particular care in neglecting false correlations, deriving from meteorological co-variation of CLF and AI. Even if the lack of temporal resolution does not allow to fully assess causality from statistics, results showed a small but significant aerosol-induced effect on cloud life-cycle, due to aerosol-cloud interaction.

It has been show that high clouds, with smaller cloud top pressure, are always more extended than low clouds. In order to minimize the effect of changes in local meteorology on CLF-AI statistics, we sorted CLF-AI relationship by CTP, from 1000 to 600 hPa (by step of 10 hPa), to allow for very small CTP variations. The strength of cloud-aerosol interaction on cloud cover (second indirect effect) has been quantified from the slope of the CLF-AI relationship in log-log scale. In case of mixed layers we found a positive slope approximately constant and equal to 0.02, for cloud top altitudes at every pressure level. This value is much smaller that those generally found from satellite-based observations (Menon et al., 2008; Quaas et al., 2009).

Indeed, when aerosol lies above cloud top, cloud cover showed very compelling responses to aerosol invigoration, strongly dependent on cloud top pressure level. Cloud fraction sensitivity ss large for lower clouds (up to 0.09 at CTP = 970 hPa), decreasing with decreasing CTP (almost zero at CTP = 750 hPa). Results indicate that aerosols enhance cloud cover, even without physical interaction between the two fields. When absorbing particles are located above cloud top, they can significantly warm the atmosphere above the inversion and increase the low tropospheric stability. Enhancement of LTS increases the strength of inversion, suppressing cloud vertical extent and maintaining a well-mixed and moist boundary layer. We have reason to believe that these processes may enhance low cloud cover over ocean. Aerosol radiative

effect is then supposed to be the major responsible of observed low cloud fraction increase, in case of unmixed layers.

From the comparison with MODIS-CALIPSO coincidences, we infer that the most important contribution to cloud lifetime effect in MODIS statistics comes from aerosol radiative effect, while the impact of aerosol-cloud interaction is of lesser importance. We quantified the contribution of aerosol indirect effect on MODIS retrieved CLFL-AI relationship, as limited to a maximum of 1/3 in total slope value.

Chapter VIII – Aerosol effect on solar radiation

8.1 Introduction

Atmospheric aerosol absorbs and scatter solar radiation and, as seen in previous chapters, may alter cloud structure and optical properties, as well as precipitation formation and cloud lifetime. A change in aerosol concentration can affect Earth climate system, altering the atmospheric radiation balance. The difference in the net radiative flux at the Top Of the Atmosphere (TOA), or surface, with and without aerosol is referred as aerosol radiative forcing, which is generally classified as direct (DRF), if it is due to scattering and absorption of solar radiation, and indirect (IRF), if it is due to aerosol influence on cloud reflectivity and persistence.

The net effect of DRF is to cool planet surface, reducing the amount of incoming solar radiation (negative forcing). Depending on particle absorption properties, aerosol may also warm the atmosphere and, in case of cloudy-sky conditions, produce a positive TOA forcing, if aerosol layer is located above the cloud deck. Atmospheric warming may alter temperature vertical profile, atmospheric stability, boundary layers height, evaporation rate and hence cloud formation and precipitation.

Aerosol absorption properties depends primary on the black carbon (BC) concentration and aerosol from biomass burning contains high concentration of BC. Solar absorption is amplified when BC is internally mixed with sulphates, that strongly reflect solar radiation (Ramana et al., 2010).

The quantification of aerosol forcing has many sources of uncertainties, that are reflected, for example, in the range given for anthropogenic aerosol DRF in the 2007 summary report of the Working Group 1 of IPCC, -0.5±0.4 W/m². Concentration, lifetime and distribution of aerosol are highly variable spatially an temporally. Main parameters to which radiative forcing calculations is sensitive are aerosol optical properties (aerosol optical depth τ_a, single scattering albedo SSA, asymmetry parameter g and wavelength dependencies of these quantities) and environmental variables (underlying surface albedo ω, solar geometry, cloud optical thickness, aerosol and cloud vertical position) used as input.

8.2 Aerosol direct radiative forcing at SW

Early estimates of DRF were calculated with simple analytical formulas. In its first calculations, global biomass burning forcing was estimated to be -1.0 W/m² (Penner et al., 1992). Haywood and Shine (1995) are the first to consider absorption properties of soot and estimated the relative DRF ranging between 0.04 and 0.18.

More recently, in the effort to have improved global estimate of DRF, many chemical transport models (CTM) have been employed (as reviewed in Chapter 2, Foster et al. 2007) together with radiative transfer model (RTM). Largest uncertainties in these estimates are mainly due to uncertainties in the amount of geographical and temporal distribution of aerosol, its optical properties, and environmental variables.
An alternative approach relies in substituting information from CTM with in situ and satellite observation. Satellite sensors as MODIS, POLDER, MISR and CALIPSO can provide highly accurate global information on aerosol and clouds optical and geometrical properties, especially resulting over ocean, where the degree of confidence of MODIS retrieval algorithm is higher than over land. Note, however, that observations made with different approaches and instruments are subjected to different uncertainties, difficult to quantifies and resulting DRF estimates can widely differ.

8.2.1 Clear-sky SW DRF estimates over land and ocean

Table 14 presents clear-sky anthropogenic and anthropogenic+natural aerosol direct radiative forcing estimates from model simulations constrained by satellite observations (Kaufman et al., 2005; Bellouin et al., 2005; Chung et al., 2005; Yu et al., 2006; Christopher et al., 2006; Matsui and Pielke, 2006; Quaas et al., 2008; Bellouin et al., 2008; Zhao et al., 2008), while Table 15 shows the DRF using models only (Schulz et al., 2006; Quaas et al., 2009).
The mean DRF satellite based estimate for anthropogenic aerosol over ocean is -1.1±0.37 W/m² (without counting Quaas et al. (2009), where forcing is weighted by the clear-sky fraction), larger of about two times than the model based calculation of -0.6 W/m² (Schulz et al., 2006). There are less studies over land, but the few results available also indicate that model estimates are larger when simulation are constrained by satellite data.

	DRF Ocean [W/m²]	DRF Land [W/m²]	DRF Global [W/m²]	Estimated uncertainty or remarks
Kaufman et al. (2005)	-1.4	-	-	30%
Bellouin et al. (2005)	-0.8	-	-1.9	15%
Chung et al. (2005)	-	-	-1.1	-
Yu et al. (2006)	-1.1	-1.8	-1.3	47% ocean, 84% land, 62% global
	-5.5	-4.9		4% ocean, 14% land **anthropogenic+natural**
Christopher et al. (2006)	-1.4	-	-	65%
Matsui and Pielke (2006)	-1.6	-	-	30S-30N
Quaas et al. (2008)	-0.7	-1.8	-0.9	45%
Bellouin et al. (2008)	-0.6	-3.3	-1.3	Same as Bellouin et al. (2005) but

				updated with MODIS C005 data.
Zhao et al. (2008)	-1.25	-	-	35%
Chen and al. (2008)	-5.0	-	-	**anthropogenic+natural**
Quaas et al. (2009)	-0.30	-0.53	-0.38	60% ocean, 47% land, 50% global. Forcing is weighted by the clear-sky fraction.

Table 14: estimated clear-sky anthropogenic (or anthropogenic plus natural where indicated) aerosol SW direct radiative forcing at TOA, from model simulations constrained by satellite data.

	DRF Ocean [W/m²]	**DRF Land [W/m²]**	**DRF Global [W/m²]**	**Estimated uncertainty or remarks**
Yu et al. (2006)	-3.5	-2.8	-	17% ocean, 21% land **anthropogenic+natural**
Schulz et al. (2006)	-0.59	-1.14	-0.77	30-40%
Quaas et al. (2009)	-0.24	-0.40	-0.27	80% ocean, 90% land, 85% global. Forcing is weighted by the clear-sky fraction.

Table 15: estimated clear-sky anthropogenic (or anthropogenic plus natural where indicated) aerosol SW direct radiative forcing at TOA, from model simulations only.

DRF forcing estimates of anthropogenic+natural aerosol show the same discrepancy between measured-based and model-based simulations.

When using satellite retrievals, aerosol forcing over both ocean and land is larger than in case of model based values of about 30-40% for Yu et al. (2006) and 20-10% for Quaas et al. (2009). A possible explanation may be the overestimation of MODIS retrieved optical depth by about 10-15%, due to contamination of clouds (especially thin cirrus), as observed by Kaufman et al. (2005b). Other satellites may be affected by similar contamination, that are not still quantified. On the other hand, satellite estimate can observe enhanced AOD due to processes that are not represented (or not well enough) in models (such as aerosol humidification).

Determination of DRF over land is more complicated than over ocean. Estimates are fewer and with larger uncertainties, since satellite measurements are not able to characterize aerosol properties over complex surface (where reflection is large, heterogeneous and anisotropic) with high accuracy.

The mean satellite based DRF for anthropogenic aerosol over ocean varies between -0.9 to -1.9 W/m², stronger than the model based mean value equal to -0.8 W/m².

8.2.2 Clear-sky SW DRF estimates over South-East Atlantic

Local estimate of clear sky DRF can reach much higher values than those reported in . For instance Quaas et al. (2008) show that over the South-East Atlantic Ocean the five-year averaged anthropogenic DRF can reach -5 W/m², by a satellite based approach. Using aerosol and radiative fluxes information from the same satellites of Quaas et al. (2008), MODIS and CERES, Chen and al. (2008) reach similar conclusions and find a mean annual clear-sky total (natural and anthropogenic) aerosol DRF over ocean equal to -5 ± 1.2 W/m². They also compute seasonal mean of aerosol DRF over the subset region of South-East Atlantic [10N, 20S; 40W, 20E], equal to -8.5 W/m² (Mar-Apr-May), -13.7 W/m² (Jun-Jul-Aug), -10.7 W/m² (Sept-Oct-Nov) and -10.6 W/m² (Dec-Jan-Feb).
Myhre et al. (2003) estimate solar radiative impact from satellite, ground based and airborne data during the SAFARI-2000 experiment (a large campaign in Souther Africa during August and September), together with a radiative transfer model, with a 1.87°×1.87° horizontal resolution. They find that, in the small [7.5E, 13.1E; 20.6S, 24.4S] over South-East Atlantic off the coast of Namibia, clear-sky normalized (per unit AOD) biomass burning aerosol radiative impact varies between -90 and -50 W/m², for various times during the day (in the period 5-19 September, 2000). In these radiative transfer calculations cloud are excluded to allow direct comparison with the observations made from a C-130 aircraft under cloud-free conditions on the September 11, 2000. They find that normalized impact in the model is 17% weaker than in the observation. However, modeled daily averaged AOD (0.04) is substantially lower than that observed during the flight (0.31).
September 2000 monthly mean radiative impact in a much larger area over Southern Africa and South-East Atlantic [0S, 35S; 35W, 60E] is -4.3 W/m² (considering a constant SSA value of 0.90, at 0.55 μm), with a minimum of -20 W/m² over Namibian region.

<table>
<tr><th></th><th colspan="4">Clear-sky DRF over South-East Atlantic [W/m²]</th><th>Remarks</th></tr>
<tr><td>Sakaeda et al. (2011)</td><td colspan="4">-1.4</td><td>Forcing weighted by clear-sky fraction. Jul-Oct 2001-2008.
Fine aerosol</td></tr>
<tr><td>Quaas et al. (2008)</td><td colspan="4">[-0.1, -5.0]</td><td>2000-2005</td></tr>
<tr><td rowspan="2">Chen et al. (2008)</td><td>Dec-Jan-Feb</td><td>Mar-Apr-May</td><td>Jun-Jul-Aug</td><td>Sept-Oct-Nov</td><td rowspan="2">Jan-Dec 2005</td></tr>
<tr><td>-10.6</td><td>-8.5</td><td>-13.7</td><td>-10.7</td></tr>
<tr><td>Abel et al. (2005)</td><td colspan="4">-7.6
[-21.6, -3.2]</td><td>Sept 2000 [SAFARI]
Fine aerosol</td></tr>
<tr><td rowspan="2">Myhre et al. (2003)</td><td colspan="4">-4.3
[-20, 0]</td><td>Sept 2000 [SAFARI]
(SSA = 0.90)</td></tr>
<tr><td colspan="4">[-90, -50]</td><td>Instantaneous normalized DRE</td></tr>
</table>

				(W/m² per unit AOD). 5-19 Sept 2000, at 0900 UTC (SSA = 0.90)
Keil et al. (2003)	SSA = 0.93	SSA = 0.90	SSA = 0.85	7 Sept, 2000 [SAFARI]
	-13.3	-13.0	-12.1	
Ichoku et al. (2003)	-10			Sept 2000 [SAFARI] (SSA = 0.90)

Table 16: estimated clear-sky aerosol (fine plus coarse mode if not specified) SW direct radiative forcing at TOA over South-East Atlantic, from model simulations constrained by satellite data.

Clear-sky aerosol direct radiative forcing is a processes relatively easy to model, that mainly depends on aerosol optical thickness and single scattering albedo. There is, however, a wide range of the clear-sky aerosol direct radiative estimates, that show how model simulations result strongly affected by uncertainties in AOD and aerosol optical properties.

8.2.3 Cloudy-sky SW direct radiative forcing

Quantification of cloudy-sky DRF is more complicated. Beside an adequate description of aerosol absorption properties, which represent the largest contributor to clear-sky DRF uncertainty (McComiskey et al., 2008), it also requires information on cloud and aerosol vertical distribution.
A simple analytic expression, presented by Charlson et al. (1991, 1992) and modified to account for aerosol absorption by Haywood and Shine (1995) and Chylek et al. (1995), can be use in first approximation to describe the direct aerosol forcing at TOA, for cloudy-sky conditions. If aerosol optical depth is smaller than 1,

$$DRF = -S_0 T_{atm}^2 AOD\left[(1-\omega)^2 \beta\, SSA - 2\omega(1-SSA)\right] \qquad (62)$$

where S_0 is the solar constant (~1365 W/m²), T_{atm} is the transmittance of the atmosphere above the aerosol layer (due to Rayleigh scattering and absorption by ozone and other gases) and β the up-scatter fraction, which describes the averaged fraction of radiation scattered into the upper hemisphere, and ω is the albedo of the surface which is under the aerosol layer. Note that the first term in the brackets represents the negative forcing, hence the cooling effect due to up-scatter, while the second term is the positive forcing, hence the warming effect, due to aerosol absorption. The resulting DRF is positive or negative depending on the balance of these two terms. We can define as SSA_c (critical single scattering albedo) the minimum single scattering albedo value that leads to a positive DRF, and hence such that

$$(1-\omega)^2 \beta\, SSA - 2\,\omega\,(1-SSA) < 0 \tag{63}$$

that yields to

$$SSA_c = \frac{2\,\omega}{(1-\omega)^2 \beta + 2\,\omega} \tag{64}$$

For a SSA < SSA_c cloudy-sky direct radiative forcing is positive. To have an idea of the order of magnitude of the critical SSA to induce TOA warming, let consider an aerosol particle with radius of 0.48 μm (fine-mode) and single scaring albedo between 0.7 and 1. According to Nemesure and Wagener (1995), its up-scatter function varies between 0.5 and 0.05, as the cosine of solar zenith angle increase from 0 to 1. The SSA_c values are shown in Figure 62, as a function of surface albedo below aerosol layer.

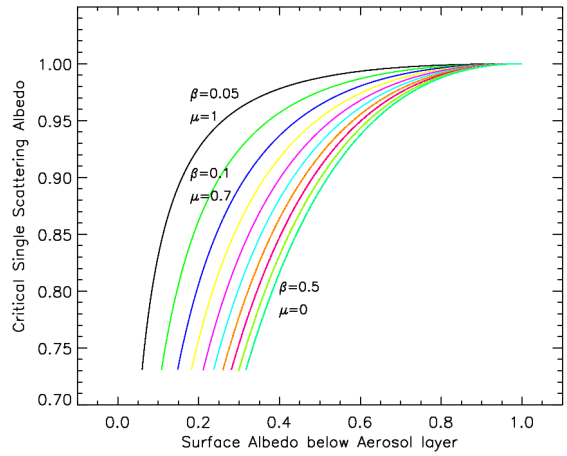

Figure 62: critical single scattering albedo as a function of the surface albedo below aerosol layer. Curves are computed from equation (64). Colors represent SSA_c calculated from up-scatter fraction (β) increasing from 0.05 (black) to 0.5 (green), by step of 0.05. β is estimated from Nemesure and Wagener (1995) and is representative of an aerosol of 0.48 μm of effective radius, SSA approximately between 0.7 and 1, for μ (cosine of solar zenith angle) varying from 0 (sunrise/sunset) to 1 (sun at zenith). SSA_c for β equal to 0.05, 0.1 and 0.5 (μ = 1, 0.7, 0) are reported in figure, next to relative curve.

Black curve represents the variation of SSA_c with increasing surface albedo, for μ = 1 (sun at zenith). The first green curve on the left represents same relationship, for μ = 0.7 (solar zenith angle of 45°) and the green curve on the right side for μ = 0 (sunrise/sunset).
Figure 62 shows that in case of μ = 0.7 and surface albedo of 0.2 (low reflective cloud), only a

SSA smaller than 0.86 (characteristic of highly absorbing, as biomass burning aerosol) will produce positive forcing. On the other hand, in case of highly reflective clouds (albedo of 0.6), critical SSA is much higher (0.97) and aerosol with a low absorption may lead to positive forcing.
According to Taylor et al. (1996), ocean albedo is parametrized as an inverse function of solar zenith angle

$$\omega(\mu)=\frac{0.037}{1.1\,\mu^{1.4}+0.15} \tag{65}$$

so that for μ = 1, 0.7, 0 it is equal to 0.03, 0.04 and 0.2. Resulting SSA_c is very small, always much smaller than the minimum value of the single scattering albedo (0.73) observed over this area. This means that the (low) ocean reflectance is not sufficient to produce positive forcing. We will see further that a positive cloudy-sky DRF is generally produced, over South-East Atlantic, by aerosol particles with SSA smaller than 0.91 above clouds with COT larger than 4.

8.2.4 All-sky SW direct radiative forcing

All-sky aerosol direct radiative forcing is then defined at the TOA as

$$DRF=\left(I_0^{clear}\uparrow-I_a^{clear}\uparrow\right)(1-CLF)+\left(I_0^{cloud}\uparrow-I_a^{cloud}\uparrow\right)CLF \tag{66}$$

where DRF represent the net irradiance in W/m² between upwelling irradiance computed with a given aerosol load (I_a), and without it (I_0), in case of cloudy and clear-sky, weighted by the respective cloud fraction (CLF) and clear-sky fraction (1-CLF).

Recent studies that account for positive forcing due to aerosol absorption are in good agreement with theory. On global scale Hatzianastassiou et al. (2007) find a DRF for SW radiation at TOA of -1.62 W/m², ranging between -15 and 10 W/m². During the month of September, Myhre et al. (2003) estimate a SW radiative impact over South-East Atlantic region that varies daily between -50 and 65 W/m², with the strongest negative impact in case of large AOD and clear-sky conditions and the strongest positive impact corresponding to high AOD over highly reflective clouds. Monthly averages show a DRF between -20 and 6.0 W/m². Chand et al. (2009) make use of CALIPSO vertical information of aerosol above cloud optical thickness over South-East Atlantic and find an all-sky DRF that varies locally from -2 to 14 W/m² (July-October 2006/2007).

	Global DRF over	Remarks

	South-Est Atlantic [W/m2]			
Sakaeda et al. (2011)	2.3			Forcing weighted by cloudy-sky fraction. Jul-Oct 2001-2008. **Carbonaceous aerosol**
Chand et al. (2009)	[-2, 14]			Jul-Oct 2006-2007 (SSA = 0.85)
Hatzianastassiou et al. (2007)	-1.62 [-15, 10]			Whole planet (ocean and land), Jan and Jul 1984-1993
Abel et al. (2005)	−3.1 [-13.1, 5.1]			Sept 2000 [SAFARI] **Fine aerosol**
Myhre et al. (2003)	-1.7 [-20, 6]			Sept 2000 [SAFARI] (SSA = 0.90)
	[-50, 65]			Instantaneous DRF. 5-19 Sept 2000, at 0900 UTC (SSA = 0.90)
Keil et al. (2003)	SSA = 0.93	SSA = 0.90	SSA = 0.85	7 Sept, 2000 [SAFARI]
	7.5	11.5	16.9	

Table 17: estimated all-sky aerosol (fine and coarse mode if not specified) SW direct radiative forcing at TOA over South-East Atlantic, from model simulations constrained by satellite data.

8.3 A new quantification of aerosol DRF

8.3.1 Method

In the effort to improve regional estimates of DRF, particular care is taken to minimize uncertainties on single scattering albedo and aerosol vertical position with respect to cloud field, probably two of the main error sources affecting DRF calculations. The use of a constant value of SSA (equal to that of biomass burning) for the region, as in many previous studies, implies a strong underestimations of radiative forcing, in case other aerosol particles dominate aerosol type. This condition often occurs over South-East Atlantic, especially during Jan-Mar over the Gulf of Guinea and in general over deep ocean West and South the coast of Namibia (Chapter 3). An incorrect quantification of absorption properties of aerosol mixture of biomass burning with highly reflective dust may largely affect radiative transfer calculations. Geographical and temporal variations of SSA are then parametrized as a function of aerosol Angstrom exponent, retrieved by MODIS instrument, to account for the different particle types, characterizing the study area during the whole year.

Time-dependent statistics of aerosol position with respect to cloud field (more than exact aerosol vertical profile, which is supposed to be of secondary importance in DRF calculations) are obtained analyzing 5 years of data from CALIPSO cloud and aerosol products, to account

for AOD fraction coming from layer above, under or within the observed cloud fields.

Radiative calculations are performed by means of the Rapid Radiative Transfer Model ShortWave (RRTM_SW), accessible from http://rtweb.aer.com/rrtm_frame.html. It makes use of the DIScrete Ordinate Radiative Transfer (DISORT) integration of the radiative transfer equation (Stamnes et al., 1988). Calculations are made with four streams in the wavelength range 820-50000 cm^{-1}. Cloud parameters (liquid water path, cloud fraction, droplet effective radius, cloud top pressure) and aerosol optical properties, (aerosol optical depth, Angstrom exponent, asymmetry parameter) are provided by monthly mean of MODIS daily product. SSA (at 0.55 μm) is calculated according to the results of the following experiments

1) DABEX (Dust and Biomass-burning Experiment) by Johnson et al. (2008): mean SSA for biomass burning is found to be equal to 0.81±0.08, ranging between 0.73 and 0.93, depending on the mixing with mineral dust, with little variation with aerosol age (chemical transformation of organic carbon do not significantly affect absorption properties). Osborn et al. (2008) find that mineral dust is almost non absorbing with a mean SSA of 0.99±0.01.

2) DODO (Dust Overflow and Deposition to the Ocean) by McConnel (2008): SSA of mineral dust particles in strong dust plumes is found to decrease from 0.98 to 0.90 upon inclusion of the coarse mode.

3) AERONET retrievals by Dubovik et al. (2002): SSA of oceanic aerosol is found to be equal or larger than 0.97.

Accounting for these estimate, we parametrize SSA as a function of Angstrom exponent (ANG),

$$\begin{aligned} SSA &= 1 - 0.18 \times ANG \qquad if\ ANG \le 1.5 \\ SSA &= 0.73 \qquad if\ ANG > 1.5 \end{aligned} \tag{67}$$

Single scattering albedo varies between 1 and 0.73 as Angstrom exponent varies between 0 and 1.5. Aerosol from biomass burning has an ANG generally between 1 and 1.5, which leads to a SSA between 0.82 and 0.73, in good agreement with Johnson et al. (2008). Mineral dust, with Angstrom exponent between 0 and 0.2, has a SSA between 1 and 0.96, in agreement with Osborn et al. (2008). When ANG = 0.6 (denoting a probable mixing of BB and mineral dust), SSA is equal to 0.90.

Mineral dust and biomass burning absorption properties seem to be well described by equation (67). Resulting radiative forcing calculations are then supposed to be more accurate and reliable than those obtained by using a single SSA value for the entire region (Keil et al. (2003), SSA = 0.85, 0.90 and 0.93, Myhre et al. (2003), SSA = 0.90; Ichoku et al. (2003), SSA = 0.90, Chand et al. (2009), SSA = 0.85).

Information on vertical distribution of aerosol and cloud layers is provided by CALIPSO.

Statistics of aerosol layer position with respect to cloud field (i.e. above, under or at the same level) are computed, from data covering the entire time period from June 2006 to December 2010. Seasonal maps at 1 degree resolution are produced, describing the probability (from 0 to 1) within each grid box that a given aerosol layer is respectively mixed, unmixed and above, unmixed and under the cloud layer. Cloud-aerosol distance threshold is 100 m, meaning that aerosol and cloud layers closer than 100 m are considered mixed (unmixed otherwise). Maps (Figure 63) are calculated for four different time-periods (Jan-Mar, Apr-Jun, Jul-Sept, Oct-Dec), to account for seasonal variability of local meteorology, but are the same each year.

Monthly means of MODIS vertically integrated aerosol optical depth are then weighed by the frequency of occurrence (from 0 to 1) of each case (mixed, unmixed above, unmixed under).

The model makes use of a standard tropical atmosphere composed of 40 vertical levels. TOA is set at 50 km. Vertical resolution is 200 m from 0 to 5 km, 500 m from 5 to 10 km, 5 km from 10 to 20 km and 15 km from 20 to 50 km. Cloud field altitude is defined by MODIS cloud top pressure, while cloud thickness is equal to the vertical width of the correspondent level. The portion of AOD relative to a mixed layer (total AOD retrieved by MODIS multiplied by the frequency of occurrence of mixed case) is supposed to be homogeneously distributed within the same layer of the cloud. If aerosol and cloud are separated, the two adjacent atmospheric layers above or under cloud level are left empty and the relative AOD is then considered homogeneously distributed within the following layer, above or under the cloud, depending on the unmixed case.

If the mutual vertical position of aerosol and cloud is supposed to be a fundamental parameter to quantify with accuracy aerosol forcing over South-East Atlantic, errors in the absolute cloud (and hence aerosol) layer altitude (due to MODIS CTP estimate biases) are not expected to sensibly affect radiative forcing estimate at shortwave.

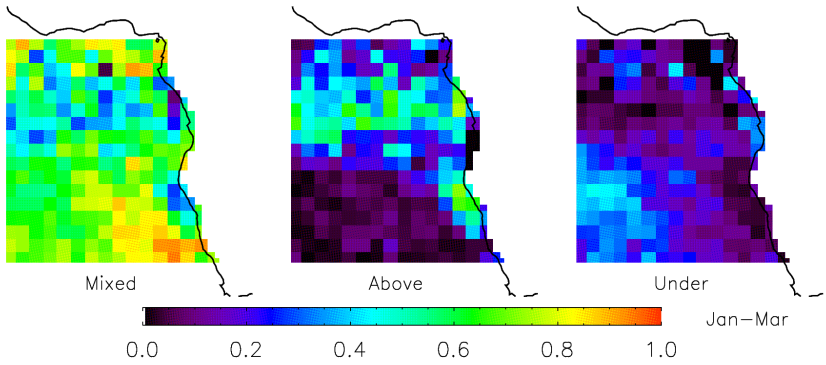

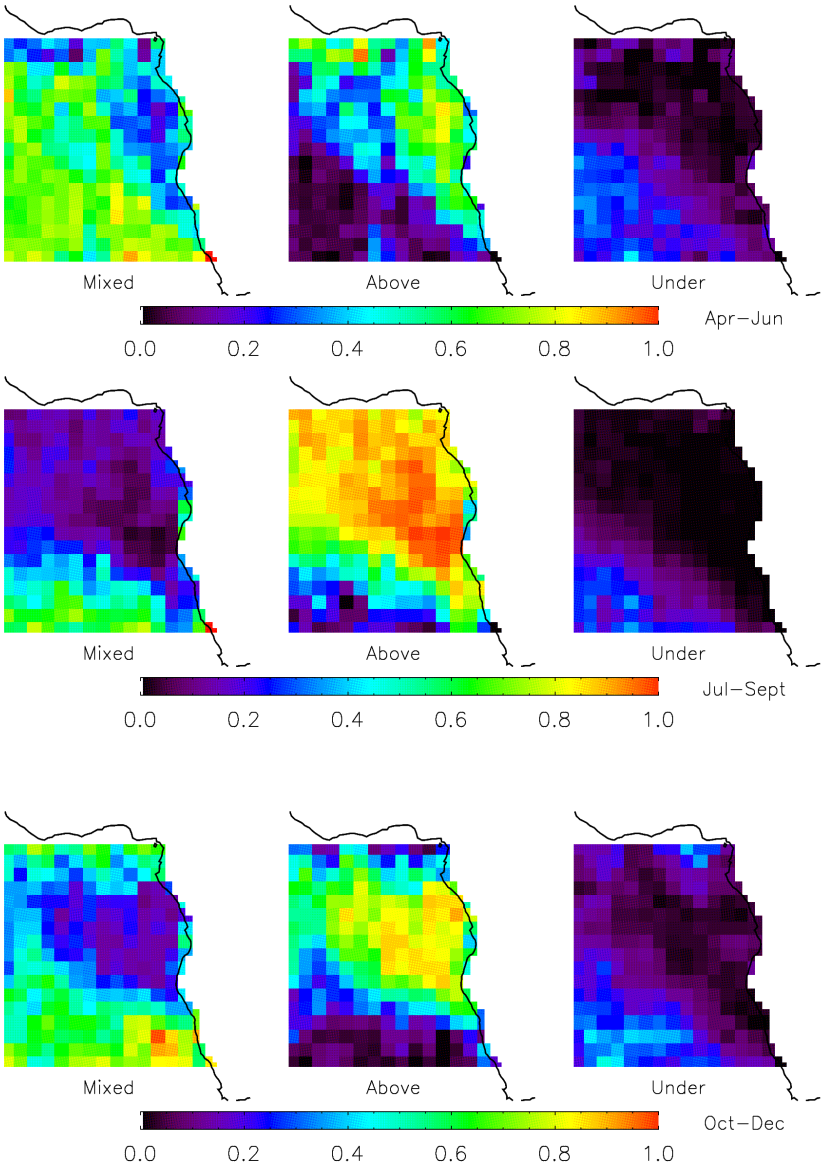

Figure 63: frequency of occurrence, from 0 and 1, of cases with aerosol layers mixed, unmixed above and unmixed under cloud layer, for the four time-periods of Jan-Mar (60572 measurements), Apr-Jun (88800), Jul-Sept (99240), Oct-Dec (82376). Data are obtained analyzing CALIPSO aerosol and cloud layer altitudes, from June 2006 and December 2010.

Figure 63 shows that during the biomass burning season of South Africa (July-August-September), characterized by the presence of absorbing smoke particles, aerosol is mostly located above cloud top (60-100% of cases). Off the coast of Angola, aerosol remains above cloud also during Oct-Dec (60-90% of cases), while the southern and northern part of the area are characterized by cloud-aerosol mixing. Mixed condition is prevalent (60-90% of cases) almost all over the area of interest in Jan-Mar. If we consider the whole dataset (970900

retrievals) cases of cloud-aerosol mixing represent the 34% (330988), cases of aerosol above cloud top the 58% (564288) and cases of aerosol below cloud base the 8% (75624).

Geographical and temporal occurrence of mixed cases, coincident with the most elevated values of Angstrom exponent, seems to suggest that they are mainly characterized by biomass burning particle, arranging conditions for strong positive radiative forcing and atmospheric warming in Jul-Sept and, more moderately, during Oct-Dec and Apr-Jun.

A fundamental parameter that governs radiative forcing is the average of the cosine of solar zenithal angle. It is estimated for each grid box averaging the daytime cosine zenithal angle (μ) calculated for every minute. Ocean surface albedo is parametrized as a function of μ, according to equation (65) and the resulting mean value of daily ω(μ) is used as model input.

8.3.2 Clear-sky DRF

Clear-sky aerosol (natural plus anthropogenic) direct radiative forcing assuming entirely clear grid boxes is defined as

$$DRF = \left(I_0^{clear} \uparrow - I_a^{clear} \uparrow \right) \tag{68}$$

and calculated for each 1×1 grid box (Figure 64), for the four time-periods of 2005. Results can be compared with previous clear-sky forcing estimates, resumed in Table 16. Under each image, the mean DRF is reported together with seasonal minimum and maximum values reached locally.

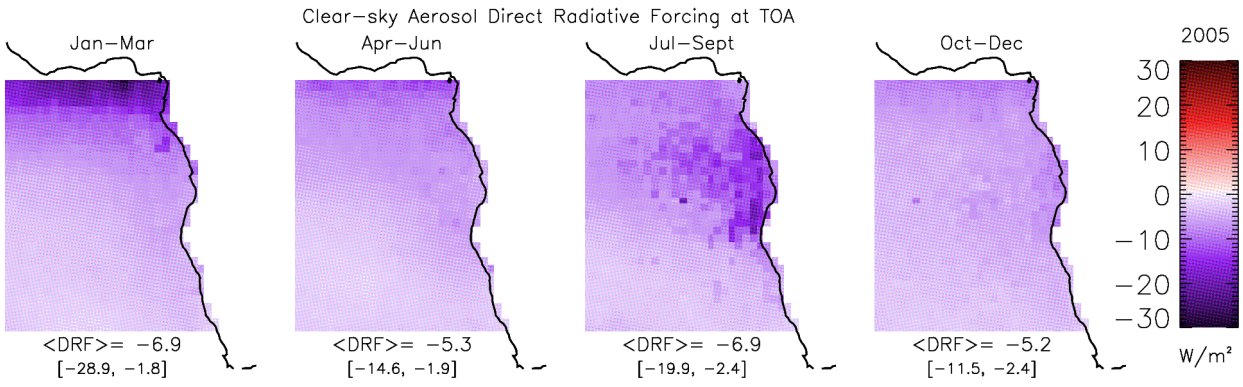

Figure 64: aerosol shortwave DRF in case of clear-sky at TOA, assuming entirely clear grid boxes, for the four time periods. Under each map, the spatial mean DRF estimate is reported

together with its local minimum and maximum value, within a 1×1 degree grid box.

As expected, DRF is always negative, since the albedo of the underlying surface is low (ocean). Seasonal and spatial averages of DRF range between -6.9 W/m² (Jan-Mar and Jul-Sept) and -5.2 W/m² (Oct-Dec). These values are approximately half of those calculated by Chen et al. (2008), from CERES and MODIS observations, over a similar region of South-East Atlantic and for similar AOD retrievals (anthropogenic+natural aerosol).

Previous studies, however, do not generally provide seasonal estimates of DRF. However several works make use of data collected during the SAFARI experiment a large campaign in Southern Africa during August and September, 2000. This field experiment has been one of the first study to provide aerosol and cloud vertical positions, from data acquired principally during two flights of a C-130 aircraft. Between those who analyzed SAFARI aerosol observations to provide DRF estimates, Keil et al. (2003), Myhre et al. (2003) and Ichoku et al. (2003) used fixed values of single scattering albedo, while more recent works (Abel et al. 2005) simulate SSA from direct measurements of the aerosol scattering and absorption properties.

If we look at the single month of September 2000, DRF is about -7.9 W/m², in very good agreement with Abel et al. (2005). They find a clear-sky biomass burning DRF of -7.6 W/m², using a general circulation model combined with aircraft retrievals and measurements from MODIS and AERONET. Since, during September biomass burning is the dominant aerosol particle type, not significant differences are expected for DRF calculation of total aerosol (natural plus anthropogenic) and biomass burning only.

Over a similar region, Myhre et al. (2003) and Ichoku et al. (2003) find two clear-sky DRF for September 2000, equal to -4.3 and -10 W/m². This is in agreement, to a certain extent, with present estimate of -7.9 W/m² (which falls in the middle between the two). The two estimates are very different to one another and this results probably from the fact that, as aerosol distribution is sensibly heterogeneous, the effective limits of analyzed regions may strongly affect DRF averages.

Clear-sky DRF shows little seasonal variability (Figure 64). The spatial mean of DRF during Jan-Mar (AOD = 0.22) and Jul-Sept (AOD = 0.37) over the whole region is equal to -6.9 W/m² in both cases, even if aerosol load increases by about 70% from one season to another. This is because during Jan-Mar, aerosol type is governed by a mix of desert dust and biomass burning particles, and the seasonal ANG average is 0.56 (Chapter 3). During Jul-Sept, biomass burning particle concentration is much larger and mean Angstrom exponent increases up to 0.87. This value is rather small, since the large spatial average includes many cases with low aerosol loads and low Angstrom coefficient. However, according to equation (67), the observed increase in Angstrom coefficient from Jan-Marc to Jul-Sept results in an overall decrease in aerosol single scattering albedo of about 6%. This rudely indicates that the radiative impact of a few percent

variation in aerosol reflectance (reflecting changes in aerosol chemical and physical composition) is comparable to that induced by an aerosol load variation one order percent larger.

During Apr-Jun and Oct-Dec, when AOD = 0.19 in both cases and ANG = 0.69, 0.71, the mean DRF for the whole region results equal to -5.3 and -5.2 W/m², respectively.

8.3.3 All-sky DRF

According to equation (66), all-sky aerosol direct radiative forcing is estimated as the sum of the clear-sky DRF fraction (weighted by clear sky fraction) plus the cloudy-sky DRF fraction (weighted by cloud cover).

Seasonally averaged maps of clear-sky and cloudy-sky DRF, as well as the resulting all-sky estimate are shown in Figure 65. Maps of cloud cover, aerosol optical depth and Angstrom exponent (described in Chapter 3) are also reported (Figure 66), to stress the strong correlation between aerosol, cloud properties and TOA forcing.

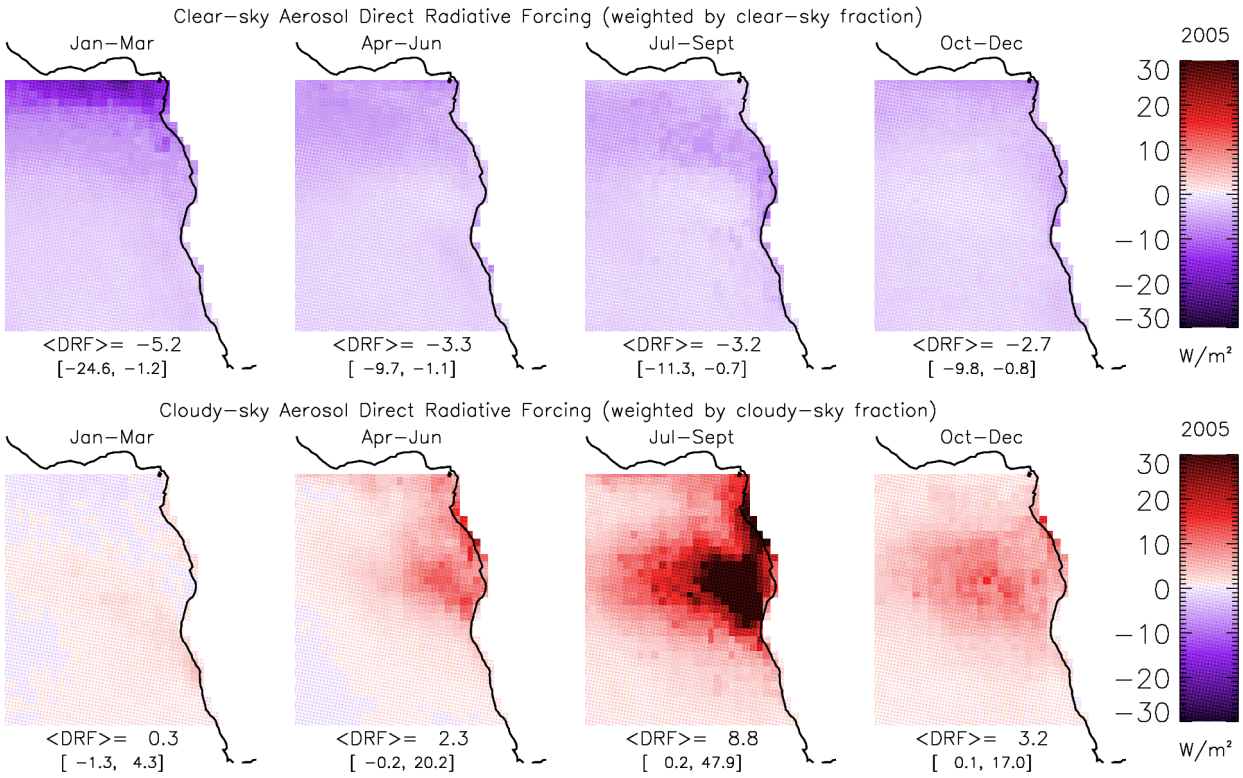

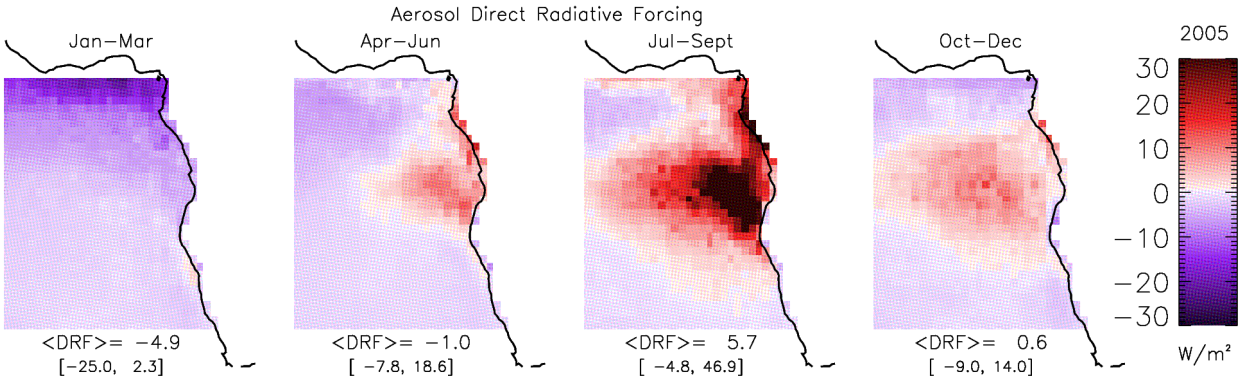

Figure 65: shortwave clear-sky DRF, weighted by clear-sky fraction (top image), cloudy-sky DRF, weighted by cloud fraction (middle image), all-sky DRF (bottom image) at TOA, with the RRTM_SW radiative transfer model, for 2005. Under each map, the spatial mean estimate of each parameter is reported together with its maximum and minimum local values, within a 1×1 degree grid box.

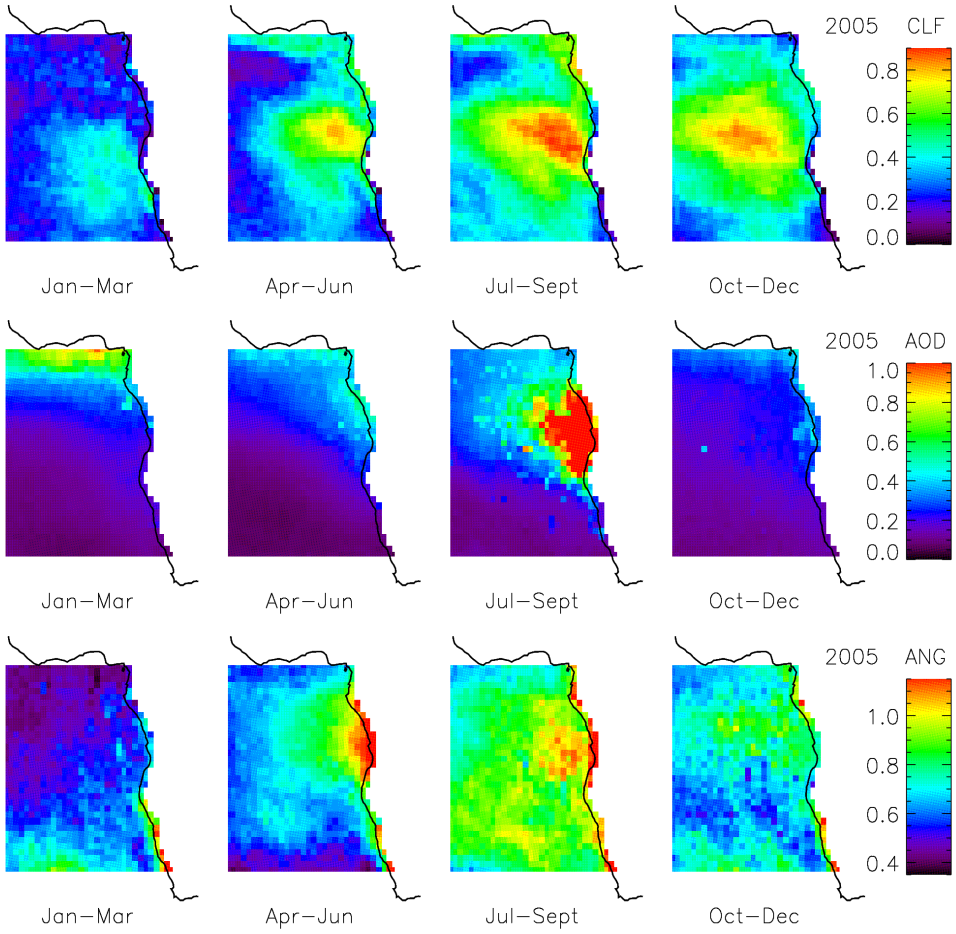

Figure 66:maps of cloud fraction, aerosol optical depth and Angstrom exponent from MODIS daily product, for 2005.

During Jan-Mar time-period, clear-sky radiative forcing weighted by the clear-sky fraction is always negative and equal in average to -5.2 W/m², while locally TOA forcing may reach -24.6 W/m² (over the Gulf of Guinea, in correspondence largest values of AOD and ANG). In the same period, cloudy-sky forcing (weighted by cloud fraction) is moderately low (0.3 W/m²), ranging between -1.3 and 4.3 W/m². During that season, presence of very low absorbing aerosol particles, generally mixed with cloud field (not above), may lead to very small negative values of cloudy-sky DRF. Resulting all-sky aerosol forcing at TOA is -4.9 W/m² (Figure 65). This indicates that clouds work in the direction of mitigate aerosol negative forcing, which is decreased by 2 W/m² from clear-sky (DRF = -6.9 W/m²) to all-sky case, characterized by a mean fraction cloud coverage of 0.26 (DRF = -4.9 W/m²).

During Apr-Jun, cloud fraction is larger than previous trimester and AOD and ANG values off the coast of Namibia (where mixed cases of cloud and aerosol layers frequently occur) are larger. These conditions are favorable for an increase of cloudy-sky forcing and a decrease of clear-sky one, to result in a all-sky DRF still negative but much smaller, in magnitude, than before (-1.0). An average fractional cloud cover of 0.36 increases aerosol DRF, from the case of completely clear-sky, of about 4.3 W/m² (from -5.3 to -1.0 W/m²).

Starting from June, the presence of high absorbing aerosol (ANG $\geq$ 1) generally above clouds (60%-100% of cases) and extended cloud fields (CLF varies mostly between 0.4 and 0.9) allows large positive cloudy-sky (weighted by the cloud cover) forcing, with spatial average of 8.8 W/m². Clear-sky DRF (-6.9 W/m²) is increased by 12.6 W/m² (all-sky forcing is positive and equal to 5.7 W/m², with local peak up to 46.9 W/m²) as a consequence of cloud field (average CLF of 0.49) introduction in radiative calculation.

During Oct-Dec aerosol load, as well as the Angstrom exponent, decreases substantially, back to typical values observed during Apr-Jun. However, highest occurrence of unmixed cases (with aerosol layers above cloud deck) together with a larger cloud fraction, with respect to Apr-Jun, leads to a small but positive all-sky DRF effect of 0.6 W/m²(instead of a negative one). This result show how relative position of aerosol and clouds, and hence meteorological conditions that dominate each time-period and determine aerosol and cloud vertical distribution, plays a critical role in atmospheric energy balance. Moderately different vertical positions of aerosol and cloud layers can lead to direct aerosol forcing estimates of opposite signs.

During Oct-Dec, the introduction of an average fractional cloud field of about 0.48 increases aerosol DRF of 5.8 W/m², from -5.2 W/m² of clear sky case to 0.6 W/m² for all-sky case.

When comparing these results with all-sky DRF estimates of Table 17, we should remind that several previous studies only consider the fine-mode fraction of total AOD (from

anthropogenic, or carbonaceous, aerosol), while present analysis aims to quantify radiative forcing of all (fine and coarse, natural and anthropogenic) species. This necessary leads to a first difference between our results and those reported in Table 17, since aerosol forcing is firstly a function of AOD. Such a difference is probably larger than that observed when comparing clear-sky estimates, since the inclusion of cloud field in radiative transfer calculation results in stronger sensitivity of TOA forcing to aerosol optical properties (as multiple scattering processes between aerosol and clouds are involved).

This consideration can (at least) partly explain the large discrepancy with result of Abel et al. (2005), that find a clear-sky forcing in very good agreement with our estimation, but a negative spatially average all-sky fine aerosol forcing of -3.1 W/m² (September 2000), while we obtain a positive average of 9.4±0.8 W/m², for September 2005-2010.

Myhre et al (2003), accounting for AOD from all aerosol species (September 2000) with a fixed SSA of 0.90, also find a negative aerosol forcing of -1.7 W/m², even if smaller than Abel et al. (2005). While Keil et al. (2003) observe very strong all-sky forcing than increase from 7.5 to 16.9 W/m² (for total AOD) as the SSA (fixed for the whole area in each simulation) decreases from 0.93 to 0.85. Their results are particularly coherent with forcing modeled inhere (9.4±0.8 W/m²), characterized by a SSA that varies between 1.0 and 0.75. However, aerosol retrievals of Keil et al. (2003) are based on aerosol measurements made on a single day (7 September, 2000), which may not be representative of entire month.

As previously stressed, a large source of uncertainty, when modeling all-sky forcing, is the vertical profile of cloud and aerosol layers, that may largely affect the sign and magnitude of TOA radiation budget. It is not surprising that we find large differences with those studies that use limited information on daily variations of cloud and aerosol layer position (as the two days aircraft campaigns, in case of SAFARI experiment), which is not generally provided by satellite (e.g. MODIS and CERES) and ground-based instruments (e.g. AERONET).

CALIPSO Lidar information may be fundamental to assess aerosol direct (and indirect) forcing, as suggested by recent works of Chand et al. (2009) and Sakaeda et al. (2011). To detect aerosol in elevated layers above clouds, they apply the method developed by Chand et al. (2008), which differs from our method in assuming that aerosol layers detected along CALIPSO orbit are fully representative of aerosol position within a 5×5 degree grid box (while we average all CALIPSO observations within a 1×1 grid box, retrieved for each season from 2005 to 2010). Uncertainties coming from both assumptions have not yet been tested and may lead to different errors in DRF estimates.

Chand et al. (2009) do not provide a regional mean of all-sky DRF. However, estimated forcing varies locally between -2 and 14 W/m² during Jul-Oct 2006-2007 time period, coherent but much smaller than present calculations (not shown in figure), where all-sky DRF is 6.4 W/m² (Jul-Oct 2006) in the [-5.3, 55.1] W/m² range and 7.2 W/m² (Jul-Oct 2007) in the [-6.7, 56.9] W/m² range.

The discrepancy with Chand et al. (2009) may be a consequence of considering AOD from

aerosol layers above cloud top only (instead of vertically integrated measurements) and hence an overall optical thickness which is reduced with respect to that used in present simulations, that results in weaker aerosol forcing. Even though aerosol contributes to the major fraction of DRF when lying above cloud top, positive forcing is also observed when particles are located within the cloud layer. Neglecting contribution of mixed layers lead to substantial underestimation of aerosol cloudy-sky DRF, and hence the all-sky value. In addiction, CALIPSO aerosol optical is generally much smaller than that retrieved by MODIS (Chapter 6) and its use may result in a further weakening of aerosol TOA forcing. Finally, Chand et al. (2009) do not consider geographical and temporal variations of aerosol chemical composition. SSA and asymmetry parameter are kept constant all over the study region (equal to 0.85 and at 0.62, respectively), in contrast with our analysis where both vary over time and space. This primary means that cases of high negative forcing due to largely reflecting aerosol, as well as cases of high positive forcing due to largely absorbing aerosol above optically thick clouds, are neglected.

Sakaeda et al. (2011) calculate the monthly and spatially averaged all-sky forcing of carbonaceous aerosol alone (over South-East Atlantic) and find a mean average value for the July-October 2001-2008, equal to 1.2 W/m². This is about six times lower than that calculated in the present work for July-October 2005-2010, of 6.8 W/m². In they simulations, aerosol load is obtained from CALIPSO, while the fine-mode fraction from MODIS monthly product, at 5 degree resolution. We have shown in Chapter 6 that CALIPSO may largely underestimate AOD, with respect to MODIS retrievals. The smaller DRF value found by Sakaeda et al. (2011) may be a consequence of using CALIPSO instead of MODIS aerosol product.

Figure 68 shows all-sky direct radiative forcing estimates for 2006-2010, which exhibit a strong and well defined annual cycle, similar to that of 2005, characterized by limited inter-annual variability with respect to seasonal variations (Table 18). Especially during the biomass burning season but also during Jan-Mar, large spatial standard deviations show a strong geographical variability of DRF, similar in all of observed years.

DRF [W/m²]	Jan Feb Mar	Apr May Jun	Jul Aug Sept	Oct Nov Dec
2005	-4.88±4.71	-0.96±3.49	5.67±9.66	0.55±3.56
2006	-3.73±3.24	-2.60±1.68	5.42±10.36	0.48±3.11
2007	-4.64±5.39	-2.19±1.43	6.12±11.12	0.34±3.08
2008	-4.55±4.83	-2.61±1.86	5.07±10.46	1.00±4.02
2009	-3.98±3.52	-2.07±1.81	5.94±10.36	0.27±2.78
2010	-3.89±3.90	-1.91±2.48	5.70±10.79	0.88±4.14
Average	-4.28±4.26	-2.06 ±2.12	5.65±10.46	0.59±3.45

Table 18: seasonally averaged aerosol DRF over ocean, within [4N, -30N; -14E, 18E], from 2005 to 2010. In the last row, we report the six-year average and standard deviation of spatial

mean DRF estimate, for each season.

Considering the full data time window from 2005 to 2010, it is possible to quantify the overall average all-sky direct aerosol TOA forcing, over the South-East Atlantic region, and analyze the clear-sky and cloudy-sky components separately.

The clear-sky DRF, weighted by clear sky fraction, has a global mean value of -3.42 W/m² with a spatial standard deviation of 2.81 W/m², indicating that clear-sky forcing, which depends only on aerosol load, is relatively homogeneous. The cloudy-sky fraction of DRF is in turn positive, with a mean value of 3.39 W/m², very similar in magnitude to clear-sky estimation. However the spatial standard deviation is 7.41 W/m², showing how cloud cover strongly modulate aerosol forcing, that results much variable in cloudy-sky than clear-sky conditions.

If we neglect aerosol layers above and under clouds and perform radiative calculation only considering the mixed AOD fraction, cloudy-sky DRF weighted by cloudy-sky fraction is equal to 0.49 W/m². The presence of aerosol above cloud is not a necessary condition to positive forcing, it can be sufficient that aerosol and cloud layers are at same altitude. Mixed cloud-aerosol layers contribute up to 15% of total cloudy-sky positive DRF. In contrast with some previous study, we stresses the importance of a good parametrization of vertical distribution of whole aerosol field, since accounting for the AOD fraction above cloud top only, there is a substantial sub-estimation of cloudy-sky DRF. The six year averaged of monthly mean of daily all-sky DRF over South-East Atlantic is negative, equal to -0.03 W/m², sign that overall mean aerosol effect results in a small radiative cooling at the top of the atmosphere. This result indicates that the net regional mean balance of DRF is almost zero, during 2005-2010. The all-sky DRF spatial standard deviation is particularly high, equal to 8.14 W/m², sign that locally (with a 1°×1° grid box) monthly averaged daily aerosol radiative impact can be significantly strong.

If we give less weight to the dramatically large negative and positive DRF values, due to the extreme characteristic of aerosol and cloud fields over the area of interest, and substitute the mean by the median daily forcing, all-sky DRF decreases up to -1.50 W/m².

Assuming completely cloud-free grid box, the mean value of clear-sky DRF results equal to -4.50 W/m² while the median to -5.72 W/m², similar to global satellite-based DRF estimates for natural+anthropogenic aerosols over ocean of -5.5 W/m² (Yu et al., 2006) and -5.0 W/m² (Chen et al., 2008), for model simulations constrained by satellite measurements.

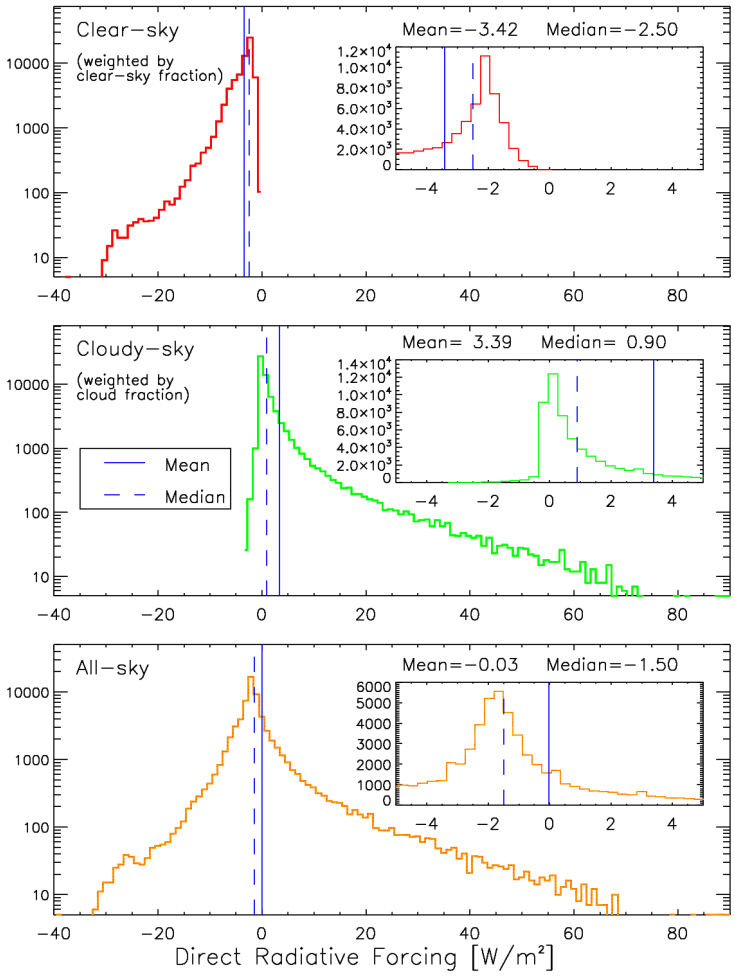

Figure 67: histograms of 1°×1° model estimates of clear-sky fraction (top image), cloud-sky fraction (middle image) and all-sky aerosol direct forcing (bottom image) for the whole 2005-2010 time period, over South-East Atlantic. Y-axis is in logarithmic scale. Within each image, inner figure represents a zoom within the [-5, 5] W/m² range (y-axis in linear scale). Mean (solid line) and median (dashed) values are reported.

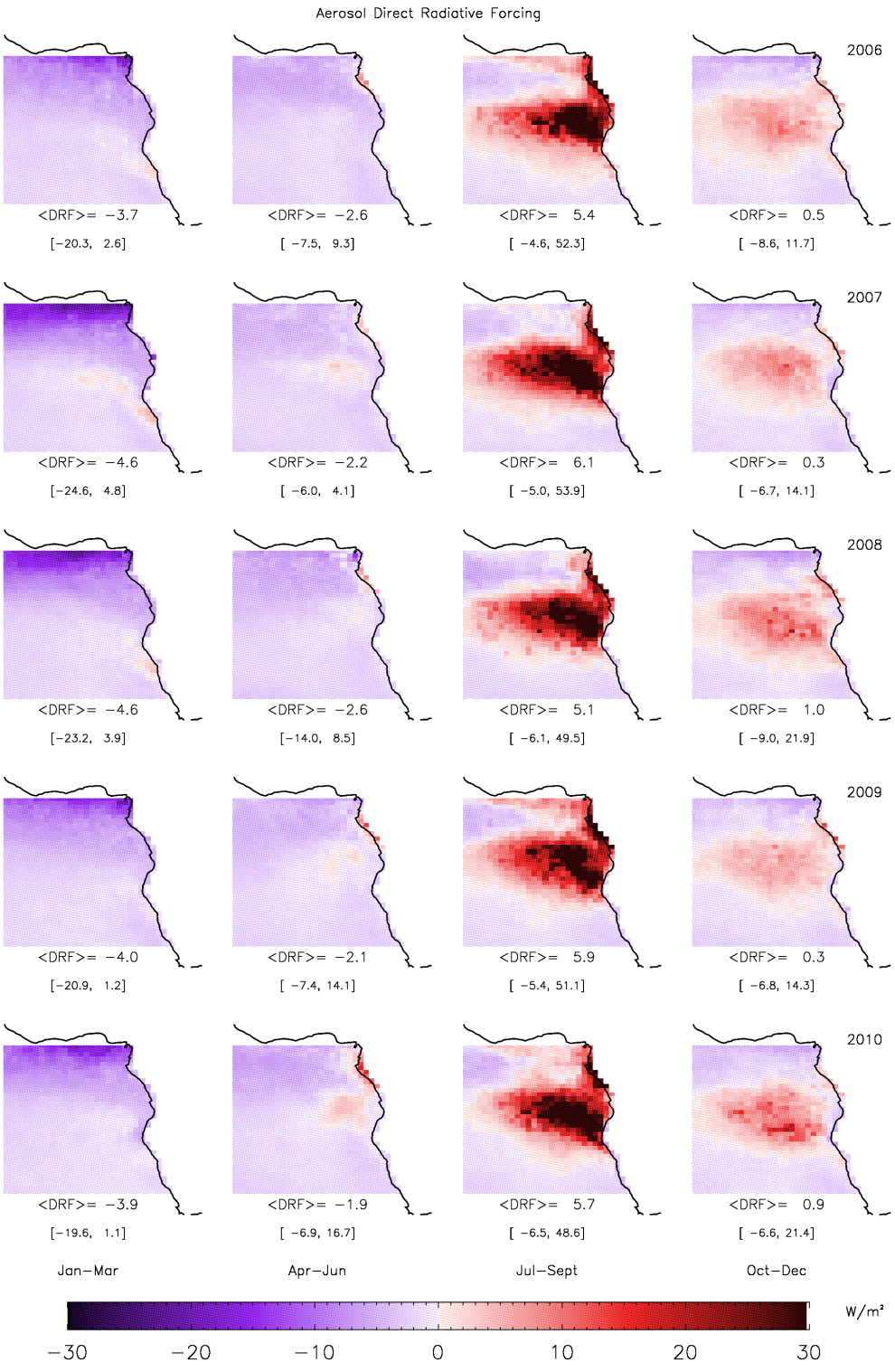

Figure 68: shortwave all-sky DRF at TOA, for 2006-2010. Spatial mean estimates of each time period are reported below the correspondent map, together with maximum and minimum local values, within a 1°×1° grid box.

8.3.4 Role of cloud fraction in all-sky DRF

As suggested by the large standard deviation of cloudy-sky DRF, and observing the all-sky DRF in Figure 65 together with cloud fraction maps of Figure 66, it is obvious that the extension of cloud field largely modulates the aerosol impact. The role of clouds is clearly demonstrated by examination of all-sky radiative forcing efficiency, DRE (i.e. DRF per unit of AOD) as a function of cloud cover. Figure 69 shows values of calculated all-sky radiative efficiency values averaged over constant bin (0.2) of cloud fraction.

There is a strong correlation between the increase of cloud coverage over the South-East Atlantic and the change in sign of aerosol forcing. DRE increase from mean values of about -50 W/m², in case of clear-sky, to very high positive values for overcast conditions, up to 100 W/m². All aerosol species are included in the statistics, as well as all aerosol layers position with respect to cloud field (mixed, under or above).

It is possible to identify a critical cloud fraction for which DRE changes sign. Previous estimates find values between 0.4 and 0.5 (Chan et al., 2009; Sakaeda et al., 2011). In particular, Chan et al. (2009) find a clear linear relationship between aerosol DRE and CLF, with a critical CLF of 0.4 for a constant regional SSA of 0.85±0.02. In the attempt to provide a more general relationship between CLF, DRE and the total amount of aerosol present in the atmosphere, we consider all aerosol species (0 < ANG < 1.5) at every position with respect to cloud layer (under, mixed and above).

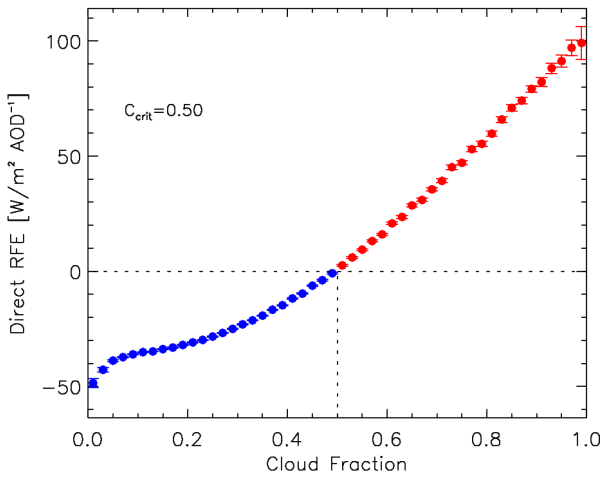

Figure 69: DRE at TOA as a function of cloud fraction. C_{crit} is the critical cloud fraction for which DRE at the top of the atmosphere changes sign. Red and blue indicate respectively positive and negative TOA warming.

Resulting CLF-DRE relationship (Figure 69) shows that cloud fraction above the critical value of 0.5 induce are associated with a positive TOA warming. Even if it is not linear, as obtained in case of elevated aerosol layers by Chan et al. (2009), such relationship shows that cloud fraction may be a good predictor of mean aerosol radiative efficiency. In addiction, critical CLF increases with increasing aerosol reflectance. For instance, if dataset is sorted by SSA, within the intervals [0.80, 0.82], [0.84, 0.86] and [0.88, 0.90], CLF_{crt} results equal to 0.36, 0.44 and 0.56, respectively.

8.3.5 Cloudy-sky aerosol DRF dependence on SSA and COT

It is interesting to consider the case of aerosol above cloud and account only for the cloudy-sky radiative forcing, weighted by the cloud fraction (i.e. the radiative forcing approximately due to the aerosol fraction geometrically above cloud). Histograms of SSA and cloud optical thickness in case of positive and negative forcing allow to analyze the dependence of the sign of cloudy-sky DRF, described analytically by equation (63).

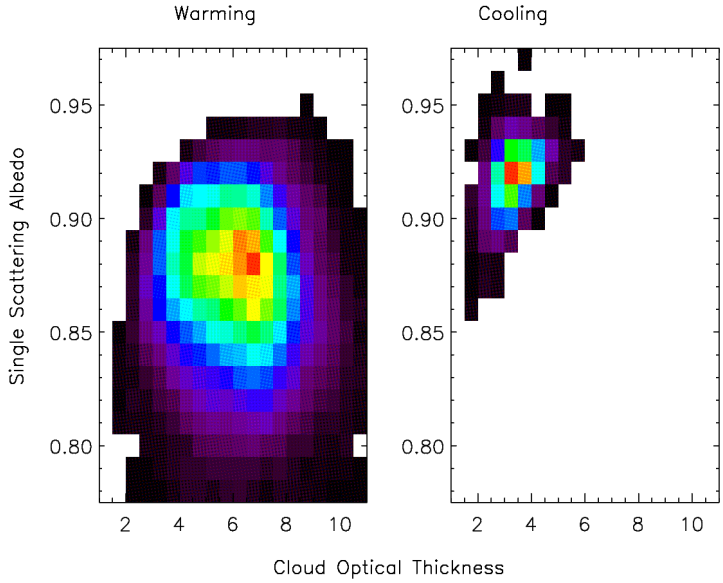

Figure 70: number concentration of SSA and COT retrievals, from MODIS daily product. The color scale represent arbitrary units, proportional to the number of points in a box of $\Delta SSA = 0.01$ and $\Delta COT = 0.5$.

Figure 70 shows cases of warming (DRF > 0) and cooling (DRF < 0) effect of aerosol situated above cloud deck. Color scale represents arbitrary units, proportional to the number of points within each bin (black/blue indicates few measurements, yellow/red indicates numerous measurements). For a total of 53549 points, great majority of cases (96%) shows positive forcing, mostly characterized by particles with SSA< 0.91 and clouds with COT > 4 (with typical SSA and COT values of about 0.88 and 7.0). As for critical cloud fraction, SSA = 0.90 and COT = 4 can be used as threshold values to predict the sign of DRF over ocean, at least for regions within [4N, -30N] (since radiative forcing is supposed to be primary dependent on zenith angle, which is a function of latitude only). On the other hand, negative forcing needs the presence of more reflecting aerosol particles, with SSA > 0.91, and optically thin clouds with COT < 4.

8.4 Aerosol Indirect Radiative Forcing

The ultimate goal of this work is to provide one of the first estimates of the radiative impact of the indirect effect of aerosol on cloud, based on observations. The aerosol-induced effect on cloud droplet size, optical thickness, liquid water path and cloud fraction is expected to have a non negligible effect on the Earth's radiative balance. A small increase in cloud reflection (as a consequence of Twomey's effect) and/or cloud fraction (as a consequence of life-time effect) increase the portion of solar radiation reflected to space, this can produce a net negative forcing at the top of the atmosphere. On the other hand, if cloud response to aerosol invigoration results in an overall decrease in cloud albedo and cloud cover and a net positive TOA forcing can be produced. However, radiative effects of changes in cloud microphysics resulting in cloud brightening may strongly depends on aerosol type, absorption properties and vertical position and can be balanced by changes in cloud cover. The forcing due to aerosol-induced variations of cloud radiative properties is called aerosol Indirect Radiative Forcing (IRF) and adds to the forcing produced by direct interaction of aerosol particles with sunlight.

Observational estimates of aerosol indirect radiative forcing are still in their infancy. Aerosol impact on shortwave radiative fluxes at TOA is often dived in the terms, the component due to aerosol-induced changes in cloud reflectance and in cloud lifetime. Two of the first studies of IRF (Nakajima et al., 2001; Sekiguchi et al. 2003), that used satellite based correlation between aerosol concentration and cloud microphysics and reflectance, estimate an indirect cloud albedo forcing ranging between -1.7 and 0.7 W/m² and -1.2 and -0.7 W/m², on global scale. Using several GCM estimates, Lohmann and Feichter (2005) find a cloud albedo indirect effect between -1.9 and -0.5 W/m², and a life-time indirect effect of similar magnitude, between -1.4 and -0.3 W/m². In its last assessment report, the IPCC quantified IFR due to cloud albedo equal

to -0.7, between -1.8 and -0.3 W/m² (Foster et al., 2007). More recent studies, constraining model simulation with satellite based observations, suggest that IPCC may overestimate the magnitude of indirect effect and quantify total aerosol indirect effect in -0.3 W/m² (Quaas et al., 2006), cloud albedo effect in -0.2 W/m² (ranging between -0.5 and -0.2 W/m² over the South-East Atlantic, Quaas et al. 2008) and total aerosol forcing in -1.2±0.4 W/m² and -2.3±0.9 W/m², over ocean and land, with a global mean value of -1.5±0.5 W/m² (Quaas et al., 2009).

As widely described in previous chapters, many sources of error are present in satellite-based estimates. The satellite-based statistical quantification of cloud response to aerosol invigoration is affected by numerous uncertainties. In addiction, cloud response to aerosol enhancement is probably regime, regional and aerosol type dependent. This means that over different regions, similar aerosol loads may affect cloud parameters in different ways and produce significantly different IRF. For instance, over South-East Atlantic, LWP-AI relationship in case of mixed cloud-aerosol layers is negative (Chapter 6). The small droplets, more numerous in polluted clouds because of aerosol-cloud interaction, evaporate as a consequence of enhanced entrainment at cloud top of dry air, transported over ocean by trade winds from the inner African continent (together with aerosol particles). Over other regions, where the air overlaying cloud top is characterized by different humidity conditions, aerosol invigoration may largely increase cloud liquid water path, as shown by Kaufman et al. (2005) and Quaas et al. (2009).

Aerosol-induced LWP variations affect cloud lifetime, cloud cover, cloud reflectance and hence the way clouds interact with solar radiation. Indirect radiative forcing can then be positive or negative, depending on the specific cloud response. Thus, we infer that the most fruitful approach to quantify IRF is to work region by region. It remains to understand how many different regimes carry the aerosol-cloud signal.

In the following paragraph, we quantify IRF over South-East Atlantic. To work through this issue, we will use the cloud-aerosol relationship calculated in previous chapters, from mixed and unmixed cloud-aerosol layer analysis.

8.4.1 Quantification of aerosol IFR and TRF, over South-East Atlantic

The main idea is that in case of mixed cloud-aerosol layers, cloud optical and physical parameters evolve. Cloud droplet effective radius and liquid water path and cloud cover (the three input parameters that define the cloud field in the RRTM model, apart from cloud altitude) will then vary in function of aerosol concentration, according to the CDR-AI, LWP-AI and CLF-AI relationships obtained from mixed statistics of Chapter 6 and Chapter 7,

$$\frac{d\log CDR}{d\log AI}=-0.15 \qquad \frac{d\log LWP}{d\log AI}=-0.16 \qquad \frac{d\log CLF}{d\log AI}=0.02 \tag{69}$$

Aerosol index considered in (68) is obtained multiplying the AI daily estimate, calculated from MODIS daily retrievals of AOD and ANG, by the (seasonally averaged) frequency of occurrence of the mixed aerosol-cloud layer condition, within each 1°×1° grid box. In case of aerosol above or below cloud, cloud parameters remain unaltered.

In case of cloud-aerosol mixing, the generic cloud parameter K transforms as

$$\begin{aligned} K &= K_0+\delta K \\ \delta\log K &= \frac{\partial\log K}{\partial\log AI}\delta\log AI = A \\ \delta K &= K_0\left(e^A-1\right) \end{aligned} \tag{70}$$

where K_0 is the unperturbed state of such parameter before aerosol-cloud interaction, δK defines the aerosol-induced variation of K_0 and K its final state.

Total aerosol forcing results from the sum of direct and indirect effects in cloudy and cloud-free conditions. It can be expressed analytically by considering that each cloud parameter, present in the all-sky direct forcing equation (66), is representative of the evolved cloud state ($K=K_0+\delta K$) induced by aerosol-cloud interaction, so that

$$\begin{aligned} TRF &= \left(I_0^{clear}\uparrow - I_a^{clear}\uparrow\right)\left[1-\left(CLF_0+\delta CLF\right)\right] \\ &+ \left(I_0^{cloud\,(LWP_0,\,CDR_0)}\uparrow - I_a^{cloud\,(LWP_0+\delta LWP,\,CDR_0+\delta CDR)}\uparrow\right)\left(CLF_0+\delta CLF\right) \end{aligned} \tag{71}$$

Where I is the upwelling irradiance with and without aerosol in case of clear-sky (I_a^{clear} and I_0^{clear}) and cloudy-sky (I_a^{cloudy} and I_0^{cloudy}). In cloudy conditions, $I_a^{cloudy(CDR+\delta CDR,\ LWP+\delta LWP)}$ and $I_a^{cloudy(CDR_0,\ LWP_0)}$ refer respectively to cases where aerosol presence modifies or not cloud parameter. After few manipulations, (70) becomes

$$\begin{aligned} TRF = &\left(I_0^{clear}\uparrow - I_a^{clear}\uparrow\right)\left(1-CLF_0\right)+\left(I_0^{cloud\,(LWP_0,CDR_0)}\uparrow - I_a^{cloud\,(LWP_0,\,CDR_0)}\uparrow\right)CLF_0 && (A) \\ &-\left(I_0^{clear}\uparrow - I_a^{clear}\uparrow\right)\delta CLF+\left(I_0^{cloud\,(LWP_0,CDR_0)}\uparrow - I_a^{cloud\,(LWP_0,\,CDR_0)}\uparrow\right)\delta CLF && (B) \\ &-\left(I_a^{cloud\,(\delta LWP,\,\delta CDR)}\uparrow\right)CLF_0 && (C) \\ &-\left(I_a^{cloud\,(\delta LWP,\,\delta CDR)}\uparrow\right)\delta CLF && (D) \end{aligned} \tag{72}$$

Term A is the direct forcing, while terms B, C and D represent the different contributions to

indirect radiative forcing (IRF). Term B quantifies the radiative impact of aerosol-induced CLF variations (IRF_B), if LWP and CDR do not change. Term C quantifies the forcing coming from aerosol-induced variations in droplet size and cloud water amount (IRF_C), with CLF remaining constant. Term D quantifies the effect of δCDR and δLWP in the δCLF portion of cloud only (IRF_D).

According to MODIS and CALIPSO information, if the AI of aerosol fraction mixed with cloud is larger than a certain value, cloud layer is considered polluted. MODIS L3 daily retrievals of CDR, LWP and CLF represent the *K* parameter of equation (69), describing the evolved cloud state after cloud-aerosol interaction. The initial state of each parameter in the aerosol-free atmosphere (CDR_0, LWP_0, CLF_0), is calculated from (69) by means of (68). Then, cloud properties in clean and polluted conditions are used in the model as input data to perform radiative calculations.

We define AI = 0.07 as the threshold value in aerosol concentration to consider mixed cloud -aerosol layers as polluted. CDR-AI, LWP-AI and CLF-AI relationships of Chapter 6 show that beyond this value, mixed case statistics sensibly differ from unmixed ones. At lower AI, nor a significant distinction between the two dataset, nor an accurate description of polluted cloud properties by the calculated linear fit in log-log scale (that largely overestimates mixed CDR and LWP) are possible.

It should be noted that the DRF defined by term A of equation (62) (DRF_A) and that resulting from equation (66) slightly differ one from another. In equation (62), the upwelling irradiance for aerosol-free scenes in case of cloudy-sky (I_0^{cloudy}) as well as the aerosol-free cloud fraction are (correctly) function of CDR_0, LWP_0, and CLF_0, describing cloud state before aerosol interaction. In equation (66), I_0^{cloudy} and aerosol-free cloud fraction are estimated from direct MODIS retrievals of CDR, LWP and CLF, representative of a polluted cloud field, if mixed AOD > 0.07. Latter method is less correct, as the radiative impact of an aerosol-free atmosphere is calculated from data of a polluted cloud scene.

Seasonal averages of DRF_A over South-East Atlantic are similar to direct forcing estimates obtained (66) (Figure 65). Bottom image of Figure 71 shows the spatial mean estimates of DRF_A and the quantity $\Delta=DRF_A$-DRF for 2005 (Δ values from 2005 to 2010 are reported in Table 19). Over the whole region, the mean difference between DRF_A and DFR is relatively small and the six year average is almost zero during Jan-Mar, -0.02 during Apr-Jun, -0.10 W/m² during Jul-Sept and -0.02 W/m² during Oct-Dec. However, Δ can reach locally (within 1 degree grid box) peak values up to -5 W/m², during Jul-Sept.

As a consequence of the increased clear-sky fraction considered in equation (62), with respect to (66), negative forcing is stronger, showing that also DRF estimates may result less accurate if cloud cover response to aerosol enhancement is not considered.

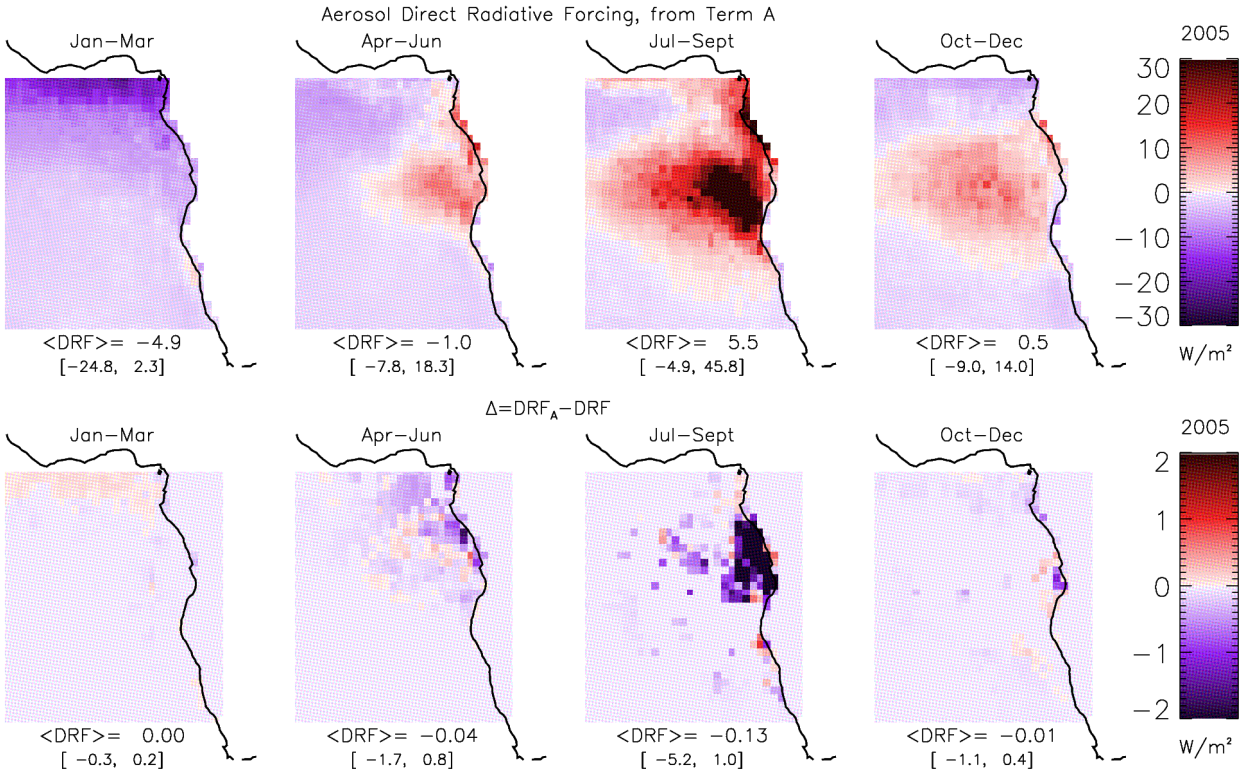

Figure 71: seasonally averaged monthly mean of daily direct aerosol forcing over South-East Atlantic (2005), calculated from term A of equation (62) (top image) and the mean difference between DRF_A and DFR (bottom image). Under each map, the spatial mean estimate is reported together with its local minimum and maximum value, within a 1°×1° grid box.

$\Delta=DRF_A$-DRF [W/m²]	Jan Feb Mar	Apr May Jun	Jul Aug Sept	Oct Nov Dec
2005	0.00±0.03	-0.04±0.14	-0.13± 0.57	-0.01± 0.07
2006	-0.00±0.03	-0.02±0.07	-0.03±0.42	-0.01±0.04
2007	0.00±0.06	-0.02±0.05	-0.12±0.60	-0.01±0.04
2008	0.00±0.04	-0.01±0.06	-0.11±0.47	-0.03±0.11
2009	0.00±0.03	-0.01±0.06	-0.13±0.59	-0.01±0.06
2010	0.00±0.04	-0.02±0.11	-0.09±0.51	-0.07±0.24
Average	0.00±0.04	-0.02±0.08	-0.10±0.53	-0.02±0.09

Table 19: spatial mean estimates of seasonal difference $\Delta=DRF_A$-DRF over ocean, within [4N, -30N; -14E, 18E], from 2005 to 2010. In the last row, we report the six-year average and standard deviation of spatial mean Δ estimate, for each season.

Seasonal averages of aerosol indirect radiative forcing (IRF_B+IRF_C+IRF_D) over South-East Atlantic are reported in Figure 72 (top row), together with the values of each single term. The contribution to total aerosol IRF resulting from aerosol-induced cloud fraction variations (term B) is shown in the second row, while the third row shows the contribution from changes in cloud droplet size and liquid water path (term C). Bottom row shows the second order contribution coming from CDR and LWP changes within the increased fraction of cloud cover (term D).

It is evident from Figure 72 that IRF_C is responsible of the largest contribution to the total IRF. It is interesting to note that in region mainly characterized by high aerosol load of low absorbing particles IRF_C is mostly positive (during Jan-Mar over the Gulf of Guinea, IRF_C~1 W/m²). Where the absorbing aerosol dominates particle type, IRF_C is mostly negative (during Jul-Sept off the coast of Angola and in minor part, during Apr-Jun, over the Gulf of Guinea and off the coast of the Democratic Republic of Congo, IRF_C is between -1 and -4 W/m²).

This shows that the indirect forcing resulting from aerosol-induced variations in CDR and LWP is sometimes opposite in sign to the cloudy-sky direct forcing (Figure 65), mostly negative in Jan-Mar over the Gulf of Guinea (about -1 W/m², comparable in magnitude to IRF_C) and largely positive off the coast of Angola during Jul-Sept (between 10 and 40 W/m², about ten times larger in magnitude than IRF_C).

These results can be explained as follows. As shown in previous paragraph, absorbing aerosol with SSA < 0.91 located above cloud top with COT > 4, generally produces a net positive direct forcing. If LWP and CDR decrease according to (68), as a consequence of indirect effect, COT and cloud reflectance get reduced. Over regions with highly absorbing aerosol above cloud top, such decrease in cloud reflectance decreases the positive cloudy-sky direct forcing and leads to a net negative indirect forcing. On the other hand, if aerosol is not located above cloud top (or the SSA is lower than the critical value needed to produce TOA warming), cloud-sky DRF is negative. In such case, a decrease in cloud reflectance decreases the amount of solar radiation reflected to space, resulting in a net positive indirect forcing.

The radiative forcing due to aerosol-induced variations in cloud fraction is always positive, but somewhat weaker than IRF_C. It is stronger whenever aerosol concentration is larger. During biomass burning season, off the coast of Angola, the IRF_B reaches a peak value of 1.28 W/m².

As expected, the contribution of CDR and LWP variations within the cloud portion increased by as a consequence of aerosol-cloud interaction is very small (second order effect).

Total aerosol IRF obtained by the sum of term B, C and D (IRF_{B+C+D}), is mostly driven by the radiative forcing resulting from the aerosol-induced changes in CDR and LWP, more than in CLF. This result is confirmed by indirect forcing estimates for 2006-2010 (Figure 73), characterized by a well defined annual cycle and limited inter-annual variability (Table 20).

IRF [W/m²]	Jan Feb Mar	Apr May Jun	Jul Aug Sept	Oct Nov Dec
2005	0.03±0.23	-0.08±0.47	-0.07±0.39	-0.06±0.27
2006	0.02±0.20	-0.08±0.22	0.02±0.43	-0.02±0.23
2007	0.01±0.49	-0.07±0.21	-0.08±0.46	-0.06±0.31
2008	-0.01±0.31	-0.03±0.19	-0.05±0.38	-0.15±0.44
2009	0.02±0.20	-0.05±0.22	-0.05±0.37	-0.05±0.26
2010	0.04±0.27	-0.07±0.40	-0.03±0.37	-0.22±0.50
Average	0.02±0.28	-0.06±0.28	-0.04±0.40	-0.09±0.34

Table 20: seasonally averaged aerosol IRF over ocean, within [4N, -30N; -14E, 18E], from 2005 to 2010. In the last row, we report the six-year average and standard deviation of spatial mean IRF estimate, for each season.

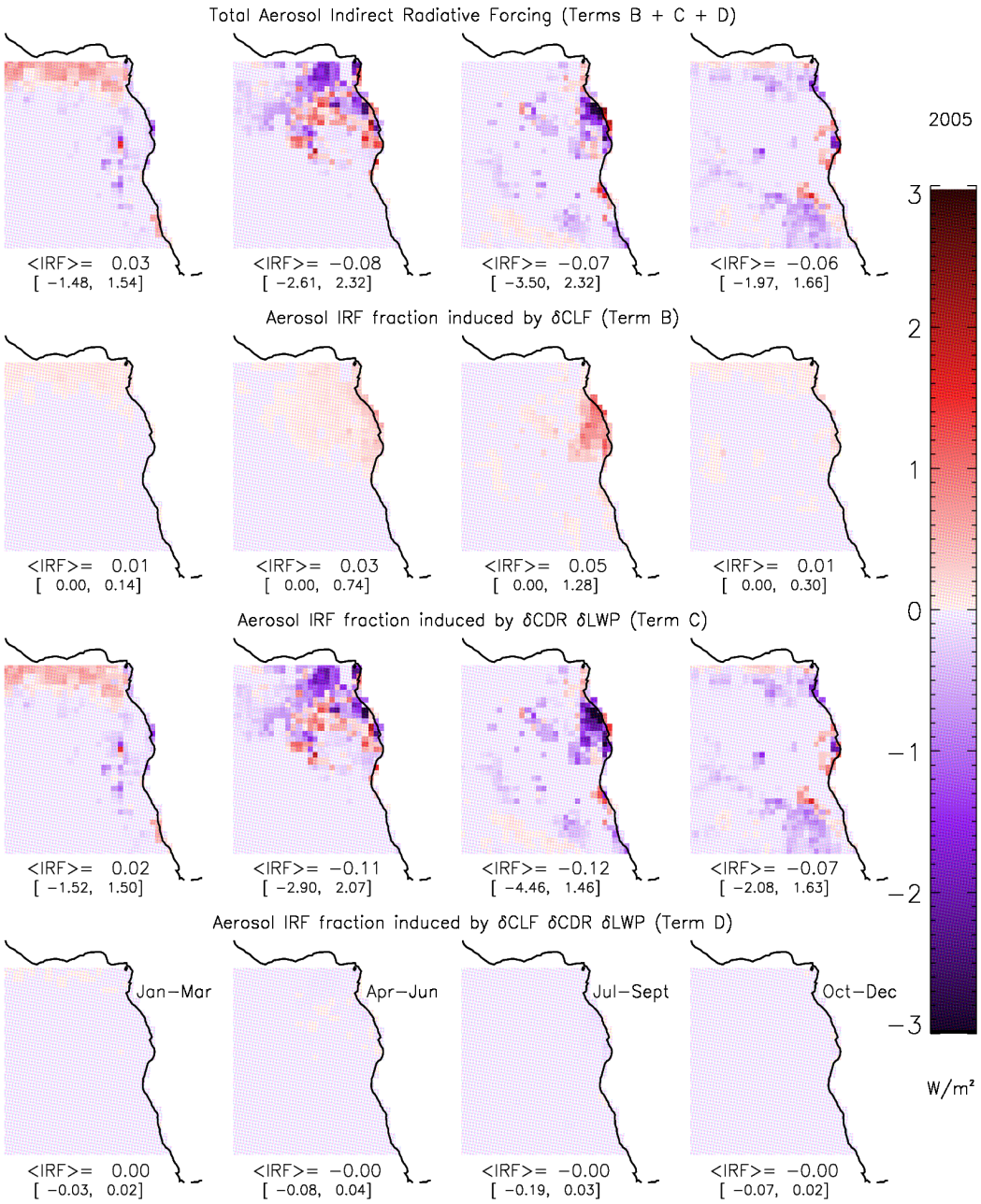

Figure 72: seasonally averaged monthly mean of daily aerosol indirect radiative forcing (top row) over South-East Atlantic (2005) and of each single term that contributes to IRF, according to equation (62). Terms B, C and D define respectively the indirect radiative impact resulting from aerosol-induced changes in CLF (IRF_B, second row), CDR and LWP (IRF_C, third row), CDR and LWP within the increased portion of CLF (IRF_D, bottom row). Under each map, the spatial mean estimate of each parameter is reported together with its local minimum and maximum values, within a 1°×1° grid box.

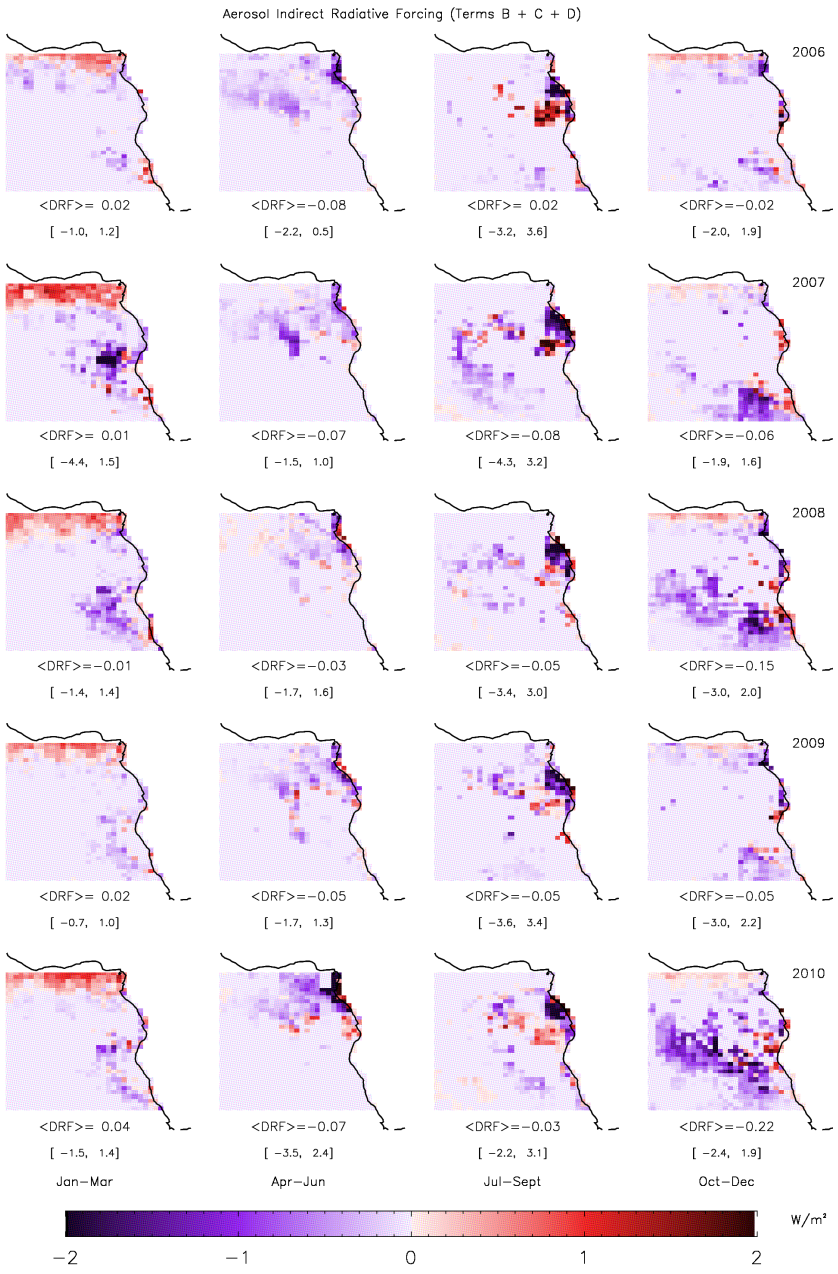

Figure 73: seasonally averaged shortwave IRF_{B+C+D} at TOA, for 2006-2010. Spatial mean estimates of each time period are reported below the correspondent map, together with maximum and minimum local values, within a 1°×1° grid box.

IRF_{B+C+D} is in general opposite in sign to DRF but smaller in magnitude. Seasonally averaged monthly mean estimates of total aerosol forcing over South-East Atlantic (the sum of DRF_A and IRF_{B+C+D}) are shown in Figure 74 (2005), Figure 75 (2006-2010) and reported in Table 21. It is evident that aerosol forcing over the area of interest is governed by the direct more than the indirect component, whose radiative impact is in general several times smaller.

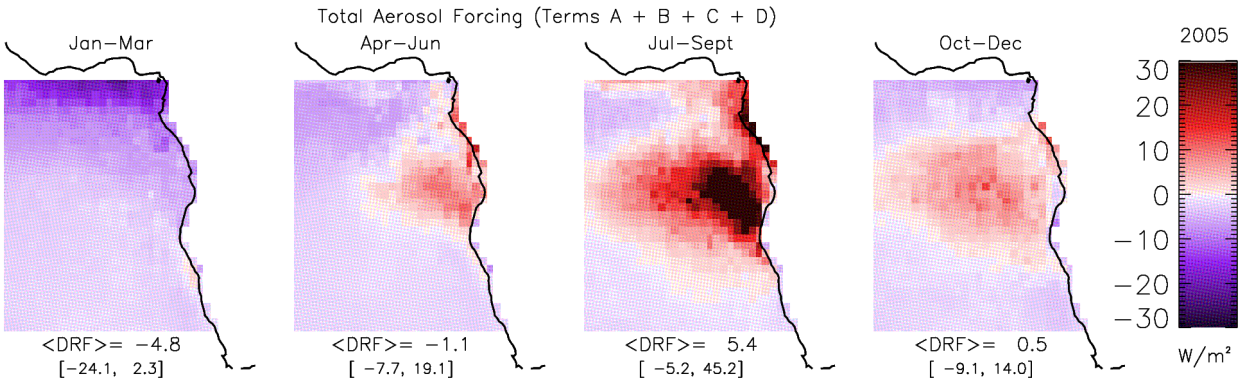

Figure 74: seasonally averaged monthly mean of daily total aerosol forcing (direct + indirect forcing) over South-East Atlantic (2005), calculated as the sum of terms A, B, C, D of equation (62). Under each map, the spatial mean TRF estimate is reported together with its local minimum and maximum values, within a 1°×1° grid box.

TRF [W/m²]	Jan Feb Mar	Apr May Jun	Jul Aug Sept	Oct Nov Dec
2005	-4.85±4.56	-1.08±3.59	5.44±9.39	0.48±3.58
2006	-3.72±3.16	-2.71±1.68	5.39±10.52	0.45±3.11
2007	-4.63±5.11	-2.28±1.43	5.90±11.05	0.27± 3.13
2008	-4.56±4.65	-2.65± 1.91	4.88±10.27	0.81±3.98
2009	-3.96±3.39	-2.13± 1.84	5.73±10.15	0.21±2.80
2010	-3.85±3.71	-2.01± 2.56	5.56±10.76	0.58±3.90
Average	-4.26±4.10	-2.14±2.17	5.48±10.36	0.47±3.42

Table 21: seasonally averaged aerosol TRF over ocean, within [4N, -30N; -14E, 18E], from 2005 to 2010. In the last row, we report the six-year average and standard deviation of spatial mean TRF estimate, for each season.

Figure 67 shows histograms of monthly DRF_A, IRF_{B+C+D} and $TRF_{A+B+C+D}$ estimates at 1°×1° resolution, for 2005-2010. Means and the medians of each dataset are reported in figure. Note that the mean value of direct radiative forcing decreases from -0.03 to -0.07 W/m² (with a spatial standard deviation of 8.03 W/m²) if it is calculated using term A of equation (62) instead of (66). At the same time, the median value increases from -1.50 to -1.46 W/m².

If we consider the whole dataset, aerosol indirect effect produces a mean radiative forcing equal to -0.05 W/m² (with a spatial standard deviation of 0.54 W/m²). We can break down aerosol indirect forcing into the component due to changes in CDR and LWP (cloud albedo effect) and that one due to changes in CLF (cloud life-time effect). Cloud albedo effect is negative and equal to -0.07±0.55 W/m², while indirect forcing from life-time effect is positive and equal to 0.02±0.12 W/m². Accounting only for cases where aerosol concentration is larger than large enough to significant affect cloud parameters (i.e. AI > 0.07), mean IRF_{B+C+D} decreases down to -0.19 W/m² (with a spatial standard deviation of 1.11 W/m²) and its median to -0.07 W/m².

It then results that the mean total aerosol forcing at shortwave is equal to -0.12 W/m², with a spatial standard deviation of 8.02 W/m². The median value of TRF, however, is much smaller than the mean one and equal to -1.49 W/m².

Results clearly indicate that direct forcing can be several times larger in magnitude than indirect forcing. However, if we consider the outgoing shortwave radiation budget at TOA over the whole study region during 2005-2010, direct forcing only accounts for about 58% of the mean total forcing and indirect forcing for the remaining 42%. We can conclude that over South-East Atlantic, even if aerosol indirect effect does not sensibly affect the seasonal atmospheric energy balance at local scale (1 degree), annual radiative forcing at regional scale (~10^3 degree) is about 70% of that produced by aerosol direct effect.

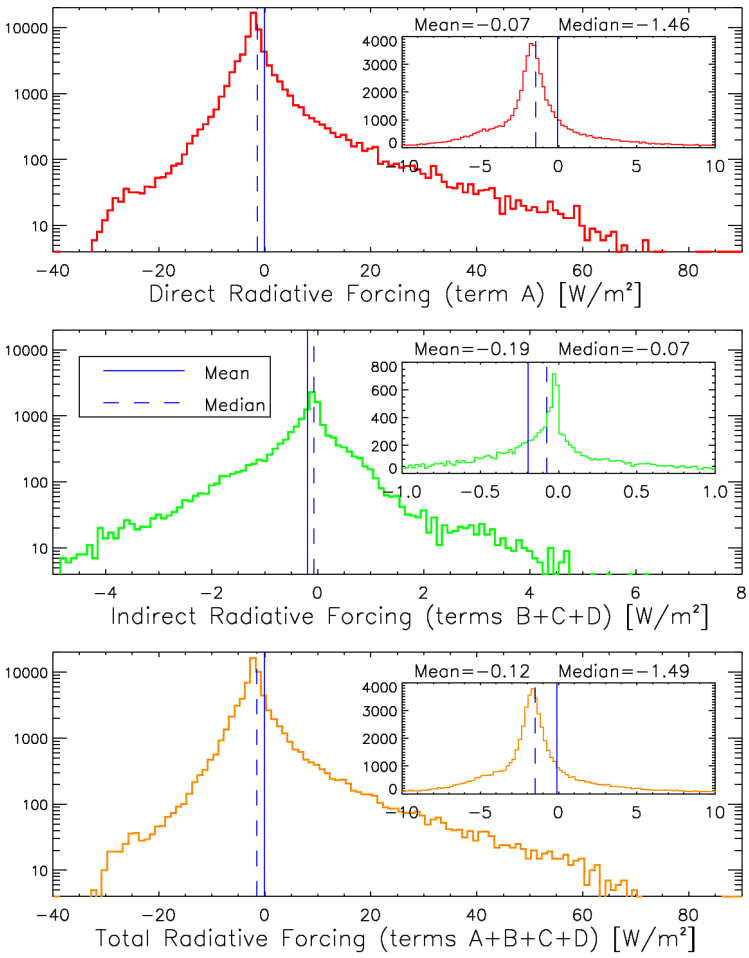

Figure 75: histograms of 1°×1° model estimates of direct radiative forcing (top image, term A of equation (62)),indirect radiative forcing (middle image, terms B+C+D) and total aerosol forcing (bottom image, terms A+B+C+D), for the whole 2005-2010 time period, over South-East Atlantic. Y-axis is in logarithmic scale. Note that the histogram of indirect radiative forcing only refers to cases where AI is larger than 0.07. Within each figure, inner images represent a zoom within a smaller range of radiative forcing values (y-axis is in linear scale). Mean (solid line) and median (dashed) values are reported.

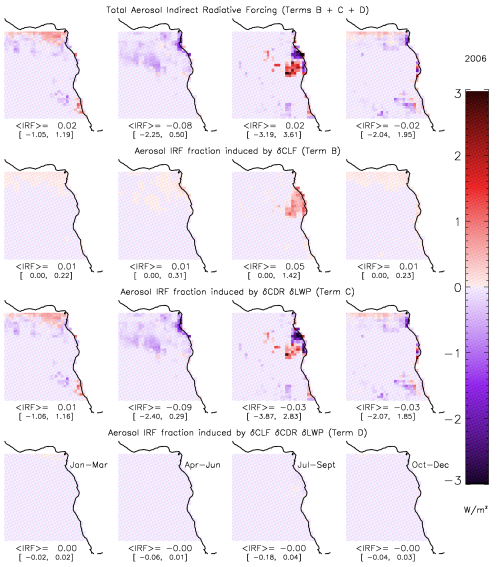

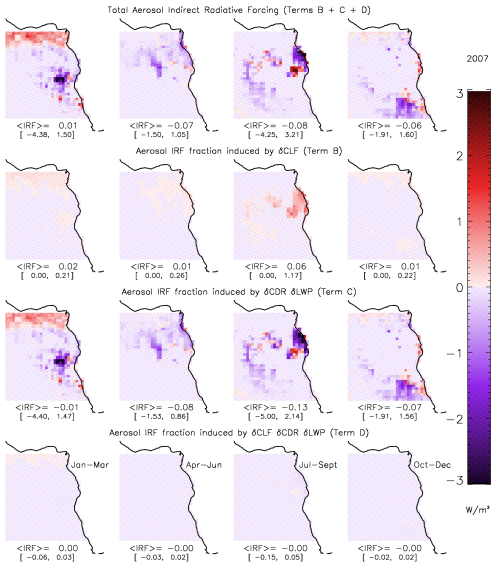

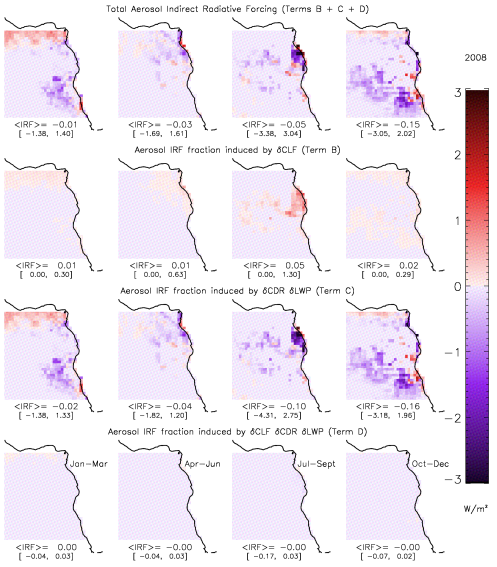

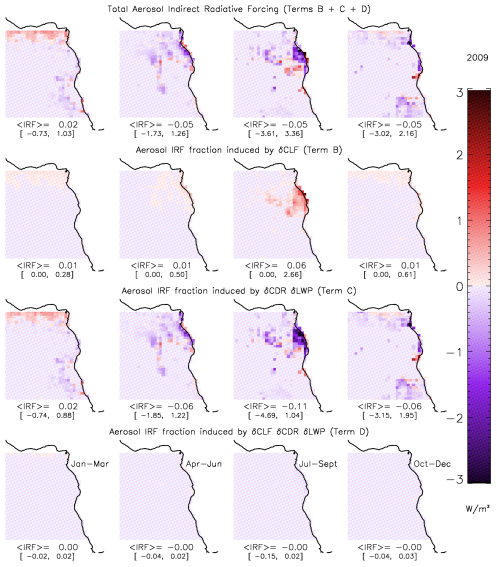

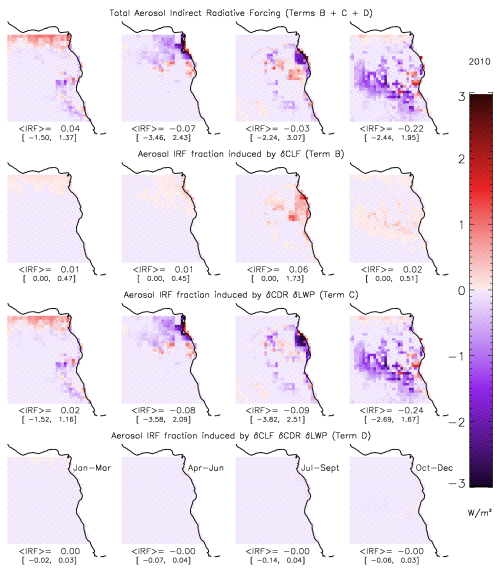

Figure 76: seasonally averaged monthly mean of daily aerosol indirect radiative forcing (top row) over South-East Atlantic, for 2006-2010. According to equation (62), the different contributing terms to total IRF (IRF_B, IRF_C, IRF_D) are reported from top to bottom. Spatial mean estimates of each time period are indicated below the correspondent map, together with maximum and minimum local values, within a 1°×1° grid box.

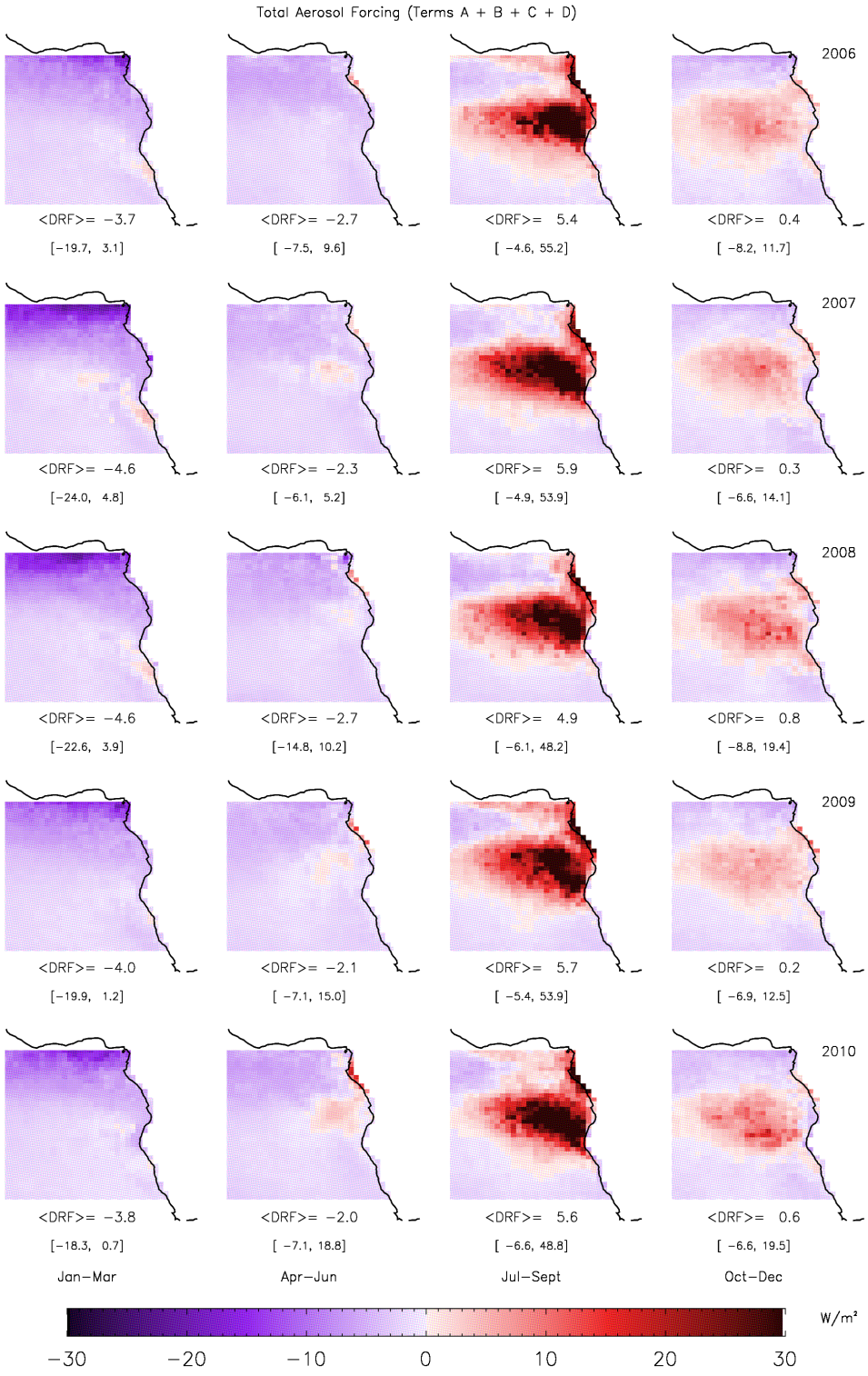

Figure 77: seasonally averaged shortwave $TRF_{A+B+C+D}$ at TOA, for 2006-2010. Spatial mean estimates of each time period are reported below the correspondent map, together with maximum and minimum local values, within a 1°×1° grid box.

8.5 Summary and conclusions

In this chapter we used the statistical relationships obtained in Chapter 6 and Chapter 7, between aerosol concentration and cloud parameters, to quantify the shortwave aerosol direct and indirect forcing at the top of the atmosphere. We define "forcing" as the difference in the net radiative flux with and without aerosol. Direct forcing refers to the radiative impact due to scattering and absorption of solar radiation by the particulate matter, while indirect forcing to aerosol-induced variations of cloud reflectivity and coverage.

We make use of the Rapid Radiative Transfer Model (RRTM_SW), to perform radiative calculation over South-East Atlantic region, at 1 degree resolution. Monthly mean of MODIS daily estimates of cloud and aerosol parameters are used as input data.

A reliable vertical description of the atmosphere and cloud-aerosol layers mutual position is fundamental to quantify the exact amount of satellite derived aerosol load which is under, above or within cloud layer. In the effort to improve the accuracy of previous radiative estimates, CALIPSO information is used to perform seasonal maps of the frequency of occurrence of mixed and unmixed cloud-aerosol layer conditions. We estimate that over South-East Atlantic, the frequency of cases with aerosol above cloud top is about 58%, aerosol under clouds 8% and aerosol mixed with clouds 34%, on annual basis. Different number have been derived for the various seasons.

All-sky DRF results in a large negative forcing over regions characterized by the presence of reflecting aerosol, as the Gulf of Guinea during January-March time period, with local peak values down to -25 W/m² (TOA cooling), within a 1°×1° grid box. On the other hand, large positive forcing is observed in correspondence of large amount of absorbing aerosol above extended clouds. During the biomass burning region, off the coast of Angola, DRF can reach local peak values up to 54 W/m² (TOA warming).

Model simulations, from 2005-2010, indicate that DRF is characterized by a strong annual cycle, with mean value of about -4.3±4.3 (Jan-Mar), -2.1±2.1 (Apr-Jun), 5.6±10.5 (Jul-Sept) and 0.6±3.4 W/m² (Oct-Dec). The inter-annual variability is limited, with respect to seasonal variations. During this six year time period, the mean direct forcing averaged over the whole region is negative and equal to 0.03±8.14 W/m², near perfect compensation between the clear-sky and the cloudy-sky forcing, equal to -3.42±2.81 and 3.39±7.41 W/m². This value decreases more than a factor of two (-0.07±8.03 W/m²), if we let aerosol particles affect cloud cover. This implies that clear-sky (cloudy-sky) fraction of direct forcing is increased (decreased) with respect to previous estimate.

It has been shown that CLF is as a good predictor of direct forcing efficiency. In particular CLF = 0.5 can be considered as the threshold value beyond which all-sky TOA forcing becomes positive, in good agreement Chan et al. (2009). At the same time, we find that positive DRF

mostly occurs in case of aerosol particles with single scattering albedo smaller than 0.91 above cloud with optical thickness larger than 4.
To quantify indirect radiative forcing, cloud properties (CDR, LWP, CLF) are modified according to mixed case statistics, when the aerosol concentration of aerosol fraction mixed with cloud layer is sufficiently high (AI > 0.07).
Indirect forcing can be decomposed into the sum of two principal terms, the radiative component coming from aerosol-induced CLF variations and that from CDR and LWP changes. We find that the larger contribution to total IRF is from CDR and LWP, which is several times lower in magnitude than direct forcing and often opposite in sign. IRF from CLF is always positive and less strong. For the 2005-2010 time period, model simulations estimated a mean seasonal indirect radiative forcing over South-East Atlantic equal to 0.02±0.28 (Jan-Mar), -0.06±0.28 (Apr-Jun), -0.04±0.28 (Jul-Sept) and -0.09±0.34 W/m² (Oct-Dec), with local peak values within a 1°×1° grid box up to -4.4 W/m² and 3.6 W/m², mostly during the biomass burning season. The six year global average of IRF is negative and equal to -0.05±0.54 W/m² (cooling). This value is very small, but its impact on the regional radiative balance is somewhat significant, if we consider that it is about 70% of global mean forcing produced by direct effect, also rather small. Breaking down aerosol indirect forcing into two components, one due to changes in CDR and LWP (cloud albedo effect) and the other one due to the changes in CLF (cloud life-time effect), cloud albedo effect results negative and equal to -0.07±0.55 W/m², while life-time effect is positive and equal to 0.02±0.12 W/m².
Results indicate that total (direct+indirect) radiative forcing can produce strong cooling or sensibly large warming at TOA, depending on a large variety of factors. Among them, aerosol optical properties (as single scattering albedo) and vertical aerosol-cloud position probably represent the main source of uncertainties. In the attempt to minimize these errors, we provided an accurate description of temporal and spatial cloud field variations, due to both meteorological-driven and aerosol-induced effects.

Over South-East Atlantic, the mean seasonal total forcing due to aerosol presence from 2005 to 2010 has been quantified in -4.3±4.1 (Jan-Mar), -2.1±2.2 (Apr-Jun), 5.5±10.4 (Jul-Sept) and 0.5±3.4 W/m² (Oct-Dec), very close to seasonal estimates of DRF. The six year global average of TRF, over the whole region, is equal to -0.12±8.03 W/m². Even though South-East Atlantic is characterized by the occurrence of large amounts of biomass burning particles, the net aerosol radiative impact results in a small cooling at the top of the atmosphere. This is due to the compensation between negative and positive forcing.

On yearly basis, average direct (-0.07±8.03 W/m²) and indirect (-0.05±0.54 W/m² given by the sum of -0.07±0.55 W/m² by cloud albedo effect and 0.02±0.12 W/m² by life-time effect) forcing over South-East Atlantic result much lower than global annual mean values reported in the International Intergovernmental Panel Climate Change report (Foster et al., 2007), equal respectively to -0.5 W/m² for direct effect (between -0.9 and -0.1 W/m²) and -0.7 W/m² for cloud albedo effect (between -1.8 and -0.3 W/m²). Our estimates are equal in sign but from 7 to

10 times smaller in magnitude.

In case of DRF, this is probably due the occurrence of large amounts of smoke particles during the biomass burning season, so that large negative forcing are compensated by large positive forcing, in case of aerosol above clouds. Seasonal maps of all-sky DRF off the coast of Angola during Jul-Sept well reproduces the large geographical variability of daily forcing found by Myhre et al. (2003) and Keil et al. (2003). They constrain model simulations with satellite and aircraft (for one day only) data on cloud-aerosol properties and vertical position. Our simulation show local peak values (within a 1 degree grid box) that are generally larger in magnitude than those studies that calculate all-sky DRF at monthly and seasonal scale. As a consequence, our spatial mean estimates over the whole region are sometimes in evident contrast with previous works. For example, during September 2005, the average all-sky forcing is positive and equal to 9.4 W/m², much larger than Abel et. al. (2005), equal to -3.1 W/m², and Myhre et al. (2003), equal to -1.7 W/m², during the same time-period.

Over South-East Atlantic, an average positive seasonal forcing of 1.2 W/m² is observed by Sakaeda et al. (2001), from July to October. They only account for carbonaceous particles. As anthropogenic aerosol is expected to produce a direct forcing about five times smaller than total aerosol, their result is close to our estimate of 6.8 W/m², considering all aerosol species during the same time period. Similarly to our analysis, that of Sakaeda et al. (2011) is one of the first satellited base study providing using an accurate time-dependent 3D parametrization of cloud-aerosol position.

In case of clear-sky, the sources of error are less numerous. The largest uncertainties are the AOD and, in case of anthropogenic forcing, the fine fraction of total AOD and the anthropogenic fraction of fine aerosol. Considering all aerosol species present over South-East Atlantic (natural+anthropogenic), we found a clear-sky direct forcing of -7.9 W/m², for September 2005, in very good agreement with the regional estimates of Abel et al. (2005) equal to -7.6 W/m², during the same time period and over the same region (similar results are also obtained by Myhre et al. (2003) and Ichoku et al. (2003)).

On yearly basis, average regional clear-sky forcing is equal to -4.7 W/m² (median of -5.7 W/m²), also in good agreement with annual mean values over global oceans of Yu et al. (2006), equal to -3.5 W/m² (from model simulations) and to -5.5 W/m² (from satellite based estimates), and Chen et al. (2008) equal to 5.0 W/m² (from satellite based data).

The spread among the large coherence of clear-sky direct forcing, between our and previous studies over South East Atlantic, and the small coherence of all-sky estimates (except for Sakaeda et al., 2011) can be reasonably attributed to the different accuracy used in describing aerosol-cloud vertical position and aerosol absorption properties. The lack of an adequate parametrization of atmospheric vertical structure and aerosol particle type, most likely to affect cases when cloud presence is taken into account, is confirmed to be the larger error source in all-sky aerosol direct forcing estimates.

Even though the strong geographical variability of aerosol load over oceans do not allow for a quantitative comparison with global annual estimates, it is evident that our regional estimate of cloud albedo effect is particularly reduced with respect to IPCC report and several GCM simulations (Lohmann and Feichter, 2005; Forster et al., 2007). This is probably a consequence of the negative relationship between LWP and aerosol enhancement, observed over the study area. On global scale, LWP of shallow clouds over oceans is generally found to be positively correlated with AI (Kaufman et al., 2005; Quaas et al., 2009). Over South East Atlantic, the enhancement in cloud reflectance due to the aerosol-induced decrease in mean droplet radius (Twomey's effect) is balanced by the cloud water loss. Cloud albedo is little affected by changes in aerosol concentration and the resulting cloud albedo effect is strongly reduced.

In good agreement with previous studies, however, the annual cloud albedo effect is of similar magnitude than annual direct forcing, even if in latter case spatial and temporal variability is several times stronger.

From model simulations constrained by satellite based relationship between cloud properties and aerosol occurrence over South-East Atlantic, Quaas et al. (2008) find an annual regional radiative forcing between -5.0 W/m² (off the cast of Angola) and -0.2 W/m² (over deep ocean), strongly overestimating our result. Note however, that they consider as life-time effect the radiative impact from aerosol-induced changes in LWP, consequence of the second aerosol indirect effect. We do not believe that this argumentation is consistent, as changes in cloud reflectance are direct function of LWP variations and resulting radiative forcing is to be considered as part of cloud albedo effect.

Life-time effect is only due to changes in cloud fraction only. In contrast with global model simulations of Lohmann and Feichter (2005), between -1.4 and -0.3 W/m², our regional annual estimate of life-time effect is smaller in magnitude and opposite in sign, equal to 0.02±0.12 W/m². The small value is a consequence of the reduced CLF sensitivity to AI variations, observed in case of aerosol-cloud interaction, which is several times times smaller than generally found. We infer that the regime-dependent response of LWP to aerosol invigoration can strongly determine CLF variations and impose to analyze both life-time and cloud albedo effects region by region.

The annual total aerosol forcing over South-Est Atlantic (-0.12±8.02 W/m²) is then sensibly smaller than the value that would be expected at global scale, from the sum of direct and indirect forcing estimates found in previous studies. In a recent work Quaas et al. (2009) use ten GCMs constrained by satellite observation to explicitly quantify annual total aerosol forcing over oceans. The find a strong negative (cooling) effect (with respect to the global annual warming due to LLGHG) equal to -1.2±0.4 W/m², about ten times stronger than over South-East Atlantic. This result shows an overall coherence between our regional estimates and those obtained over global oceans, where the occurrence of highly absorbing particle is in average

certainly lower, and the aerosol negative TOA forcing is expected to be much stronger.

In model simulations, uncertainties in the calculated radiative forcing reflect the uncertainties in aerosol and cloud input parameters, as their spectral dependence and spatial-temporal variability. This work does not examine the dependence of DRF and IRF on the measurement uncertainties associated at these variables. Further analysis is required to quantify the change radiative flux sensitivity to changes in aerosol optical properties, cloud and aerosol spatial distribution, surface albedo, cloud optical thickness and solar geometry, in order to identify the most important parameters that need to be target by a more accurate observation and a better description inside the radiative transfer model. In particular, we supposed that the largest errors come from uncertainties in single scattering albedo (as suggested by McComiskey et al., 2008) and vertical mutual position of cloud and aerosol layers. For that reason our primary effort has been to produce vertical resolved seasonal maps of aerosol and cloud position, together with monthly maps of aerosol and cloud optical properties. Monthly average, however, are obtained from daily product derived from instantaneous satellite overpass, so that aerosol and cloud diurnal cycle is not taken into account. To test the impact of cloud and aerosol diurnal variability on radiative forcing estimates, MODIS measurements from Terra satellite (morning overpass) can replace MODIS Aqua retrievals (afternoon overpass). Using Terra instead of Aqua satellite, Abel et al. (2005) find a general increase in cloud cover and optical thickness that results in an average increase in direct forcing of about 14%, over both ocean and land of Southern Africa. To build a more global picture of cloud diurnal cycle, not limited to two measurements of an individual scene each day, geostationary satellite (Meteosat-8) observations can be used as well, to provide high temporal resolution.

Finally, aerosol impact on atmospheric radiative budget at longwave has not been analyzed. Even though it is supposed to be almost zero in case of direct forcing and of second order in case of indirect forcing (with respect to shortwave forcing), further studies are needed to prove this assumption. Over a region, as South-East Atlantic, where the annual shortwave TRF is particularly low, longwave IRF could be not completely negligible.

Chapter IX – Summary and conclusions

The aim of this work has been to provide a comprehensive analysis of cloud and aerosol interaction over South-East Atlantic, to quantify the full aerosol radiative forcing.
We used remote sensing data from the A-Train constellation to retrieve cloud and aerosol properties over the oceans. Aerosol load and optical properties (Angstrom coefficient and particle effective radius) are retrieved by MODIS spectroradiometer, aboard Aqua satellite. Cloud properties are retrieved by both MODIS (for droplet effective radius, optical thickness, liquid water path, top pressure and cloud fraction) and POLDER (for effective radius only) instrument, aboard PARASOL satellite. POLDER and MODIS retrieve vertically integrated measurements of column radiance and do not allow for vertical description of the atmosphere. The information on cloud and aerosol altitude is provided by CALIOP instrument, the first space-borne lidar, aboard CALIPSO satellite.
MODIS, PARASOL and CALIPSO fly in close proximity on the same sun-synchronous orbit and allow for coincident observations of the same portion of the atmosphere, within a few minutes.

The main originality of our analysis is to use CALIPSO information to define whether or not aerosol and cloud layers observed by MODIS and PARASOL are mixed and presumably interacting. Coincident MODIS-PARASOL-CALIPSO retrievals showed that, in case of interaction, cloud properties are strongly influenced by aerosol. On the other hand, in case of well separated layers, cloud properties do not show any significant variation with aerosol invigoration.
In particular, we analysed the CDR-AI relationship, showing a decrease in droplet effective radius of mixed case clouds, approximately from 15 to 7 μm, as aerosol index varies from 0.02 to 0.5. When aerosol is located above cloud top, as it often occurs over South-East Atlantic, effective radius remains almost constant, close to 10 μm. Results are in good agreement with Twomey's hypothesis (Twomey, 1974; Twomey, 1977), according to which fine aerosol particles (efficient CCN) may largely increase cloud droplet number concentration. As a consequence, more numerous droplets lead to smaller mean droplet sizes, if cloud water amount remains constant. The fact that unmixed case statistics do not show any consistent correlation between changes in CDR and in AI, confirmed that aerosol-cloud interaction is the leading factor governing the observed cloud response.
Using coincident MODIS-CALIPSO observations (i.e. substituting PARASOL information by MODIS cloud product) we obtained similar results. In case of mixed layers, CDR decreases from 15-16 to 11 μm with increasing AI from 0.02 to 0.5. On the other hand, when cloud and aerosol layers were well separated, droplet radius remains almost constant, close to 14 μm.
This result confirms a good coherence between MODIS and PARASOL radius estimates, although MODIS statistics are biased high, by about 4 μm. This value if larger than the observed mean error (~1.7±2.3 μm) between coincident MODIS-PARASOL CDR retrievals, at

150 km resolution, from cloud fields with mean optical thickness larger than 5 (according to MODIS product). We infer this is mainly due to the high heterogeneity of observed cloud field, when looking for aerosol-cloud coincidence. A strong broken-cloud condition can increase MODIS retrieval errors.

Similar to CDR, we also performed statistics of LWP-AI and COT-AI, to investigate the response of cloud water amount and optical properties to changes in cloud microphysics. According to Twomey's theory, we expect an increase in cloud reflectance, when mean droplet size drops down (first indirect effect). At the same time, theoretical calculation indicates that cloud optical thickness decreases, when liquid water path decreases.
Coincident MODIS-CALIPSO observations show a clear decrease in LWP, from 90-100 to 60 g/m^2, as AI varies between 0.02 to 0.5, in case of interaction of cloud and aerosol layers. LWP remains almost constant with increasing AI, when aerosol is above cloud top and cannot interact with underlying layer. We infer that aerosol-induced LWP diminution is due to the enhancement of dry air entrainment, that enhances droplet evaporation at cloud top. Dry air is presumably transported, together with aerosol particle, from inner continent by trade winds. In Southern African, absolute humidity can reach extremely low values, during the biomass burning season.
Cloud optical thickness response to aerosol enhancement, resulting from the balance of LWP depletion and CDR increase, is very weak in both cases of mixed and unmixed layers.
Although aerosol impact on cloud microphysics is strong, the effect on cloud optical properties is not evident, as liquid water path assumption is not valid over the study area. Twomey's effect on cloud reflectance cannot be demonstrated and further work is needed. To address this issue, independent measurements of LWP (MODIS algorithm calculates LWP directly from CDR and COT estimates) can be useful to analyze the case of constant liquid water path.

According to Twomey's parametrization, we quantified the strength of aerosol-cloud interaction by the slope of linear relationship between the logarithm of a given cloud property and the logarithm of aerosol index, in case of mixed aerosol and cloud layers. We call this quantity as cloud *sensitivity* to aerosol enhancement. For CDR, it is equal to -0.23 (MODIS-PARASOL-CALIPSO) and -0.15 (MODIS-CALIPSO). Liquid water path and cloud optical thickness sensitivity are respectively equal to -0.16 and -0.02.

Although we do not dispose of independent LWP estimates, we analyse the constant liquid path case sorting CDR-AI and COT-AI relationship by small interval of LWP. Resulting statistics are very compelling. CDR and COT sensitivity are shown to be dependent on LWP amount. In case of mixed layers, the larger is the liquid water path, the stronger is the cloud response. This effect does not depend on time-period and it is not observed when aerosol particles lie above clouds. Results suggest that cloud response to aerosol invigoration is no more to be considered as a simple function of aerosol concentration, but a more complicated cloud regime-dependent process.

We also analyzed aerosol impact on precipitation and cloud life-cycle. Other studies have shown that occurrence of precipitation is detectable by studying the relationship between CDR and COT. A change in the sign of the curve slope can reliably be attributed to the transition from non precipitating to precipitating clouds. In both mixed and unmixed case, precipitation was observed to occur for COT values larger than 10 and CDR between 15 and 20 μm.
For non precipitating clouds, CDR is expected to be a positive exponential function of COT. The calculated exponent is equal to 0.14 (calculated from MODIS daily product, spatially-averaged at 1 degree resolution), 0.59 (in case of mixed layers) and 0.80 (in case on unmixed layers), while the theoretical value for adiabatic clouds is 0.2. MODIS daily product has a much larger horizontal resolution than single retrievals used in mixed-unmixed statistics. At this scale (1 degree), it seems that liquid water path of non precipitating clouds respects the adiabatic assumption, although it is not valid at smaller scale (5 km).
In precipitating clouds, CDR shows an exponential function of COT, with negative exponent. According to theoretical calculations, the smaller the exponent, the more precipitating is the cloud. In case of mixed layers, the calculated exponent is -0.11, while in case of aerosol above clouds the exponent is four times smaller and equal to -0.43 (-0.47, from MODIS daily product). We infer an aerosol-induced effect on precipitation, which is inhibited in polluted clouds. This is expected to be a consequence of collision-coalescence suppression, by aerosol-driven change in cloud microphysics. Smaller droplets convert to rain less efficiently.
In conclusion, optically thin clouds are generally non-precipitating. They carry more water in clean than in polluted environments (as show by LWP-AI relationship in case of mixed and unmixed cases, when COT is about 9). As COT overpasses 10, clouds begin to precipitate and clean ones precipitate more. As a consequence, more water is removed trough rain. Beyond a COT value of approximately 12, polluted clouds are generally characterized by higher LWP than clean ones. Results are in good agreement with Albrecht's hypothesis (Albrecht, 1989).

The cloud fraction (CLF) response to aerosol-induced changes in LWP has been investigated from the analysis of CLF-AI relationship.
We found that CLF is strongly correlated to cloud top pressure, which is a good proxy to approximately estimate cloud vertical extension. If clouds form under the same quantity of aerosol but different meteorological condition, they would develop differently and present different vertical extensions. Since changes in local meteorology can produce spurious correlation between changes in CLF and AI, we decided to minimize the effect of considering clouds under different meteorological conditions sorting data by CTP, from 1000 to 600 hPa. In that way, differences between mixed and unmixed case statistics can be reliably attributed to the effect of aerosol-cloud interaction.
In case of mixed layers, we found a positive CLF sensitivity equal to 0.02, for cloud top altitude at every pressure level. This value is much smaller that those generally found from satellite-based observations (Menon et al., 2008; Quaas et al., 2009). Indeed, when aerosol lies above cloud top, cloud fraction sensitivity is large for lower clouds, (up to 0.09 at CTP = 970 hPa),

decreasing with decreasing CTP (almost zero at CTP = 750 hPa). Absorbing particle above cloud top may largely warm the atmosphere and increase the low tropospheric stability. The enhancement of LTS increases the strength of inversion, suppressing cloud vertical extent and maintaining a well-mixed and moist boundary layer. We have reason to believe that these processes may enhance low cloud cover over ocean. Aerosol radiative effect is then supposed to be a major driver of cloud fraction increase, in case of unmixed layers.
Using MODIS daily product, CLF sensitivity was much larger, equal in averaged to about 0.30. CLF-AI relationship showed a CTP dependence similar to mixed-unmixed layer statistics. From the comparison with MODIS-CALIPSO coincidences, we estimated that the contribution of aerosol-induced changes in cloud microphysics is limited to a maximum of 1/3 in total slope value, while aerosol radiative effect is the most important.

In the second part of the study, we used a rapid radiative transfer model (RRTM_SW) to quantify the aerosol direct and indirect forcing, at the top of the atmosphere, constrained by temporal and spatial (horizontal and vertical) variations in aerosol concentration and cloud properties (due to both meteorology and aerosol-induced effects). Horizontal information is supplied by MODIS aerosol and cloud daily product. Cloud top altitude is estimated from MODIS cloud top pressure, while the mutual position of aerosol and cloud layers (above, under or mixed) from CALIPSO.
Over South-East Atlantic, we estimate that unmixed layer condition is the most frequent occurring in the 58% (for aerosol above clouds) and 8% (for aerosol under clouds) of cases, while aerosol and clouds are mixed and interacting for other cases 34%.
For the direct effect, there is a competition between cooling (negative) and warming (positive), at the top of the atmosphere. Negative forcing is due to light scattering by the aerosols and is mostly expected in case of polluted environment in clear sky condition (e.g. over the Gulf of Guinea during Jan-Mar). Positive forcing is due the absorption by the same particles and only occurs if the albedo of aerosol underling surface is large enough. Over the ocean, this condition is often valid when moderately absorbing aerosols are located above cloud top (e.g. off the cast of Angola, during Jul-Sept).
Indirect effect is due to changes in cloud reflectance, induced by aerosol-cloud interaction and can be positive or negative, depending on cloud response and aerosol vertical position.
From 2005 to 2010, model simulations over South-East Atlantic region within [4N, -30N; -14E, 18E] showed a strong DRF annual cycle, with seasonal means equal to -4.3±4.3 W/m² (Jan-Mar), -2.1±2.1 (Apr-Jun), 5.6±10.5 (Jul-Sept) and 0.6±3.4 (Oct-Dec) and local peak values up to -25 W/m² (over the Gulf of Guinea during Jan-Mar) and 54 W/m² (off the coast of Angola, during Jul-Sept), within 1 degree grid box. Six year mean estimate of direct forcing averaged over the whole region is negative (net TOA cooling) and equal to -0.03±8.14 W/m². This annual value slightly decreases to -0.07±8.03 W/m², if it is re-calculated letting aerosol affecting cloud fraction. In both cases, however, regional annual mean forcing is mall. It results from the balance between the clear-sky and the cloudy-sky forcing, equal respectively to -3.42±2.81 and 3.39±7.41 W/m². The strong temporal and geographical variability of direct forcing (more in

case of cloudy-sky than clear-sky) is shown by the large standard deviation.
Cloud fraction is found to be a good predictor of radiative forcing efficiency. In particular, fractional cloud cover larger (smaller) than the critical value of 0.5 are associated with positive (negative) TOA forcing. This result is in good agreement with previous studies (Chan et al., 2009), that estimate critical cloud fraction between 0.4 and 0.5 (depending on aerosol single scattering albedo). At the same time, we find that positive DRF mostly occurs in case of aerosol particles with single scattering albedo smaller than 0.91, above cloud with optical thickness larger than 4.
Seasonal mean IRF is equal to 0.02±0.28 W/m² (Jan-Mar), -0.06±0.28 (Apr-Jun), -0.04±0.28 (Jul-Sept) and -0.09±0.34 (Oct-Dec), with local peak values up to -4.4 W/m² and 3.6 W/m² (mostly during the biomass burning season). The six year global average of IRF is negative and equal to -0.05±0.54 W/m² (TOA cooling). This value is small, but its impact on the regional radiative balance is somewhat significant, if we consider that it about 70% of the global mean forcing value produced by direct effect, also rather small. We differentiate between aerosol perturbation of radiative fluxes at TOA due to changes in CDR and LWP (cloud albedo effect) and changes in CLF (cloud life-time effect), indirect forcing from cloud albedo effect is negative and equal to -0.07±0.55 W/m², while indirect forcing from life time effect is positive and equal to 0.02±0.12 W/m².
Total aerosol forcing results from the sum of IRF and DRF. Seasonal mean TRF over the study region was found to be equal to -4.3±4.1 (Jan-Mar), -2.1±2.2 (Apr-Jun), 5.5±10.4 (Jul-Sept) and 0.5±3.4 W/m² (Oct-Dec), very close to seasonal estimates of DRF. The six year global average of TRF, over the whole region, is equal to -0.12±8.02 W/m².

In conclusion, our annual regional estimate of aerosol direct radiative forcing and cloud albedo effect is from 7 to 10 times lower than previous global estimates, reported in Lohmann and Feichter (2005) and IPCC (2007). A similar result is observed in a more recent work of Quaas et al. (2009), where several model simulations of total aerosol forcing, constrained by satellite observations show that over global ocean the observed TRF is approximately ten times stronger than over South-East Atlantic.
At the same time, regional life time effect is observed to be larger (smaller in magnitude but positive) than previous model simulations that inferred a forcing magnitude on global scale similar to cloud albedo effect (Lohmann and Feichter, 2005). This result is supposed to be a consequence of the reduced CLF sensitivity observed in our analysis, in case of aerosol-cloud interaction, with respect to the strong positive CLF-AI relationship, generally found in satellite based statistics (Quaas et al., 2009).
From the comparison with indirect forcing estimates from model simulations focusing over the study region, our results suggest that cloud albedo effect can be strongly overestimated if the decrease of cloud water loss with increasing aerosol concentration is not properly quantified.

IRF and hence TRF are then shown to be strongly dependent on cloud sensitivity, which is expected to be regime dependent. Largely different LWP responses are possible over different

regions. If humid condition above cloud top is sufficiently large, aerosol intrusion into low cloud layers can enhance LWP. At this point, cloud reflectance and cloud fraction can undergo a radiatively significant increase. Further work is needed to analyse aerosol signature on cloud property changes over the different regions, before assessing the global aerosol forcing at global scale.

Over South-East Atlantic, the occurrence of thick smoke layers from savanna burning is particularly high and depends on season. In cloudy condition, positive DRF can be as large as twice the magnitude of clear-sky negative forcing. During the biomass burning season the direct forcing, which is mostly due to aerosol absorption over cloud layers, is larger than the impact of long-lived green house gases.
The comparison with previous estimates of clear-sky and cloudy-sky direct forcing over South-East Atlantic clearly stress the importance of an accurate parametrization of cloud-aerosol vertical position and aerosol single scattering albedo to properly quantify the positive forcing due to absorbing aerosol above clouds. Otherwise, while negative forcing in clear-sky would result little affected, cloudy-sky and hence all-sky forcing is dramatically underestimated.

Model simulations, from 2005 to 2010, showed that aerosol-induced regional seasonal cooling (up to -4.85 W/m²) and warming (up to 5.90 W/m²) effects are somewhat balanced, on yearly basis. The full annual mean forcing is negative but small. Therefore, other regions of the ocean characterized by lower occurrence of absorbing particles, are expected to produce much stronger TOA cooling. Although negative forcing can counteract Earth's global warming by green house gasses, the decrease in the amount of solar radiation reaching planet surface may alter evaporation rate, decrease absolute humidity and give rise to unfavorable conditions to cloud formation. These processes can alter hydrologic cycle, in a way that is still purely understood.

In this this work, dwelling on the way aerosol affect the environment, it has also been suggested that anthropogenic pollution can directly alter cloud life cycle. As well as microphysics and optical properties, we find evidence that aerosol intrusion into low cloud systems can suppress precipitation and lead to longer-lived clouds. This stress a further possible pathway by which human activity is associated to changes in hydrologic cycle and more generally to climate change. Further work is needed to better quantify pollution impact on rain development and, more generally, on low cloud coverage enhancement (with and without physical interaction between aerosol and cloud droplets). In order to address this issue, the use of precipitable water retrievals together with low tropospheric stability estimates would be a valuable addition to our aerosol-cloud statistics.

References

Abel, S.J., E.J. Highwood, J.M. Haywood, and M.A. Stringer, 2005: The direct radiative effect of biomass burning aerosol over southern Africa. Atmos. Chem. Phys. Discuss., 5, 1165–1211.

Ackerman, A.S., M.P. Kirkpatrick, D.E. Stevens, and O.B. Toown, 2004: The impact of humidity above stratiform clouds on indirect aerosol climate forcing. Nature, 432, 1014-1017, doi:10.1038/nature03174.

Ackerman, A.S., O.B. Toon, D.E. Stevens, A.J. Heymsfield, V. Ramanathan and E.J. Welton, Reduction of tropical cloudiness by soot, Science 288 (2000), pp. 1042–1047.

Albrecht, B. A. Aerosols, Cloud Microphysics, and Fractional Cloudiness. Science, 245:1227 – 1230, 1989.

Andreae, M. O. and P. Merlet. 2001. Emission of trace gases and aerosols from biomass burning. Global Biogeochemical Cycles, 15: 955-966, 2000GB001382.

Andreae, M. O. and Rosenfeld, D.: Aerosol-cloud-precipitation interactions. Part 1: The nature and sources of cloud-active aerosols, Earth Sci. Rev., 89(1–2), 13–41, doi:10.1016/j.earscirev.2008.03.001, 2008.

Bellouin N., A. Jones, J. Haywood, and S.A. Christopher, 2008: Updated estimate of aerosol direct radiative forcing from satellite observations and comparison against the Hadley Centre climate model. J. Geophys. Res. 113:D10205, doi:10.1029/2007JD009385.

Bellouin N., O. Boucher, J. Haywood, and M. Reddy, 2005: Global estimates of aerosol direct radiative forcing from satellite measurements. Nature 438:1138-1140, doi:10.1038/nature04348.

Bennartz, R. (2007), Global assessment of marine boundary layer cloud droplet number concentration from satellite, J. Geophys. Res., 112, D02201, doi:10.1029/2006JD007547.

Brenguier, J. L., and L. Chaumat, Droplet spectra broadening in cumulus clouds. Part I: Broadening in adiabatic cores, J. Atmos. Sci., 58, 628 – 641, 2000.

Brenguier, J.-L,, H. Pawlowska, and L. Schüller, Cloud microphysical and radiative properties for parameterization and satellite monitoring of the indirect effect of aerosol on climate, J. Geophys. Res., 108(D15), 8632, doi:10.1029/2003JD002682

Brenguier, J.-L., H. Pawlowska, L. Schüller, R. Preusker, J. Fischer and Y. Fouquart (2000), Radiative properties of boundary layer clouds: droplet effective radius versus droplet concentration J. Atmos. Sci., 57, 803-821.

Bréon F.M., Doutriaux-Boucher M., 2005 : A comparison of cloud droplet radii measured from space. IEEE Trans Geosc. Rem. Sens., 43, 1796-1805.

Bréon, F.-M., D. Tanré, and S. Generoso (2002), Effect of aerosols on cloud droplet size monitored from satellite, Science, 295(5556), 834–838, doi:10.1126/science.1066434.

Cattani, E., M. J. Costa, F. Torricella, V. Levizzani, and A. M. Silva, 2006: Influence of the aerosol particles from biomass burning on cloud microphysical properties and radiative forcing. Atmos. Res., 82, 310-327.

Chand, D., Wood, R., Anderson, T. L., Satheesh, S. K., and Charlson, R. J.: Satellite-derived direct radiative effect of aerosols dependent on cloud cover, Nat. Geosci., 2, doi:10.1038/ngeo437, 2009.

Charlson, R. J., et al. (1991), Perturbation of the northern hemisphere radiative balance by backscattering from anthropogenic aerosols, Tellus, Ser. AB, 43, 152–163.

Charlson, R. J., et al. (1992), Climate forcing by anthropogenic aerosols, Science, 255, 423– 430.

Chen Lin; Guang-Yu Shi; Ling-Zhi Zhong; , "Short-Wave Direct Radiative Effect of Aerosols in the Clear-Sky over Oceans from Satellites Observations," Education Technology and Training, 2008. and 2008 International Workshop on Geoscience and Remote Sensing. ETT and GRS 2008. International Workshop on , vol.1, no., pp.567-570, 21-22 Dec. 2008 doi: 10.1109/ETTandGRS.2008.177

Christopher S., J. Zhang, Y. Kaufman, and L. Remer, 2006: Satellite-based assessment of top of atmosphere anthropogenic aerosol radiative forcing over cloud-free oceans. Geophys. Res. Lett. 33:L15816.

Chu, D. A., Y. J. Kaufman, et al. (2002). "Validation of MODIS aerosol optical depth retrieval over land." Geophysical Research Letters 29(12): art. no.-1617.

Chung C., V. Ramanathan, D. Kim, and I. Podgomy, 2005: Global anthropogenic aerosol direct forcing derived from satellite and ground-based observations. J. Geophys. Res. 110:D24207, doi:10.1029/2005JD006356.

Chylek, P., and J. Wong (1995), Effect of absorbing aerosols on global radiation budget, Geophys. Res. Lett., 22, 929– 931.

Coakley, J.A. Jr., R.L. Bernstein and P.A. Durkee, 1987: Effects of ship-track effluents on cloud reflectivity. Science, 255: 423–430.

Costantino, L., and F.-M. Bréon (2010), Analysis of aerosol-cloud interaction from multi-sensor satellite observations, Geophys. Res. Lett., 37, L11801, doi:10.1029/2009GL041828.

Decesari, S., S. Fuzzi, M.C. Facchini, M. Mircea, L. Emblico, F. Cavalli, W. Maenhaut, X. Chi, G. Schkolnik, A. Falkovich, Y. Rudich, M. Claeys, V. Pashynska, G. Vas, I. Kourtchev, R. Vermeylen, A. Hoffer, M. O. Andreae, E. Tagliavini, F. Moretti, and P. Artaxo (2005). Characterization of the organic composition of aerosols from Rondônia, Brazil, during the LBA-SMOCC 2002 experiment and its representation through model compounds. Atmos. Chem. Phys. Discuss., 5, 5687-5749.

Dubovik O, Holben BN, Eck TF, Smirnov A, Kaufman YJ, KinG MD, Tanr´ D, Slutsker I. 2002. Variability of absorption and optical properties of key aerosol types observed in worldwide locations. J. Atmos. Sci. 59: 590–608.

Durkee, P.A., K.J. Noone, R.J. Ferek et al., 2001: The impact of ship-produced aerosols on the microstructure and albedo of warm marine stratocumulus clouds: a test of MAST Hypotheses 1i and 1ii. J. Atmos. Sci., 57: 2554–2569.

Durkee, P.A., R.E. Chartier, A. Brown, E.J. Trehubenko, S.D. Rogerson, C. Skupniewicz, K.E. Nielsen, S. Platnick and M.D. King, 2000: Composite ship track characteristics. J. Atmos. Sci., 57: 2542-2553.

Edwards, D. P., Emmons, L. K., Gille, J. C., Chu, A., Attie, J. L., Giglio, L., Wood, S. W., Haywood, J., Deeter, M. N., Massie, S. T., Ziskin, D. C., and Drummond, J. R.: Satellite-observed pollution from Southern Hemisphere biomass burning, J. Geophys. Res.-Atmos., 111, D14312, doi:10.1029/2005jd006655, 2006.

Forster, P., V. Ramaswamy, P. Artaxo, T. Berntsen, R. Betts, D.W. Fahey, J. Haywood, J. Lean, D.C. Lowe, G. Myhre, J. Nganga, R. Prinn, G. Raga, M. Schulz and R. Van Dorland, 2007: Changes in Atmospheric Constituents and in Radiative Forcing. In: Climate Change 2007: The Physical Science Basis. Contribution of Working Group I to the Fourth Assessment Report of the Intergovernmental Panel on Climate Change [Solomon, S., D. Qin, M. Manning, Z. Chen, M. Marquis, K.B. Averyt, M.Tignor and H.L. Miller (eds.)]. Cambridge University Press, Cambridge, United Kingdom and New York, NY, USA.

Giglio, L., Descloitres, J., Justice, C. O. and Kaufman, Y. 2003. An enhanced contextual fire detection algorithm for MODIS. Remote Sensing of Environment 87:273-282. doi: 10.1016/S0034-4257(03)00184-6

Han, Q., W. B. Rossow, J. Zeng, and R. Welch (2002), Three different behaviors of liquid water path of water clouds in aerosol-cloud interactions, 59, 726 – 735.

Han, Q., W.B. Rossow, J. Chou, and R.M. Welch, 1998: Global survey of the relationships of cloud albedo and liquid water path with droplet size using ISCCP. J. Climate, 11, 1516-1528,

Hansen, J., M. Sato, and R. Ruedy (1997), Radiative forcing and climate response, J. Geophys. Res., 102(D6), 6831–6864, doi:10.1029/96JD03436.

Harshvardhan, Schwartz, S. E., Benkovitz, C. M., and Guo, G. Aerosol influence on cloud microphysics examined by satellite measurements and chemical transport modeling. J. Atmos. Sci. 59, 714-725 (2002).

Harshvardhan, Zhao, G., Di Girolamo, L., and Green, R.N., 2009. Satellite-observed location of stratocumulus cloudtop heights in the presence of strong inversions. IEEE Trans. Geosci. Remote Sensing, 47, doi: 10.1109/ TGRS.2008. 2005406, 1421-1428.

Hatzianastassiou, N., Matsoukas, C., Drakakis, E., Stackhouse Jr., P. W., Koepke, P., Fotiadi, A., Pavlakis, K. G., and Vardavas, I.: The direct effect of aerosols on solar radiation based on satellite observations, reanalysis datasets, and spectral aerosol optical properties from Global Aerosol Data Set (GADS), Atmos. Chem. Phys., 7, 2585–2599, http://dx.doi.org/10.5194/acp-7-2585-2007doi:10.5194/acp-7-2585-2007, 2007.

Haywood J. and K. Shine, 1995: The effect of anthropogenic sulfate and soot aerosol on the clear sky planetary radiation budget. Geophys. Res. Lett. 22:603-606.

Haywood, J. M., et al. (2008), Overview of the Dust and Biomass-burning Experiment and African Monsoon Multidisciplinary Analysis Special Observing Period-0, J. Geophys. Res., 113, D00C17, doi:10.1029/2008JD010077.

Hinds, W. C., Aerosol Technology: Properties. Behavior, and Measurement of Airborne Particles. John Wiley & Sons, New York, 1982.

Holben, B. N., T. F. Eck, et al. (1998). "AERONET - A federated instrument network and data archive for aerosol characterization." Remote Sensing of Environment 66(1): 1-16.

Ichoku, C., L. A. Remer, et al. (2003). "MODIS observation of aerosols and estimation of aerosol radiative forcing over southern Africa during SAFARI 2000." Journal of Geophysical Research-Atmospheres 108(D13): art. no.-8499.

Ichoku, C., Y. J. Kaufman, L. A. Remer, and R. Levy, 2004: Global aerosol remote sensing from MODIS. Advances in Space Research, 34 (2004), 820-827.

Johnson, BT; Shine, KP; Forster, PM (2004) The semi-direct aerosol effect: Impact of absorbing aerosols on marine stratocumulus, Q J ROY METEOR SOC, 130, pp.1407-1422. doi:10.1256/qj.03.61

Kaskaoutis, D. G., Shailesh Kumar Kharol, N. Sifakis, P. T. Nastos, Anu Rani Sharma, K. V. S. Badarinath and H. D. Kambezidis, Satellite monitoring of the biomass burning aerosols during the wildfires of August 2007 in Greece: Climate implications, Atmospheric Environment, vol. 45, pp. 716-726, doi: 10.1016/j.atmosenv.2010.09.043, 2011.

Kaskaoutis, D. G., Kumar Kharol, S., Sinha, P. R., Singh, R. P., Kambezidis, H. D., Rani Sharma, A., and Badarinath, K. V. S.: Extremely large anthropogenic aerosol component over the Bay of Bengal during winter season, Atmos. Chem. Phys. Discuss., 11, 7851-7907, doi:10.5194/acpd-11-7851-2011, 2011.

Kaskaoutis, D. G., Shailesh Kumar Kharol, P. R. Sinha, R. P. Singh, H. D. Kambezidis, Anu Rani Sharma and K. V. S. Badarinath, Extremely large anthropogenic-aerosol contribution to total aerosol load over the Bay of Bengal during winter season, Atmospheric Chemistry and Physics , vol. 11, pp. 7097-7117, doi:10.5194/acp-11-

7097-2011, 2011.

Kaufman Y., L. Remer, D. Tanré, R. Li, R. Kleidman, S. Mattoo, R. Levy, T. Eck, B. Holben, C. Ichoku, J. Martins, and I. Koren, 2005b: A critical examination of the residual cloud contamination and diurnal sampling effects on MODIS estimates of aerosol over ocean. IEEE Trans. On Geoscience & Remote Sensing, 43:2886-2897.

Kaufman Y., O. Boucher, D. Tanré, M. Chin, L. Remer, and T. Takemura, 2005a: Aerosol anthropogenic component estimated from satellite data. Geophys. Res. Let. 32: L17804, doi:10.1029/2005GL023125.

Kaufman, Y. and Tanré, D.: Algorithms for remote sensing of tropospheric aerosol from MODIS. NASA MODIS Algorithm Theoretical Basis Document, Goddard Space Flight Center, 85~pp., 1998.

Kaufman, Y. J. and Fraser, R. S.: The effect of smoke particles on clouds and climate forcing, Science, 277, 1636–1639, 1997.

Kaufman, Y. J., and I. Koren (2006), Smoke and pollution aerosol effect on cloud cover, Science, 313, 655 – 658.

Kaufman, Y. J., D. Tanré, et al. (1997). "Operational remote sensing of tropospheric aerosol over land from EOS moderate resolution imaging spectroradiometer." Journal of Geophysical Research-Atmospheres 102(D14): 17051-17067.

Kaufman, Y. J., I. Koren, L. A. Remer, D. Rosenfeld, and Y. Rudich (2005), The effect of smoke, dust and pollution aerosol on shallow cloud development over the Atlantic Ocean, Proc. Natl. Acad. Sci. U. S. A., 102, 11,207–11,212, doi:10.1073/pnas.0505191102.

Kaufman, Y. J., R. S. Fraser, and R. L. Mahoney, Fossil fuel and biomass burning effect on climate-Heating or cooling?,J. Clim., 4, 578-588, 1991.

Kaufman, Yoram J., Teruyuki Nakajima, 1993: Effect of Amazon Smoke on Cloud Microphysics and Albedo-Analysis from Satellite Imagery. J. Appl. Meteor., 32, 729–744. doi: http://dx.doi.org/10.1175/1520-0450(1993)032<0729:EOASOC>2.0.CO;2

Keil, A., and J. M. Haywood (2003), Solar radiative forcing by biomass burning aerosol particles during SAFARI 2000: A case study based on measured aerosol and cloud properties, J. Geophys. Res., 108(D13), 8467, doi:10.1029/2002JD002315.

Khan, R. A., Chen, Y., Nelson, D. L., Leung, F.-Y., Li, Q., Diner, D., and Logan, J. A., (2008), Wildfire smoke injection heights: Two perspectives from space, Geophys. Res. 432 Letters, 35(04)

Kim, S.-W., Berthier, S., Raut, J.-C., Chazette, P., Dulac, F., and Yoon, S.-C., (2008), Validation of aerosol and cloud layer structures from the space-borne lidar CALIOP using a ground-based lidar in Seoul, Korea, Atmos. Chem. Phys., 8, 3705-3720.

King, M. D., W. P. Menzel, Y. J. Kaufman, D. Tanré et al., 2003: Cloud and aerosol properties, precipitable water, and profiles of temperature and water vapor from MODIS. IEEE Trans. Geosci. Remote Sens., 41, 442-458.

King, Tsay, Platnick, Wang, & Liou, 1998: Cloud Retrieval Algorithms for MODIS: Optical Thickness, Effective Particle Radius, and Thermodynamic Phase.

Klein, S. A., and D. L. Hartmann, 1993: The seasonal cycle of low strati-form clouds. J. Climate, 6, 1588–1606.

Klein, Stephen A., 1997: Synoptic variability of low-cloud properties and meteorological parameters in the subtropical trade wind boundary layer. J. Climate, 10, 2018–2039.

Kobayashi, T., (2007), Significant differences in the cloud droplet effective radius between nonprecipitating

and precipitating clouds, Geophys. Res. Lett., 34, L15811, doi:10.1029/2007GL029606.

Labonne, M., F.-M. Bréon, and F. Chevallier (2007), Injection height of biomass burning aerosols as seen from a spaceborne lidar, Geophys. Res. Lett., 34, L11806, doi:10.1029/2007GL029311.

Lebsock, M. D., G. L. Stephens, and C. Kummerow (2008), Multisensor satellite observations of aerosol effects on warm clouds, J. Geophys. Res., 113, D15205, doi:10.1029/2008JD009876.

Lebsock, M.D., G.L. Stephens, and C. Kummerow (2008), Multisensor satellite observations of aerosol effects on warm clouds, J. Geophys. Res., 113, D15205, doi:10.1029/2008JD009876.

Lee, S. S., J. E. Penner, and S. M. Saleeby (2009), Aerosol effects on liquid-water path of thin stratocumulus clouds, J. Geophys. Res., 114, D07204, doi:10.1029/2008JD010513.

Levin, Z. and Cotton, W.: Aerosol Pollution Impact on Precipitation: A Scientific Review, Springer, New York, 2009.

Levy, R. C., L. A. Remer, and O. Dubovik, (2007a) Global aerosol optical properties and application to MODIS aerosol retrieval over land . J. Geophys. Res., 112, D13210, doi:10.1029/2006JD007815.

Levy, R. C., L. A. Remer, D. Tanré, Y. J. Kaufman, C. Ichoku, B. N. Holben, J. M. Livingston, P. B. Russell, and H. Maring, 2003: Evaluation of the Moderate Resolution Imaging Spectroradiometer (MODIS) retrievals of dust aerosol over the ocean during PRIDE. J. Geophys. Res., 108, 8594, doi:10.1029/2002JD002460.

Levy, R. C., L. Remer, S. Mattoo, E. Vermote, and Y. J. Kaufman, (2007b). Second-generation algorithm for retrieving aerosol properties over land from MODIS spectral reflectance. J. Geophys. Res., 112, D13211, doi:10.1029/2006JD007811.

Loeb, N. G., and G. L. Schuster (2008), An observational study of the relationship between cloud, aerosol and meteorology in broken low-level cloud conditions, J. Geophys. Res., 113, D14214, doi:10.1029/2007JD009763.

Lohmann, U., and J. Feichter (2005), Global indirect aerosol effects: a review, Atmos. Chem. Phys., 5, 715–737.

Lohmann, U., G. Tselioudis, and C. Tyler, 2000: Why is the cloud albedo-particle size relationship different in optically thick and optically thin clouds? Geophys. Res. Lett., 27, 1099 1102, doi:10.1029/1999GL011098.

M. J. Garay, S. P. de Szoeke, and C. M. Moroney (2008), Comparison of marine stratocumulus cloud top heights in the southeastern Pacific retrieved from satellites with coincident ship-based observations, J. Geophys. Res., 113, D18204, doi:10.1029/2008JD009975.

Marshak A, and A. B. Davis (2005). Horizontal Fluxes and Radiative Smoothing 3D Radiative Transfer in Cloudy Atmospheres, ed., A.M. Marshak and A.B. Davis, Springer, c2005, 686pp

Marshak A., G. Wen, J. Coakley, L. Remer, N. G. Loeb, and R.F. Cahalan (2008). A simple model for the cloud adjacency effect and the apparent bluing of aerosols near clouds J. Geophys. Res., D14S17, 113, doi :10.1029/2007JD009196

Martins, J. V., D. Tanré, et al. (2002). "MODIS Cloud screening for remote sensing of aerosols over oceans using spatial variability." Geophysical Research Letters 29(12): art. no.-1619.

Matsui T., and R. Pielke, Sr., 2006: Measurement-based estimation of the spatial gradient of aerosol radiative forcing. Geophys. Res. Lett. 33: L11813, doi:10.1029/2006GL025974.

Matsui, T., H. Masunaga, S. M. Kreidenweis, R. A. Pielke Sr., W.-K. Tao, M. Chin, and Y. J. Kaufman (2006), Satellite-based assessment of marine low cloud variability associated with aerosol, atmospheric stability, and the diurnal cycle, J. Geophys. Res., 111, D17204, doi:10.1029/ 2005JD006097.

McComiskey, A, SE Schwartz, B Schmid, H Guan, ER Lewis, P Ricchiazzi, and JA Ogren. 2008. "Direct

aerosol forcing: Calculation from observables and sensitivities to inputs." Journal of Geophysical Research 113, D09202, doi:10.1029/2007JD009170.

McFiggans, G., P. Artaxo, U. Baltensperger, H. Coe, M. C. Facchini, G. Feingold, S. Fuzzi, M. Gysel, A. Laaksonen, U. Lohmann, T. F. Mentel, D. M. Murphy, C. D. O'Dowd, J. R. Snider, and E. Weingartner. The effect of physical and chemical aerosol properties on warm cloud droplet activation. Atmospheric Chemistry and Physics, 6(9):2593–2649, 2006.

McGill, M. J., M. A. Vaughan, C. R. Trepte, W. D. Hart, D. L. Hlavka, D. M. Winker, and R. Kuehn (2007), Airborne validation of spatial properties measured by the CALIPSO lidar, J. Geophys. Res., 112, D20201, doi:10.1029/2007JD008768.

Menon, S., A.D. Del Genio, Y. Kaufman, R. Bennartz, D. Koch, N. Loeb, and D. Orlikowski, 2008: Analyzing signatures of aerosol-cloud interactions from satellite retrievals and the GISS GCM to constrain the aerosol indirect effect. J. Geophys. Res., 113, D14S22, doi:10.1029/2007JD009442.

Menzel, Frey, Baum, 2010: Cloud Top Properties and Cloud Phase - Algorithm Theoretical Basis Document.

Menzel, WP, Frey, RA, Zhang, H, Wylie, DP, Moeller, CC, Holz, RE, Maddux, B, Baum, BA, Strabala, KI, Gumley, LE (2008). MODIS global cloud-top pressure and amount estimation: Algorithm description and results. JOURNAL OF APPLIED METEOROLOGY AND CLIMATOLOGY, 47(4), 1175-1198.

Mielonen, T., Arola, A., Komppula, M., Kukkonen, J., Koskinen, J., de Leeuw, G., and Lehtinen, K. E. J., Comparison of CALIOP level 2 aerosol subtypes to aerosol types derived from AERONET inversion data, Geophys. Res. Lett., 36, L18804, doi:10.1029/2009GL039609, 2009.

Myhre, G., T.K. Berntsen, J.M. Haywood, J.K. Sundet, B.N. Holben, M. Johnsrud, and F. Stordal, 2003, Modelling the solar radiative impact of aerosols from biomass burning during the Southern African Regional Science Initiative (SAFARI-2000) experiment, J. Geophys. Res.,108, 8501, doi:10.1029/2002JD002313.

Nakajima, T., A. Higurashi, K. Kawamoto, and J. E. Penner, A possible of correlation between satellite-derived cloud and aerosol microphysical parameters, Geophys. Res. Lett., 28, 1171 – 1174, 2001.

Nakajima, T., and M. D. King, 1990: Determination of the optical thickness and effective particle radius of clouds from reflected solar radiation measurements. Part I: Theory. J. Atmos. Sci., 47, 1878-1893.

Nemesure S. and Schwartz S. E., Effect of Absorbing Aerosol on Shortwave Radiative Forcing of Climate. 8th Atmospheric Radiation Measurement (ARM) Science Team Meeting, Tucson, AZ, Mar. 23-26, 1998.

Pawlowska, H., and J. L. Brenguier, 1996: A study of the microphysical structure of stratocumulus clouds. Proc. 12th Int. Conf. on Clouds and Precipitation, Zurich, Switzerland, International Commission on Clouds and Precipitation (ICCP) and International Association of Meteorology and Atmospheric Science (IAMAS), 23–26

Pawlowska, H., and J. L. Brenguier, Microphysical properties of stratocu mulus clouds during ACE-2, Tellus, Ser. B, 52, 867 – 886, 2000.

Penner J., R. Dickinson, and C. O'Neill, 1992: Effects of aerosol from biomass burning on the global radiation budget. Science 256:1432-1434.

Platnick, S., and S. Twomey, 1994: Determining the susceptibility of cloud albedo to changes in droplet concentration with the advanced very high resolution radiometer. J. Appl. Meteorol., 33, 334-347.

Platnick, S., and S. Twomey, Determining the susceptibility of cloud albedo to changes in droplet concentrations with the Advanced Very High Resolution Radiometer, J. Appl. Meteorol., 33, 334 –347, 1994.

Platnick, S., M. D. King, S. A. Ackerman, W. P. Menzel, B. A. Baum, J. C. Riedi, and R. A. Frey, 2003: The MODIS cloud products: Algorithms and examples from Terra. IEEE Trans. Geosci. Remote Sens., 41, 459-473.

Pruppacher, H.R., Klett, J.D., 1997. Microphysics of Clouds and Precipitation. Reidel, Dordrecht. 954 pp.

Quaas, J., B. Stevens, P. Stier, and U. Lohmann, 2010: Interpreting the cloud cover – aerosol optical depth relationship found in satellite data using the general circulation model. Atmos. Chem. Phys., 10, 6129 - 6135. 10.5194/acp-10-6129-2010.

Quaas, J., Ming, Y., Menon, S., Takemura, T., Wang, M., Penner, J. E., Gettelman, A., Lohmann, U., Bellouin, N., Boucher, O., Sayer, A. M., Thomas, G. E., McComiskey, A., Feingold, G., Hoose, C., Kristjánsson, J. E., Liu, X., Balkanski, Y., Donner, L. J., Ginoux, P. A., Stier, P., Grandey, B., Feichter, J., Sednev, I., Bauer, S. E., Koch, D., Grainger, R. G., Kirkevåg, A., Iversen, T., Seland, Ø., Easter, R., Ghan, S. J., Rasch, P. J., Morrison, H., Lamarque, J.-F., Iacono, M. J., Kinne, S., and Schulz, M.: Aerosol indirect effects – general circulation model intercomparison and evaluation with satellite data, Atmos. Chem. Phys., 9, 8697-8717, doi:10.5194/acp-9-8697-2009, 2009.

Quaas, J., O. Boucher, and U. Lohmann, Constraining the total aerosol indirect effect in the LMDZ and ECHAM4 GCMs using MODIS satellite data, Atmos. Chem. Phys., 6, 947–955, 2006.

Quaas, J., O. Boucher, N. Bellouin, and S. Kinne (2008), Satellite-based estimate of the direct and indirect aerosol climate forcing, J. Geophys. Res., 113, D05204, doi:10.1029/2007JD008962.

Queface AJ, Piketh SJ, Annegarn HJ, Holben BN, Uthui RJ (2003) Retrieval of aerosol optical thickness and size distribution from the CIMEL sun photometer over Inhaca island, Mozambique. J Geophys Res 108:8509. doi:8510.1029/2002JD002374

Ramana, M. V., Ramanathan, V., Feng, Y. et al. (2010). "Warming influenced by the ratio of black carbon to sulphate and the black-carbon source," Nature Geoscience 3, 542-545. DOI: 10.1038/ngeo918.

Raut, J.-C. and Chazette, P.: Radiative budget in the presence of multi-layered aerosol structures in the framework of AMMA SOP-0, Atmos. Chem. Phys., 8, 6839-6864, doi:10.5194/acp-8-6839-2008, 2008.

Reid, J. S., Koppmann, R., Eck, T. F., and Eleuterio, D. P: A review of biomass burning emis- sions part II: intensive physical properties of biomass burning particles, Atmos. Chem. Phys., 5, 799–825, 2005.

Remer, L. A., D. Tanré, et al. Validation of MODIS aerosol retrieval over ocean, Geophys. Res. Lett., 29,8008, doi:10.1029/2001GL013204, 2002.

Remer, L. A., Y. J. Kaufman, et al. (2005). "The MODIS aerosol algorithm, products, and validation." Journal of the Atmospheric Sciences 62(4): 947-973.

Remer, Tanre, Kaufman, Levy, & Mattoo, 2009: Algorithm for Remote Sensing of Tropospheric Aerosol from MODIS for Collection 005: Revision 2 provide more recent descriptions.

Sakaeda, N., R. Wood, and P. J. Rasch (2011), Direct and semidirect aerosol effects of southern African biomass burning aerosol, J. Geophys. Res., 116, D12205, doi:10.1029/2010JD015540.

Schüller, L., J.-L. Brenguier, and H. Pawlowska (2003), Retrieval of microphysical, geometrical, and radiative properties of marine stratocumulus from remote sensing, J. Geophys. Res., 108(D15), 8631, doi:10.1029/2002JD002680.

Schulz M., C. Textor, S. Kinne, et al., 2006: Radiative forcing by aerosols as derived from the AeroCom present-day and pre-industrial simulations. Atmos. Chem. Phys., 6:5225-5246.

Schwartz, S. E., Harshvardhan, and Benkovitz, C. M. Influence of anthropogenic aerosol on cloud optical depth and albedo shown by satellite measurements and chemical transport modeling. Proc. Natl. Acad. Sci. 99, 1784-1789 (2002).

Sekiguchi, M., T. Nakajima, K. Suzuki, K. Kawamoto, A. Higurashi, D. Rosenfeld, I. Sano, and S. Mukai

(2003), A study of the direct and indirect effects of aerosols using global satellite data sets of aerosol and cloud parameters, J. Geophys. Res., 108(D22), 4699, doi:10.1029/ 2002JD003359.

Smirnov A, Holben BN, Kaufman YJ, Dubovik O, Eck TF, Slutsker I, Pietras C, Halthore RN. 2002. Optical properties of atmospheric aerosol in maritime environments. Journal of Atmospheric Sciences 59: 501–523.

Squires, P. (1958), The Microstructure and Colloidal Stability of Warm Clouds. Tellus, 10: 256–261. doi: 10.1111/j.2153-3490.1958.tb02011.x

Stamnes, K., S-Chee Tsay, Warren Wiscombe, and Kolf Jayaweera, "Numerically stable algorithm for discrete-ordinate-method radiative transfer in multiple scattering and emitting layered media," Appl. Opt. 27, 2502-2509 (1988)

Stephens G; Vane DG; Boain RJ; Mace GG; Sassen K; Wang Z; Illingworth AJ; O'Connor EJ; Rossow WB; Durden SL; Miller SD; Austin RT; Benedetti A; Mitrescu C; The CloudSat Science Team (2002). The CloudSat mission and the A-Train. Bull Am Meteorol Soc, 83: 1771-1790.

Stevens B, Feingold G (2009) Untangling aerosol effects on clouds and precipitation in a buffered system. Nature 461, doi:10.1038/nature0828.

Stevens, B. and Feingold, G. (2009) Untangling aerosol effects on clouds and precipitation in a buffered system, Nature, 461, 607-613, doi:10.1038/nature08281

Tanré, D., M. Herman, and Y. Kaufman, 1996: Information on the aerosol size distribution contained in the solar reflected spectral radiances. J. Geophys. Res., 101, 19043-19060

Tanré, D., Y. J. Kaufman, et al. (1997). "Remote sensing of aerosol properties over oceans using the MODIS/EOS spectral radiances." Journal of Geophysical Research-Atmospheres 102(D14):16971-16988.

Thieuleux, F., Moulin, C., Bréon, F. M., Maignan, F., Poitou, J., and Tanré, D.: Remote sensing of aerosols over the oceans using MSG/SEVIRI imagery, Ann. Geophys., 23, 3561-3568, doi:10.5194/angeo-23-3561-2005, 2005.

Toledano, C., V. E. Cachorro, M. Sorribas, A. Berjon, B. A. de la Morena, A. M. de Frutos, and P. Gouloub, 2007: Aerosol optical depth and Angstrom exponent climatology at El Arenosillo AERONET site (Huelva, Spain). Quart. J. Roy. Meteor. Soc., 133, doi:10.1002/qj.54.

Twohy, C. H., M. D. Petters, J. R. Snider, B. Stevens, W. Tahnk, M. Wetzel, L. Russell, and F. Burnet (2005), Evaluation of the aerosol indirect effect in marine stratocumulus clouds: Droplet number, size, liquid water path, and radiative impact, J. Geophys. Res., 110, D08203, doi:10.1029/2004JD005116.

Twomey, S. (1984), An assessment of the impact of pollution on global cloud albedo, Tellus, Ser. B, 36, 356 – 366.

Twomey, S. Pollution and the planetary albedo. Atmos. Environ., 8:1251 – 1256, 1974.

Twomey, S., and J. Warner, 1967: Comparison of measurements of cloud droplets and cloud nuclei. J. Atmos. Sci., 24, 702-703.

Twomey, S., The influence of pollution on the shortwave albedo of clouds, J. Atmos. Sci., 34, 1149 – 1152, 1977.

Varnai, T. & Marshak, A. MODIS observations of enhanced clear sky reflectance near clouds. Geophys. Res. Lett. 36, L06807 (2009).

Vaughan, M. A., K. A. Powell, D. M. Winker, C. A. Hostetler, R. E. Kuehn, W. H. Hunt, B. J. Getzewich, S. A. Young, Z. Liu, and M. J. McGill (2009), Fully automated detection of cloud and aerosol layers in the CALIPSO lidar measurements, J. Atmos. Oceanic Technol., 26 (10), 2034–2050.

Vaughan, M., S. Young, D. Winker, K. Powell, A. Omar, Z. Liu, Y. Hu, and C. Hostetler (2004), Fully automated analysis of space-based lidar data: An overview of the CALIPSO retrieval algorithms and data products, Proc. SPIE Int. Soc. Opt. Eng., 5575, 16 – 30.

Vehkamäki, H., 2006. Classical Nucleation Theory in Multicomponent Systems. Springer, Berlin, New York. 176 pp.

Vergaz R, Cachorro VE, de Frutos AM, Vilaplana JM, de la Morena BA. 2005. Columnar characteristics of aerosols by spectroradiometer measurements in the maritime area of the Cadiz Gulf (Spain). Int. J. Climatol. 25: 1781–1804.

Warner, J. 1968: A reduction in rainfall associated with smoke from sugar-cane fires: an inadvertent weather modification. J. Appl. Meteorol. 7: 247–251.

Warner, J., and S.A. Twomey (1967). The production of cloud nuclei by cane fires and the effect on cloud droplet concentration. J Atmos Sci 24: 704-06.

Wen, G., A. Marshak, and R. F. Cahalan (2008), Importance of molecular Rayleigh scattering in the enhancement of clear sky reflectance in the vicinity of boundary layer cumulus clouds, J. Geophys. Res., 113, D24207, doi:10.1029/2008JD010592.

Wilcox, E. M., Stratocumulus cloud thickening beneath layers of absorbing smoke aerosol. Atmos. Chem. Phys., 10, 11769-11777,doi:10.5194/acp-10-11769-2010, 2010.

Winker, D. M., B. H. Hunt, and M. J. McGill (2007), Initial performance assessment of CALIOP, Geophys. Res. Lett., 34, L19803, doi:10.1029/2007GL030135.

Winker, D. M., J. R. Pelon, and M. P. McCormick (2003), The CALIPSO mission: Spaceborne lidar for observation of aerosols and clouds, in Lidar Remote Sensing for Industry and Environment Monitoring III, edited by U. Singh, T. Itabe, and Z. Liu, Proc. SPIE Int. Soc. Opt. Eng., 4893, 1 – 11.

Winker, D. M., M. A. Vaughan, A. Omar, Y. Hu, K. A. Powell, Z. Liu, W. H. Hunt, and S. A. Young (2009), Overview of the CALIPSO mission and CALIOP data processing algorithms, J. Atmos. Oceanic Technol., 26(11), 2310–2323.

Winker, D. M., W. H. Hunt, and C. A. Hostetler (2004), Status and performance of the CALIOP lidar, Proc. SPIE Int. Soc. Opt. Eng., 5575, 8 – 15.

Wood, R., and D. L. Hartmann, 2006: Spatial variability of liquid water path in marine boundary layer clouds: The importance of mesoscale cellular convection. J. Climate, 19, 1748-1764.

Yu H., Y. Kaufman, M. Chin, G. Feingold, L. Remer, T. Anderson, Y. Balkanski, N. Bellouin, O. Boucher, S. Christopher, P. DeCola, R. Kahn, D. Koch, N. Loeb, M. S. Reddy, M. Schulz, T. Takemura, and M. Zhou, 2006: A review of measurement-based assessments of aerosol direct radiative effect and forcing. Atmos. Chem . Phys. 6:613-666.

Zhao T. X.-P., H. Yu, I. Laszlo, M. Chin, and W.C. Conant, 2008: Derivation of component aerosol direct radiative forcing at the top of atmosphere for clear-sky oceans. J. Quant. Spectro. Rad. Trans. 109:1162-1186.